

# Far Beyond Anodic Stabilities of Organic Electrolytes – the 5V Cathode $\text{LiNi}_{0.5}\text{Mn}_{1.5}\text{O}_4$

## Doctoral Thesis

**Dipl.-Ing. Colin God**

Submitted in fulfillment for doctors degree of technical science

This work has been carried out under the supervision of

**Univ.-Prof. Dipl.-Ing. Dr. techn. Franz Stelzer**

at the

Institute for Chemistry and Technology of Materials (ICTM)

Graz University of Technology

Stremayrgasse 9/II

8010 Graz, AUSTRIA

In cooperation with BASF – The Chemical Company

67056 Ludwigshafen, Germany

September 2011

Deutsche Fassung:

Beschluss der Curricula-Kommission für Bachelor-, Master- und Diplomstudien vom 10.11.2008,  
Genehmigung des Senates am 01.12.2008

## EIDESSTATTLICHE ERKLÄRUNG

Ich erkläre an Eides statt, dass ich die vorliegende Arbeit selbstständig verfasst, andere als die angegebenen Quellen/Hilfsmittel nicht benutzt, und die den benutzten Quellen wörtlich und inhaltlich entnommene Stellen als solche kenntlich gemacht habe.

Graz, am .....

.....

(Unterschrift)

Englische Fassung:

## STATUTORY DECLARATION

I declare that I have authored this thesis independently, that I have not used other than the declared sources/resources, and that I have explicitly marked all material which has been quoted either literally or by content from the used sources.

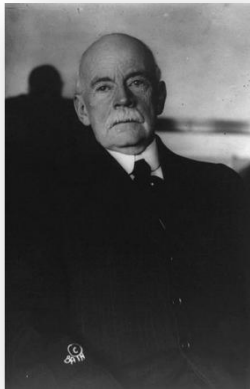
.....

date

.....

(signature)

## Matter of Opinion



“Everything that can be invented has been invented.”  
**(Charles Duell, Commissioner of US Patent Office, 1899)** <sup>(1)</sup>



“I think there is a world market for maybe five computers.”  
**(Thomas J. Watson, CEO of IBM, 1943)** <sup>(2), (3)</sup>



„Alle grundlegenden Probleme der Chemie sind im Wesentlichen schon gelöst“, sagte Christoph Kratky, Präsident des Wissenschaftsfonds, bei der Wiener Eröffnung des (von der UNO ausgerufenen) „Jahres der Chemie“. Er ist selbst Chemiker, er darf sagen, was offensichtlich ist: Im Gegensatz zu Physik und Biologie sind in der Chemie keine Rätsel mehr zu lösen, auch mit großen Überraschungen ist nicht zu rechnen. Man weiß, wie Atome und Moleküle reagieren und, so Kratky (etwas übertreibend), „man kann praktisch alles herstellen, wofür man eine Formel aufschreiben kann“. So werde die Chemie zur „angewandten Disziplin“, Chemiker wenden sich zunehmend benachbarten Fächern (Materialwissenschaften, Molekularbiologie etc.) zu. So erklärte Kratky auch, dass nur mehr sechs Prozent des FWF-Geldes in Chemieprojekte gehen, vor 20 Jahren waren es mehr als doppelt so viel.

**(Dr. Christoph Kratky, President of FWF, taken literally from the newspaper article in "Die Presse", Print-Ausgabe, 05.02.2011)** <sup>(4), (5)</sup>



„... powerhouse of energy, whipping up a fury, dominating flurry, we create the battery ...”  
**(Metallica, lyrics of "Battery" from the album "Master of Puppets", 1986)** <sup>(6)</sup>

## *Acknowledgement*

I want to express my gratitude to my supervisor, the head of the Institute for Chemistry and Technology of Materials (ICTM) at the University of Technology Graz, Univ.-Prof. Dipl.-Ing. Dr.techn. Franz Stelzer for his valuable guidance and support during my PhD time, which enabled me to work independently.

Many thanks go to Dipl.-Ing. Dr.techn. Stefan Koller not merely for proof-reading my doctoral thesis, but rather for the lots of excellent and marvelous discussions, which were conducive to the successful outcome of this present work.

A special thank goes to the “BASF – The chemical company” for the financial support of this doctoral thesis. Particularly I would like to thank Dipl.-Ing. Dr.techn. Klaus Leitner and Dr. Martin Schulz-Dobrick providing me with chemical and battery materials at any time. But principally I am deeply grateful to Dipl.-Ing. Dr.techn. Klaus Leitner for his serenity during interchanging scientific informations, which led to valuable suggestions and exciting discussions.

I want to say a pure and simple “thank you” to Dipl.-Ing. Cornelia Bayer for her encouragement during strenuous times and above all for her endeavors to run interference for me! Moreover I would like to thank her for the numerous technical arguments and words of advice shedding light on different problems of my work.

In addition, I would like to mention and thank my friends for laughter within my leisure time making it possible to live down hard times of my study! Special thanks go to my oldest friend Dipl.-Ing. Christoph Stangl not only for his long-term friendship, but also for the technical discussions and point of views within this interesting science field.

Furthermore I have to thank all my colleagues of the former LPG group (most of them belong to the Varta Micro Innovation by now) for their fellowship providing an enjoyable atmosphere; Andrea Droisner, Katharina Gruber, Dipl.-Ing. BSc Laura Kaltenböck, MSc Sandra Pötz, Dipl.-Ing. Dr.techn. Barbara Rupp, Dipl.-Ing. BSc Michaela Scharfegger, Dipl.-Ing. Dr.techn. Harald Kren, Dipl.-Ing. Dr.techn. Martin Schmuck, Dipl.-Ing. Dr.techn. Bernd Fuchsbichler, Dipl.-Ing. Roland Hohl and Dipl.-Ing. Dr.techn. Michael Sternad.

I would like to express particular thanks to our technician Johann Schlegl for his great patience trying to convert my wishes and ideas concerning technical futures scores of times.

I won't forget to thank our (non-) scientific/technical staff of the ICTM, who treated my wishes and needs equal patiently; Christina Albering, Ing. Diana Cujez, Dipl.-Ing. (FH) Mathilde Frießnegg, Liane Hochgatterer, Manuela Pögl, Margareta Maierhofer, Rosina Kerschbaumer and Angela Hampl.

Last but not least, I would particularly like to thank my parents and my brother, whose support has enabled me to study and naturally a “thank you” for being there for me at any time!

Calling all, thank you very much once again!

## ***Abstract***

Lithium-Ion-Batteries are outstanding within the field of electrochemical energy storage technologies due to their high energy density and excellent cycling stability. They are the most promising system as energy source for hybrid electric- (HEV) and electric-vehicles (EV).

However, improvements of these systems are still necessary to meet the high energy demand of HEV & EV applications. One strategy to increase the battery energy density is the use of “new” cathode materials with 5 V working voltage. An auspicious cathode material represents the modification of the spinel-structured  $\text{LiMn}_2\text{O}_4$  with the general composition  $\text{LiM}_x\text{Mn}_{2-x}\text{O}_4$  (M = transition metal). This modification increases the average discharge voltage to 4.7 V, whereby in combination with a common graphite anode a theoretical specific energy of about  $470 \text{ Wh}\cdot\text{kg}^{-1}$  could be achieved.

Many investigations concerning these so called “5 V cathode materials” have been done already and due to the high working potential of this cathode material the oxidative stability of the electrolyte system plays an important role. In the present work the anodic stability of carbonate based electrolyte systems are focused. To achieve knowledge not only on the decomposition potential but also on the reaction mechanism cyclic voltammetry was combined with “in-situ” mass spectrometry. Unfortunately, this method is not sensitive enough to provide information on the small quantities of gas that are formed at the working potential of the material. For quantification the pressure gain in a modified Swagelok®-cell during cycling was tested, which sheds also light on the amount of decomposed electrolyte.

## *Kurzfassung*

Aufgrund ihrer hohen Energiedichte und exzellenten Zyklenstabilität nehmen Lithium-Ionen-Batterien eine herausragende Position innerhalb aller elektrochemischen Energiespeichersysteme ein. Dadurch stellen sie auch die vielversprechendste Energiequelle für Hybridfahrzeuge (HEV) und rein elektrisch betriebene Fahrzeuge (EV) dar.

Um den hohen Energieanforderungen für HEV und EV aber gerecht werden zu können, müssen noch immer Verbesserungen dieser Speichersysteme erzielt werden. Eine mögliche Strategie zur Energieerhöhung stellt die Verwendung eines „neuen“ Aktivmaterials für Kathoden dar, deren Arbeitspotential bei 5 V liegt. Innerhalb dieser Materialien sticht die Modifikation des  $\text{LiMn}_2\text{O}_4$  Spinells hervor, welche die allgemeine Summenformel  $\text{LiM}_x\text{Mn}_{2-x}\text{O}_4$  besitzt (M = Übergangsmetall). Diese Verbindung hebt das Arbeitspotential auf 4,7 V an und in Kombination mit herkömmlichem Graphit als Anode kann theoretisch eine spezifische Energie von  $470 \text{ Wh}\cdot\text{kg}^{-1}$  erreicht werden.

Bisher wurden viele elektrochemische Untersuchungen an diesen so genannten „5 V Kathodenmaterialien“ unternommen, wobei die oxidative Stabilitätsgrenze des Elektrolytsystems aufgrund der hohen Arbeitsspannung dieses Kathodenmaterials eine wichtige Rolle spielt. Die vorliegende Arbeit widmet sich der Untersuchung der oxidativen Stabilität Kohlensäureester basierender Elektrolytsysteme. Es sollen aber nicht nur Informationen über deren Zersetzungsspannung erhalten werden, sondern auch über deren Reaktionsprodukte, weshalb Zyklovoltammetrie mit einem Massenspektrometer „in-situ“ gekoppelt wurde. Unglücklicherweise ist diese Untersuchungsmethode nicht geeignet, um auch Informationen über die Quantität der Gasmengen zu sammeln, die bei diesem Potential gebildet werden. Aus diesem Grund wurde während der Zyklisierung der Druckanstieg in einer modifizierten Swagelok®-Zelle gemessen, um einen Blick auf die Quantität der Zersetzungsprodukte werfen zu können.

# Contents

---

<b>1</b>	<b>Introduction .....</b>	<b>1</b>
<b>2</b>	<b>Theoretical Principles .....</b>	<b>4</b>
2.1	Elementary Electrochemistry .....	4
2.2	Thermodynamic Point of View .....	6
2.2.1	General Remarks .....	6
2.2.2	Kinetic Aspects .....	10
2.2.2.1	The Electric Double Layer .....	10
2.2.2.2	The Butler-Volmer Equation.....	11
2.2.2.3	Different Types of Overpotentials.....	14
2.3	Lithium-Batteries .....	17
2.3.1	Key Figures of Batteries.....	17
2.3.2	The Importance of Lithium and Its Effect to Battery Technologies .....	18
2.3.3	Setup of Lithium-Ion-Batteries.....	20
2.3.4	Active Materials for the Negative Electrode .....	22
2.3.4.1	Properties of Carbonaceous Materials.....	22
2.3.4.2	Different Types of Carbonaceous Materials, Graphite, Soft and Hard Carbon.....	22
2.3.4.3	Lithium Intercalation into Graphite.....	24
2.3.4.4	Lithium Alloys and Intermetallic Phases as Anode Materials .....	25
2.3.4.5	Transition Metal Oxides as Anodes.....	26
2.3.5	Active Materials for the Positive Electrode .....	28
2.3.5.1	Olivine Structured Compounds .....	29
2.3.5.2	Layered Transition Metal Oxides.....	30
2.3.5.3	Spinel Framework Cathode .....	32
2.3.6	Electrolyte Systems for Lithium-Ion-Batteries .....	36
2.3.7	Anode/Electrolyte Interactions – the Solid Electrolyte Interphase .....	40
<b>3</b>	<b>Experimental Part .....</b>	<b>45</b>
3.1	General Remarks on 5V Cathodes.....	45
3.1.1	State of the Art .....	45
3.1.2	Theoretical Enhancement of Battery Energy .....	48
3.2	Preparatory Works .....	50
3.3	Experimental Results.....	52
3.3.1	Basic Characterization of the BASF $\text{LiNi}_{0.5}\text{Mn}_{1.5}\text{O}_4$ Spinel.....	52

3.3.2	Concepts for Improving the Electrochemical Behavior of $\text{Li}_{0.5}\text{Mn}_{1.5}\text{O}_4$ .....	60
3.3.3	Electrochemical Comparison of Modified and Unmodified NMO Electrodes .....	63
3.3.3.1	Cyclic Voltammetry and Constant Current Cycling Behavior .....	63
3.3.3.2	Investigation of Electrolyte Decomposition via In-Situ Mass Spectroscopy .....	69
3.3.3.2.1	Introduction.....	69
3.3.3.2.2	Electrochemical and Mass Spectrometric Results .....	71
3.3.3.3	In-Situ Pressure Detection during Constant Current Cycling .....	81
3.3.4	Further Progress.....	87
3.3.4.1	New NMO Batch – Introduction.....	87
3.3.4.2	Comparison of Morphology by the Use of SEM .....	88
3.3.4.3	Electrochemical Differences of Both Batches .....	92
3.3.4.4	Determination of the Space Group with XRD and TEM .....	94
3.3.4.5	Modification of Non-Aqueous Electrolyte Systems for Electrochemical Improvements.....	95
3.3.4.5.1	Electrochemical Impact of Additives.....	95
3.3.4.5.2	Few Aspects on High Oxidative Stable Electrolyte Systems.....	108
3.3.4.6	Cell Assembling – Balancing Graphite and the BASF NMO Spinel .....	112
<b>4</b>	<b>Conclusion.....</b>	<b>121</b>
<b>5</b>	<b>Appendix.....</b>	<b>123</b>
5.1	References.....	123
5.2	List of Figures.....	134
5.3	Explanation of Abbreviations .....	143
5.3.1	Table of Chemicals .....	143
5.3.2	Table of Miscellaneous Abbreviations .....	145

# 1 Introduction

Increasing popular portable applications encounter us within our every day's life in the shape of entertainment, communication and working stations, which are represented by the 4C market (cellular phones, computers, cameras and cordless tools). Enhanced features of these widespread product line-ups lead to the need of high efficient energy storage systems. At the same time the protection of our environment is on everyone's lips. For instance the climate warming caused by air pollution, which is predominantly referable to exhaust of greenhouse gas emissions, such as CO<sub>2</sub>, of common cars equipped with combustion engines. In particular, the automotive industry has to face a huge challenge, meaning nowadays economical, but especially ecological issues combined with everybody's request of its individual mobility. Therefore, a partial substitution of fossil fuels is envisaged at least using the (greener) advantages renewable resources can provide. Inside of the rather huge field of renewable resources rechargeable batteries awaken hope to solve problems like the pollutant emission. In turn, within several battery types Lithium-Ion-Batteries (LIBs) expose their merits of these energy storage and power sources, respectively, such as sustainability, environmental- and (especially) user friendliness, high efficiency, low self-discharge and low weight. Furthermore LIBs can score with different designs facilitating the implementation in several devices. For that reason LIBs give point to be a very promising alternative to accomplish the currently required energy demands and environment concerns.

Figure 1 shows a comparison of different battery types with their corresponding energy densities and the pollutant emission values of different energy sources based on the well to wheel study<sup>(7)</sup>. This kind of study constitutes a complete analysis of greenhouse gas development for every process step of the entire scope of fuel generation, starting at the raw material extraction right up to fuel consumption. In this way three areas can be defined to ensure permissible comparisons of the obtained results:

- **Well to tank (WtT):** incorporates the development of greenhouse gases (CO<sub>2</sub>, CH<sub>4</sub>, NO<sub>x</sub>) during extraction, process, storage and transport of raw materials completed with pollutant generation within production, transport, storage and finally distribution of prepared fuels<sup>(7)</sup>.
- **Tank to wheel (TtW):** this part includes the generation of greenhouse gases during the usage of the final consumers (vehicles)<sup>(7)</sup>.
- **Well to wheel (WtW):** both systems WtT and TtW are combined and display the entire process<sup>(7)</sup>.

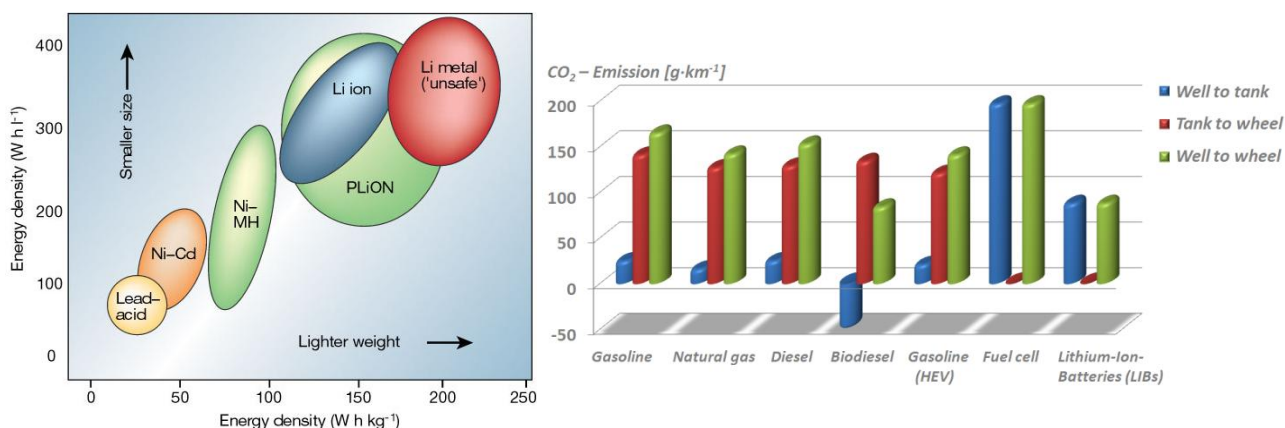


**Figure 1:** left) distribution of different battery technologies contributed by volumetric vs. gravimetric energy densities<sup>(8)</sup>; right) well to wheel constitution of produced greenhouse house gases, in this case produced CO<sub>2</sub> in gram per km, for fossil and renewable sources. Biodiesel has a negative balance within the well to tank (WtT) process due to optimal utilization of exploitable side products during manufacturing process<sup>(drawn from (7))</sup>.

Thus it appears that Lithium-Ion-Batteries have least emission indeed, but improvements have still to be done. Figure 2 makes this difficulty abundantly clear by constituting merits and drawbacks between nowadays available vehicles operated by electricity and/or gasoline. Furthermore this illustration includes pie charts comparing two Hybrid vehicles (HEV), Chevy Volt and Prius Plug-In and four full electric vehicles (EV), Tesla Roadster, Mini E, Th!nk City and G-Wiz L-ion. Hybrid cars use the battery pack only for short distances and switch to a common combustion machine for a longer range, therefore, Chevy Volt would approach 640 km and Toyota Prius 600 km<sup>(9)</sup>. But on this account the cruising ranges are compared solely for the case that the cars run on the battery pack.

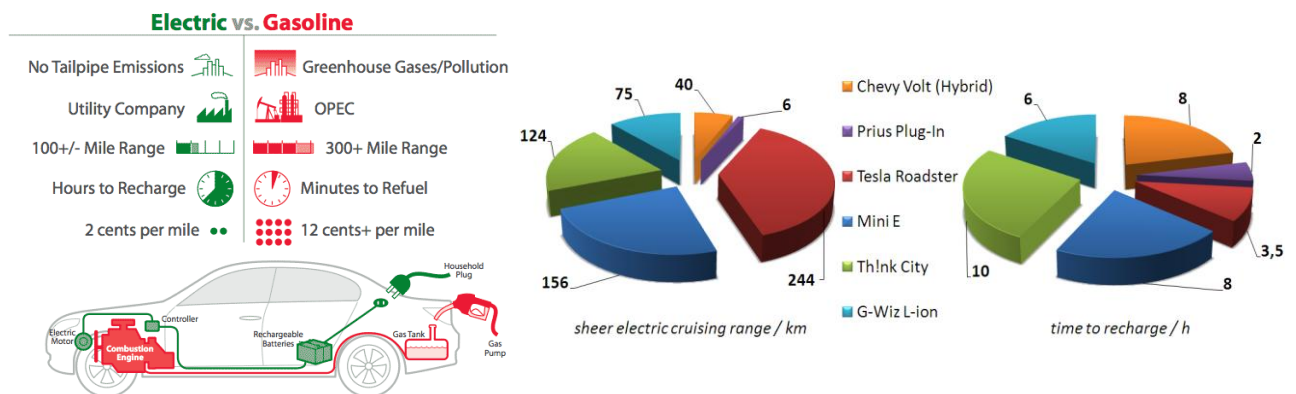


**Figure 2:** left) illustration of merits and drawbacks between electrical and gasoline vehicles<sup>(9)</sup>; middle) cruising ranges of HEV and EV (pie chart shows only cruising ranges of HEVs powered by a battery, in combination with a combustion machine, Chevy Volt reaches 640 km, Toyota Prius 600 km)<sup>(9)</sup>; right) time for fully recharge of the batteries<sup>(drawn from (9))</sup>.

A comparison of specific energies between combustion and electric engines emphasizes this problem:  $160 \text{ Wh}\cdot\text{kg}^{-1}$  of energy storage systems (LIBs) need to compete with  $1500 \text{ Wh}\cdot\text{kg}^{-1}$  of gasoline engines<sup>(10)</sup>. As a consequence safe, cheap and especially well performing batteries with higher energies should mitigate this wide margin for what improvements are necessary. On these accounts, research is ruled by the demand for electrode materials based on naturally occurring and not expensive materials for cost reduction. At the same time novel and stable electrolyte systems are needed in particular to fulfill requirements concerning safety issues. In addition, these cells should offer good capacities and power capabilities and of course they should meet the ability to guarantee a long cycle life for up to ten years. All together an optimization and/or development of electrode materials and electrolytes tailored to needed battery systems constitute the subject of present global battery research.

This doctoral thesis deals with the enhancement of energy of Lithium-Ion-Batteries. Despite different cell designs or the search for lower weight of all battery components to maximize the energy density, the search for “completely-new” cell chemistry is in progress. Therefore, two possible ways can be followed to meet the energy demand. In general, energy is defined through the product of voltage and capacity. On the one hand anodes with a higher capacity increase energy (up to  $4200 \text{ mAh}\cdot\text{g}^{-1}$  for pure silicon). On the other hand capacities of cathode materials are limited to  $160 - 200 \text{ mAh}\cdot\text{g}^{-1}$  indeed, but may offer a high working potential approaching  $5 \text{ V vs. Li/Li}^+$  (cf. Figure 2)<sup>(11)</sup>. Hence, advanced Lithium-Ion-Batteries would increase even more the energy of batteries if they consist of a high capacity anode ( $> 372 \text{ mAh}\cdot\text{g}^{-1}$ ) and/or a high voltage cathode ( $> 4.7 \text{ V vs. Li/Li}^+$ ). One aim of this doctoral thesis deals with the characterization of a spinel cathode material ( $\text{LiMn}_2\text{O}_4$ ). More precisely, it is a modification of the nickel-manganese spinel with the composition  $\text{LiNi}_{0.5}\text{Mn}_{1.5}\text{O}_4$ . It is a very promising material, because it exhibits an average discharge voltage of  $4.7 \text{ V vs. Li/Li}^+$  and a specific capacity of around  $140 \text{ mAh}\cdot\text{g}^{-1}$ . Furthermore in combination with a

common used graphite anode a theoretical specific energy of  $\sim 470 \text{ Wh}\cdot\text{kg}^{-1}$  could be achieved, which would be more than 30 % of improvement than batteries exhibit at the moment.

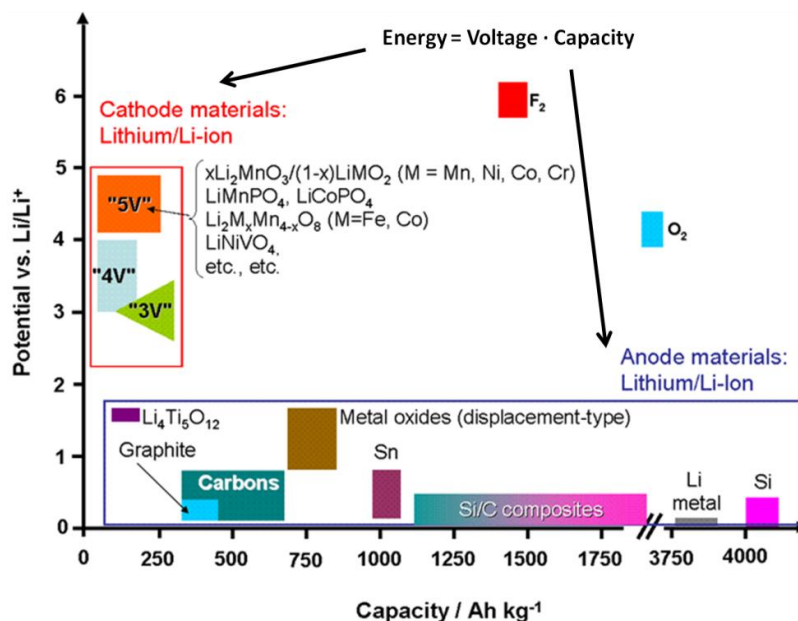


**Figure 3:** potential vs. capacity – possibilities to enhance energy of Lithium-Ion-Batteries <sup>(12)</sup>.

If so called 5 V cathode materials are used another problem joins the difficulty constituting the second aim of this doctoral thesis - the investigation and improvement of the oxidative stability of electrolyte systems. Commonly used electrolytes have an electrochemical stability window up to a maximum of 4.4 V vs.  $\text{Li/Li}^+$ , which is too low for high voltage cathodes materials. Beyond this border decomposition of electrolyte components takes place, whereby the electrolyte should still meet properties such as sufficient SEI formation, good ion conductivity over a large temperature range, low vapor pressure and flashpoint, etc.. For a better understanding of electrolyte stability and its decomposition products investigations of several electrolyte systems were focused within the present work.

## 2 Theoretical Principles

### 2.1 Elementary Electrochemistry

In the 18<sup>th</sup> century, when Luigi Galvani made tremendous investigations concerning muscular contractions of frog legs by touching them with different metals (iron and copper), he couldn't know that he will be the pioneer for a very important basement of today's electrochemistry. Interpretations and developments from Alessandro Volta and Wilhelm Ritter evolved Galvani's sensational discoveries and led to the knowledge of the galvanic cell representing the smallest unit of a battery. In general, the purpose of such a battery is the transformation of chemical into electrical energy. It has to be considered that the term "battery" signifies the combination of one or more electrically connected galvanic cells. Depending on the application merely the desired voltage and capacity of the battery determine the way and amount of connected galvanic cells - in series and/or parallel <sup>(13)</sup>.

Each galvanic cell exhibits two half cells. These in turn are composed of electrodes (mostly metals or metal oxides, e.g. zinc and copper) located in different chambers and immerse into an electrolyte at standard conditions (25°C, 1 M electrolyte solution, e.g. ZnSO<sub>4</sub> (aq) and CuSO<sub>4</sub> (aq)). A diaphragm or salt bridge spatially separates the electrodes and thus, prevents an internal short circuit. The atoms of every (metal-) electrode have a specific tendency to solve in the electrolyte, whereas the electrons remain in the electrode. Due to the fact that zinc is a less noble metal than copper, more zinc ions migrate from the electrode surface into the solution than copper ions. As a consequence, the tin electrode gets charged more negative compared to the copper one. This charge distribution leads to different potentials and reflects the ability to convert chemical into electric energy which is named cell voltage and electromotive force (EMF), respectively.

By closing an external circuit two linked reactions take place, namely oxidation of the negative electrode (anode, e.g. zinc) and reduction of the positive electrode (cathode, e.g. copper). The oxidation leads to further dissolution of Zn<sup>2+</sup>-ions accompanied by a current flow from the anode to the cathode via the external circuit. These electrons reduce the dissolved Cu<sup>2+</sup>-ions and cause metallic copper deposition on the surface of the positive electrode. The charge balancing of the galvanic cell is obtained by the migration of SO<sub>4</sub><sup>2-</sup>-ions through the diaphragm or separator. If all copper ions are exhausted from solution or the zinc electrode is completely dissolved, the current flow takes not any longer place.

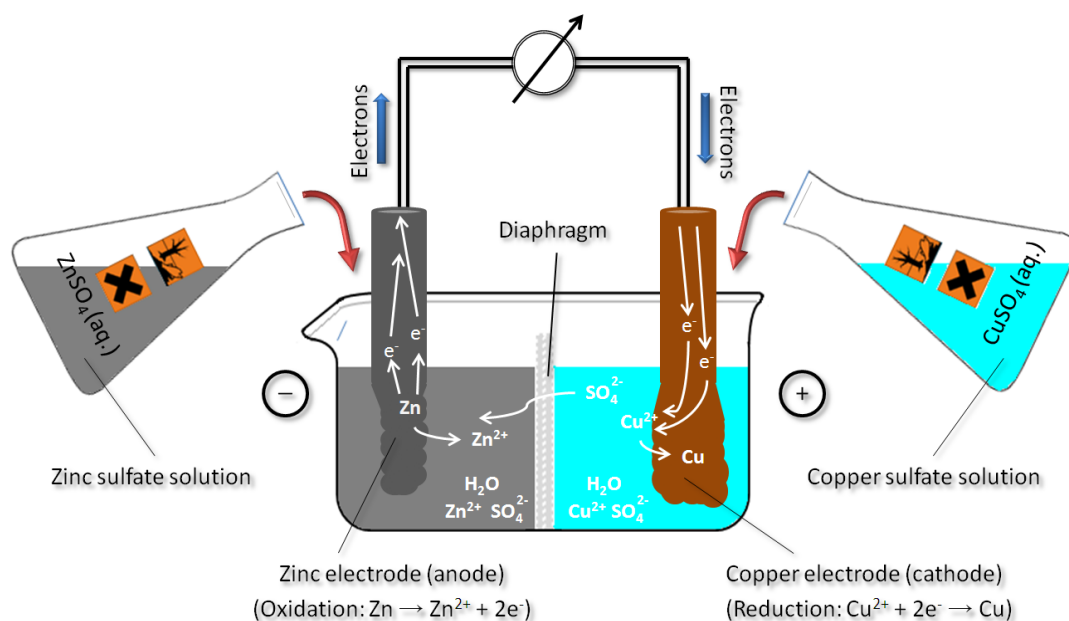


**Figure 4:** schematic draft of a galvanic cell or Daniell element <sup>(source: author)</sup>, the negative electrode (zinc) dissolves and the remaining electrons flow to the positive electrode (copper) and reduce the bivalent copper ions (deposition on the electrode surface).

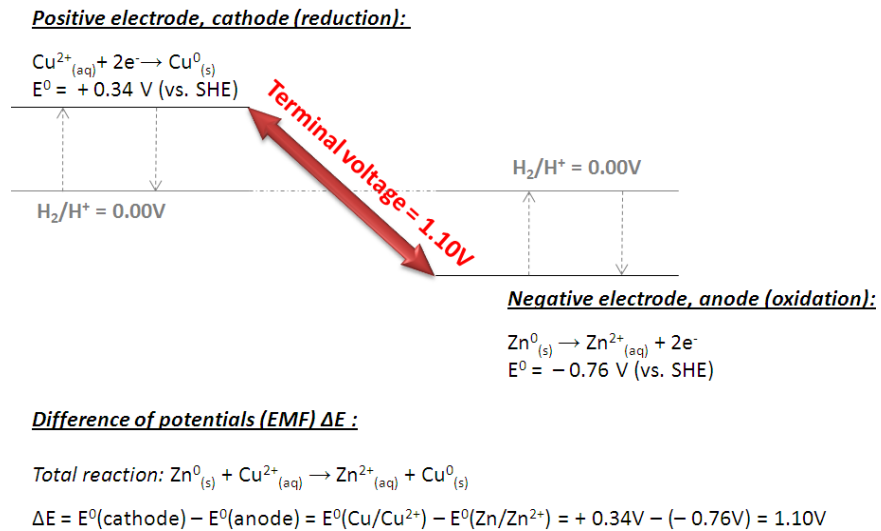
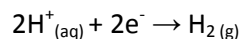


**Figure 5:** determination of the electromotive force (EMF) and the chemical reactions and their potentials of each half cell with the total reaction (drawn from (14)).

In summary, a galvanic cell consists of two connected half cells with their specific potentials. Unfortunately, it is not possible to measure the potentials of each half cell individually, but on the other hand the voltage difference between the electrodes. For that reason the establishment of a reference electrode with an arbitrary point for the potential is necessary, which enables the measurement of this difference for every redox active species. Such a kind of reference and standard electrode, respectively, is represented by the standard hydrogen electrode (SHE), whose potential of reaction, the reduction of  $\text{H}^+$ -ions to  $\text{H}_2$ , is defined with 0 V at standard conditions (15).



**Eq. 1**

If a metal electrode (e.g.  $\text{Zn/Zn}^{2+}$ ) is connected to the SHE, so called standard electrode potential  $E^0$  is obtained. The characteristic of the metal depends on the algebraic sign of the standard electrode potential, meaning negative standard potentials ( $E^0 < 0$ ) are known as base and positive standard electrode potentials ( $E^0 > 0$ ) as noble metals. They can be listed in tabular form termed the electrochemical series of metals (14).

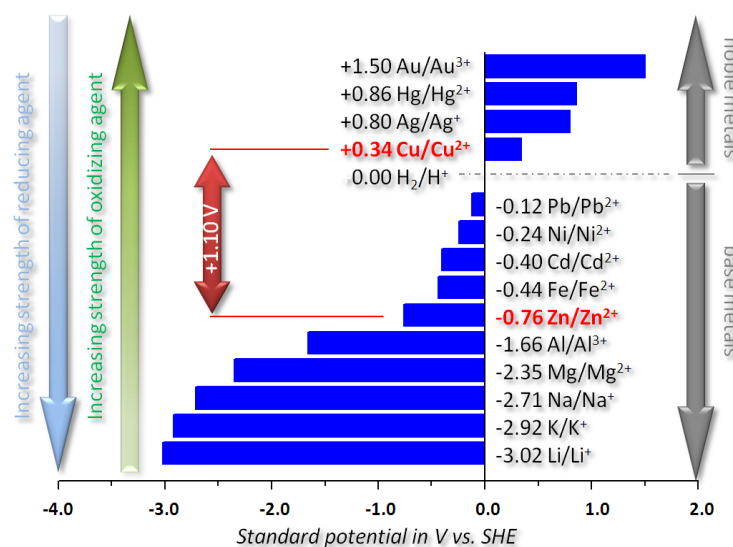


**Figure 6:** electrochemical series of metals with their specific standard electrode potentials measured against SHE; the difference of the potentials (EMF) red marked corresponds to the above described Daniell element (cf. Figure 4, page 4) (drawn from (14)).

## 2.2 Thermodynamic Point of View

### 2.2.1 General Remarks

Despite the determination of potentials at standard conditions, they can also be measured with the help of thermodynamic data. Measureable factors influencing the potentials and electromotive force, respectively, are temperature, concentration, changing pressure and pH-value. In general, an electrochemical equilibrium at phase boundaries is required for their determination, which actually means that no external current flow takes place associated with no reactions at all. From microscopic point of view a continuous exchange of charges at a phase boundary can be observed, for instance at the interface electrode/electrolyte of the Daniell element shown in Figure 7. Anodic and cathodic currents compensate each other and thus, the status of equilibrium is reached <sup>(14), (16)</sup>.

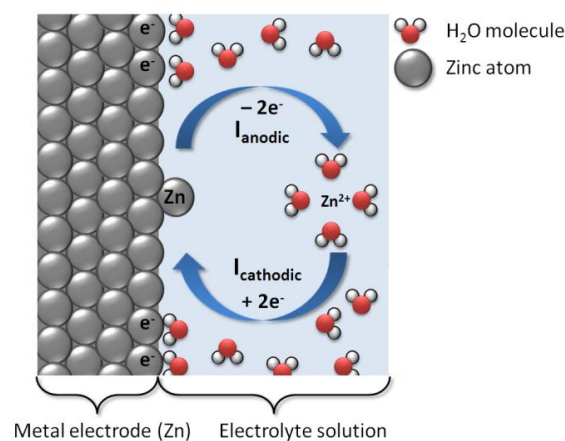


**Figure 7:** electrode/electrolyte interface in the equilibrium state <sup>(drawn from (14))</sup>.

The determination of the equilibrium cell voltage can be made by calculation of the reaction free energy with the Gibbs-Helmholtz equation <sup>(17)</sup>

$$\Delta G = \Delta H - T \cdot \Delta S$$

**Eq. 2**

$\Delta G$  ... Reaction enthalpy

$\Delta H$  ... Enthalpy

$T$  ... Temperature

$\Delta S$  ... Entropy

containing important thermodynamic factors ( $\Delta H$  and  $\Delta G$ ) which are dependent on the concentration or activity of the reactants when they get solved in the electrolyte <sup>(14), (15), (17)</sup>:

- **Enthalpy  $\Delta H$ :** signifies the enthalpy or heat content by meaning the amount of released or absorbed energy of a reaction.
- **Entropy  $\Delta S$ :** represents the entropy of a reaction and delivers the reversible energy loss or increase within a chemical process.
- **Reaction enthalpy  $\Delta G$ :** describes the maximum of achievable work, especially for an exergonic process.

The following formulations lead to the relationship of the EMF and activities of reactants. First of all the chemical potential of composites is defined by <sup>(16), (18)</sup>

$$\mu_J = \left( \frac{\partial G}{\partial n_J} \right)_{p,T,n'}$$

**Eq. 3**

- $\mu$  ... Chemical potential of a substance  $J$
- $G$  ... Gibbs energy
- $n$  ... Amount of a substance  $J$
- $n'$  ... Amount of every substance with a constant composition except component  $J$

and describes the change of the free reaction enthalpy depending on its system composition and therefore, the material conversion of the reactions. In response, the change of the free enthalpy  $G$  depends beside the composition on temperature and pressure and we obtain <sup>(16)</sup>

$$dG = V \cdot dp - S \cdot dT + \sum_J \mu_J \cdot dn_J$$

**Eq. 4**

If temperature and pressure are constant <sup>(16)</sup>

$$dG = \sum_J \mu_J \cdot dn_J = dw_{e,max}$$

**Eq. 5**

meaning that a system can generate volumetric and electrical work, for instance an electrochemical cell. The maximum of achievable work, especially for a volunteer process is described by the reaction free energy (Gibbs energy)  $\Delta G$  <sup>(16)</sup>.

If the reaction  $A \rightarrow B$  takes place with a transformation of an infinitesimal quantity of  $A$  to the product  $B$ , we get the reaction duration signed  $\xi$ , which symbolizes the performance of a reaction. In addition, this factor describes the change of the free enthalpy  $G$ , which is caused by the change of the composition of several components during a reaction <sup>(16)</sup>

$$dG = \mu_A \cdot dn_A + \mu_B \cdot dn_B = -\mu_A \cdot d\xi + \mu_B \cdot d\xi$$

**Eq. 6**

Eq. 6 transformed results in <sup>(16)</sup>

$$\left( \frac{\partial G}{\partial \xi} \right)_{p,T} = \mu_B - \mu_A$$

**Eq. 7**

showing the dependence of the slope of the free enthalpy  $G$  on the reaction duration. If the formation of 1 mol  $B$  from 1 mol  $A$  with no changes of its composition takes place we are talking about the free reaction enthalpy  $\Delta_R G$  <sup>(16)</sup>.

$$\Delta_R G = \left( \frac{\partial G}{\partial \xi} \right)_{p,T} = \mu_B - \mu_A = \sum_J \nu_J \cdot \mu_J$$

Eq. 8

$\Delta_R G$  ... Free reaction enthalpy

$\nu_J$  ... Stoichiometric factor

Thus, the relationship between the free reaction energy and the equilibrium cell voltage or electromotive force (EMF) is described through  $\Delta_R G$  and can be formulated mathematically by <sup>(14), (16)</sup>

$$\Delta_R G = -\nu \cdot F \cdot E = -z \cdot F \cdot E$$

Eq. 9

$z$  ... Number of exchanged electrons

$F$  ... Faraday constant (96485 C·mol<sup>-1</sup>)

$E$  ... Equilibrium cell voltage or EMF

whereby a negative algebraic sign symbolizes that the electrochemical cell generates work <sup>(19)</sup>. Depending on the value of the free reaction enthalpy three possible situations can be defined, which correlate with the trend of an electrochemical reaction to occur voluntary (exergonic), forced (endergonic) or to be located in equilibrium <sup>(16)</sup>:

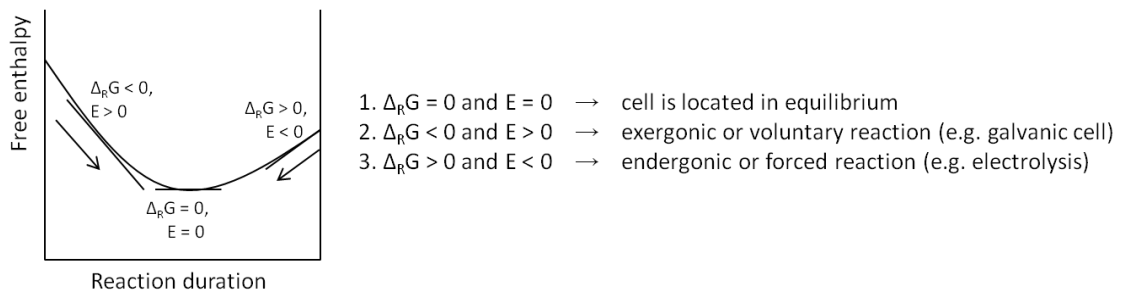


Figure 8: possibilities for the procedures of an electrochemical process <sup>(drawn from (14))</sup>.

As a consequence of Figure 8 the cell voltage or EMF can be calculated with the free reaction enthalpy as well. Attention should be paid to the proportionality of the slope of the free reaction enthalpy as a function of the reaction duration and the cell voltage. The more a reaction is far away from the level of equilibrium (detectable with a big slope of reaction) the higher the cell prefers to reach the steady state which results in a high cell voltage or EMF. On the contrary we obtain a low cell voltage with a lower slope <sup>(16)</sup>.

Now we can connect the dots between the EMF and the activities of the reactants. The relationship between free reaction enthalpy and composition of the reaction mixture goes along with following equation <sup>(16)</sup>

$$\Delta_R G = \Delta_R G^0 + RT \cdot \ln Q \quad \text{with} \quad Q = \prod_{J=1}^k (a_J)^{\nu_J}$$

Eq. 10

$\Delta_R G^0$  ... Free reaction enthalpy at standard conditions

$R$  ... Universal gas constant (8.314 J·K<sup>-1</sup>·mol<sup>-1</sup>)

Dividing both sides by “ $-v \cdot F$ ” leads to <sup>(16)</sup>

$$E = -\frac{\Delta_R G^0}{v \cdot F} - \frac{R \cdot T}{v \cdot F} \cdot \ln Q$$

**Eq. 11**

The first term on the right side represents the EMF or potential of the cell at standard conditions which becomes obviously with following equation <sup>(16)</sup>

$$\Delta_R G^0 = -v \cdot F \cdot E^0$$

**Eq. 12**

and leads to the Nernst equation <sup>(16)</sup>

$$E = E^0 - \frac{R \cdot T}{v \cdot F} \cdot \ln Q$$

**Eq. 13**

As a matter of fact the chemical potential of a half cell depends on the concentration of the reactants <sup>(14), (19)</sup>

$$\mu = \mu^0 + RT \cdot \ln c_J$$

**Eq. 14**

$c_J$  ... Concentration of the compound  $J$

$\mu^0$  ... Chemical potential at standard conditions

which modifies the Nernst equation (cf. Eq. 13) <sup>(14), (16), (19)</sup>

$$E = E^0 + \frac{R \cdot T}{v \cdot F} \cdot \ln \left( \frac{c_{ox}}{c_{red}} \right)$$

**Eq. 15**

regarding the activities of the relevant species <sup>(16), (19), (20)</sup>

$$E = E^0 + \frac{R \cdot T}{v \cdot F} \cdot \ln \left( \frac{a_{red}}{a_{ox}} \right)$$

**Eq. 16**

As a summary the Nernst equation connects the electrical factor “voltage” (or potential of the electrode) and the chemical factor “concentration” and activity, respectively. In addition, this connection has its validity only for systems or electrochemical cells without mass transfers and current flows, but serves as basis for calculations within current carrying systems.

## 2.2.2 Kinetic Aspects

### 2.2.2.1 The Electric Double Layer

A simple imagination of the phase boundary electrode/electrolyte is provided by the Helmholtz model. This theory is based on the assumption that the solvated ions and electrical dipoles are arranged rigidly on the surface of the electrode. Due to their solvation sheaths they keep a certain distance, but are arranged as closely as possible. The distance of the ions to the electrode surface is defined as the half diameter  $a/2$  of the ions. As a result, the Helmholtz plane can be thought of as two parallel layers of opposite charge whereby one of these layers can be found in the metal electrode and the other in the solvent. An extension of Helmholtz' model leads to the Gouy-Chapman model, which includes the before unattended thermal movement of ions with a continuous replacement of them outside of the Helmholtz layer. Hence, this leads to a diffuse double layer which means that ions of both charges exist at the electrode surface. A further development and most realistic model of the double layer are described by the combination of Helmholtz' and Gouy-Chapman's theories called the Stern model. Stern's assumption deals with the position of the Helmholtz plane meaning a specific adsorption of ions and dipole molecules on an electrode surface occurs parallel to the development of the double layer. Thus, ions especially anions may cast off their solvation sheaths and approach the surface closely (inner Helmholtz plane, IHP) even the electrode is charged negatively. Other ions may not lose their solvation sheaths and stick to the minimum distance to the surface  $a/2$  at the outer Helmholtz plane (OHP). These adsorptions give rise to Van-der-Waals forces or Coulombic interactions respectively. In general, the weaker the solvation of the anion, the stronger is its specific adsorption <sup>(16), (18), (21), (22), (23), (24)</sup>.

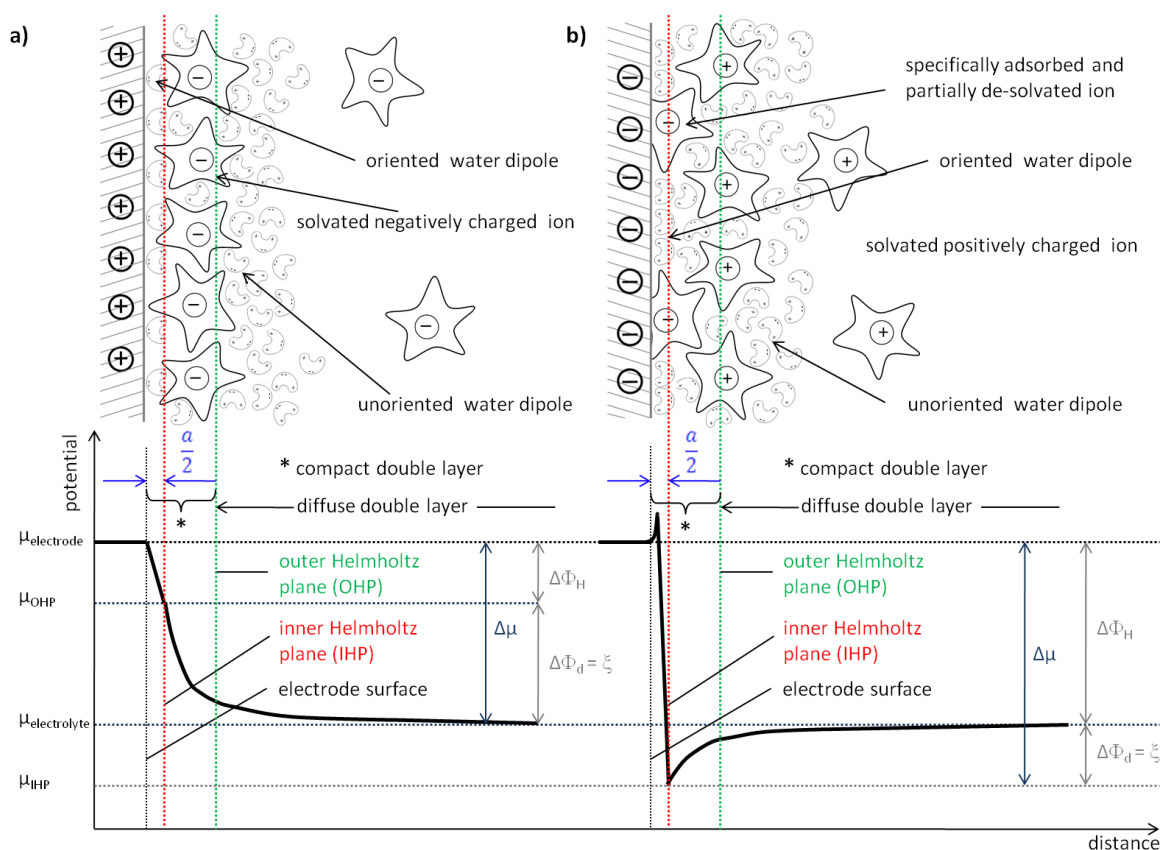


**Figure 9:** Stern model of the potential distribution within the double layer for a positively a) and negatively b) charged electrode <sup>(drawn from (16), (18), (21), (22), (23), (24))</sup>.

The electric double layer causes a difference between the potentials of the surface and the electrolyte components, which is known as the surface potential. According to the characteristics of the potential in Figure 9a we can see that the potential at first decreases nearly linear when we leave the electrode surface. Furthermore we will notice an exponentially decreasing potential from the Helmholtz plane to the bulk of the electrolyte through the whole diffuse layer. On the contrary, when we leave the electrode surface in Figure 9b, the inner double layer causes an increase of the potential, which is followed by an exponentially rising potential. The potential of the entire double layer for both cases is described by the difference of the interior of the electrode (Galvani potential) and the interior of the electrolyte through following equation:

$$\Delta\mu = (\mu_{electrode} - \mu_{OHP,IHP}) + (\mu_{OHP,IHP} - \mu_{electrolyte}) = \Delta\mu_H + \Delta\mu_d$$

**Eq. 17**

- $\Delta\mu_{OHP}$  ... Potential at the outer Helmholtz plane (OHP)
- $\Delta\mu_{IHP}$  ... Potential at the inner Helmholtz plane (IHP)
- $\Delta\mu_H$  ... Potential across the Helmholtz plane
- $\Delta\mu_d$  ... Potential across the diffuse double layer (zeta potential  $\xi$ )

whereby  $\Delta\mu_d$  is also known as zeta potential  $\xi$  which is very important for electrode kinetics.

### 2.2.2.2 The Butler-Volmer Equation

The relationships shown in the chapters before are only valid for systems in steady state and are not accurate for the generation of work produced for instance by an electrochemical cell. If such a cell is out of equilibrium a change of the charges at a phase boundary (e.g. electrode/electrolyte interface, cf. chapter 2.2.2.1) occurs resulting in a measurable difference of the potentials. In the following some considerations are constituted about the reaction rates for galvanic cells and battery systems respectively. To determine the rate of a mass flow of electrode reactions we use the reaction of first order<sup>(16)</sup>

$$\frac{p}{t \cdot a} = k_{[reagent]}$$

**Eq. 18**

- p ... Produced substance (amount of substance)
- t ... Time
- a ... Area
- k ... Constant of the rate (length·time<sup>-1</sup>)
- [reagent] ... Concentration of the defining substance in the solution (amount of substance·volume<sup>-1</sup>)

The expression for the rate of the oxidizing and reducing processes in the electrolyte (solution), but out of the double layer is defined by<sup>(16)</sup>

$$Reaction\ rate\ Ox = k_c \cdot [Ox]$$

**Eq. 19**

- Reaction rate Ox ... Rate of reducing Ox
- $k_c$  ..... Cathodic rate constant
- [Ox] ... Concentration of the oxidized substance

and the same for the opposite process <sup>(16)</sup>

$$\text{Reaction rate Red} = k_A \cdot [\text{Red}]$$

**Eq. 20**

Reaction rate Red	... Rate of oxidizing Red
$k_A$	... Anodic rate constant
[Red]	... Concentration of the reduced substance

The difference of the current densities of Ox and Red represents the entire current density occurring on an electrode. Furthermore only one electron is transferred within these redox processes. Thus, we can define the current densities for both reactions by the product of their reaction rates (Eq. 19 and Eq. 20) and the amount of charge transferred per mol, which is given by the Faraday constant. As a result we can express the cathodic current density <sup>(16)</sup>

$$j_C = F \cdot k_C \cdot [\text{Ox}]$$

**Eq. 21**

and the anodic current density <sup>(16)</sup>

$$j_A = F \cdot k_A \cdot [\text{Red}]$$

**Eq. 22**

and finally the entire current density <sup>(16)</sup>

$$j = j_A - j_C = F \cdot k_A \cdot [\text{Red}] - F \cdot k_C \cdot [\text{Ox}]$$

**Eq. 23**

According to Eq. 23, the total current density determines if the oxidizing or reducing process is prevalent. Hence, we obtain an entire anodic current associated with oxidation of the particles in the electrolyte in the case that  $j_A > j_C$ . By contrast, if  $j_A < j_C$  occurs, a cathodic current can be observed and the entire reaction process is a reduction <sup>(16)</sup>.

By applying a potential to the electrode, a net chemical conversion process takes place accomplished by its equal net current flow via the external circuit. For oxidation and reduction the solvation sheaths of ions or neutral molecules have to be shed off. In addition, the substances diffuse through the electrical double layer and for the opposite reaction a near surface substance solves from the surface and diffuses through the double layer as well (quantum mechanical tunneling effect). Within a cathodic reaction the transfer of an electron takes place from the conduction band of the metal or electrode to an unoccupied molecular orbital of the ion or neutral molecule. By contrast, an anodic reaction corresponds to an electron transfer from an occupied molecular orbital of a neutral molecule into an empty space of the electrode or metal surface. In general, ions or neutral molecules, which are involved within these electron transfers are located in the electrolyte solution and/or adsorbed on the electrode surface. Both oxidation and reduction processes require an activation energy. For the formal reaction  $A + B \rightarrow \text{products}$  the reagents A and B pass through an activated complex  $AB^\ddagger$  representing an area around maximum of the potential energy with the transition state at the maximum. This point describes the reaction kinetics for the above stated reaction. If

the reagents A and B reach the area of the activated complex and pass the transition state in further consequence, the equilibrium is situated on the side of the products and vice versa for the opposite reaction. Both reactions have a certain reaction rate expressed by <sup>(16), (18)</sup>

$$k = B \cdot e^{-\frac{\Delta^\ddagger G}{R \cdot T}}$$

**Eq. 24**

B ... Constant with the same dimension like constant k

$\Delta^\ddagger G$  ... Free activation enthalpy

and applied to Eq. 23 <sup>(16)</sup>

$$j = F \cdot B_A \cdot [Red] \cdot e^{-\frac{\Delta^\ddagger G_A}{R \cdot T}} - F \cdot B_C \cdot [Red] \cdot e^{-\frac{\Delta^\ddagger G_C}{R \cdot T}}$$

**Eq. 25**

At the reduction process following connection between current density  $j$  and Galvani potential difference  $\Delta\Phi$  is valid <sup>(16)</sup>

$$\Delta^\ddagger G_C = \Delta^\ddagger G_C(0) + \alpha \cdot F \cdot \Delta\Phi$$

**Eq. 26**

$\Delta^\ddagger G(0)$  ... Free activation enthalpy with the value 0

$\alpha$  ... Symmetry factor (dimensionless with values between 0 and 1)

For the oxidizing process <sup>(16)</sup>

$$\Delta^\ddagger G_A = \Delta^\ddagger G_A(0) - (1 - \alpha) \cdot F \cdot \Delta\Phi$$

**Eq. 27**

A simplification <sup>(16)</sup>

$$f = \frac{F}{R \cdot T}$$

**Eq. 28**

and apply of Eq. 26 and Eq. 27 to Eq. 25 leads to a entire current density <sup>(16)</sup>

$$j = F \cdot B_A \cdot [Red] \cdot e^{-\frac{\Delta^\ddagger G_A}{R \cdot T}} \cdot e^{(1-\alpha) \cdot f \cdot \Delta\Phi} - F \cdot B_C \cdot [Red] \cdot e^{-\frac{\Delta^\ddagger G_C}{R \cdot T}} \cdot e^{-\alpha \cdot f \cdot \Delta\Phi} = j_A - j_C$$

**Eq. 29**

If the cell stays in steady state by an external voltage source the Galvani potential  $\Delta\Phi$  can be substituted by the equilibrium electrode potential  $E$ . As a consequence, the current densities of anodic and cathodic terms exhibit the same absolute values which is called exchange current density  $j_0$  <sup>(16)</sup>.

Leaving this steady state caused by current delivery of the electrochemical cell, the potential will change its value from  $E$  to  $E'$ . This difference is called overpotential  $\eta$  and signifies the inhibition of the current, meaning the higher the inhibition the bigger the overvoltage gets <sup>(16), (18)</sup>.

$$\eta = E' - E$$

Eq. 30

$\eta$  ... Overpotential [V]

$E'$  ... Potential at steady state [V]

$E$  ... Measured potential [V]

Thus,  $\Delta\phi$  changes <sup>(16)</sup>

$$\Delta\phi = E + \eta$$

Eq. 31

and in addition the current densities for reduction and oxidation <sup>(16)</sup>

$$j_A = j_0 \cdot e^{(1-\alpha) \cdot f \cdot \eta} \quad \text{and} \quad j_C = j_0 \cdot e^{-\alpha \cdot f \cdot \eta}$$

Eq. 32

As a result of this we obtain the Butler-Volmer equation <sup>(16)</sup>

$$j = j_0 \cdot (e^{(1-\alpha) \cdot f \cdot \eta} - e^{-\alpha \cdot f \cdot \eta})$$

Eq. 33

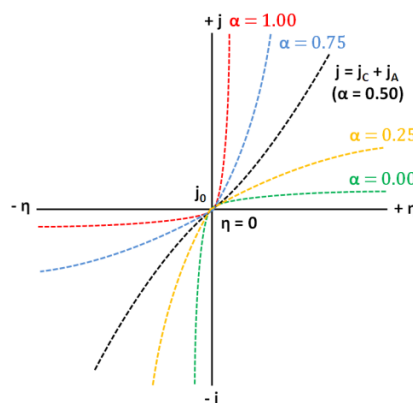


Figure 10: sketch draft of the Butler-Volmer equation with different values for the symmetry factor  $\alpha$  <sup>(drawn from (18), (25))</sup>.

According to Figure 10 the electrochemical reactions of both reductive and oxidative processes take place faster with the increasing absolute values of the overpotential. As a result of this, the reaction rate constant associated with the current density increases with increasing overpotential <sup>(16)</sup>.

### 2.2.2.3 Different Types of Overpotentials

Reactions at steady state and their maximum of deliverable energies are expressed by thermodynamics. If a current is drawn we can observe a voltage drop from the equilibrium voltage (open circuit voltage, OCV) to a lower voltage. This difference is termed overpotential  $\eta$ . This phenomenon induces kinetically inhibitions and constitutes the rate determining step within electrode reactions. Furthermore the entire overpotential consists of different overpotentials which may arise overlapped during measurements and therefore, the total overpotential is expressed by the sum of them <sup>(26)</sup>.

- Ohmic polarization (IR-Drop):

The ohmic polarization and resistance overpotential, respectively, can be defined by a potential loss, which occurs as soon as a current flow is observed (ohmic voltage drop). This overpotential is attributed to the electric resistance all materials provide and follows the Ohms Law (linear relationship between current and this potential drop). Its composition is constituted by the sum of inner resistances, for instance resistances of the electrolyte system <sup>(13), (26), (27), (28)</sup>.

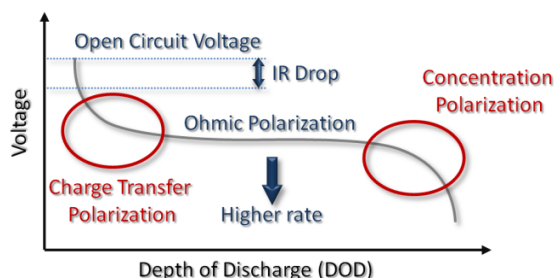


**Figure 11:** constitution of a discharge profile of a battery and their overpotentials <sup>(29)</sup>.

- The diffusion overpotential:

A current flow causes a change of the ion concentration from  $c$  to  $c'$  outside the Helmholtz layer. The concentration  $c$  shows a constant behavior until a specific distance  $\delta$  to the outer Helmholtz plane is reached imposing a linear concentration drop from  $c$  to  $c'$ . This distance is termed Nernst diffusion layer with a typical thickness of 0.1 mm (depending strongly on hydrodynamic conditions, for instance viscosity of the solution, etc.). The concentration gradient accomplishes an ion flow to the electrode maintaining supplies of the redox active substances and ions, respectively. In addition, the higher gradient the faster the diffusion takes place, shown in Figure 12 at point  $c' = 0$  meaning every ion which passed the Helmholtz plane transfers its electron to the electrode very fast. Due to high current densities an impoverishment of the reacting substance may occur at the electrode/electrolyte interface. As a result, the rate of mass flow is determined by the diffusion process only. Hence, the electrochemical turnover at the electrode itself as well as the inhibition of the electron transfer is controlled by diffusion. The mass flow takes place through the rigid Helmholtz plane which is only possible by diffusion <sup>(14), (16), (18), (19)</sup>.

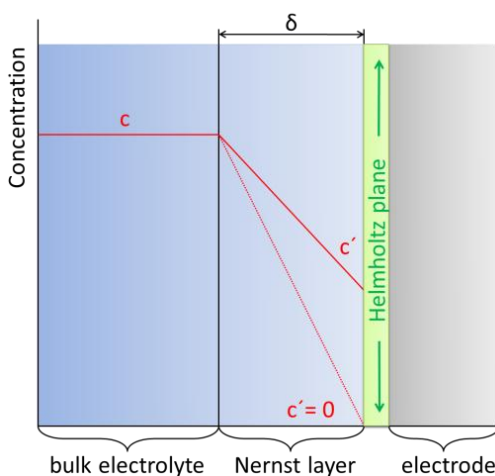


**Figure 12:** simplified model of the Nernst diffusion layer <sup>(drawn from (16))</sup>.

- The reaction overpotential:**

The reaction rate can be limited by phenomena occurring in the electrolyte or during electrode processes. These reactions are upstream or downstream processes and are attributed to adsorption, desorption, complex formation or complex disintegration. A downstream reaction could be the formation of two discharged hydrogen atoms to a hydrogen molecule and an upstream reaction the development of dischargeable metal ions and complexes, respectively, by the way of illustration. The reaction overpotential and the diffusion overpotential are attributed to the concentration overpotential which is influenced by ion-concentration and mass transport <sup>(13), (14), (26), (30), (31)</sup>.
- The charge transfer overpotential:**

This type of overpotential can be described by the speed of any electron transfer through the phase boundary electrode/electrolyte. Considering a simple reaction such as metal deposition, the solvation sheaths are shaped off at least with the result that the ion can pass the inner Helmholtz layer and comes close enough to the electrode surface for the charge transfer. By contrast, the electron migrates through the Helmholtz plane and triggers the discharge process. The inhibition of the charge transfer is called charge transfer overpotential, which is influenced by the characteristics of the electrolyte, participating substances and electrodes themselves. This overpotential is interrelated to the Butler-Volmer equation <sup>(14), (26), (27)</sup>.
- The crystallization overpotential:**

The crystallization overpotential occurs by the inhibition of the intercalation of metal ions into their lattice. Two consecutive steps are characteristic for this kind of overpotential. After passing the electric double layer crystal nucleation may take place in the first instance which is followed by the growth of the crystal. Both mechanisms require a specific overpotential, but the substantial amount of it is owned by the nucleation induced by higher activation energy compared to that of the growth. In addition, this process takes place at certain places of the electrode surface only. If the metal ions reach the electrode surface at another point than the nucleation proceeds, the ions have to diffuse to the stages of growth at the surface directly <sup>(26), (31), (27)</sup>. This phenomenon is important in the proper sense for metal deposition on the cathode surface, but especially for secondary battery systems during the charging step with respect to metal deposition on the negative electrode side <sup>(14)</sup>.

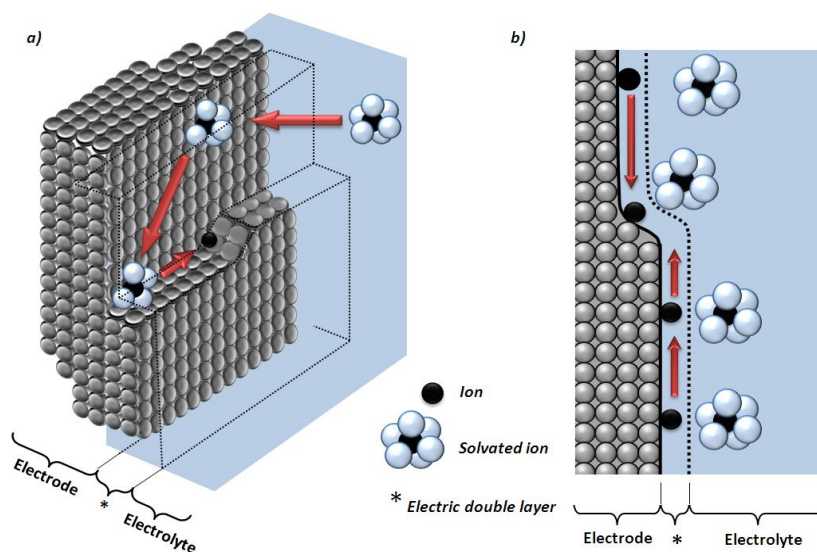


**Figure 13:** a) diffusion of ions to energetic favorable place for crystal nucleation (e.g. edges); b) ions pass through the electric double layer to these energetic favorable positions <sup>(drawn from (31))</sup>.

## 2.3 Lithium-Batteries

### 2.3.1 Key Figures of Batteries

Batteries provide a huge amount of different sizes and configurations depending on their application. Every battery system, primary or secondary type, is characterized by certain cell parameters. On the one hand the terminal voltage  $U$  provides information about the difference of the negative and positive pole voltages during charge and discharge processes. Its calculation can be accomplished by thermodynamic data. The obtained values may drift slightly from the measured ones caused by inhibited equilibrium states or side reactions. The terminal voltage is related to the power a battery system can deliver <sup>(14), (32) (33)</sup>.

$$P = U \cdot I$$

**Eq. 34**

- P ... Electric power [W]
- U ... Voltage [V]
- I ... Current [A]

If the power is related to the weight or volume of the battery another parameter plays a role - the specific power ( $W \cdot kg^{-1}$ ) and the specific power density ( $W \cdot l^{-1}$ ). The storable charge of a battery system is denoted as capacity (Ah) and depends besides of the temperature on the charge and discharge current. The charge and discharge current is expressed by the C-rate which is defined by the discharge current and the theoretical capacity of the cell system <sup>(14), (32)</sup>.

$$C = \frac{\text{discharge current}}{\text{nominal capacity}}$$

**Eq. 35**

A given C-rate with the value of 1C corresponds to the required current for charging a battery completely within one hour. In general, the higher the C-rate the stronger the decrease of the voltage gets in the case of a current flow. For a better association a typical profile terminal voltage vs. the discharge capacity of a commercial available cell is depicted in Figure 14 <sup>(14), (32), (33)</sup>.

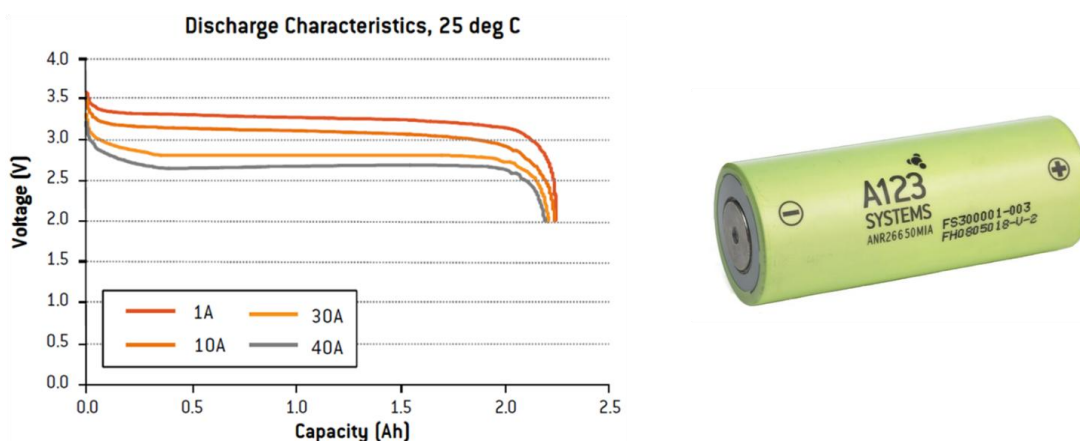


**Figure 14:** discharge characteristics of a commercial available battery (A123, 26650 with nominal capacity 2.3 Ah and nominal voltage 3.3 V) <sup>(34), (35)</sup>.

The storage capacity can be defined by the value of the specific charge per mass ( $\text{Ah}\cdot\text{kg}^{-1}$ ) and per volume through the charge density ( $\text{Ah}\cdot\text{l}^{-1}$ ). The stored energy of a battery is characterized by the specific energy ( $\text{Wh}\cdot\text{kg}^{-1}$ ) and energy density ( $\text{Wh}\cdot\text{l}^{-1}$ ), which are determined by the integration of the capacity in terms of the voltage. High specific energies and densities can be obtained with the combination of materials providing a high cell voltage, high specific charges and high densities <sup>(14), (32), (33)</sup>.

A point of interest for the quality establishment of a battery deals with the question of efficiency. This parameter represents the ratio of converted to the consumed energy and prevails for secondary battery systems. For the efficiency calculation two values are important <sup>(14)</sup>:

- Coulometric efficiency:

Charging a battery requires a certain charge  $Q_{\text{ch.}}$ , which is always higher than the delivered charge  $Q_{\text{disch.}}$ . Typical coulometric efficiencies with values of nearly 100 % are achievable for Lithium-Ion-Batteries depending on the chosen materials <sup>(14)</sup>.

$$\text{Efficiency}_{\text{coulometric}} = \frac{Q_{\text{disch.}}}{Q_{\text{ch.}}}$$

Eq. 36

- Energy efficiency:

Here the voltages during charge and discharge steps are required. The discharge voltage is subjected to overpotentials and internal resistance reflecting a ratio with higher values for the voltages during charge step  $U_{\text{ch.}}$  than the discharge step  $U_{\text{disch.}}$  <sup>(14)</sup>.

$$\text{Efficiency}_{\text{energy}} = \text{efficiency}_{\text{coulometric}} \cdot \frac{U_{\text{disch.}}}{U_{\text{ch.}}}$$

Eq. 37

### 2.3.2 The Importance of Lithium and Its Effect to Battery Technologies

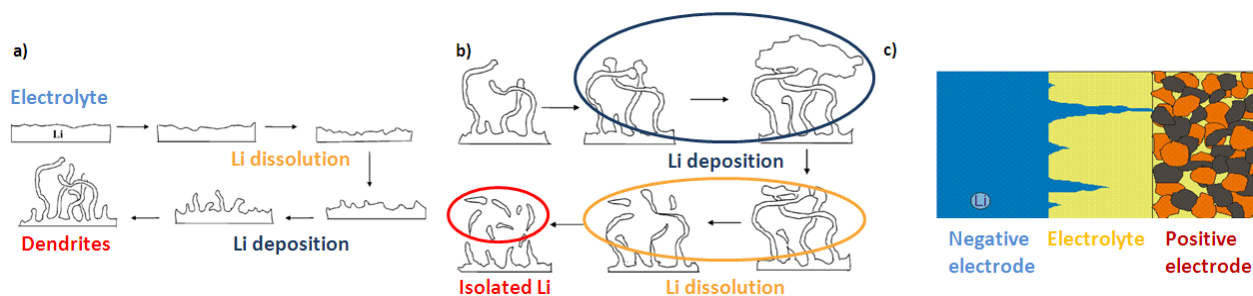
The desire of battery technologies to enable the implementation of lithium metal anodes in batteries gets obviously with a view on Table 1. Properties like the negative potential (-3.01 V vs. SHE) as well as the lightest weight among all metals ( $6.94 \text{ g}\cdot\text{mol}^{-1}$ ) favor lithium as a very attractive anode material. Moreover, in combination with appropriate cathodes lithium metal can impress with a high specific capacity and high cell voltage. The utilization of these advantages was effected by the implementation of metallic lithium as anode for primary batteries since the 1970s yielding many applications like watches, medical or hearing devices, etc. keeping their position on the market until the present days <sup>(20), (33), (36), (37)</sup>.

**Table 1:** properties of metals as thinkable anode materials for Lithium-Batteries <sup>(20)</sup>.

Anode material	Atomic weight [g·mol <sup>-1</sup> ]	Standard potential at 25°C [V]	Electron exchange	Melting point [°C]	Density [g·cm <sup>-3</sup> ]	Electric capacity		
						[Ah·g <sup>-1</sup> ]	[g·Ah <sup>-1</sup> ]	[Ah·cm <sup>-3</sup> ]
Lithium	6.94	-3.01	1	180	0.54	3.86	0.259	2.06
Sodium	23.0	-2.71	1	98	0.97	1.16	0.858	1.14
Magnesium	24.3	-2.38	2	650	1.74	2.20	0.454	3.80
Aluminum	26.9	-1.66	3	659	2.69	2.98	0.335	8.10
Calcium	40.1	-2.84	2	851	1.54	1.34	0.748	2.06
Iron	55.8	-0.44	2	1528	7.85	0.96	1.04	7.50
Zinc	65.4	-0.76	2	419	7.14	0.82	1.22	5.80
Cadmium	112.4	-0.40	2	321	8.65	0.48	2.10	4.10
Lead	207.2	-0.13	2	327	11.34	0.26	3.87	2.90

The reason behind the facilitation for the implementation of lithium metal in primary batteries is its property to be thermodynamically unstable indeed, but kinetically stable in aprotic, organic electrolytes. The negative reduction potential of lithium leads to a decomposition of electrolyte components and thus, to the formation of a passivation film on the lithium surface. This film is permeable for lithium ions, but electric insulating and behaves like a solid electrolyte layer and therefore, it is called “solid electrolyte interphase” (SEI, detailed information in chapter 2.3.7, page 40). In addition, a sustained decomposition of electrolyte products is prevented by the SEI and the commercialization of the applications in the 1970s is attributed to the formation of this passivation layer <sup>(33), (38)</sup>.

Other metals with similar reduction potentials like sodium or magnesium are not able to build such a passivation layer on the metal surface. Protection films of Sodium are not corrosion resistant, whereas magnesium builds a layer which is on the one hand electrical isolating, but on the other hand not permeable for the Mg<sup>2+</sup>-ions. If lithium is used, this corrosion layer possesses Li<sup>+</sup>-ion conductivity and ensures the ability for metallic lithium deposition on the electrode surface. These lithium plating products have a needle like shape and are called dendrites. On that account, these dendrites constitute the biggest disadvantage of lithium metal as anode material within secondary (rechargeable) batteries. The dendrite formation is generated by continually lithium deposition upon charging. In contrast, the discharge step causes inhomogeneous dissolution at different locations of the needle-shaped dendrites leading to electrically isolated lithium particles. This “dead” lithium has a high surface area and is chemically very reactive. If dendrites grow through the separator they cause an internal short circuit with local overheating processes higher than the melting point of lithium metal (180°C). This causes the risk of a thermal runaway of the cell, because molten lithium is about three magnitudes of order more reactive to other components of the battery, for example the flammable organic electrolyte <sup>(33), (38), (39), (40)</sup>.


**Figure 15:** a) mechanism of the formation of dendrites; b) schematic constitution of the formation of isolated lithium dendrites; c) the growth of dendrites from anode surface through the electrolyte to the cathode leading to an internal short circuit <sup>(32), (38)</sup>.

As a consequence of these serious safety problems lithium metal suffers from this drawback in secondary battery systems until today. Therefore, many efforts have been made to ensure the safety of lithium cells yet by running another path, for example the use of host/guest or intercalation and insertion anodes. These materials provide higher safety within the Lithium-Ion-Batteries, because no dendrites are formed. Based on patented intercalation compounds from 1971, Sony commercialized the first secondary battery types (Lithium-Ion-Batteries) in 1990. They were used in cell phones and consisted of intercalation electrodes - petroleum-coke as anode and  $\text{LiCoO}_2$  as cathode. These batteries had a higher safety impact indeed, but on account of a lower capacity compared to metallic lithium anodes. Further developments led to the new generation or advanced Lithium-Ion-Batteries with higher safety, once more by Sony in 2004<sup>(33), (36), (40), (41), (42)</sup>.



**Figure 16:** left) variety of primary button cells from Varta (the notation 2450 means 24 mm in diameter and 5.0 mm height)<sup>(43)</sup>; right) new generation or advanced Lithium-Ion-Batteries established by Sony in 2004<sup>(44)</sup>.

### 2.3.3 Setup of Lithium-Ion-Batteries

The main setup of Lithium-Ion-Batteries (LIBs) is basically equal to primary cells, but with slightly differences. Primary cells contain as primary step the discharge process whose electrochemical reactions are irreversible meaning primary batteries are not rechargeable. However, secondary batteries are rechargeable due to reversible chemical reactions which enable energy storage and transformation of chemical into electrical energy a plenty of times (> 1000 times)<sup>(45)</sup>.

The prerequisite for a rechargeable Lithium-Ion-Battery is the ability of both electrodes to store lithium within their lattice or layers, providing a reversible insertion and extraction of  $\text{Li}^+$ -ions without destruction of the host material's structure. Thus, the elementary principle of the charge and discharge behavior of LIBs can be encountered in the exchange of  $\text{Li}^+$ -ion between anode and cathode accompanied by an external electron flow. The switching or shuttle back and forth of lithium-ions between the host electrodes donates LIBs its name and nickname "rocking-chair" or "shuttlecock"<sup>(46)</sup>.

Upon the charging process  $\text{Li}^+$ -ions are extracted from the positive electrode host material (oxidation), pass through with ion conducting electrolyte soaked separator and get intercalated within the negative electrode host material (reduction). Therefore, the primary step belongs to the charge and the secondary to the discharge process. Figure 17 illustrates these processes within common ("rocking-chair") Lithium-Ion-Battery containing graphite as anode and a layered metal oxide ( $\text{LiCoO}_2$ ) as cathode<sup>(47)</sup>.

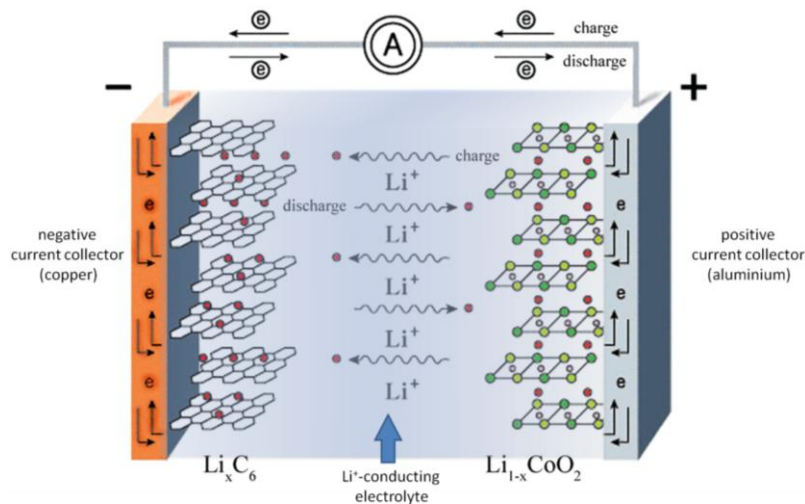
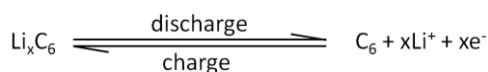


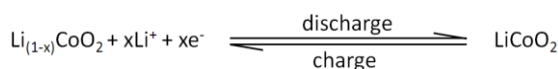
**Figure 17:** schematic draft of the electrode processes within a common Lithium-Ion-Battery <sup>(revision from (48))</sup>.

The insertion (reduction) and extraction (oxidation) process for a LIB using graphite as anode host material can be formulated by following chemical reaction <sup>(38), (49)</sup>



**Eq. 38**

According to the used LiCoO<sub>2</sub> cathode material (cf. Figure 17) the insertion (reduction) and extraction (oxidation) processes are



**Eq. 39**

As already mentioned, Sony produced the first Lithium-Ion-Battery in 1990 using host compounds as electrode materials (c.f. chapter 2.3.2, page 18). The battery components were coiled into a cylindrical shape with the dimension 14500, whereby the number 14 defines the diameter, the number 50 the length in mm and the last 0 is insignificant. For the subsequent implementation of batteries in cellular phones Sony used 20500 (same manner of numeric coding as before) <sup>(50)</sup>. Depending on the application, dimensions of today's batteries vary within their shapes (cylindrical or coffee/pouch bag) and nominal capacities <sup>(49)</sup>.

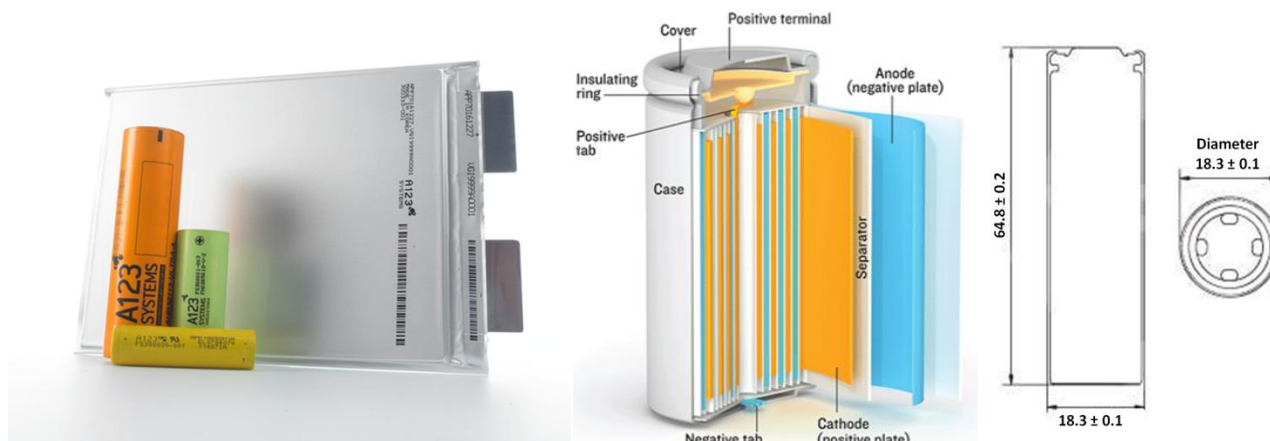


**Figure 18:** left) different shapes of commercial available Lithium-Ion-Batteries <sup>(51)</sup>; right) setup of cylindrical manufactured 18650 (18 mm diameter, 65 mm height) <sup>(52), (53)</sup>.

## 2.3.4 Active Materials for the Negative Electrode

### 2.3.4.1 Properties of Carbonaceous Materials

Anodes within today’s commercial available Lithium-Ion-Batteries (LIBs) consist predominantly of carbonaceous materials. Comparing properties of carbon anodes with a desirable anode material like lithium metal, carbonaceous materials show a much lower achievable capacity,  $372 \text{ mAh}\cdot\text{g}^{-1}$  (graphite, KS6) and  $3860 \text{ mAh}\cdot\text{g}^{-1}$  (lithium metal). In turn, lithiated carbons gain similar negative redox potentials, but have a better long-term cycleability accomplished with better dimensional stability. Additionally, from economic point of view, material synthesis exhibits lower costs which makes them very promising anode materials for Lithium-Ion-Batteries. However, in view of the permanent increasing market of electronic devices, the call from manufacturers is getting louder for improvements of energy/power density and the reduction of irreversible capacity caused by lithium loss. For this reason further developments are still in spotlight of researcher’s interest <sup>(33), (49), (54)</sup>.

As already mentioned before, the mechanism of energy storage within LIBs proceeds with the insertion reaction of lithium-ions into electrode host materials, in this case into carbon anodes, also noted intercalation. In addition, the lithium insertion process is possible for several types of carbons depending besides the used electrolyte system on the crystallinity, microstructure and morphology of the carbonaceous material and can be classified roughly into graphite, soft carbon and hard carbon <sup>(49), (54), (55), (56)</sup>.

### 2.3.4.2 Different Types of Carbonaceous Materials, Graphite, Soft and Hard Carbon

Due to a huge number of available types of carbon a general classification is basically elusive, but they can be categorized roughly into graphitic (ordered) and non-graphitic (disordered) carbons. Graphitic carbons and natural graphite, respectively, is a layered compound of  $\text{sp}^2$ -hybridized carbon atoms arranged in honeycombed hexagonal graphene layers held together by weak Van-der-Waals forces. Regarding crystallography this definition is only correct for carbonaceous materials having a layered lattice structure with a perfect stacking order. Thus, two structures are existent, the hexagonal structure (ABAB) called  $\alpha$ -graphite with a substructure termed arm-chair or zig-zag face which consists of two different characteristic surfaces shifted parallel to the c-axis, named basal and edge plane. On the other hand exists the less common rhombohedral configuration (ABC) called  $\beta$ -graphite. Due to small activation energy for the blend into each other of both structures, perfectly stacked graphite is nearly available. For that reason the term “graphite” is used for all ordered carbons without any exact specification of their real stacking order of the microstructure <sup>(14), (49), (57)</sup>.

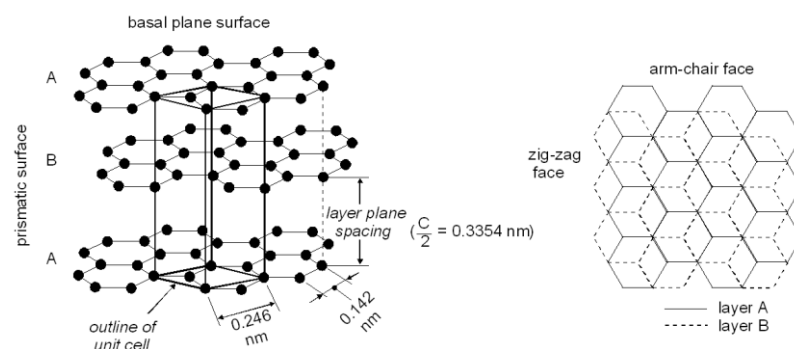


**Figure 19:** left) crystal structure (AB) of the hexagonal shape of  $\alpha$ -graphite, right) arm-chair or zig-zag face - vertical view through the separate basal and edge plane <sup>(33)</sup>.

Beside natural graphite artificial types of graphite exist as well. Syntheses with several conditions at different temperatures lead to many kinds of carbonaceous materials such as carbon black, cokes, activated carbons, pyro-carbons or nanotubes. Furthermore most of these artificial carbons own disordered structure and count to the family of non-graphitic carbons. These materials are arranged in planar hexagonal planes, but their real order consists of partially and randomly amorphous phases. Its distribution in terms of surface area depends on the material precursors and process conditions, such as temperature and pressure. An overview of the possible carbon products and the phase distribution is constituted in Figure 20<sup>(33), (56), (58)</sup>.

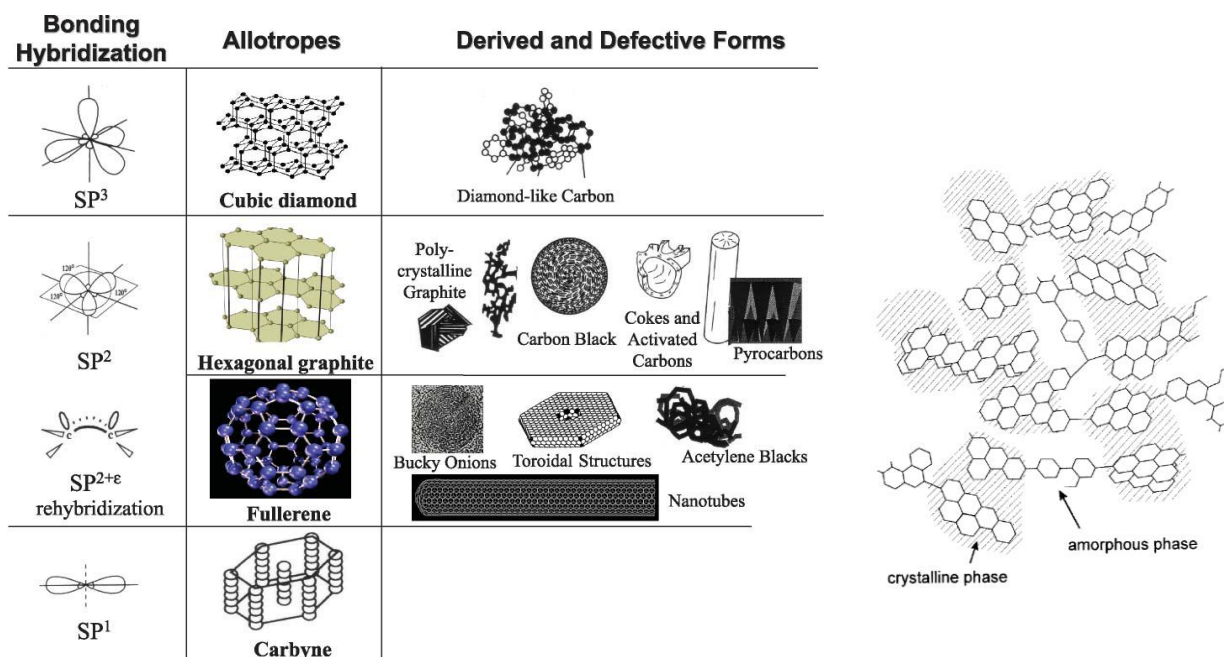


Figure 20: different artificial types of non-graphitic carbons and their arrangement of crystalline and amorphous phases<sup>(33), (56)</sup>.

Most of non-graphitic carbons are synthesized by pyrolysis of organic, hydrocarbon compounds or other precursors beneath 1500°C. After further heat treatment two effects may occur. Either the formation of graphitic structures takes place at temperatures over 2000°C meaning graphitization process can be obtained easily. On the other hand some carbonaceous materials cannot build graphitization structures even at higher temperatures of 3000°C, because of the immobilization of carbon layers by internal crosslinking. Beside the possible graphitization the two kinds of non-graphitic carbons are distinguished by their mechanical hardness resulting in the “soft” one with graphite structures, called soft carbon and the “hard” one without graphite structures termed hard carbon (glass like carbon). The structural difference of soft, hard carbon and graphite reflects Figure 21<sup>(33), (54), (58) (59)</sup>.

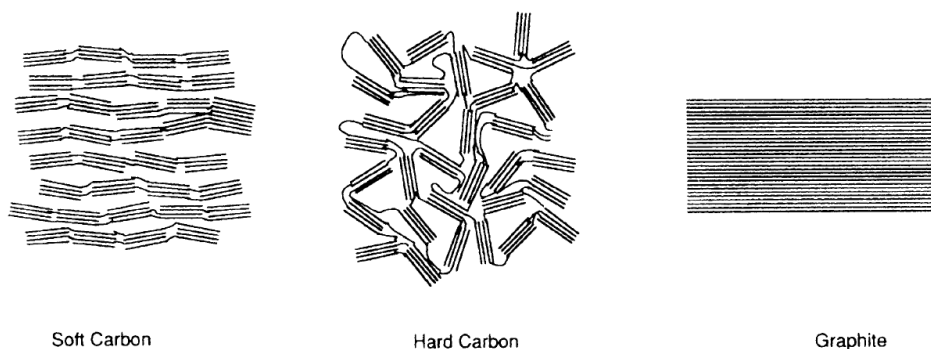
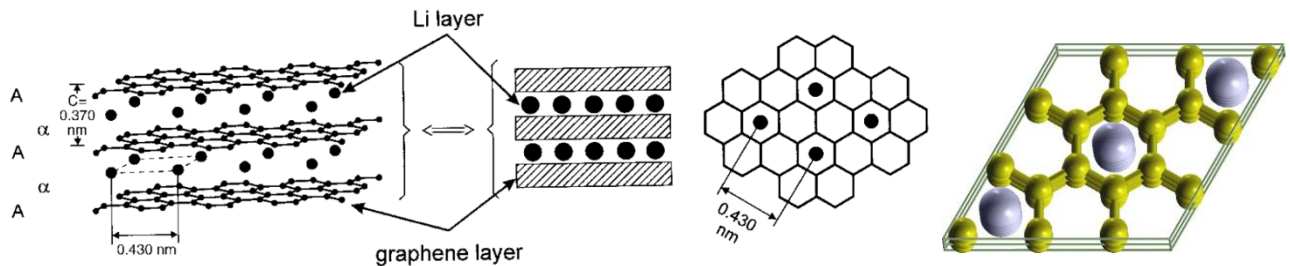


Figure 21: schematic constitution of the three types of the carbonaceous materials<sup>(54)</sup>.

### 2.3.4.3 Lithium Intercalation into Graphite

The intercalation of lithium into graphitic carbons (graphite) takes place via the basal planes at defect side, but mainly through the prismatic structure (zig-zag or armchair faces), cf. Figure 19. The progress of lithiation causes a shift of the internal structure of graphite from previously AB to the energetically favored AA resulting in a direct face to face position of lithiated graphite structure. Since the 1950's the maximum stage of lithiated graphite is noted as one lithium atom per six carbon atoms  $\text{LiC}_6$ . According to the lithiation the distance of the graphene layers changes about 10.3 % <sup>(14), (33), (60)</sup>.



**Figure 22:** left) scheme of the AA stacking order of lithiated graphite, middle) distribution of lithium within  $\text{LiC}_6$  <sup>(33)</sup>; right) AA stacking order of the Li intercalated  $\text{LiC}_6$  with ab-initio DFT relaxation <sup>(61)</sup>.

Due to thermodynamic reasons the intercalation of lithium into graphite proceeds stepwise building several stoichiometric compounds (stage formation) during the electrochemical reduction of graphite. The phenomenon of the single constructed lithiation stages is referred to the required energy for enlarging the graphene layers, which are held together by Van-der-Waals forces. Therefore, graphite passes several intermediate compounds within the stepwise intercalation, for example  $\text{LiC}_{30}$ ,  $\text{LiC}_{18}$ ,  $\text{LiC}_{12}$  and  $\text{LiC}_6$ , whereby the transitions from one stage to another occur not separately, but rather merged. The degree of lithiation is assignable with galvanostatic, voltammetric and optical measurements shown in Figure 23. Other methods for the confirmation of these stepwise intercalation levels are represented by X-ray diffraction and Raman spectroscopy <sup>(33), (62), (63), (64)</sup>.

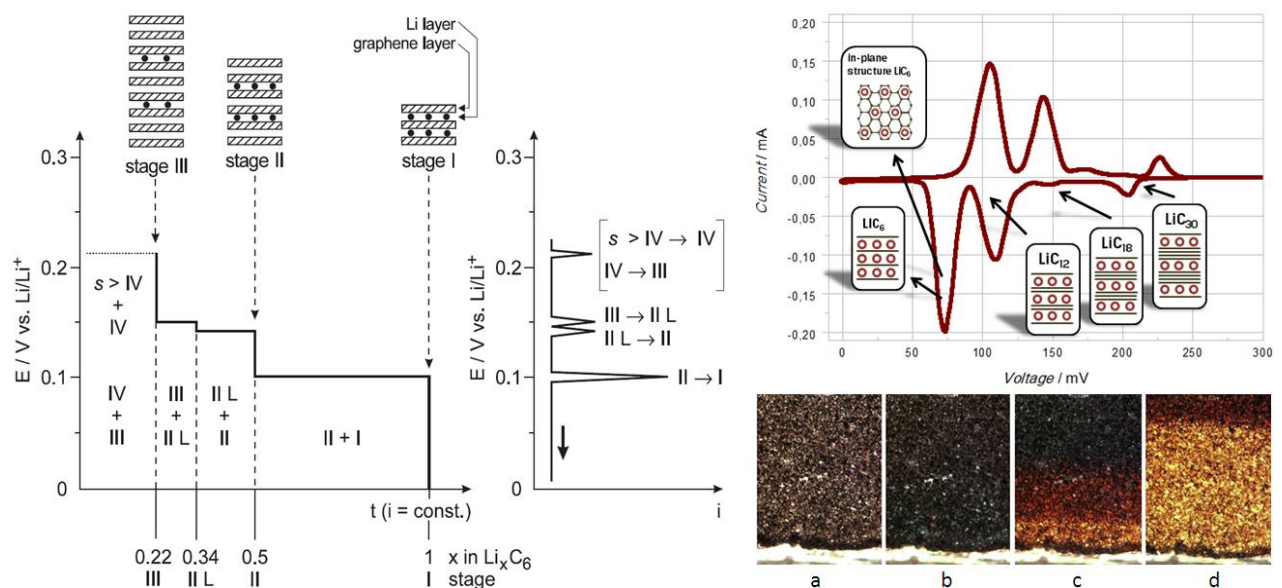


**Figure 23:** left) electrochemical stage formation during lithium intercalation within organic electrolytes containing lithium salts; right) electrochemical proof of the stepwise lithium insertion process into graphite, cyclic voltammetry with a scan rate of  $10 \mu\text{V}\cdot\text{s}^{-1}$ , electrolyte system EC/DEC, 3:7, v:v, 1M  $\text{LiPF}_6$ ; bottom) pictures of graphite, taken after different lithiation degrees: a) pristine graphite, b) graphite shows blue color (stage III,  $\text{LiC}_{18}$ ), c) three lithiation stages blue (stage III,  $\text{LiC}_{18}$ ), red and gold (stage I,  $\text{LiC}_6$ ) and d) two stages are visible - the red (stage II,  $\text{LiC}_{12}$ ) and golden one (stage I,  $\text{LiC}_6$ ) <sup>(33), (34), (63)</sup>.

In theory, the lithiation (charge) and delithiation (discharge) are fully reversible, so a capacity equivalent to  $372 \text{ mAh}\cdot\text{g}^{-1}$  can be estimated for both processes. Nevertheless, the consumed charge within the first intercalation step exceeds the theoretical capacity and in further consequence the lithium release recovers only 80-95% of the initially charge. In the following cycles the achieved capacity is lower than the theoretical  $372 \text{ mAh}\cdot\text{g}^{-1}$ , but the coulometric efficiency is nearly 100%<sup>(33), (49), (54)</sup>.

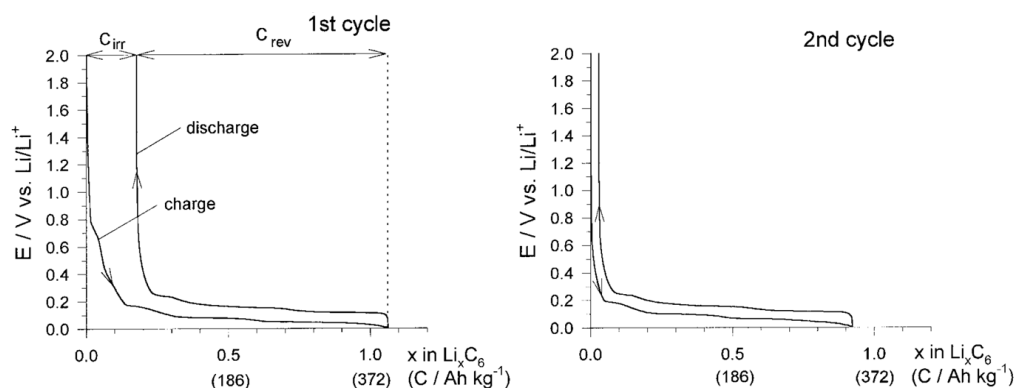


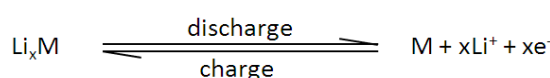
**Figure 24:** constitution of the charge and discharge capacities during constant current cycling (CCC); left) CCC for the first cycle showing the irreversible capacity  $C_{irr}$ ; right) CCC for the following second cycle<sup>(33)</sup>.

The high charge capacity and irreversible capacity  $C_{irr}$ , respectively, disappear ideally after the first cycle. It can be attributed to the lithium loss caused by the formation of the SEI and corrosion like reactions of  $\text{Li}_x\text{C}_6$  compound. The lithium intercalation takes place at a very negative potential which is responsible for the thermodynamically instability of lithiated graphites, metallic lithium and lithium-alloys in all known electrolytes so far. For that reason the SEI is needed as a protecting film generated by decomposition products of the electrolyte preventing further reductive degradation steps of the electrolyte<sup>(33), (49), (54), (62)</sup>.

### 2.3.4.4 Lithium Alloys and Intermetallic Phases as Anode Materials

In search of anode materials for fulfilling the requirement of high specific energy batteries and to avoid problems with dendritic depositions of metallic lithium, researchers have recourse to investigations from the 1970s<sup>(65)</sup>. At that time investigations have been done, for instance by Dey who tried to form alloy compounds consisting of lithium and several chemical elements such as Sn, Pb, Al, Au, Pt, Zn, Cd, Hg and Mg<sup>(66)</sup>. Within the research of Sharma and Seefurth another lithium-alloy is demonstrated including the element silicon<sup>(67)</sup>.

Similar to the carbonaceous materials the chemical elements which serve as host materials exist pure and unlithiated initially. Only during the first lithium insertion the intermetallic phase  $\text{Li}_x\text{M}$  (M = metallic host material) is formed<sup>(65)</sup>.



**Eq. 40**

Lithium alloys can accomplish the task to increase the specific capacity by providing the same or even higher lithium packing densities than metallic lithium itself. For instance  $\text{Li}_{22}\text{Si}_5$  has a specific capacity of  $4200 \text{ mAh}\cdot\text{g}^{-1}$  and a packing density of  $0.0851 \text{ mol}\cdot\text{ml}^{-1}$  compared with lithium which provides a capacity of  $3200 \text{ mAh}\cdot\text{g}^{-1}$  and a packing density of  $0.0769 \text{ mol}\cdot\text{ml}^{-1}$ <sup>(11), (65), (68)</sup>. Unfortunately, lithium insertion causes a

high volume expansion up to 100 – 300 % leading to mechanical stress of the host material particles and subsequently of the entire electrode. Furthermore these intermetallic phases are brittle and cause a degradation of the host material’s structure which is accompanied by loss of electrical contact between particles. All things together induce a large capacity fading and electrolyte decomposition <sup>(14), (49)</sup>.

Approaches to solve these problems are minimization of particle sizes for suppressing volume changes and embedding alloy host compounds into stable matrices for higher dimensional stability <sup>(65)</sup>. Such a stable matrix array is constituted by silicon/carbon composite electrodes.

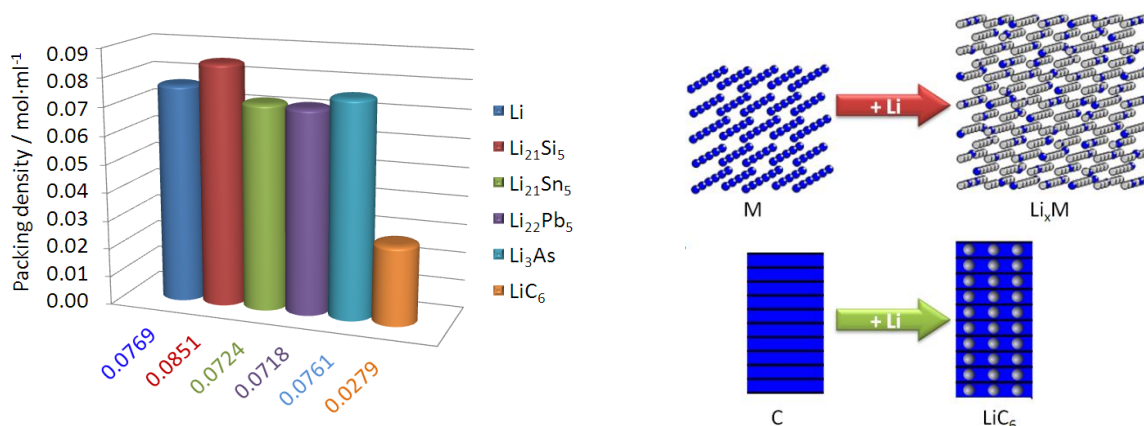
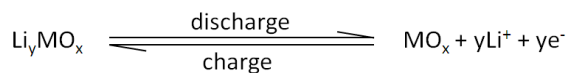


**Figure 25:** left) packing densities of several lithium alloys in comparison to metallic lithium <sup>(drawn from (65), (68))</sup>; right) schematic comparison of volume expansions between graphite and lithium alloy compounds Li<sub>x</sub>M after lithiation <sup>(12)</sup>.

### 2.3.4.5 Transition Metal Oxides as Anodes

In spite of relatively high charge potentials (1.4 V – 1.8 V) and lower capacities than graphite many compounds which contain transition metal oxides are in spotlight as negative electrode material due to their high structure stability and safety issues. Depending on the reaction mechanism in the first cycle two groups of transition metal oxides can be distinguished: transition metal oxides with insertion reaction and with conversion reaction <sup>(47), (69)</sup>.

Lithium insertion into the lattice of the electrode material takes place without structural changes of the host material. Its reaction can be expressed through <sup>(69)</sup>



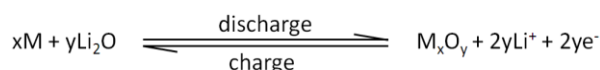
**Eq. 41**

Typical representatives of the insertion mechanism are Ti-based oxides, such as lithium-titanate (Li<sub>4</sub>Ti<sub>5</sub>O<sub>12</sub>, LTO) and titanium-dioxide (TiO<sub>2</sub>). Despite the low specific capacity (175 mAh·g<sup>-1</sup>) LTO regains interest for large scale-up batteries due to several advantages. The crystal structure of LTO is a spinel configuration providing fast lithium-ion diffusion. Lithium insertion and extraction during charging and discharging does not cause a transformation of the structure (zero strain or no swelling material) resulting in a very good cycling performance. Another advantage is the mitigation of safety concerns, because the average potential of 1.5 V vs. Li/Li<sup>+</sup> excludes lithium plating and prevents the electrolyte system from decomposition. Thus, no passivation layer (SEI) is built on the anode surface which results in less lithium loss and ageing effects. On the other hand this positive impact is bought with a low cell voltage <sup>(47), (69), (70)</sup>. A further side effect is the

bad conductivity of the active material itself leading to a slightly rate characteristic for LTO. Hence, many investigations have been done to overcome this problem. Approaches are modifications of the active material particles like carbon coating or increasing the surface area by reducing the particle sizes to the nano scale <sup>(71), (72)</sup>.

TiO<sub>2</sub> draws attraction as anatase polymorph and slightly nanocrystalline anode material as well because of the higher capacity than LTO (335 mAh·g<sup>-1</sup> for LiTiO<sub>2</sub>). On the contrary, TiO<sub>2</sub> exhibits the same drawback as LTO in terms of bad kinetics. A decrease of the particle size from micro to nano scale leading to higher lithium storage ability from 0.1 to 0.8 indeed, but a higher irreversible capacity in the first cycle as well <sup>(69)</sup>.

Within conversion reactions a complete decomposition of metal oxide structure takes place forming Li<sub>2</sub>O at the lithiation. After the delithiation process the initial structures of the former oxides are built and Li<sub>2</sub>O is dissolved again <sup>(73)</sup>. The oxidation state of the transition metals determines the number of exchanged electrons, but more than one electron in any case. By contrast, only up to one electron is involved in the insertion reaction using merely the vacant sites of the transition metal compound. But conversion reactions can use all oxidation states resulting in high reversible Li-storage capacities of 400 – 1000 mAh·g<sup>-1</sup> combined with a high average working potential of 1.8 – 2.0 V vs. Li/Li<sup>+</sup> <sup>(69), (74)</sup>.



Eq. 42

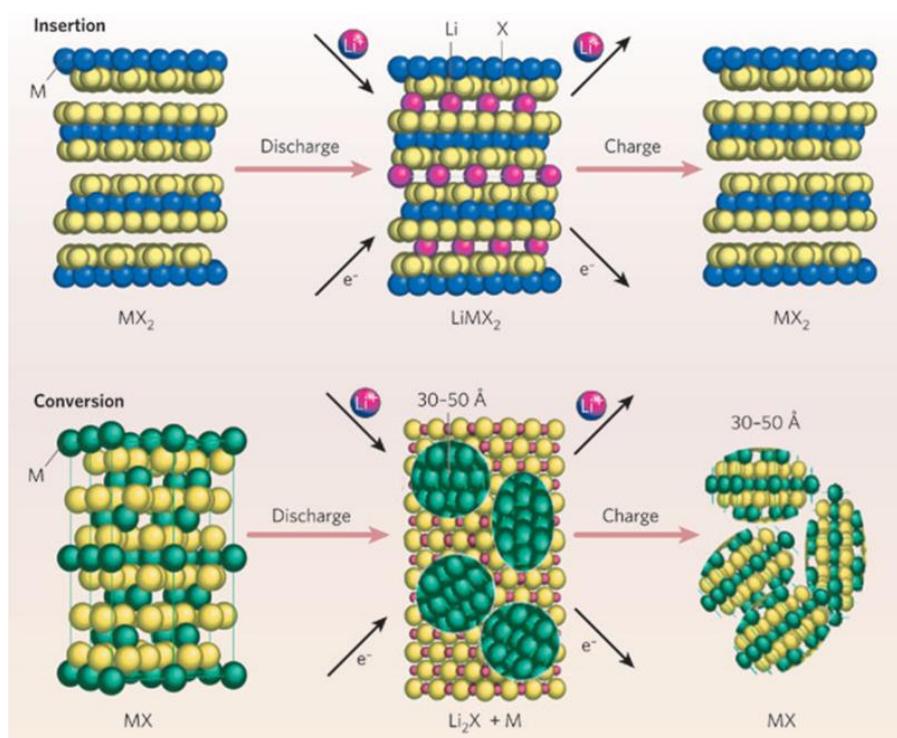


**Figure 26:** schematic draft of an insertion (top) and a conversion (bottom) reaction, whereby a maximum of one electron can be removed within an insertion reaction and 2 – 6 electrons inside of a conversion one <sup>(75)</sup>.

### 2.3.5 Active Materials for the Positive Electrode

The cathode and positive electrode, respectively, serves as lithium resource in Lithium-Ion-Batteries. Typical cathode materials are metal oxides, whose corner stone was laid by Goodenough and Mizushima in the 1970s. At that time first steps were taken to form a lithium battery consisting of lithium and titanium-sulfide ( $\text{TiS}_2$ ). Goodenough and Mizushima noted that  $\text{TiS}_2$  had either semiconducting or semi-metal character for what reason the voltage increase of this battery was denied when sulfides were used as cathodes. In addition, they tried to extract lithium from layered  $\text{LiMO}_2$  compounds (e.g.  $\text{LiCoO}_2$ ,  $\text{LiNiO}_2$ ) as much as possible until a breakdown of its internal structure took place. Finally, they demonstrated an open circuit voltage (OCV) of 4.0 V vs.  $\text{Li/Li}^+$  which motivated the Sony Corporation Japan to use these oxide materials. In addition, the “high voltage” permitted the use of carbon anodes to achieve satisfying energy densities for batteries and launched the very first wireless mobile phones <sup>(76)</sup>.

Transition metal oxides change their oxidation states to higher values during charging. These materials often undergo a phase shift due to the lithium removal within the crystal structure of the positive electrode pointing out the need of materials with high dimensional and structural stability over a wide voltage range. Inside of the discharging process Li-ions get back inserted into the cathode material and the inherent electrons reduce the transition metal. Besides the electrode/electrolyte interface crossing of Li-ions, microstructure and morphology of the cathode material, as well as the rates of lithiation and delithiation (oxidation and reduction) determine the electrochemical properties <sup>(77)</sup>. In particular the lithium diffusion is one of the key factors concerning the charge and discharge rate of a battery. On that account crystal structures with different lithium diffusions can be classified <sup>(33)</sup>:

- **One dimensional Li-diffusion (1D):**  $\text{Li}^+$ -ion extraction/insertion is only possible from one site of the particle, e.g. olivine structure,  $\text{LiMPO}_4$  (M = Fe, Mn, Co, Ni)
- **Two dimensional Li-diffusion (2D):**  $\text{Li}^+$ -ion extraction/insertion takes place from two sides of the particle, e.g. layered materials,  $\text{LiMO}_2$  (M = Mn, Co, Ni and its mixtures)
- **Three dimensional Li-diffusion (3D):**  $\text{Li}^+$ -ion extraction/insertion is possible from all sites of the particle, e.g. spinel structure,  $\text{LiM}_2\text{O}_4$  (M = Mn)

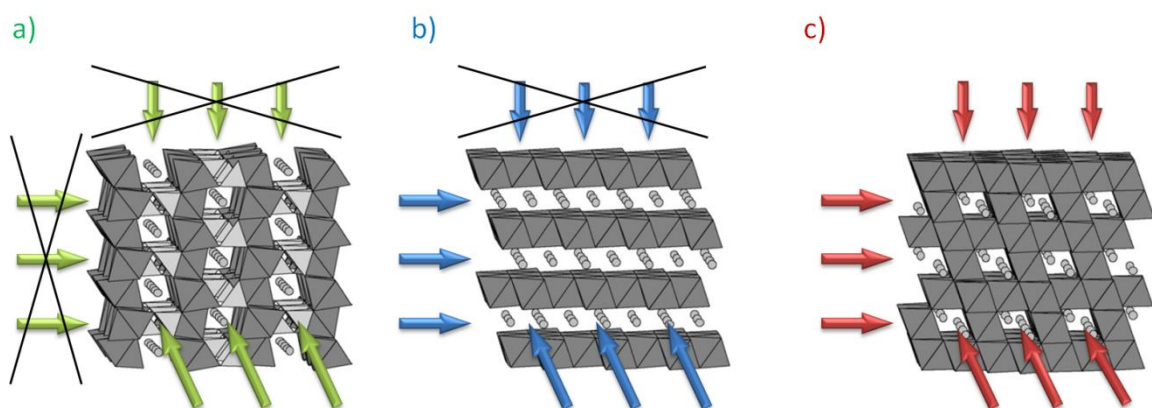


**Figure 27:** crystal structures of cathode host materials constituting different lithium diffusions; a) one dimensional (1D) insertion within olivine structure (e.g.  $\text{LiFePO}_4$ ); b) two dimensional (2D) insertion upon layered materials (e.g.  $\text{LiCoO}_2$ ) and c) three dimensional (3D) insertion of spinel structures (e.g.  $\text{LiMn}_2\text{O}_4$ ) <sup>(revision from (46))</sup>.

### 2.3.5.1 Olivine Structured Compounds

The phospho-olivines have attracted special interest as positive electrode material for Lithium-Ion-Batteries within the last years due to their relatively high theoretical capacities, high energy densities, environmental friendliness, high safety aspects and low manufacturing costs<sup>(78), (79)</sup>. As the name implies phospho-olivines are based on an ordered olivine structure with the general composition  $\text{LiMPO}_4$  ( $M = \text{Fe, Mn, Co, Ni}$ ). Hence, they have a 3D framework indeed, but are counted to the 1D material due to the one dimensional lithium diffusion pathways<sup>(76), (80), (81)</sup>. Depending on the incorporated transition metal different theoretical capacities, potentials and Li-diffusivities can be obtained.

**Table 2:** Electrochemical and physical properties of different phospho-olivines  $\text{LiMPO}_4$  ( $M = \text{Fe, Mn, Co, Ni}$ )<sup>(78)</sup>.

Phospho-olivine compound	Discharge voltage vs. $\text{Li/Li}^+$ [V]	Theoretical capacity [ $\text{mAh}\cdot\text{g}^{-1}$ ]	Diffusivity [ $\text{cm}^2\cdot\text{s}^{-1}$ ]
$\text{LiFePO}_4$	3.4	170	$10^{-8}$
$\text{LiMnPO}_4$	4.1	171	$10^{-7}$
$\text{LiCoPO}_4$	4.8	167	$10^{-9}$
$\text{LiNiPO}_4$	5.1	167	$10^{-5}$

Among these phospho-olivines especially  $\text{LiFePO}_4$  (LFP) is in the spotlight of research and particularly the automotive industry. Due to the fact that the framework of the  $\text{LiFePO}_4$  structure has a very high stability even at fully charged level, its decomposition can be prevented in the case of overcharge which results in the minimization of safety issues. The reason behind this behavior is the strong covalent P-O bond inside of the  $(\text{PO}_4)^{3-}$  tetrahedra<sup>(80), (81)</sup>. Nature and character, respectively, of the chemical bonding between phosphor and oxygen can be simulated by the calculation of distribution of the electron density with full-potential linearized augmented-plane-wave method (FLAPW) combined with the computer program Wien2k package<sup>(82)</sup>.

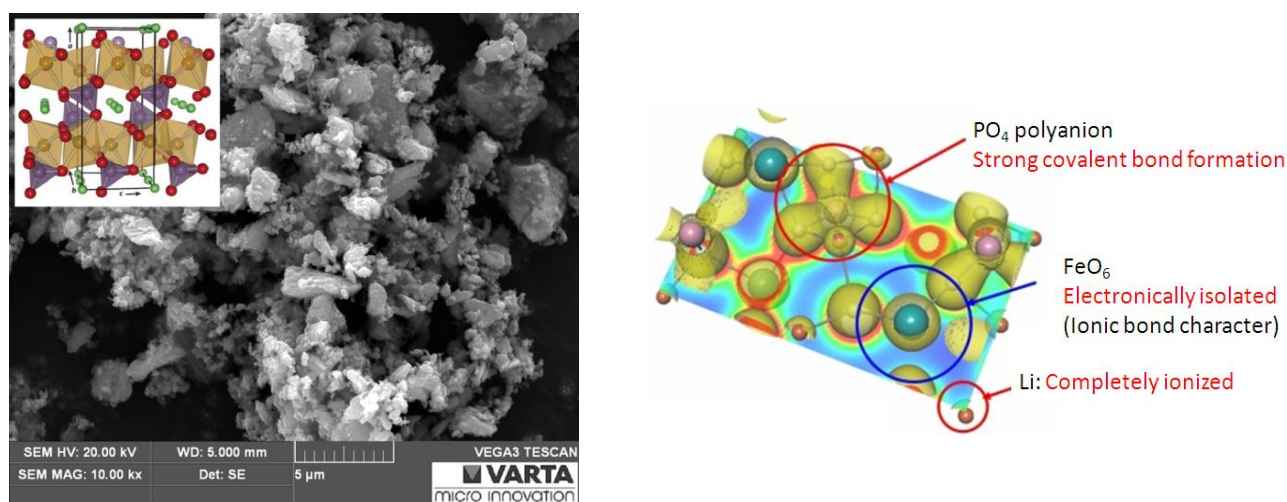


**Figure 28:** left) SEM image of  $\text{LiFePO}_4$ <sup>(source: author)</sup> with the crystal structure of  $\text{LiFePO}_4$ ; the green spots correspond to Li, purple to the  $\text{PO}_4$  tetrahedron and yellow to the  $\text{FeO}_6$  octahedron<sup>(83), (84)</sup>; right) distribution of the electron density of  $\text{LiFePO}_4$ , calculated by Wien2k (FLAPW method) and drawn with Venus developed by R.A. Dilanian & F. Izumi<sup>(82)</sup>.

During lithiation/delithiation a structural phase change from orthorhombic  $\text{LiFePO}_4$  to trigonal quartz-like  $\text{FePO}_4$  occurs, but leaves the structure and 1D channels, respectively, intact. The phase change causes a real flat discharge and charge voltage profile at 3.4 V and 3.5 V vs.  $\text{Li/Li}^+$ .

On the other hand the main drawback of olivine phosphates is the poor rate capability due to low intrinsic electronic conductivity and the one dimensional Li-diffusion at room temperature. As a consequence, theoretical capacities are only achievable at low current densities and/or elevated temperatures<sup>(81), (85)</sup>. Therefore, many researchers focused on several synthesis techniques for mitigating these problems. Hence, the electrochemical performance could be increased with smaller particle sizes, various methods of particle coatings with carbons or even doping with multivalent cations (e.g.  $\text{Mg}^{2+}$ ,  $\text{Al}^{3+}$  and  $\text{Ti}^{4+}$ )<sup>(84), (86), (87), (88), (89)</sup>.

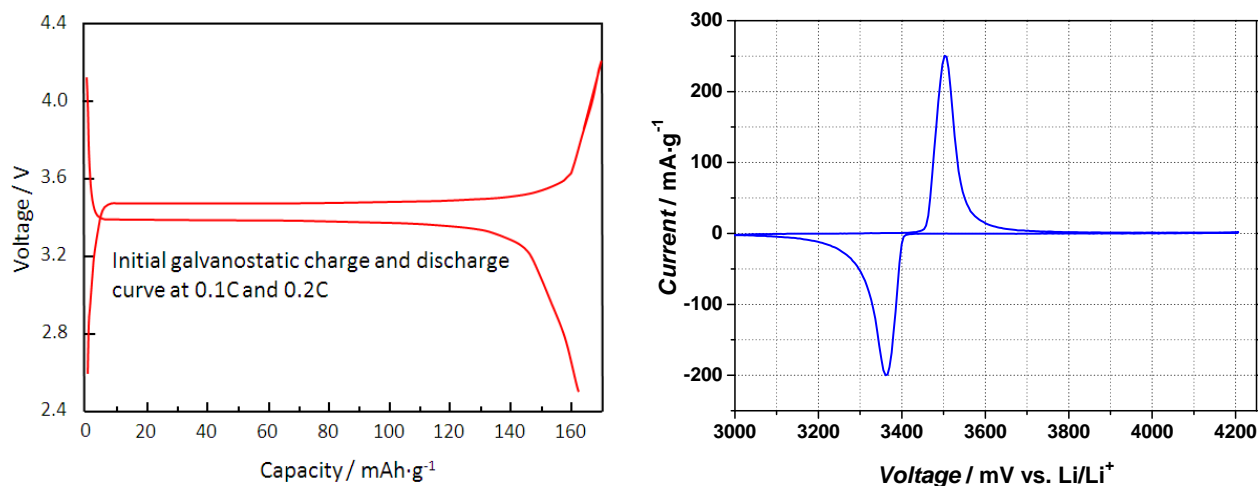


**Figure 29:** left) typical flat charge and discharge profile of  $\text{LiFePO}_4$  at 3.5 V and 3.4 V vs.  $\text{Li/Li}^+$ <sup>(90)</sup> and right) its corresponding cyclic voltammetry (CV) with a scan rate of  $30 \mu\text{V}\cdot\text{s}^{-1}$  (CV provided by M. Scharfegger/Varta Micro Innovation GmbH).

### 2.3.5.2 Layered Transition Metal Oxides

Since Goodenough and Mizushima shed light on the electrochemical removal of lithium in the 1970s, layered structured transition metal oxides became interesting as viable cathode materials. In general these layered oxides have the composition  $\text{LiMO}_2$  ( $\text{M} = \text{Mn}, \text{Co}, \text{Ni}$ ), whereby a well-known representative is lithium-cobalt-oxide,  $\text{LiCoO}_2$  (LCO).

$\text{LiCoO}_2$  is classified into two types depending on synthesis conditions – the high temperature (HT- $\text{LiCoO}_2$ ) and the low temperature LCO (LT- $\text{LiCoO}_2$ ). LT- $\text{LiCoO}_2$  has a spinel-like or cubic structure and is not ideally layered with a cation disorder, which actually means that 6 % of cobalt ions are located in the octahedral sites of the lithium layers. By contrast, HT- $\text{LiCoO}_2$  adapts a trigonal or rhombohedral structure, also referred as a distorted rock salt structure (NaCl) or hexagonal  $\alpha$ - $\text{NaFeO}_2$  crystal structure. The cations ( $\text{Co}^{3+}$  and  $\text{Li}^+$ ) are located in the octahedral interstitial sites between the cubic close-packed oxygen arrays in terms of the  $\text{CoO}_2$  planes, which are formed by edge sharing  $\text{CoO}_6$  octahedras. This arrangement leads to positively charged Li-ion planes screening and stabilizing the slight negatively charged  $\text{CoO}_2$  sheets. From literature it is predicated that the Co-O bond has a strong ionicity, which is responsible for the negative charge on the oxygen anion and destabilizes the layered structure. Only the insertion of the lithium cations between O-Co-O planes accomplishes the structure stability<sup>(91)</sup>. Simulation models such as the FLAPW show no or only a partially lapping of the cobalt and oxygen electron clouds reflecting a strong ionic character as well<sup>(92)</sup>. In addition, an ideal ordered ABCABC stacking order (denoted as O3 stacking sequence) is

obtained, through which lithiation and delithiation is accessible within two-dimensional pathways (2D)<sup>(77), (93), (94), (95), (96)</sup>.

The divergent structures of LT-LiCoO<sub>2</sub> and HT-LiCoO<sub>2</sub> implicate differences within the electrochemical behavior as well. Therefore, capacities can be expected – about 80 mAh·g<sup>-1</sup> for LT-LiCoO<sub>2</sub> and around 140 mAh·g<sup>-1</sup> for HT-LiCoO<sub>2</sub><sup>(97)</sup>. Hence, only the HT-LiCoO<sub>2</sub> is of peculiar interest and will be merely termed LiCoO<sub>2</sub>.

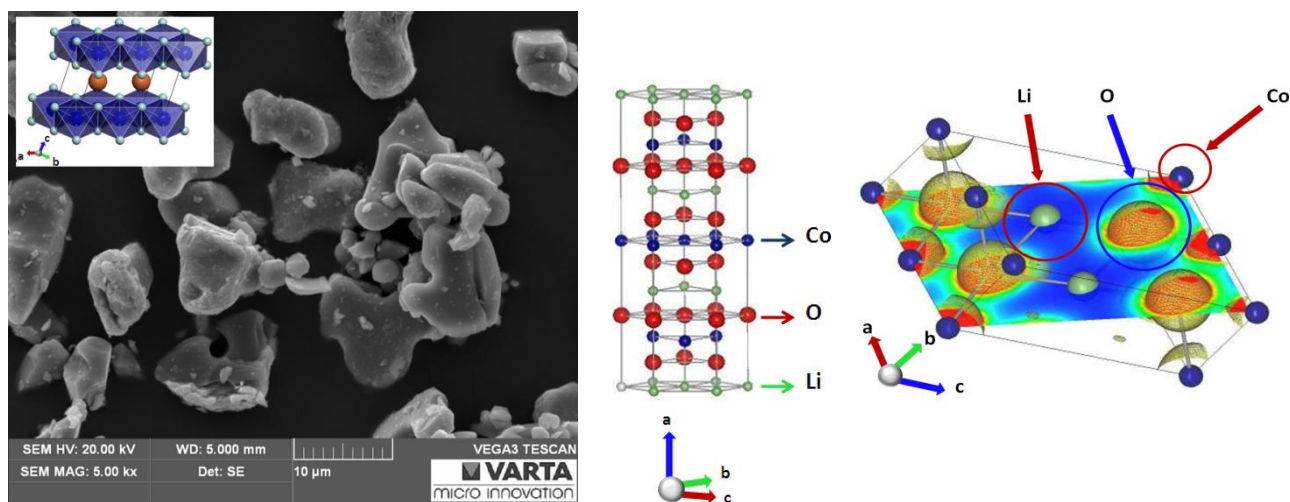


**Figure 30:** left) SEM image of LiCoO<sub>2</sub><sup>(source: author)</sup> with the crystal structure of LiCoO<sub>2</sub>, the red spots correspond to Li, the CoO<sub>6</sub> octahedras are constituted in blue<sup>(98)</sup>; middle) explanation of the arrangement of the α-NaFeO<sub>2</sub> crystal structure for LiCoO<sub>2</sub><sup>(99)</sup>; right) Vienna *ab initio* simulation package (VASP) used for computation of the electron density of LiCoO<sub>2</sub> for determination of the bond character<sup>(92)</sup>.

Figure 31 depicts a cyclic voltammogram of LiCoO<sub>2</sub> showing its typical oxidation and reduction peaks. During oxidation (delithiation) a hexagonal-monoclinic-hexagonal phase transition occurs between 4.1 V and 4.2 V vs. Li/Li<sup>+</sup> representing an order/disorder transformation. In addition, this phase change includes an expansion of 1.2 % of the lattice along the c-axis, which is above the tolerance limit for the elastic strain of cathodes and oxides, respectively ( $\approx 0.1\%$ )<sup>(100), (101), (102)</sup>.

Although LiCoO<sub>2</sub> has a theoretical capacity of 274 mAh·g<sup>-1</sup>, the reversible lithium extraction actually has its capacitive limit at around 140 mAh·g<sup>-1</sup><sup>(103), (104)</sup>. This connotes an upper cut off voltage (charging voltage) during cycling at 4.2 V vs. Li/Li<sup>+</sup>, which corresponds to the stoichiometric formula Li<sub>0.5</sub>CoO<sub>2</sub>. Extracting more Li-ions by going above 4.2 V (vs. Li/Li<sup>+</sup>) causes an increase of cell voltage and capacity indeed, but on the other hand the entire removal of lithium ( $x > 0.5$  in Li<sub>1-x</sub>CoO<sub>2</sub>) leads to a change within crystal symmetry. As a consequence phase changes take place and constitute partially irreversible reactions combined with an irreversible Co loss. Amatucci et al. could demonstrate that the Co loss is related to the amount of unacceptable capacity fading after charging higher than 4.2 V vs. Li/Li<sup>+</sup><sup>(93)</sup>. MacNeil and Dahn supposed decomposition of LiCoO<sub>2</sub> to LiCoO<sub>2</sub> and CoO via a CoO<sub>3</sub> intermediate that even entails a release of oxygen<sup>(76), (105)</sup>. Furthermore the shift in lattice parameters arises through the change in lithium content and may imply micro-cracking of the cathode particles right up to a shear off from the electrode surface<sup>(47), (54), (77), (99)</sup>. All things considered connote a safety risk in the case of charging higher than 4.2 V vs. Li/Li<sup>+</sup>.

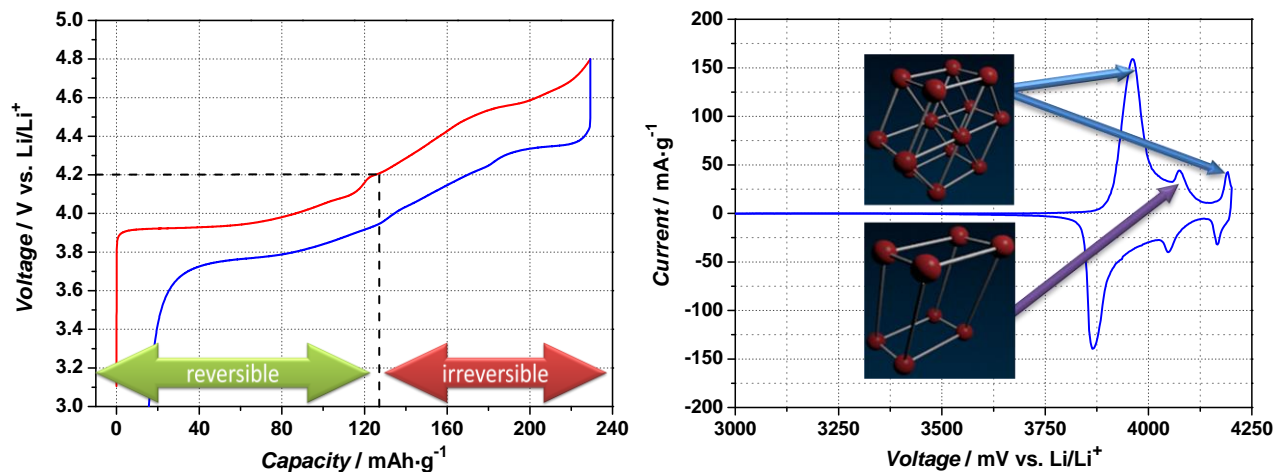


**Figure 31:** left) CCC of  $\text{LiCoO}_2$  – the red line corresponds to charge and the blue line to the discharge profile; the green arrow indicates the area of reversible and the red arrow the area of irreversible lithium extraction/insertion <sup>(data provided by A. Droisner/Varta Micro Innovation GmbH, edited by author)</sup>; right) the corresponding cyclic voltammogram (CV) showing the oxidation peaks during delithiation with hexagonal (blue) and monoclinic (purple) phases <sup>(data provided by M. Scharfegger/Varta Micro Innovation GmbH, edited by author), (106)</sup>.

The endeavor to charge  $\text{LiCoO}_2$  higher than 4.2 V vs. lithium and to improve cycling performance is still a point of interest <sup>(107)</sup>. An approach to overcome these problems is constituted by surface coatings of the active material serving as mechanical restraint, which should eliminate volume changes and structural instabilities of the  $\text{LiCoO}_2$  lattice. Those coating materials are metal oxides such as  $\text{MgO}$ ,  $\text{Al}_2\text{O}_3$ ,  $\text{ZrO}_2$ ,  $\text{TiO}_2$  or  $\text{Li}_2\text{CO}_3$ , carbons or even phosphates, for instance  $\text{FePO}_4$  <sup>(100), (108), (109), (110), (111), (112)</sup>.

Since the market launch by Sony in the 1990s,  $\text{LiCoO}_2$  is used in commercial available batteries until today and constitutes the most common cathode material on market <sup>(81)</sup>. From that time merely an increase of the cell capacity occurred, for instance a 18650 cell exhibited 1200 mAh in 1991 and  $2600 \text{ mAh g}^{-1}$  in 2005 <sup>(46), (112)</sup>. But in spite of its commercial breakthrough  $\text{LiCoO}_2$  has drawbacks besides the limited lithium extraction, namely the toxicity of cobalt and the evanescent resource availability, which is reflected in high material costs <sup>(76), (81), (107)</sup>. Hence, many efforts were made to replace cobalt within this layered structure by other transition metal elements such as nickel and manganese. In this way compounds emerged in which  $\text{Co}^{3+}$  ions were replaced by  $\text{Ni}^{3+}$  and  $\text{Mn}^{3+}$  ions resulting in compositions like  $\text{LiNi}_x\text{Mn}_x\text{Co}_{1-2x}\text{O}_2$  still maintaining the  $\alpha\text{-NaFeO}_2$  crystal structure <sup>(113)</sup>. Several values for  $x$  have been examined, which led to a host material consisting of thirds of Ni, Mn and Co, respectively, with the stoichiometric formula  $\text{LiNi}_{1/3}\text{Mn}_{1/3}\text{Co}_{1/3}\text{O}_2$  (NMC) adopting  $\text{Ni}^{2+}$ ,  $\text{Mn}^{4+}$  and  $\text{Co}^{3+}$  as valence states <sup>(46)</sup>. NMC has experienced attraction within the last years due to its high reversible capacity, lower costs and less toxicity <sup>(114)</sup>.

### 2.3.5.3 Spinel Framework Cathode

Since the discovery of reversible lithium extraction and insertion of layered cathode materials, a common run for the search of new positive electrode materials conflagrated to improve rechargeable Lithium-Ion-Batteries. In the 1980s Scrosati and Thackeray could demonstrate independently of each other the lithium insertion into magnetite  $\text{Fe}_3\text{O}_4$  which has a spinel framework. In cooperation with Goodenough Thackeray tried to lithiate a spinel with the composition  $\text{LiMn}_2\text{O}_4$  and could demonstrate the lithium insertion into this host material as well <sup>(76), (115)</sup>. Advantages of  $\text{LiMn}_2\text{O}_4$  that give point to be a interesting cathode material are for instance low costs of manganese and its good availability, low toxicity, better safety in case of overcharge (compared with  $\text{LiCoO}_2$ ) and a good rate capability <sup>(104), (107)</sup>.

$\text{LiMn}_2\text{O}_4$  and all spinel oxides crystallize in the cubic spinel structure in which manganese occupies the octahedral ( $\text{MnO}_6$ ) and lithium the tetrahedral ( $\text{LiO}_4$ ) sites. Thus, the spinel structure can be seen as a framework of cross-linked tetrahedral and octahedral interstices providing three dimensional pathways for Li-diffusion (3D). Advantages of the three dimensional framework compared to layered structures (2D) are the smaller volume changes during delithiation/lithiation and faster  $\text{Li}^+$ -ion diffusion<sup>(116)</sup>.

Calculation models such as FLAPW show the nature of the chemical bonding. In terms of three dimensional electron density distributions a covalent bonding between manganese and oxygen atoms could be demonstrated<sup>(107), (117), (118), (119)</sup>.

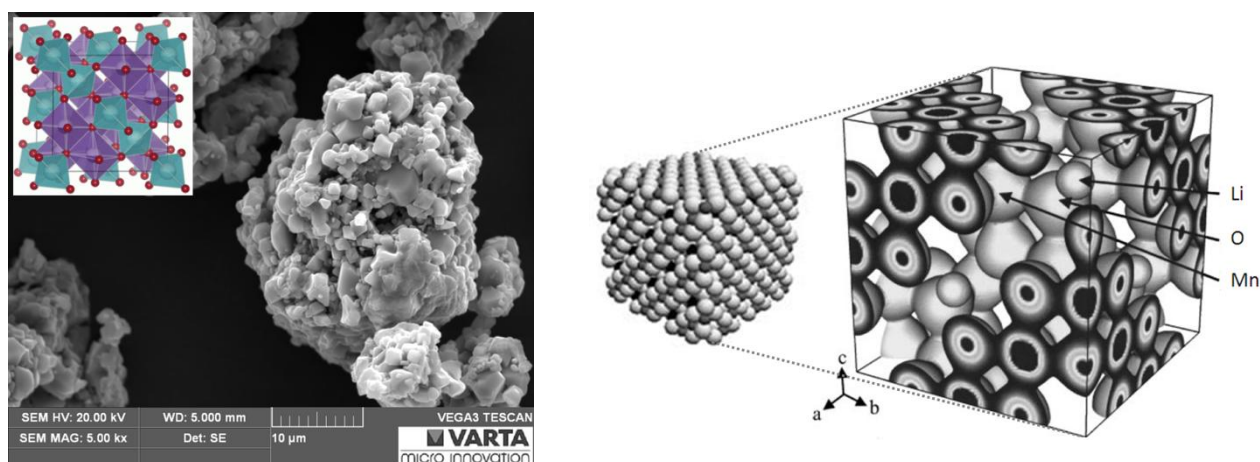


**Figure 32:** left) SEM image of  $\text{LiMn}_2\text{O}_4$ <sup>(source: author)</sup> with the crystal structure of the spinel  $\text{LiMn}_2\text{O}_4$ ; the cyan tetrahedras correspond to Li ( $\text{LiO}_4$ ), purple octahedras ( $\text{MnO}_6$ ) represent Mn and in red oxygen atoms are constituted<sup>(120)</sup>; right) spatial constitution of  $\text{LiMn}_2\text{O}_4$  and the distribution of the electron density calculated by FLAPW method<sup>(117), (121)</sup>.

Thackeray et al. established a ternary Li-Mn-O phase diagram in the 1990s<sup>(122), (123)</sup>. An excerpt out of it shows that  $\text{LiMn}_2\text{O}_4$  exhibits two distinguishable, reversible capacity regions at 3 V and 4 V vs.  $\text{Li}/\text{Li}^+$ . Depending on lithium extraction or insertion,  $\text{LiMn}_2\text{O}_4$  passes through several phases within the compositional range  $\text{Li}_x\text{Mn}_2\text{O}_4$  ( $0 \leq x \leq 2$ ). The bicolored tie line in Figure 33 depicts Li-extraction from the cubic compound  $\text{LiMn}_2\text{O}_4$  leading to cubic  $\lambda\text{-MnO}_2$  ( $\text{Mn}^{4+}$ , blue line) and Li-insertion to tetragonal  $\text{Li}_2\text{Mn}_2\text{O}_4$  ( $\text{Mn}^{3+}$ , red line)<sup>(122), (123), (124)</sup>.

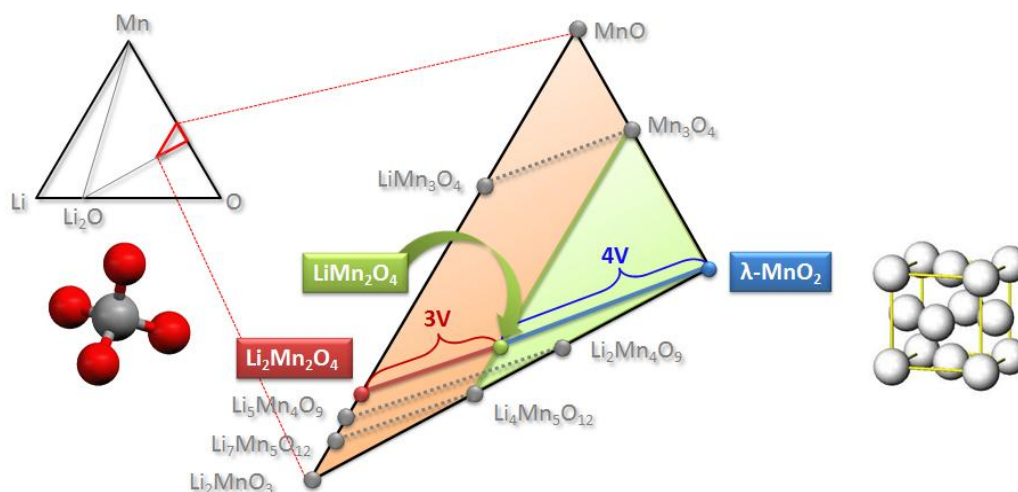


**Figure 33:** excerpt of the ternary Li-Mn-O phase diagram showing the defect spinel phases (orange area) and defect rock salt phases (green area)<sup>(drawn from (122))</sup> with the tetrahedral structure (left) and the cubic close packed structure (right)<sup>(125), (126)</sup>; Li-extraction from  $\text{LiMn}_2\text{O}_4$  leads to cubic  $\lambda\text{-MnO}_2$  ( $\text{Mn}^{4+}$ , blue line) and Li-insertion to tetragonal  $\text{Li}_2\text{Mn}_2\text{O}_4$  ( $\text{Mn}^{3+}$ , red line)<sup>(122), (124), (127)</sup>.

Regardless whether oxidation or reduction of  $\text{LiMn}_2\text{O}_4$  takes place, the theoretical capacity for both processes is  $148 \text{ mAh}\cdot\text{g}^{-1}$  <sup>(122), (123), (124)</sup>. Figure 34 demonstrates that  $\text{LiMn}_2\text{O}_4$  exhibits a flat voltage profile at 4.1 V vs.  $\text{Li}/\text{Li}^+$  with a low obtained capacity in contempt of the attractive high capacity  $148 \text{ mAh}\cdot\text{g}^{-1}$ . In literature it is reported that merely a maximum of about  $120 - 130 \text{ mAh}\cdot\text{g}^{-1}$  can be achieved in practice, because it is not possible to extract the entire lithium electrochemically below 5 V vs.  $\text{Li}/\text{Li}^+$  to form  $\lambda\text{-MnO}_2$  <sup>(107), (123), (127)</sup>.

As already mentioned, the expanded region of the ternary Li-Mn-O phase diagram illustrates a segregation leading to a 3 V and 4 V regions. The 3 V regions (orange area) include defect rock salt structures and the 4 V region (green area) defect spinel structures. Rock salt structures result in displacement reactions destroying the spinel structure continuing until the terminal point at  $\text{Mn-Li}_2\text{O}$  is reached <sup>(122)</sup>. These phase transitions during the lithiation process are associated to the Jahn-Teller effect of the trivalent manganese ion which causes an asymmetric expansion and contraction of the lattice. As a consequence a tetrahedral structure is formed which is characterized by a low symmetry and high disorder <sup>(107), (108), (128), (129), (130)</sup>. If charging and discharging take place within the 3 V areas a flat voltage profile vs. lithium can be achieved indeed, but the structural reorientation produces a two phase region consisting of cubic and tetragonal spinel structures. This structural change causes capacity fade and in the end a poor cycling behavior <sup>(76), (107)</sup>. Hence, the usage of  $\text{LiMn}_2\text{O}_4$  for Lithium-Ion-Batteries requires a limitation of the utilizable working potential window between ca. 3.6 V and 4.5 V vs.  $\text{Li}/\text{Li}^+$  (see green box in Figure 34).

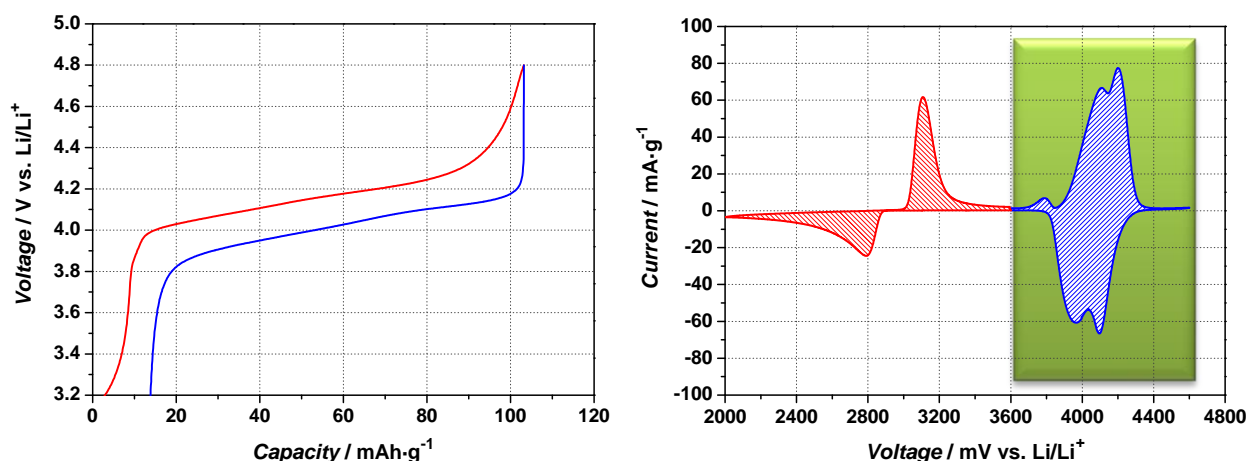
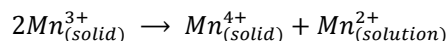


**Figure 34:** left) charge (red line) and discharge (blue line) profile of  $\text{LiMn}_2\text{O}_4$  <sup>(data provided by A. Droisner/Varta Micro Innovation GmbH, edited by author)</sup>; right) the corresponding cyclic voltammetry (CV) shows oxidation and reduction peaks within the cubic (4 V region, blue area;  $\text{LiMn}_2\text{O}_4$ ) and tetragonal (3 V region, red area;  $\text{Li}_2\text{Mn}_2\text{O}_4$ ) phases, respectively, and the range for the utilizable working potential for LIBs (green box) <sup>(data provided by A. Droisner/Varta Micro Innovation GmbH, edited by author)</sup>.

The CV describes the behavior of oxidation and reduction. It is obviously that the 4 V plateau exhibits two redox peaks which are not separated exactly but rather may overlap each other <sup>(128)</sup>. Ying et al. construed this split as a two-step  $\text{Li}^+$ -extraction/insertion which implies a strong Li-Li interaction inducing on the one hand a removal of lithium ions from the half of the tetrahedral site and on the other hand a transition from  $\text{Mn}^{3+}$  to  $\text{Mn}^{4+}$  forming the stoichiometric compound  $\text{Li}_{0.5}\text{Mn}_2\text{O}_4$ . An arising potential and increasing amount of tetravalent manganese ion cause stronger Mn-O bonding and impair the Li-O interaction. Thus, the second half of lithium with weak Li-Li interaction gets extracted and in further consequence two peaks of the two binary equilibrium systems appear, namely  $\text{LiMn}_2\text{O}_4$  with  $\text{Li}_{0.5}\text{Mn}_2\text{O}_4$  and  $\text{Li}_{0.5}\text{Mn}_2\text{O}_4$  with  $\lambda\text{-MnO}_2$  <sup>(117), (128), (131)</sup>.

Unfortunately, the trivalent manganese ion has the tendency to undergo a disproportionation reaction illustrated by following equation <sup>(108), (132)</sup>



**Eq. 43**

The dissolution of  $Mn^{2+}$  into the electrolyte solution constitutes a big drawback of  $LiMn_2O_4$ , because the solvated bivalent manganese ion poisons the surface of the anode and the Solid Electrolyte Interphase (SEI), respectively, having a negative effect on the cycling behavior of the LIB <sup>(76)</sup>. Another negative effect on the capacity fading is the oxidation ability of the tetravalent manganese ions being not stable at the end of charge leading to decomposition of electrolyte solvents <sup>(108), (132)</sup>. Many researches deal with these problems and demonstrate that doping of lithium on octahedral sub lattice forming  $Li_{1+x}Mn_{2-x}O_4$  has a positive impact on the manner of dissolution. These dopants are for instance metal oxides such as  $Al_2O_3$ ,  $MgO$ ,  $SiO_2$ ,  $V_2O_5$  or partial substitution of manganese content through heteroatoms like Cr, Mg or Al, fluorine substitution for oxygen and oxide surface coatings <sup>(104), (108), (132), (133), (134), (135)</sup>. The most common addition and dopant to  $LiMn_2O_4$  is nickel which forms the compound  $LiNi_xMn_{2-x}O_4$  which is introduced and discussed within the scope of the experimental part of this doctoral thesis (cf. chapter 3.1.1, page 45). However, the improvements are only valid at room temperature, because at elevated temperatures the dissolution behavior is still remaining due to the generation of HF from fluoride based inorganic electrolyte salt <sup>(108)</sup>.

### 2.3.6 Electrolyte Systems for Lithium-Ion-Batteries

While important battery components such as negative/positive electrodes determine capacity and therefore, the available energy of a battery, the electrolyte system is assigned to be the third key component. Hence, electrolytes establish a connection between both electrodes providing the required lithium ion flow. Electrolytes can be considered as solutions including solvents and solutes (salts) and can be classified roughly into aqueous and non-aqueous electrolyte systems. On the one hand a comparison of their conductivities demonstrates that aqueous electrolytes exhibit higher values than non-aqueous ones. For instance the 29.4 w% KOH electrolyte of a conventional NiCd accumulator has  $540 \text{ mS}\cdot\text{cm}^{-1}$  at room temperature ( $20^\circ\text{C}$ ) compared to  $11 \text{ mS}\cdot\text{cm}^{-1}$  of a conventional state-of-the-art organic electrolyte (EC/DMC (2:1), 1 M LiPF<sub>6</sub>) used in Lithium-Ion-Batteries. The up to 50 times lower conductivity of non-aqueous electrolytes is restricted to the lower dielectric constants and higher viscosity organic solvents provide, meaning higher molecular masses (lower quantity of molecules per volume) induce lower dielectric constants and higher viscosities of the electrolytes. On the other hand, the conductivity of aqueous electrolytes occurs via a charge transfer of protons (Grotthuss-mechanism), while the conductivity of non-aqueous electrolytes is limited by the solvodynamic volume of the solvated ions <sup>(16), (136), (137), (138)</sup>.

On the other side the applied electrodes have extreme working potentials which occur at 0.0 - 0.2 V for highly reduced anodes (e.g. lithium metal, lithiated carbons) and at 3.0 - 4.5 V for strongly oxidized cathodes (e.g. transition metal oxide) <sup>(38)</sup>. The electrolyte remains in contact with both electrodes and for that reason an oxidative and reductive stability window beyond 3 V is required to prevent decomposition of the electrolyte by reduction or oxidation at both electrodes. But the decomposition voltage of aqueous electrolytes and H<sub>2</sub>O, respectively, creates a narrow electrochemical stability window of merely 1.23 V. As a consequence, the use of aqueous electrolytes is excluded for Lithium-Ion-Batteries <sup>(54), (139)</sup>. By contrast, organic solvents generally decompose at higher potentials vs. lithium and thus, accomplish that high stability demand. Depending on the kind of organic, polar solvents different anodic stabilities can be expected. Therefore, the C-O-C bonds of ether compounds (polymer electrolytes based on polyethers, e.g. polyethylene-oxide, PEO) get oxidized beneath 4 V versus lithium, whereas organic esters and alkyl carbonates have an anodic stability of 4.5 – 5 V vs. Li/Li<sup>+</sup> <sup>(38), (140)</sup>.

Beside the sufficient electrochemical stability organic electrolytes provide a large liquidity range over a wide temperature area. Thus, a broad scope for Lithium-Ion-Batteries is enabled, even at temperatures at the freezing point and below ( $< -40^\circ\text{C}$ ), which would be inaccessible for aqueous electrolytes <sup>(38), (54), (141), (142)</sup>.

Organic, aprotic solvents appear in a huge variety and each solvent exhibits different properties referred to dielectric constants, viscosities or conductivities. In general organic electrolytes should meet properties that are of importance for contemplation <sup>(38), (54), (138), (141)</sup>.

- Compounds with polar groups like carbonyl- (C=O), nitrile- (C≡N), sulfonyl- (S=O) or ether- (-O-) groups and high dielectric constants  $\epsilon$ , respectively, to dissolve salts to sufficient concentrations
- Appropriate (low) viscosities  $\eta$  for adequate ionic ( $\sigma_{\text{Li}}$ ) conductivity,  $\sigma_{\text{Li}} > 10^{-4} \text{ S}\cdot\text{cm}^{-1}$
- No or low electronic conductivity ( $\sigma_{\text{e}}$ ),  $\sigma_{\text{e}} < 10^{-10} \text{ S}\cdot\text{cm}^{-1}$
- Thermal stability over the temperature range in which LIBs usually operate ( $-20^\circ\text{C}$  to  $60^\circ\text{C}$ )
- Broad liquidity range over a large temperature area (low melting  $T_{\text{m}}$  and high boiling point  $T_{\text{b}}$ )
- Chemical stability in terms of anode and cathode to form a sufficient solid electrolyte interphase (SEI) rapidly, because formation takes place outside of the stability window of electrolyte solvents
- Inertness to all battery components
- High flash point  $T_{\text{f}}$ , low toxicity and ecological benignancy to minimize safety issues

Organic solvents such as ethylene-carbonate (EC), propylene-carbonate (PC) or  $\gamma$ -butyrolactone (GBL) fulfill the criterion of an acceptable dielectric constant (high dielectric solvents, HDS) indeed, but just that high dielectric constant causes a higher viscosity<sup>(143)</sup>. Anyhow, electrolyte criteria require low viscosities for sufficient ion transportation. Furthermore, due to their high melting points HDS components are solid at room temperature. For circumvention of these problems a compromise has to be accepted and therefore, HDS are combined with dilution components (low viscosity solvents, LVS) for instance (linear) alkyl carbonates like dimethyl-carbonate (DMC), diethyl-carbonate (DEC) or ethyl-methyl-carbonate (EMC). On that account mixtures of HDS and LVS are used as electrolytes for Lithium-Ion-Batteries enabling a reasonable viscosity and working performance even at low temperatures<sup>(38), (54), (140), (144)</sup>. An overview of the most commonly used organic solvents and their physical properties is depicted in Table 3.

**Table 3:** physical properties of aprotic, organic solvents used for electrolyte systems in Lithium-Ion-Batteries; solvents from EC to NMO constitute high dielectric solvents (HDS) and from DMC to EB low viscosity (LVS) electrolyte components<sup>(38)</sup>.

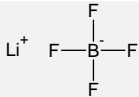
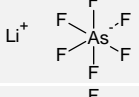
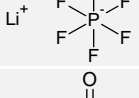
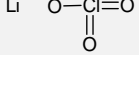
Solvent	Structure	Molecular weight [g·mol <sup>-1</sup> ]	T <sub>m</sub> [°C]	T <sub>b</sub> [°C]	T <sub>f</sub> [°C]	$\eta$ [cP] (25°C)	Dipole moment [debye]	density [g·cm <sup>-3</sup> ] (25°C)	$\epsilon$ (25°C)
Ethylene-carbonate (EC)		88	36.4	248	160	1.90 (40°C)	4.61	1.321	89.78
Propylene-carbonate (PC)		102	-48.8	242	132	2.53	4.81	1.200	64.92
$\gamma$ -Butyrolactone (GBL)		86	-43.5	204	97	1.73	4.23	1.057	39
$\gamma$ -Valerolactone (GVL)		100	-31	208	81	2.0	4.29	1.057	34
3-Methyl-2-oxazolidinone (NMO)		101	15	270	110	2.5	4.52	1.17	78
Dimethyl-carbonate (DMC)		90	4.6	91	18	0.59 (20°C)	0.76	1.063	3.107
Diethyl-carbonate (DEC)		118	-74.3	126	31	0.75	0.96	0.969	2.805
Ethyl-methyl-carbonate (EMC)		104	-53	110	-	0.65	0.89	1.006	2.958
Ethylacetate (EA)		88	-84	77	-3	0.45	-	0.902	6.02
Methylbutyrate (MB)		102	-84	102	11	0.6	-	0.898	-
Ethylbutyrate (EB)		116	-93	120	19	0.71	-	0.878	-

Electrolyte systems assume the main task of the ion conductor and determine the rate of the delivered energy of the battery. To achieve a sufficient conductivity in general, the addition of a conductive salts is indispensable. The ion transport is proposed to be a two-step process. Solvation and dissociation of a conductive salt by polar solvents takes place at first which is followed by the migration of the solvated ions through the solvent media. However, an ideal conductive salt should feature following properties<sup>(38)</sup>:

- Ability to dissolve and dissociate completely in non-aqueous solvents
- Solvated ions should have a high ion-mobility in non-aqueous media
- Oxidative stability of the anion at the cathode surface and inertness to electrolyte solvents
- Stability of the anion against thermal induced reactions of electrolyte solvents and cell components
- No toxicity of the anion and inertness against all cell components (separator, electrodes, etc.)

The choice of conducting salts is very limited compared to the broad spectrum of organic solvents. One reason for this is the confined choice of the electro-active species in the electrolyte, namely the  $\text{Li}^+$ -ion which can't be switched. As a result, only lithium salts can be taken into consideration. But most lithium salts with small anions like halides  $\text{LiX}$  ( $\text{X} = \text{Cl}, \text{F}$ ) don't accomplish the required solubility in low dielectric medias. Anions based on soft Lewis bases such as  $\text{S}^{2-}$ ,  $\text{Br}^-$  or  $\text{I}^-$  would be soluble indeed, but in turn they don't fulfill the criteria of a sufficient oxidative stability ( $< 4.0 \text{ V vs. Li/Li}^+$ ). Lewis acids (e.g.  $\text{AlX}_3$ ,  $\text{X} = \text{halides}$ ) are strongly electron withdrawing components and provide a distribution of the negative charge over the entire anion. However, the stronger the acidity of Lewis acids, the stronger they may attack many of non-aqueous solvents, because weak bases like fluoride or chloride cannot neutralize the activity of the strong acids.  $\text{AlX}_4^-$  compounds remain stable with solvents, but cause corrosion of cell components like polypropylene separators, seals or metallic packing materials of the battery. Therefore, most of nowadays used conducting salts are based on a complex of an anion which is stabilized by a milder Lewis acid like  $\text{PF}_5$ ,  $\text{AsF}_5$  or  $\text{BF}_3$ . For instance the anion  $\text{F}^-$  of lithium-hexafluorophosphate ( $\text{LiPF}_6$ ) is stabilized by the Lewis acid  $\text{PF}_5$ . The usage of these complexes is attributed to their stability at low and high potentials and solubility in low dielectric solvents. In addition,  $\text{LiClO}_4$  or components with the general composition  $\text{LiMX}_n$  ( $\text{M} = \text{B}, \text{As}, \text{P}, \text{Sb}$  and  $n = 4$  or  $6$ ) remain stable at ambient temperatures<sup>(38), (144)</sup>. The electron withdrawing effect of fluorine atoms on the electron donor group and the compared to lithium taller ionic radius of the counter ion  $\text{MX}_n$  engenders a concomitant strong  $\text{Li}^+$ - and weak salt anion solvation<sup>(145), (146)</sup>. Thus, these conducting salts are taken into consideration for usage within LIBs.

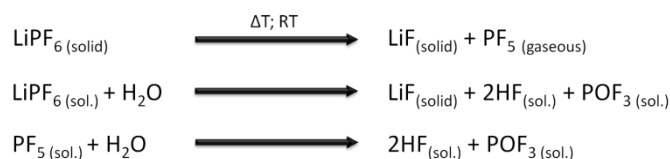
**Table 4:** physical properties of main lithium salts for LIB electrolyte solutions<sup>(38)</sup>.

Conducting salt	Structure	Molecular Weight [g·mol <sup>-1</sup> ]	T <sub>m</sub> [°C]	T <sub>decomposition</sub> [°C] in solution	Al-corrosion	Conductivity $\sigma$ [mS·cm <sup>-1</sup> ] (1M, 25°C)	
						In PC	In EC/DMC
Lithium-tetraborate (LiBF <sub>4</sub> )	Li <sup>+</sup> 	93.9	293	> 100	no	3.4	4.9
Lithium-hexafluoroarsenate (LiAsF <sub>6</sub> )	Li <sup>+</sup> 	195.9	340	> 100	no	5.7	11.1
Lithium-hexafluorophosphate (LiPF <sub>6</sub> )	Li <sup>+</sup> 	151.9	200	~ 80	no	5.8	10.7
Lithium-perchlorate (LiClO <sub>4</sub> )	Li <sup>+</sup> 	106.4	236	> 100	no	5.6	8.4

$\text{LiBF}_4$  electrolyte solutions exhibit too low ion conductivities, especially at lower temperatures leading to a bad battery cycling performance.  $\text{LiAsF}_6$  in turn possesses a high conductivity, but the toxicity of arsenic limits its implementation in Lithium-Ion-Batteries. Properties of  $\text{LiClO}_4$  like a sufficient conductivity, solubility and good oxidative stability make this salt a promising candidate had the heptavalent chlorine not a strong oxidizing character. Therefore, the heptavalent chlorine in perchlorate reacts with many organic solvents, especially at high temperatures and high current strains. Furthermore  $\text{LiClO}_4$  is able for explosive reactions if it's used with transition metal electrodes. From this perspective only  $\text{LiPF}_6$  remains to be the mainly deployed conducting salt for Lithium-Ion-Batteries. Although  $\text{LiPF}_6$  exhibits poorer values of its properties, it prevails against the other salts owing to a series of well-balanced properties. More precisely,  $\text{LiPF}_6$  can fulfill nearly all requirements a salt should meet. For instance a high ionic conductivity (at room

temperature), a high oxidative stability of the  $\text{PF}_6^-$  anion ( $> 5 \text{ V vs. Li/Li}^+$ ) and a good passivation of the aluminum current collector even at high potentials ( $> 5 \text{ V vs. Li/Li}^+$ )<sup>(38), (144), (147), (148), (149)</sup>.

Unfortunately,  $\text{LiPF}_6$  reveals chemical and thermal instabilities as well, which have to be accepted so far. Chemical instability is attributed to the weak P-F bond against water impurities of non-aqueous solvents. Thus,  $\text{LiPF}_6$  hydrolyses due to moisture impurities and generates hydrofluoric-acid (HF) and phosphor-oxitri-fluoride ( $\text{POF}_3$ ). The generation of HF constitutes a problem due to negative effects on film formation on graphite surfaces and stability on cathodes (transition metal oxides). Furthermore at higher temperatures, but even at room temperature a decomposition process takes place which forms phosphor-pentafluoride ( $\text{PF}_5$ ).  $\text{PF}_5$  initiates reactions like ring opening polymerizations or cleavage of solvent linkages (e.g. carbonates). Although  $\text{LiPF}_6$  has become the conducting salt of choice in the last two decades, these drawbacks lead to the need of improvements towards better salts. That's why even salts like  $\text{LiBF}_4$ ,  $\text{LiAsF}_6$  or  $\text{LiClO}_4$  are further subject of investigation even until today<sup>(38), (148), (149)</sup>.



**Eq. 44**

Beside the choice of solvents and conducting salts the concentration of both plays a very important role. Since solvents cannot exhibit concomitant high dielectric constant  $\epsilon$  and low viscosity  $\eta$ , binary or ternary mixtures of solvents were used to fulfill required properties an electrolyte should meet. Matsuda et al. made big efforts to investigate dependences of the conductivity of mixed solvents and electrolytes, respectively<sup>(150), (151), (152), (153)</sup>.

A solvated ion can only migrate through an applied electric field if it's shielded from the formation of ion pairs with its counter ion of the solvating solvent. Solvents with higher dielectric constants provide a good dissociation level at certain salt concentrations and as a consequence ion pair formation occurs less. For good ion mobility the viscosity should be hold down as low as possible. Figure 35 describes the interaction between mixture solvents and used single solvents in terms of their opposite dielectric constants and viscosities. Actually, the conductivity influenced by the dielectric constant and viscosity of the solvents, passes through a maximum of solvent and conductive salt concentrations<sup>(38)</sup>.

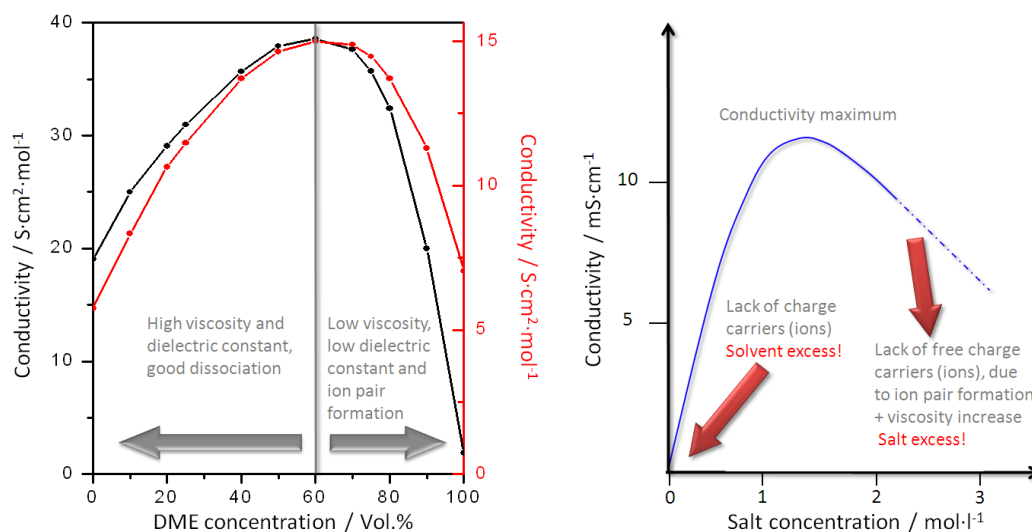


**Figure 35:** left) variation of the conductivity of  $\text{LiClO}_4$  in a mixed electrolyte PC/DME with different electrolyte compositions for two salt concentrations,  $c = 0.1 \text{ mol}\cdot\text{l}^{-1}$  (black curve) and  $c = 1.0 \text{ mol}\cdot\text{l}^{-1}$  (red curve)<sup>(drawn from (152))</sup>; right) dependency of the conductivity of salt concentrations without varying the solvent composition<sup>(revision from (32))</sup>.

It should be mentioned that many efforts were made to improve liquid electrolyte systems by addition of additives. These compounds were added between one and five percent and aim for positive effects on the battery performance or safety concerns (cf. chapter 3.3.4.5, page 95).

Beside liquid electrolytes other types of electrolytes got into the spotlight of research due to advantages such as more flexible design, construction of flat cells and the prevention of electrolyte leakage<sup>(154)</sup>. Following different types of electrolytes should be mentioned shortly:

- **Polymer electrolytes:** this type of electrolyte was released by Sony within the first Lithium-Ion-Polymer-Batteries (LiPB) in 1998. The principle is the combination of chemical properties with the merit of the mechanical stability of polymers. As a consequence the organic electrolyte is embedded into a polymeric matrix. For instance, mainly deployed polymers are polyethylene-oxide (PEO) or polyvinylidene-difluoride (PVdF). However, these polymer electrolytes suffer problems like bad conductivities of the polymer itself and are subject of investigations until today<sup>(155), (156), (157), (158)</sup>.
- **Solid electrolytes:** a huge variety of solid electrolytes beginning with crystalline inorganic lithium ion conductors like NASICON or LiSICON types right up to amorphous inorganic lithium ion conductors (LiPON) belong to ceramic materials. Foremost advantages of these solid electrolytes are their inflammability, prevention of leakage and thermal stability. By contrast, these materials don't exhibit either sufficient conductivities or a large electrochemical stability area, but anyhow not both at the same time. Furthermore due to the hardness of ceramics sheet manufacturing techniques prove difficult, which are required for large scale batteries<sup>(159), (160), (161), (162), (163)</sup>.
- **Ionic liquids:** ionic liquids (IL) are defined as molten salts at room temperature and even temperatures below 100°C. Electrolytes based on IL consist merely of their ions and conducting salt ions, but without any solvent. IL provide a large liquid range which facilitates battery operations within a wide temperature range. But other properties must not be disregarded like a low volatility, inflammability and especially an excellent electrochemical stability window even at potentials of 5 V. As a consequence ionic liquids seem to be promising candidates for LIB electrolytes, if these compounds wouldn't have some drawbacks. Hence, they exhibit a high viscosity, especially strongly increased by the addition of conducting salts which is necessary to achieve a sufficient conductivity. Moreover, IL don't form a suitable solid electrolyte interphase on graphite anodes. Last but not least, IL are very expensive by reason of their synthesis and purification<sup>(136), (155), (164)</sup>.

### 2.3.7 Anode/Electrolyte Interactions – the Solid Electrolyte Interphase

As already described within the electrolyte chapter, the extreme working potentials of anodes (e.g. graphite) and cathodes (e.g. transition metal oxides) forces nearly most of today's known electrolytes to cross their thermodynamic stability edges. The strong negatively polarized anode implies a reductive decomposition of electrolyte components at the surface and at the same time oxidation occurs at cathode surfaces. The decomposition products form a passive film at the anode, which is located at the interphase electrode/electrolyte. In addition, this layer behaves like a solid electrolyte and due to this reason Peled named it "solid-electrolyte-interphase" (SEI)<sup>(33), (142), (165), (166)</sup>.

SEI formation takes place on all types of anodes such as lithium metal, lithium alloys ( $\text{Li}_x\text{M}$ ) and lithiated carbons ( $\text{Li}_x\text{C}_n$ ). If metallic lithium is immersed into suitable electrolytes, electrolyte components react with

lithium electrodes spontaneously by forming a SEI on the anode surface. Besides, a concomitant electronic insulation and permeability for Li-ions, the merit of this formed layer is the protection of anode surfaces from ongoing corrosion processes. This is attributed to the kinetic stability of the electrolyte against further reduction. These reactions can be demonstrated on lithium alloys and lithium-graphite-intercalation-compounds (Li-GIC) as well, but compared to metallic Lithium, film formation takes place mainly during the first charging step of the battery. Basically, film formation is completed when the entire electrode surface is covered and a certain thickness is attained. According to literature the thickness of the SEI varies from 1 nm and below up to 10 nm and above <sup>(38), (167), (168), (169), (170)</sup>. Therefore, the thickness depends on used anode material and electrolyte. For instance graphite exhibits only low volume changes during lithiation and delithiation (about 10 %), which restricts SEI formation to the first few cycles. On the contrary, SEI formation on lithium intermetallic surfaces varies greatly in quantity caused by their large volume changes during cycling (from 100 up to 300 %) <sup>(14)</sup>. As a result, the formed layer may break up or possibly parts of it break off. If native, unfiled surfaces of the anode are exposed to the electrolyte, a new SEI will be formed at this place (cf. Figure 36). As a consequence SEI formation can occur after a large number of cycles even up to the entire cycle life of the electrode. It should be mentioned that SEI formation is always associated with irreversible electrolyte and lithium loss and thus, with a decrease of capacity <sup>(33), (38), (146), (170)</sup>.

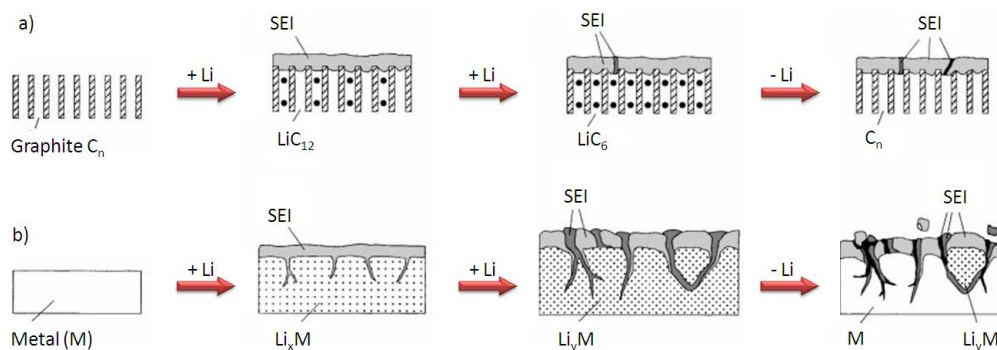


**Figure 36:** sketch draft of the SEI formation during cycling for a) on carbonaceous and b) metallic host materials; the different formations of the SEI arising due to different volume changes of metal compounds and graphite during lithiation/delithiation are depicted as shaded areas <sup>(revision from (146))</sup>.

The chemical composition and morphology of the SEI depends mainly on the used electrolyte components. Therefore, it constitutes a very complex film consisting of inorganic components originating from salt decomposition and organic components deriving from reduction processes of the organic solvents. A very simple constitution of the SEI composition is shown in Figure 37 <sup>(38), (142), (171)</sup>.

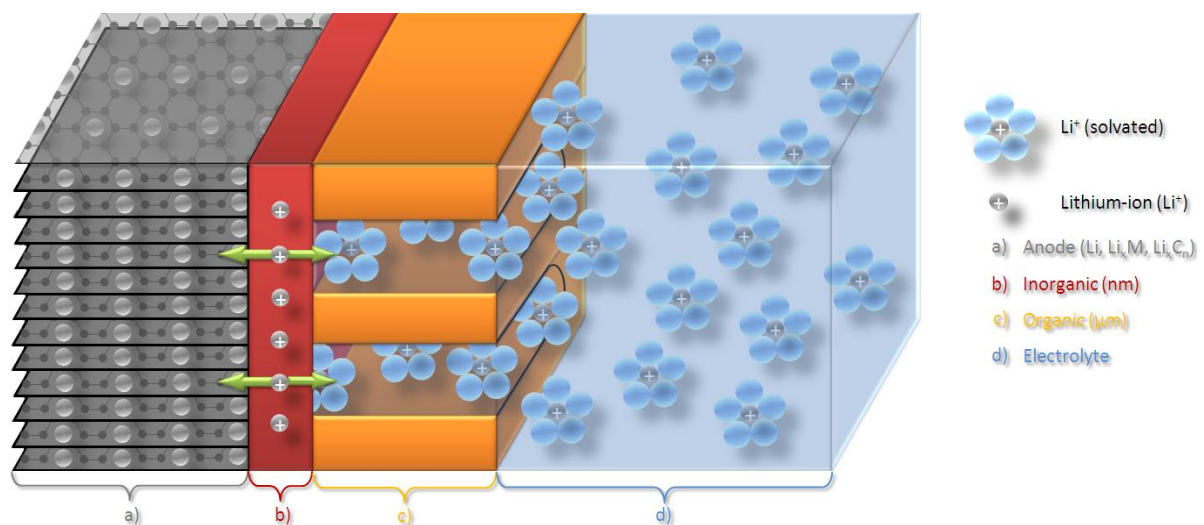


**Figure 37:** schematic composition of the solid electrolyte interphase (SEI) on a graphite surface in non-aqueous organic electrolytes; on other anodes (lithium metal, lithium alloys) the SEI formation can be found as well <sup>(drawn from (142))</sup>.

Factors having an impact on the SEI in terms of its composition, quality and efficiency appear in a huge variety. Therefore, factors like the type of carbon used as anode play a role as well as electrolyte composition, cycling conditions (especially temperature during cycling) and/or overpotentials. As a result, the exact composition of it is still pending and point of discussion between research groups<sup>(38), (165), (172)</sup>.

Decomposition products of electrolyte solvents are responsible for the buildup of the organic part of the SEI. In particular, properties that play an important role for decomposition are for instance dielectric constants, polarities, viscosities or reactivities. The order of reactivities in which common carbonates can be arranged is  $EC > PC > DMC > DEC$ . If EC and/or PC (HDS) is used in electrolyte solutions two possible reactions may take place depending on the concentration of the carbonates. High concentrations engender the passivation components lithium-alkyl-dicarbonates  $(CH_2OCO_2Li)_2$  and  $ROCO_2Li$ , respectively, and at lower concentrations lithium-carbonate  $(Li_2CO_3)$  is the mainly reduced product<sup>(165), (171), (173), (174)</sup>.

The first reduction step is the formulation of a radical anion. One of the subsequent pathways is attributed to the conclusions of Dey et al. suggesting that PC undergoes a two electron reduction forming gaseous propylene (EC forms ethylene) and insoluble  $Li_2CO_3$ <sup>(175)</sup>. Aurbach et al. consider a second pathway concerning a one electron mechanism. Within this reaction the cleavage of C-O bond forms a stable radical anion in which the negative charge is compensated by ion pair formation with a  $Li^+$ -cation from the electrolyte and the radical is located at the secondary carbon. The subsequent reactions constitute one electron transfer per PC molecule by radical termination and disproportionation and lead to a mixture of alkyl carbonates (reaction pathway with green arrows in Figure 38). In addition, Xu mentions a third reduction process which Aurbach excludes indeed, namely a two electron process forming a radical anion intermediate from cleavage of alkyl-oxygen bond which finally leads to products like lithium-oxalate  $(Li_2C_2O_4)$  and alkyl-oxides combined with gaseous carbon-monoxide (reaction pathway with red arrows in Figure 38)<sup>(45), (171), (173), (176), (177), (178), (179)</sup>.

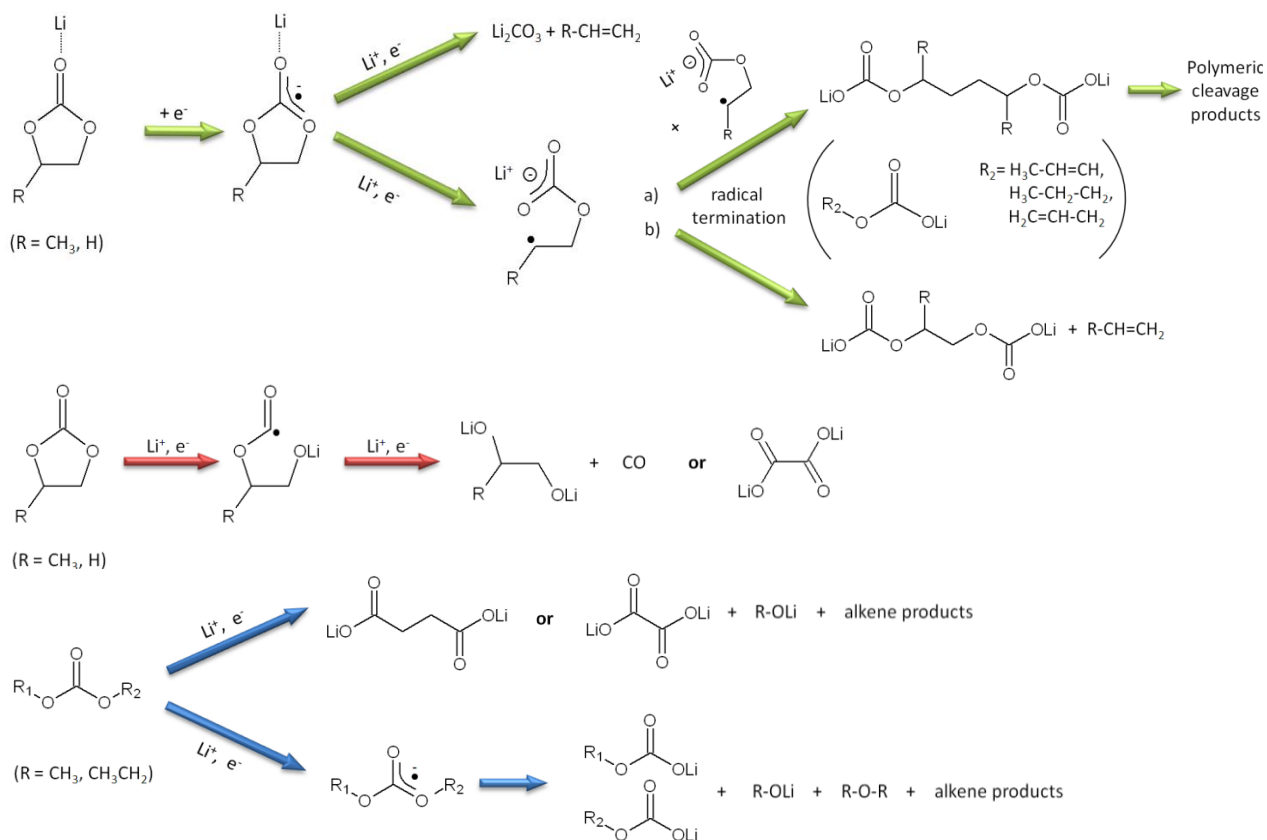
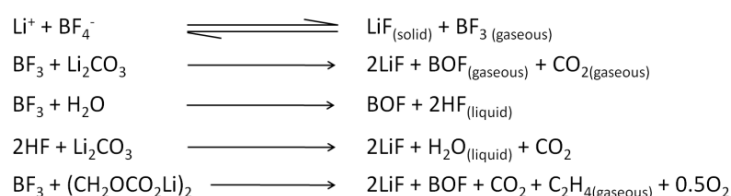


**Figure 38:** reductive decomposition of organic solvents like cyclic carbonates (EC, PC; green and red arrows) and linear carbonates (DEC, DMC; blue arrows) on anode surfaces<sup>(revision from (38), (176) (178))</sup>.

Similar to the reduction processes of cyclic carbonates, low viscosity solvents (LVS) like DEC and DMC get reduced on the anode surface as well. At first nucleophilic attack on the linear carbonates takes place followed by the formation of radicals, which in turn are converted to the reduced decomposition products, such as lithium-succinate ( $\text{LiO}_2\text{C}-\text{CH}_2\text{CH}_2\text{CO}_2\text{Li}$ ), lithium-oxalate ( $\text{Li}_2\text{C}_2\text{O}_4$ ), lithium-methoxide ( $\text{LiOCH}_3$ ) and other side products (cf. Figure 38, page 42; blue arrows) <sup>(38), (165), (167), (180)</sup>.

Besides solvent decomposition salt reduction and side reactions occur as well and intervene at least in the inorganic buildup of the SEI. Conduct salts give initially a porous and polymer rich surface with a high amount of salt residues in the presence of fluorinated salts ( $\text{LiPF}_6$ ,  $\text{LiBF}_4$ , etc.). The main reduction product is lithium-fluoride ( $\text{LiF}$ ) and represents the major inorganic component of the SEI. Edström et al. intend that a high  $\text{LiF}$  concentration impinges on battery behavior in terms of power fade, because  $\text{LiF}$  is distributed as large crystals in SEI matrix dependent on used salt, cycling conditions and temperature. In addition,  $\text{LiF}$  films exhibit a much higher interfacial resistance for  $\text{Li}^+$ -ion migration than carbonates do. Furthermore salt decomposition of  $\text{LiBF}_4$  or  $\text{LiPF}_6$  produces  $\text{HF}$  as well, whose reaction with carbonates (e.g.  $\text{Li}_2\text{CO}_3$ ) reduces the amount of carbonates within the SEI. As a consequence, if  $\text{LiF}$  substitutes the carbonates completely an efficient passivating layer cannot be formed. For instance,  $\text{Li}^+$  reacts with  $\text{BF}_4^-$  and forms  $\text{LiF}$  and  $\text{BF}_3$ , whereby  $\text{BF}_3$  is a highly reactive Lewis acid and reacts with Lewis bases ( $\text{H}_2\text{O}$ ) violently.  $\text{HF}$  in turn reacts with  $\text{Li}_2\text{CO}_3$  and forms  $\text{LiF}$ ,  $\text{CO}_2$  and water. Other reactions with electron rich groups are given in Eq. 45 and those of  $\text{LiPF}_6$  in Eq. 44, page 39 <sup>(38), (45), (165), (168), (171), (173), (181)</sup>.

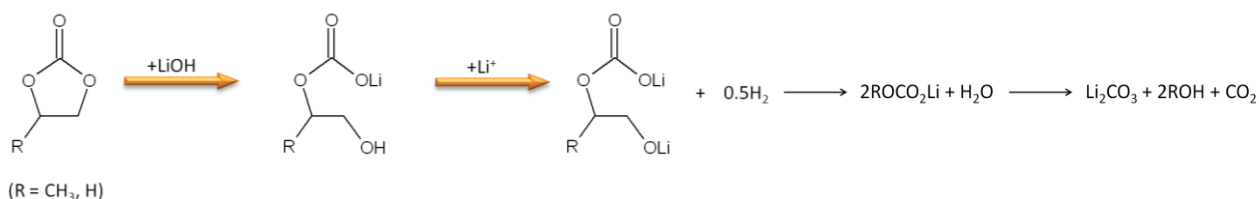


Eq. 45

Side and secondary reactions participate in the SEI buildup and can be attributed to contaminants as oxygen, water, carbon-dioxide and  $\text{HF}$ . Side reactions of oxygen or carbon-dioxide with lithium form  $\text{Li}_2\text{O}$  and  $\text{Li}_2\text{CO}_3$ , respectively (cf. Eq. 46).  $\text{H}_2\text{O}$  reacts with  $\text{Li}$  to lithium-hydroxide ( $\text{LiOH}$ ) and hydrogen ( $\text{H}_2$ ).  $\text{LiOH}$  in turn attacks nucleophilically cyclic carbonates according to the reaction given in Figure 39. The formed  $\text{RCO}_3\text{Li}$  compounds are sensitive to moisture and thus, they react with  $\text{H}_2\text{O}$  by forming  $\text{Li}_2\text{CO}_3$ ,  $\text{ROH}$  and  $\text{CO}_2$  <sup>(38), (45), (176)</sup>.



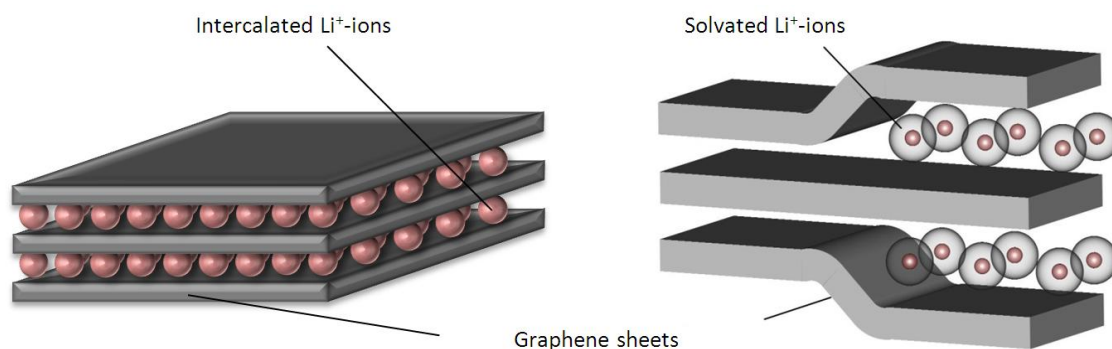
Eq. 46


 Figure 39: nucleophilic attack by  $\text{LiOH}$  on a cyclic carbonate solvent leading to lithium-carbonate <sup>(revision from (38), (176))</sup>.

In general, good passivation of anodes and buildup of an ideal SEI, respectively, is attained if compounds like  $(\text{CH}_2\text{OCO}_2\text{Li})_2$ ,  $\text{Li}_2\text{CO}_3$  and  $\text{Li}_2\text{O}$  are formed, while metastable compounds such as  $\text{ROLi}$  and  $\text{ROCO}_2\text{Li}$

exhibit a poor passivation behavior. The reason for the good passivation behavior is their less solubility in the solvents and good adhesion to graphite surfaces, which is induced by their polar ionic structure. Furthermore it is assumed that an ideal SEI is built completely before lithium intercalation takes place. The most widely represented onset potential for SEI formation is 0.8 V vs.  $\text{Li}/\text{Li}^+$ , whereby the onset of the SEI buildup depends strongly on reaction kinetics. Materials having a low rate constant require a high overpotential and thus, get reduced at low potentials (vs. lithium). By contrast, materials having a high rate constant are formed at higher potentials (vs.  $\text{Li}/\text{Li}^+$ )<sup>(165), (173), (174), (182)</sup>.

If a good passivation is obtained, the SEI prevents anode surfaces from further corrosion processes and ensures a good cycling behavior. Nevertheless, failure mechanisms occur as well due to inability of certain electrolytes to establish a sufficient SEI and are attributed to chemical reactions causing exfoliation of graphite. Besenhard et al. propose that beside lithium ions solvent molecules co-intercalate between graphene gaps as well and form the ternary graphite intercalation compound (GIC)  $\text{Li}_x(\text{solv})_y\text{C}_n$ . This solvent co-intercalation occurs due to the fact that the solvation energy of lithium ions is larger than the weak Van-der-Waals forces between the graphene layers. As a result, the graphene structure distorts in terms of volume expansion of about 150%. Moreover, the irreversible reduction products result in the before mentioned destruction and exfoliation, respectively, which inhibits any further lithium exchange. As a consequence, the storage capability decreases drastically<sup>(33), (38), (165)</sup>.



**Figure 40:** left) schematic of lithium intercalation into graphite<sup>(drawn from (33))</sup>; right) solvated  $\text{Li}^+$ -ions are intercalated and form a ternary graphite intercalation compound (GIC)  $\text{Li}_x(\text{solv})_y\text{C}_n$ , which leads to an extreme volume expansion of about 150%<sup>(183)</sup>.

Once again, the formation of the SEI takes place at ca. 0.8 V vs. lithium. Unfortunately, the decomposition of Propylene-carbonate (PC) induces the solvent co-intercalation at the same potential. Its decomposition mechanism or the formation of this ternary GIC is suggested to proceed via two competitive pathways. Shu et al. suggest that radical termination forms alkyl carbonates and the parallel occurring reduction process constitutes a one electron process forming  $\text{Li}_2\text{CO}_3$  and propylene gas. It is proposed that the gaseous products strain the weak bonded graphene layers reflecting the exfoliation of graphite. On that account film formation resulting in a fast SEI formation should occur before solvent intercalation can take place.

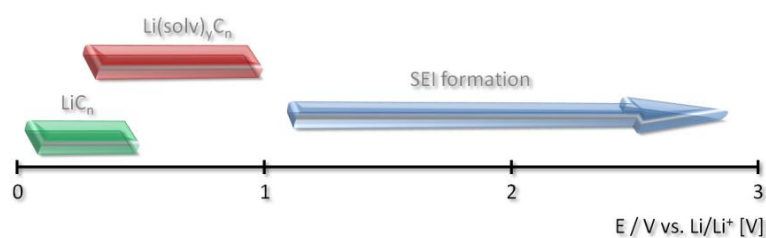


**Figure 41:** potential regions in which SEI formation should occur, namely before  $\text{Li}^+$ -intercalation into graphite  $\text{LiC}_n$  and/or solvated lithium intercalation  $\text{Li}_x(\text{solv})_y\text{C}_n$  into graphite takes place<sup>(revision from (146))</sup>.

## 3 Experimental Part

### 3.1 General Remarks on 5V Cathodes

#### 3.1.1 State of the Art

As already mentioned, most of commercial available cathodes for Lithium-Ion-Batteries are lithium intercalation compounds with different crystal structures such as olivines, layered oxides or spinel oxides (cf. chapter 2.3.5, page 28 ff.). Among these possible cathode materials the spinel framework compound  $\text{LiMn}_2\text{O}_4$  got into spotlight due to its low cost and toxicity. Furthermore it provides three dimensional pathways for lithium-ion diffusion, which is expected to improve electrochemical properties and privileges spinel compounds towards layered and olivine structures. Nevertheless, a replacement of the non-economic and non-ecological  $\text{LiCoO}_2$  in commercial Lithium-Ion-Batteries didn't occur so far, which is attributed to the lower specific capacity and, in particular, the rapid capacity fade of  $\text{LiMn}_2\text{O}_4$  upon cycling. This effect is caused by the Jahn-Teller-distortion of the trivalent manganese ions, the dissolution of manganese into the electrolyte via disproportionation ( $2 \text{Mn}^{3+}_{(\text{solid})} \rightarrow \text{Mn}^{2+}_{(\text{soluble})} + \text{Mn}^{4+}_{(\text{solid})}$ ) and lattice instability of  $\text{LiMn}_2\text{O}_4$  <sup>(184), (185)</sup>.

Solutions to prevent the capacity loss during cycling are expected by partial substitution of the manganese amount with 3d-transition metals forming quaternary spinels of the general composition  $\text{LiM}_x\text{Mn}_{2-x}\text{O}_4$  ( $\text{M} = \text{Cu}, \text{Co}, \text{Mg}, \text{Cr}, \text{Ni}, \text{Fe}, \text{Al}, \text{Ti}$  or  $\text{Zn}$ ). Actually, the capacity fade can be alleviated in this manner and at the same time two operating voltage areas appear, one at around 4 V originating from  $\text{Mn}^{3+}/\text{Mn}^{4+}$  and the second around 5 V originating from the applied metal (both potentials vs.  $\text{Li}/\text{Li}^+$ ). For instance, the compound  $\text{LiFe}_{0.5}\text{Mn}_{1.5}\text{O}_4$  slightly decreases the capacity at 4 V (redox couple  $\text{Mn}^{3+}/\text{Mn}^{4+}$ ) accompanied by an enhancement of the capacity at 5 V caused by the  $\text{Fe}^{3+}/\text{Fe}^{4+}$  redox couple. Depending on nature and content of the dopant the capacity distribution of these voltage areas differ. Among all dopants investigated so far, the most impact on the improvement of electrochemical behavior has cobalt and nickel. In general these quaternary spinels can be cycled at higher potentials leading to 5 V class cathode materials (vs.  $\text{Li}/\text{Li}^+$ ) <sup>(186), (187), (188), (189)</sup>.

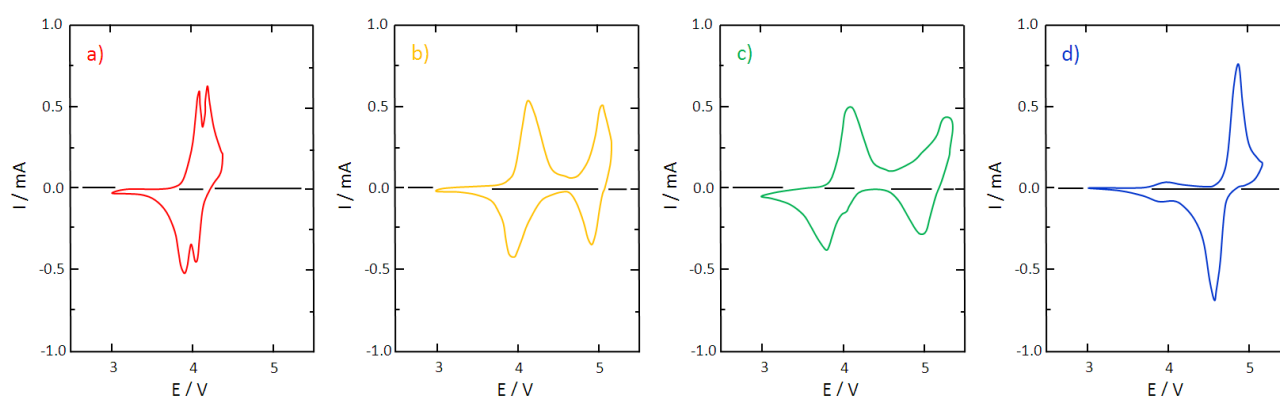


**Figure 42:** cyclic voltammetry behaviors of different spinels of the compound a)  $\text{LiMn}_2\text{O}_4$ , b)  $\text{LiFe}_{0.5}\text{Mn}_{1.5}\text{O}_4$ , c)  $\text{LiCo}_{0.5}\text{Mn}_{1.5}\text{O}_4$  and d)  $\text{LiNi}_{0.5}\text{Mn}_{1.5}\text{O}_4$  with the electrolyte system EC/DEC (1:1, v:v), 1 M  $\text{LiPF}_6$  at a scan rate of  $0.2 \text{ mV}\cdot\text{s}^{-1}$  (drawn from (186)).

Compared to the undoped  $\text{LiMn}_2\text{O}_4$  spinel and all dopants, especially the compound  $\text{LiNi}_x\text{Mn}_{2-x}\text{O}_4$  ( $\text{Ni} = 0 < x < 0.5$ ) and its most common composition  $\text{LiNi}_{0.5}\text{Mn}_{1.5}\text{O}_4$  (NMO), respectively, constitute the most attractive candidates for the usage as cathode material within Lithium-Ion-Batteries. The main advantages of this material derive from its good cycling stability against lithium, its good rate capability, and the

relative high discharge capacity of  $146.7 \text{ mAh g}^{-1}$ . Furthermore, nickel passes the valence states  $\text{Ni}^{2+}/\text{Ni}^{3+}/\text{Ni}^{4+}$  and, thus, can exchange two electrons, while most of the other metals exchange only one <sup>(190), (191), (192), (193)</sup>.

Considering a cyclic voltammogram measurement, the most remarkable property of NMO is its very low “manganese peak” at 4 V and its high nickel peak around 5 V reflecting in a flat average discharge voltage of 4.7 V vs.  $\text{Li}/\text{Li}^+$ . The peak distribution occurs due to the fact that merely the redox couple  $\text{Ni}^{2+}/\text{Ni}^{4+}$  assumes redox activity at the 5 V domain while manganese remains in the valence state  $4+$  <sup>(194)</sup>. However, by using high calcinations temperatures during the synthesis of NMO an oxygen deficiency appears in stoichiometric  $\text{LiNi}_{0.5}\text{Mn}_{1.5}\text{O}_4$  which causes a reduction of  $\text{Mn}^{4+}$  to  $\text{Mn}^{3+}$  participating on redox reactions that take place at the 4 V region <sup>(186), (195), (196), (197)</sup>. The metal or nickel doping of  $\text{LiMn}_2\text{O}_4$  causes a strong bonding between metal and oxygen and improves the structural stability. On the other side the stronger Ni-O bonding compared to the Mn-O bonding increases the redox potential which leads to a requirement of higher energy to extract/insert lithium-ions from/into the host structure <sup>(195), (198)</sup>.

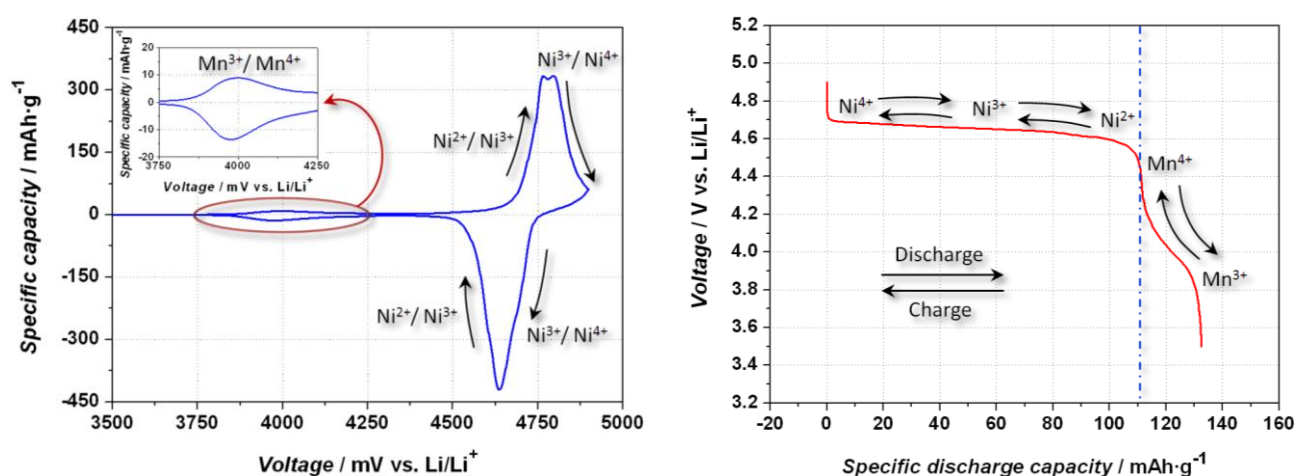


**Figure 43:** left) measured cyclic voltammogram (CV) of the BASF  $\text{LiNi}_{0.5}\text{Mn}_{1.5}\text{O}_4$  (NMO) spinel with the electrolyte system EC/DEC (3:7, v:v), 1 M  $\text{LiPF}_6$  and a scan rate of  $0.1 \text{ mV}\cdot\text{s}^{-1}$ ; right) typical discharge profile of this NMO spinel (blue dashed line symbolizes the border between oxidized or reduced redox-couple Mn and Ni <sup>(source of both diagrams: author)</sup>).

Similar to the structure of  $\text{LiMn}_2\text{O}_4$ , NMO and other substituted spinel compounds feature a cubic close packed oxygen array. Additionally, NMO has two different space groups  $Fd3m$  or  $P4_332$ . In general, these two phases are dependent on synthesis conditions and can be distinguished by the ordering of Mn and Ni in the lattice. The crystal structure  $Fd-3m$  corresponds to a non-stoichiometric compound  $\text{Li}_{0.5}\text{Mn}_{1.5}\text{O}_{4-\delta}$  with a Mn/Ni disorder in which manganese ions are mainly present as  $\text{Mn}^{4+}$  with slightly impurities of trivalent manganese ions ( $\text{Mn}^{3+}$ ). By contrast, the stoichiometric ordered  $\text{LiNi}_{0.5}\text{Mn}_{1.5}\text{O}_4$  ( $P4_332$  symmetry) constitutes regularly ordered Mn- and Ni-ions in which manganese-ions are solely present as  $\text{Mn}^{4+}$ -ions. The non-stoichiometric NMO ( $Fd-3m$ ) exhibits a face centered cubic spinel structure,  $\text{Li}^+$ -ions occupy the tetrahedral sites (8a),  $\text{O}^{2-}$ -ions sit at the 32e sites and  $\text{Mn}^{4+}$  and  $\text{Ni}^{2+}$ -ions are distributed randomly at the octahedral 16d sites. Synthesis conditions like a very low cooling rate influence manganese and nickel (Mn/Ni ratio (3:1)) to get ordered at these octahedral positions. As a consequence, the stoichiometric NMO ( $P4_332$ ) has a simple cubic structure in which nickel occupies the 4a, manganese the 12d and lithium the 8c site, oxygen sits in the 8c and 24e sites <sup>(195), (196), (199), (200)</sup>.

In general, the lithium diffusion into spinels proceeds by migration of the lithium-ion from one tetrahedral site to the next vacant octahedral site. Therefore, the lithiation into disordered  $Fd-3m$  NMO occurs from 8a site (tetrahedral) to the 16c site (octahedral) and again to the next 8a site. These diffusion pathways

(8a-16c-8a) are three-dimensionally connected and provide a fast intercalation and deintercalation of the  $\text{Li}^+$ -ions. Due to the fact that each tetrahedral site within the ordered NMO ( $P4_332$ ) is surrounded by one 4a site (Ni) and three 12d sites (Mn), two different lithium diffusion paths exist<sup>(193), (200), (201)</sup>.

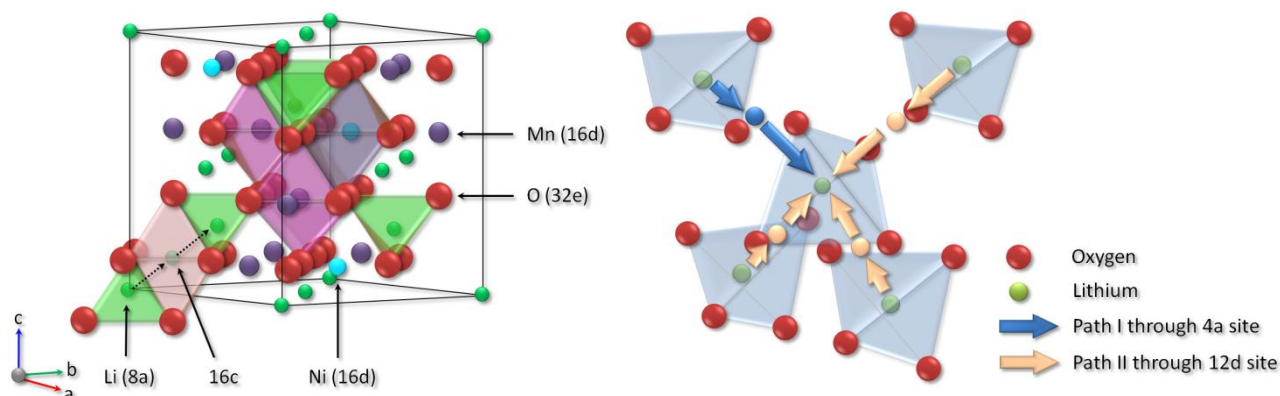


**Figure 44:** left) draft diffusion pathway of lithium into the disordered  $\text{LiNi}_{0.5}\text{Mn}_{1.5}\text{O}_4$  ( $Fd-3m$ ) spinel<sup>(drawn from (193))</sup>; right) two possible lithium diffusion pathways into the ordered  $\text{LiNi}_{0.5}\text{Mn}_{1.5}\text{O}_4$  ( $P4_332$ ) spinel<sup>(drawn from (201))</sup>.

However, it is reported in literature that the electrochemical behavior of the disordered phase ( $Fd-3m$ ) and the ordered one ( $P4_332$ ) are different. Kim et al. demonstrate that lithiation- and delithiation-mechanisms are the reason for the distinct electrochemistry. The disordered  $\text{LiNi}_{0.5}\text{Mn}_{1.5}\text{O}_{4-6}$  ( $Fd-3m$ ) undergoes a one-step phase transition during cycling. With ongoing lithium-extraction from  $\text{LiNi}_{0.5}\text{Mn}_{1.5}\text{O}_{4-6}$  the pristine cubic structure shifts to another cubic phase after more than 50 % of  $\text{Li}^+$ -deintercalation. At fully charged state ( $\text{Li}_{0.04}\text{Ni}_{0.5}\text{Mn}_{1.5}\text{O}_{4-6}$ ) the second cubic phase is dominant. The lattice parameters of the pristine cubic phase decrease linearly upon lithium extraction, while those of the second cubic phase remain constant. In contrast, ordered  $\text{LiNi}_{0.5}\text{Mn}_{1.5}\text{O}_4$  ( $P4_332$ ) exhibits three cubic phases during cycling, one after 25 % of delithiation, the second at around 50 % and the third at fully charged state. The lattice parameters of this two-step phase transition are constant within their corresponding cubic phase. However, NMO with space group  $P4_332$  has a higher resistance than  $Fd-3m$  during delithiation, especially at high C-rates<sup>(195), (202), (203)</sup>.

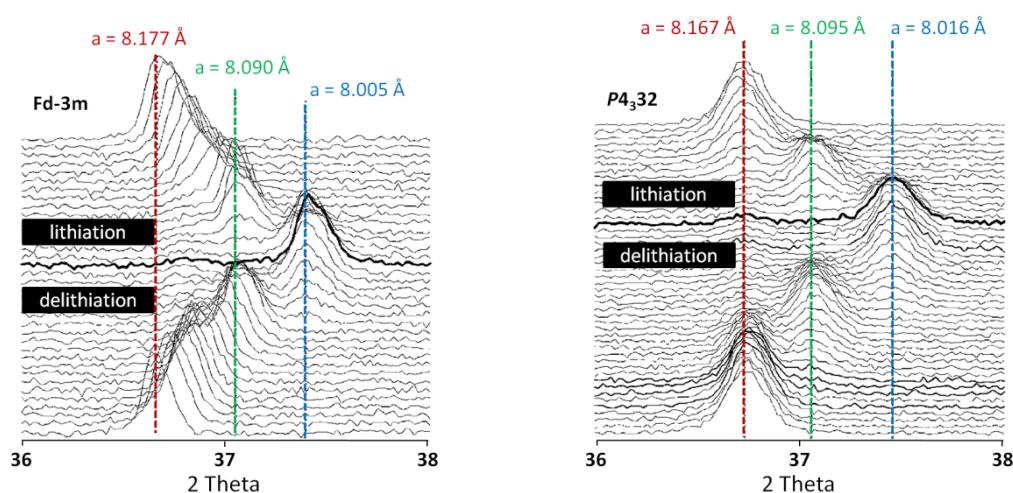


**Figure 45:** in-situ XRD patterns of disordered NMO spinel (left) and ordered NMO spinel (right) showing their phase transitions during cycling<sup>(revision from (203))</sup>.

Additionally, Kunduraci et al. demonstrate different transport properties of both phases. They investigated that  $P4_332$  exhibits a poorer electronic and ionic conductivity ( $10^{-7} \text{ S}\cdot\text{cm}^{-1}$  at room temperature) compared

to the Fd-3m one ( $10^{-5} \text{ S}\cdot\text{cm}^{-1}$  at room temperature). All things together, support the assumption of a better electrochemical behavior and structural reversibility of Fd-3m compared to  $P4_332$  (cf. Figure 46) <sup>(202)</sup>.

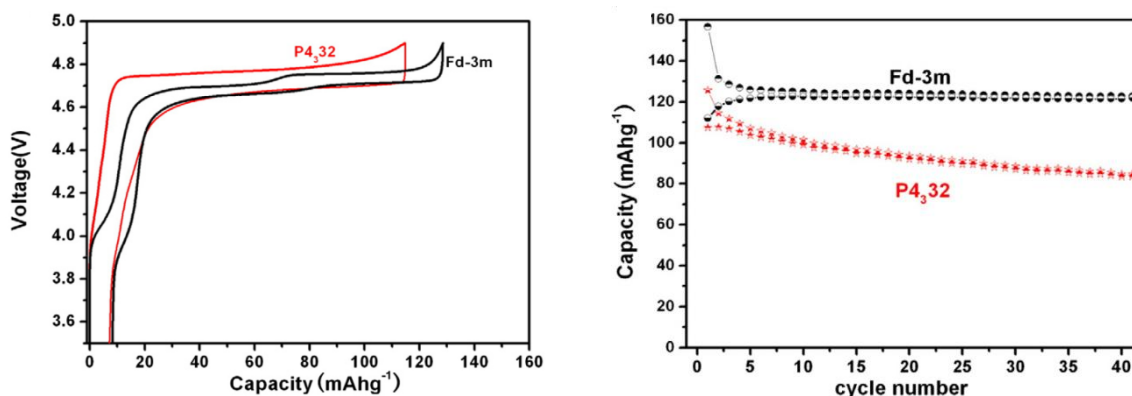
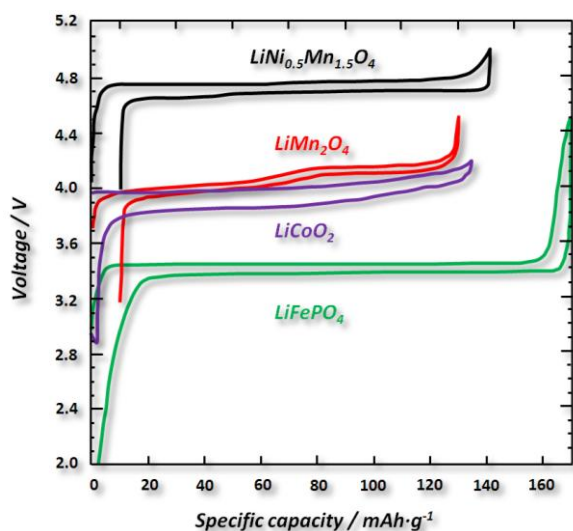


**Figure 46:** left) charge and discharge voltage profiles of disordered  $\text{LiNi}_{0.5}\text{Mn}_{1.5}\text{O}_4$  (Fd-3m) spinel and ordered  $\text{LiNi}_{0.5}\text{Mn}_{1.5}\text{O}_4$  ( $P4_332$ ) spinel; right) cycle performance of the different spinel phases between 3.5 V and 4.9 V vs.  $\text{Li}/\text{Li}^+$  at 0.2 C <sup>(both illustrations from (202))</sup>.

### 3.1.2 Theoretical Enhancement of Battery Energy

Cathode materials should deliver a high reversible storage capacity to provide high energy and a fast  $\text{Li}^+$ -ion diffusion within the electrode combined with a swift electron transport for high power density. In addition, thermal stability (especially at high state of charge), benignity and low costs of raw materials are required. Unfortunately, no cathode material is known to meet all these requirements so far and thus, cathode materials constitute the most limiting component within Lithium-Ion-Batteries in terms of specific energy.



Active material	Theoretical capacity [ $\text{mAh}\cdot\text{g}^{-1}$ ]
$\text{LiFePO}_4$	170
$\text{LiCoO}_2$	140
$\text{LiMn}_2\text{O}_4$	148
$\text{LiNi}_{0.5}\text{Mn}_{1.5}\text{O}_4$	147
Graphite	372
Lithium metal	3860

**Figure 47:** left) comparison of main cathode materials showing their typical charge and discharge profiles at characteristic voltages <sup>(drawn from (191))</sup>; right) table of theoretical capacities of left depicted cathode materials (colored) and two anodes (grey) <sup>(values obtained from (78), (104), (122), (190))</sup>.

Due to the fact that energy is defined as the product of capacity and voltage, high working potentials at around 5 V vs.  $\text{Li}/\text{Li}^+$  are reasonable to accomplish high energy demands. The flat and high average discharge potential of  $\text{LiNi}_{0.5}\text{Mn}_{1.5}\text{O}_4$  (4.7 V vs.  $\text{Li}/\text{Li}^+$ ) favors this material as possible cathode material within Lithium-Ion-Batteries. Following calculations of full cells should support this assumption (the calculations of

the combinations of LiCoO<sub>2</sub> or LiNi<sub>0.5</sub>Mn<sub>1.5</sub>O<sub>4</sub> with graphite are based on material specifics without consideration on lithium loss and inactive materials).

$$\text{Specific energy} = \frac{\text{Capacity of the full cell [Ah]} \cdot \text{Voltage of the full cell [V]}}{\text{Mass of anode active material [kg]} + \text{Mass of cathode active material [kg]}}$$

**Eq. 47**

According to the Faraday's laws of electrolysis the theoretical capacity can be calculated by Eq. 48:

$$Q = I \cdot t = n \cdot z \cdot F = \frac{m \cdot z \cdot F}{M}$$

Q ... Total electric charge

I ... Current (if I is constant, Q is proportional to time of electrolysis; Q = I·t)

t ... Time of electrolysis

n ... Amount of substance (number of moles; the quotient of mass m and molecular mass M)

z ... Number of exchanged electrons and extracted Li<sup>+</sup>-ions respectively

F ... Faraday constant (F = e·N<sub>A</sub> = 1.60217649·10<sup>-19</sup> C · 6.02214179·10<sup>23</sup>·mol<sup>-1</sup> = 96485.3400 C·mol<sup>-1</sup>)

**Eq. 48**

Applying the molecular mass and 1 mole extracted Li<sup>+</sup>-ions from the LiNi<sub>0.5</sub>Mn<sub>1.5</sub>O<sub>4</sub> compound applied to Eq. 48 delivers a capacity of 146.70 Ah:

$$Q = \frac{1000 \text{ g} \cdot 1 \cdot 96485.34 \text{ C} \cdot \text{mol}^{-1}}{182.69 \text{ g} \cdot \text{mol}^{-1}} = 528,130.11 \text{ C} \equiv 146.70 \text{ Ah}$$

As already mentioned, graphite is able to insert one Li<sup>+</sup>-ion per six carbon atoms which reveals the capacity of 372.91 Ah

$$Q = \frac{1000 \text{ g} \cdot 1 \cdot 96485.34 \text{ C} \cdot \text{mol}^{-1}}{6 \cdot 12.011 \text{ g} \cdot \text{mol}^{-1}} = 1.34 \cdot 10^6 \text{ C} \equiv 372.91 \text{ Ah}$$

The average voltage difference between graphite and NMO is 4.5 V (4.7 V – 0.2 V). The capacity ratio of graphite/cathode is generated as described in Eq. 49:

$$\text{Ratio}_{\text{Capacity}} \left( \frac{\text{Graphite}}{\text{LiNi}_{0.5}\text{Mn}_{1.5}\text{O}_4} \right) = \frac{372.91 \text{ mAh} \cdot \text{g}^{-1}}{146.70 \text{ mAh} \cdot \text{g}^{-1}} = 2.54$$

**Eq. 49**

Eq. 49 illustrates that the capacity of graphite is about 2.54 times higher than that of NMO. Applying the full cell capacity of graphite/NMO (372.91 mAh·g<sup>-1</sup>), the average voltage difference (4.5 V) and the capacity ratio (2.54) to Eq. 47 delivers the specific energy of this full cell:

$$\text{Specific energy} = \frac{372.91 \text{ Ah} \cdot 4.5 \text{ V}}{1 \text{ kg} + 2.54 \cdot 1 \text{ kg}} = 473.42 \text{ Ah} \cdot \text{V} \cdot \text{kg}^{-1} \equiv 473.42 \text{ Wh} \cdot \text{kg}^{-1}$$

These calculations actually constitute that the substitution of layered  $\text{LiCoO}_2$  by  $\text{LiNi}_{0.5}\text{Mn}_{1.5}\text{O}_4$  generates 30 % more energy than a common “standard” full cell graphite/ $\text{LiCoO}_2$  ( $359.91 \text{ Wh}\cdot\text{kg}^{-1}$ ).

### 3.2 Preparatory Works

At first it should be mentioned that all experimental results refer to the  $\text{LiNi}_{0.5}\text{Mn}_{1.5}\text{O}_4$  spinel synthesized by the BASF-SE.

Due to the fact that active materials are solely available as powders, an electrode preparation process is required. Thus, an electrode paste called “slurry” has to be prepared that consists of active and inactive components (cf. Table 5). The amount of inactive materials influences the optimization of the specific charge of the electrode as well as the energy density of the electrochemical cell. In general, the higher the amount of active materials of the limited volume of an electrode or battery, respectively, the more energy a battery is able to provide. Hence, a compromise has to be found, whereby the percentage composition of all prepared cathodes within the doctoral thesis is given in Table 5 <sup>(204), (205)</sup>.

One reason for the unavoidable implementation of inactive materials is to keep particles of the active material together and in particular to ensure a sufficient contact to the current collector (aluminum foil for cathodes and copper foil for anodes). The binder system in turn should meet properties such as a high melting point, chemical, reductive and oxidative stability as well as insolubility towards the electrolyte system even at high temperatures. Furthermore the binder must not swell beyond a certain extent, otherwise the adhesion between the particles itself and between electrode active layer and the current collector gets lost which would lead to capacity fade at least. The electrode processing step causes a partial coating of the active particles with binder, which connotes the importance of a well  $\text{Li}^+$ -ion conductivity through this layer anyway. For instance, polyvinylidene-difluoride (PVdF) exhibits excellent properties and is therefore mainly used for cathodes <sup>(204)</sup>.

Although the doping of  $\text{LiMn}_2\text{O}_4$  with nickel decreases lattice parameters and improves electric conductivity of the spinel indeed, the addition of a conducting agent like Super-P carbon black (Timcal) for a sufficient electric conductivity is unavoidable. Carbon materials decrease the inner electrical resistance and don't influence the electrochemical processes. Despite environmental benignity these materials score with a low weight, high purity, easy handling and high corrosion resistance <sup>(204), (206)</sup>.

**Table 5:** constitution of the percental composition of BASF  $\text{LiNi}_{0.5}\text{Mn}_{1.5}\text{O}_4$  electrodes (inactive materials are grey shaded); the gap of the doctor blade is given as well.

Material	Composition [%]	Thickness of coating [ $\mu\text{m}$ ]
Active material (BASF, $\text{LiNi}_{0.5}\text{Mn}_{1.5}\text{O}_4$ )	88	150
Binder (Creavis/Degussa), PVdF Kynar 761	7	
Conductive agent (Timcal, Super-P carbon black)	5	

For the slurry preparation PVdF (Kynar 761, from Evonik formerly known as Degussa) is dissolved in N-methyl-2-pyrrolidone (NMP, Sigma-Aldrich) at first. After the dissolution process the addition of the active material ( $\text{LiNi}_{0.5}\text{Mn}_{1.5}\text{O}_4$ , BASF) and carbon black (Super-P from Timcal) takes place and the slurry is stirred for about twelve hours to provide a uniform mixture. The slurry is applied onto an aluminum foil (the aluminum foil is etched before in  $70^\circ\text{C}$  hot 5 w% aqueous KOH solution) using the doctor blade Multicator 411 from Erichsen with a gap of  $150 \mu\text{m}$  and the 509 coater from Erichsen. The subsequent step

is the removal of NMP within a drying process in an air circulation compartment dryer at 70°C over night. After this step discs and electrodes can be punched out with a diameter of 12 mm. The electrodes are dried again in a glass tube furnace (Büchi) for about 24 hours at 100°C under vacuum ( $< 10^{-1}$  mbar). Hereafter, the electrodes are weighed for determination of the real active mass per electrode and get dried again under the same conditions as before.

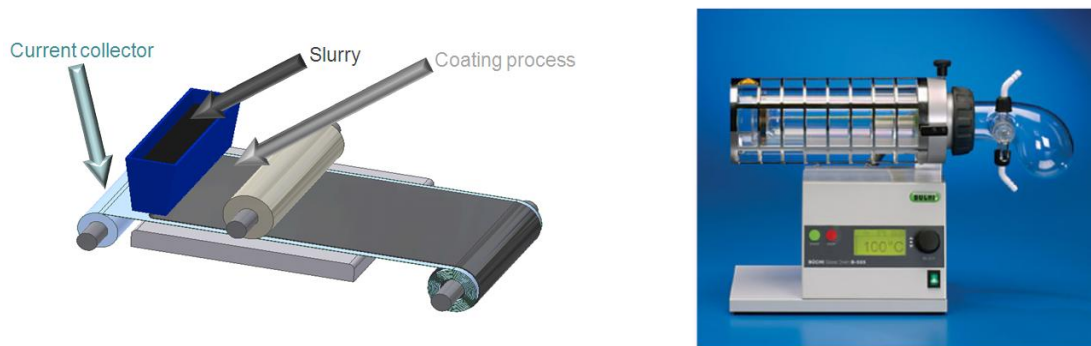


**Figure 48:** left) coating process of the electrode paste (slurry) onto the current collector <sup>(32)</sup>; right) glass tube furnace (Büchi) of the drying process of several electrode types <sup>(207)</sup>.

All electrochemical measurements are carried out in special Swagelok®-test cells, which are assembled in an argon filled glove box ( $< 1$  ppm  $\text{H}_2\text{O}$  and  $\text{O}_2$ ). Anode and cathode are divided by a separator and from above the reference is separated by a separator as well (cf. Figure 49). Thus, this type of electrochemical cell provides a three electrode arrangement enabling an exact monitoring of anode-, cathode- and cell potential. A common composition for an electrochemical experiment within this work is:

- **Reference electrode:** metallic lithium in any case
- **Counter electrode:** lithium (half cells), otherwise graphite or  $\text{Li}_4\text{Ti}_5\text{O}_{12}$  (LTO) on copper foil (full cells)
- **Working electrode:** BASF  $\text{LiNi}_{0.5}\text{Mn}_{1.5}\text{O}_4$  (NMO) on aluminum foil at any time
- **Separator:** six layers of the Freudenberg fleece 2126 (polypropylene, PP) with a diameter of 12 mm
- **Electrolyte:** 80  $\mu\text{l}$  of a common electrolyte composition, e.g. EC/DEC (3:7, v:v),  $1 \text{ mol}\cdot\text{l}^{-1}$   $\text{LiPF}_6$

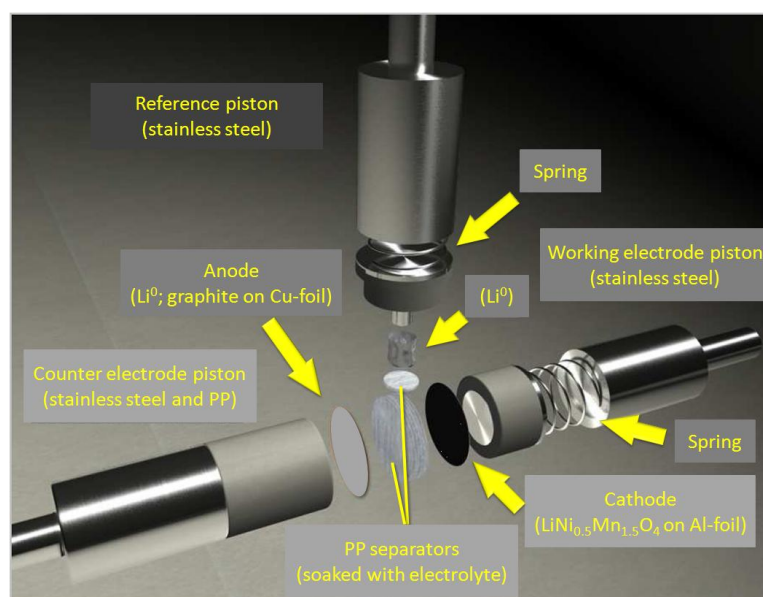


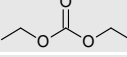
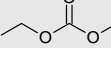
**Figure 49:** schematic drawing of the Swagelok®-test cell for all electrochemical measurements showing the three electrode arrangement <sup>(revision from (137))</sup>.

### 3.3 Experimental Results

#### 3.3.1 Basic Characterization of the BASF $\text{LiNi}_{0.5}\text{Mn}_{1.5}\text{O}_4$ Spinel

The cycle life of Lithium-Ion-Batteries strongly depends on long-term reversibility of the entire cell chemistry. In this connection cathode materials working at potentials beyond 4 V vs.  $\text{Li/Li}^+$  require electrolyte systems with high oxidation and low reduction potentials. However, solvents exhibit different oxidation potentials depending on kinetic factors in particular on electrode surface, scan rate and concentration of the species. Electrolytes based on carbonates exhibit anodic stabilities of more than 5 V vs.  $\text{Li/Li}^+$  (cf. Table 6) indeed, whereby it has to be considered that most of oxidative stability measurements are carried through against inert materials such as gold, silver or platinum. However, inert electrodes and composite electrodes differ from each other in terms of porosity of the electrode surface. Inert materials are usually non porous, while composite materials, which are used in real battery devices, exhibit porous surfaces. These porosities impinge on catalytic activities in different manner and, thus, all measurements against inert materials constitute only an approach for overestimation of electrochemical stability of the electrolyte components<sup>(38), (208)</sup>.

**Table 6:** oxidation potentials of organic solvents<sup>(38), (49), (209)</sup>

Solvent	Structure	Reduction potential [V vs. $\text{Li/Li}^+$ ]	Oxidation potential [V vs. $\text{Li/Li}^+$ ]
Ethylene-carbonate (EC)		1.36	6.2
Propylene-carbonate (PC)		1.00 – 1.60	6.6
Dimethyl-carbonate (DMC)		1.32	6.7
Diethyl-carbonate (DEC)		1.32	6.7
Ethyl-methyl-carbonate (EMC)		-	6.7

In particular the combination of ethylene-carbonate (EC) and propylene-carbonate (PC) in addition with the commonly used conductive salt lithium-hexafluorophosphate ( $\text{LiPF}_6$ ) constitutes a promising electrolyte system, because both solvents show a high oxidative stability ( $> 6$  V vs.  $\text{Li/Li}^+$ ). In addition, EC forms an effective protective film (SEI) on the anode surface. A disadvantage of EC is the too high melting point, whereas PC exhibits a large liquidity range providing a good low temperature behavior. Furthermore both solvents provide a high permittivity (higher than water,  $\epsilon > 79$ ) and due to this fact this liquid electrolyte system is chosen for the first electrochemical characterizations<sup>(38)</sup>.

The first electrochemical measurement belongs to cyclic voltammetry, which is excellent electrochemical technique giving information about characteristic attributes and parameters of the active material (redox reactions, capacities, etc.). Cyclic voltammetry is also called triangle voltage method, which originates from the triangular voltage performance arising from a first increasing potential and a followed decreasing potential applied to the working electrode.

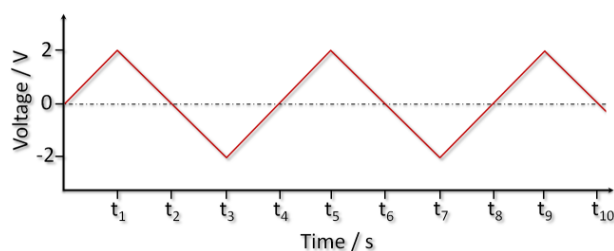


**Figure 50:** example of the applied voltage leading to the triangle voltage method <sup>(drawn from (210))</sup>.

The three electrode arrangement of the Swagelok®-cell allows to carry through cyclic voltammetric measurements. The reference electrode (RE, e.g. lithium metal) serves as zero point potential and ensures the determination of the real potential of the working electrode (WE, e.g.  $\text{LiNi}_{0.5}\text{Mn}_{1.5}\text{O}_4$ ), while the applied voltage between WE and counter electrode (CE) changes in dependency of the (voltage-) scan rate. If a redox- and electrochemical reaction, respectively, takes place a current flow can be detected. The appearance of the obtained current-voltage profile depends on the ratio scan rate to reaction rate of the active material. The current-peaks occur at characteristic potentials, which arise from oxidation (lithium-ion deintercalation) and reduction (lithium-ion intercalation). Furthermore conclusions about possible electrolyte reactions can be determined (oxidative decomposition at high potentials).

All cyclic voltammetry measurements were carried through at measurement devices “Adesys”, “Autolab” or “Biologic”. All used parameters like electrolyte system, scan rate and cut-off voltages are quoted within the legend of the respective measurement explicitly.

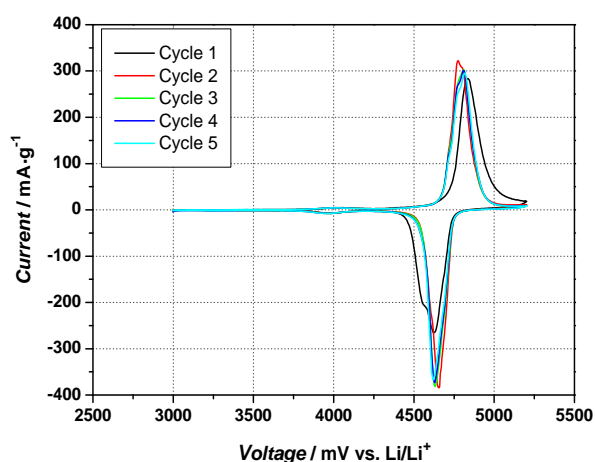


**Figure 51:** typical cyclic voltammogram (CV) of the BASF  $\text{LiNi}_{0.5}\text{Mn}_{1.5}\text{O}_4$  (NMO) electrode in combination with the electrolyte system EC/PC (1:1, v:v), 1M  $\text{LiPF}_6$  within the voltage area 3.0 V and 5.2 V vs.  $\text{Li/Li}^+$  and metallic lithium as counter electrode; the scan rate is  $0.1 \text{ mV}\cdot\text{s}^{-1}$ .

**Table 7:** obtained data from cyclic voltammetry analysis of the BASF NMO cathode between 3.0 V and 5.2 V vs.  $\text{Li/Li}^+$  (cf. Figure 51).

Electrolyte	Cycle	Charge capacity [ $\text{mAh}\cdot\text{g}^{-1}$ ]	Discharge capacity [ $\text{mAh}\cdot\text{g}^{-1}$ ]	Efficiency [%]
EC/PC 1:1 (v:v), 1M $\text{LiPF}_6$	1.	157.8	133.6	84.65
	2.	144.6	131.5	90.90
Mass of electrode [mg] 2.556	3.	141.1	129.9	92.03
	4.	138.9	131.1	94.43
	5.	138.4	130.8	94.54

The cyclic voltammogram shows typical oxidation and reduction peaks at the 4 V and 5 V plateaus a nickel doped  $\text{LiMn}_2\text{O}_4$  spinel should provide (cf. chapter 3.1.1, page 45 f.). Although the scan rate is set to a high value ( $0.1 \text{ mV}\cdot\text{s}^{-1}$ ) the peaks are very sharp and are not distorted, which permits the conclusion that the BASF  $\text{Li}_{0.5}\text{Mn}_{1.5}\text{O}_4$  (NMO) spinel exhibits excellent reaction kinetics. Apparently, the BASF NMO spinel exhibits the non-stoichiometric and face centered space group Fd-3m, which - according to literature - should achieve higher capacities. The corresponding Table 7 contains the quantitative analysis of the cyclic voltammogram. The values are too high compared to the theoretical capacity (the absolute maximum of this cathode material is  $146.7 \text{ mAh}\cdot\text{g}^{-1}$ ). This difference of  $11.1 \text{ mAh}\cdot\text{g}^{-1}$  can be originated from either electrolyte decomposition, oxidation of the manganese disproportionation or from both processes.

The second “standard” electrochemical characterization is the constant current cycling (CCC) simulating charge and discharge processes, which occur within real battery usage. If only half cells (lithium metal as anodes) are used for electrochemical measurements, the charge/discharge program has following parameters (always given within the plot of the respective measurement explicitly). These measurements were made in Swagelok®-cells at the battery tester “Maccor-Test Series 4000”:

- **1. Open circuit voltage (OCV) phase:** rest step for six hours to ensure complete wetting of the active materials and to provide temperature equilibration of the test cell at around  $21^\circ\text{C}$  (air-conditioned laboratory)
- **2. Constant current charging:** delithiation of the cathode with a current rate of 1C (charge or lithiation of the anode)
- **3. Constant voltage charging:** constant voltage holding step at 4.9 V vs.  $\text{Li}/\text{Li}^+$  to delithiate the cathode or to charge the anode and battery, respectively, to a maximum. Usually this step lasts for about one hour, but due to the high voltage which may cause electrolyte decomposition and due to fast reaction kinetics of the used NMO spinel the applied time for constant voltage was reduced to a value of  $\frac{1}{4}$  hour.
- **4. Constant current discharging:** delithiation of the anode with 1C (discharge or lithiation of the cathode)
- **5. Repetition:** the charging-, constant voltage charging- and finally the discharging step (listed points 2. – 4.) constitute one cycle. The entire measurement lasts for 100 cycles

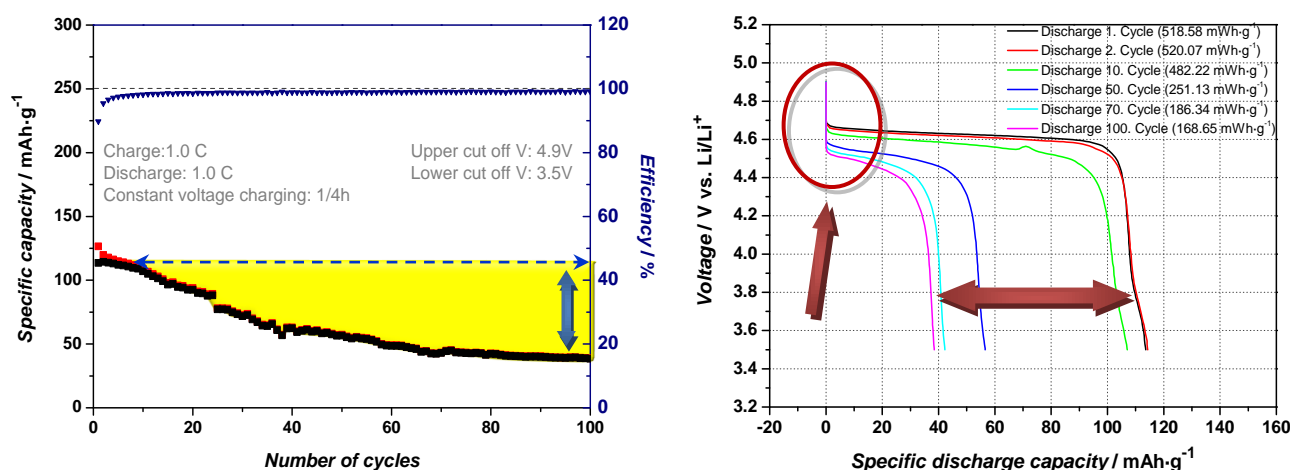


**Figure 52:** left) constant current cycling (CCC) of a not calendered BASF NMO spinel electrode in combination with the electrolyte system EC/PC (1:1, v:v), 1 M  $\text{LiPF}_6$  and metallic lithium as counter electrode (cycling conditions are given within the diagram; red boxes correspond to charge and black boxes to discharge capacity, the yellow area indicates the capacity fade); right) selected discharge profiles of the CCC measurement and their specific energies (integration of the area beneath the discharge curve); the ellipse symbolizes the IR-drop.

The constant current cycling measurement shows initially lower charge capacities ( $126.5 \text{ mAh}\cdot\text{g}^{-1}$ ) and discharge capacities ( $113.6 \text{ mAh}\cdot\text{g}^{-1}$ ) than the cyclic voltammetry, but exhibits a better efficiency (89.9 %). One reason for the lower capacities is the cut-off voltage: within the cyclic voltammetry the upper cut-off voltage is 5.2 V and within the CCC 4.9 V (both vs.  $\text{Li}/\text{Li}^+$ ) meaning more capacity can be obtained at higher voltages. The reason behind the lower cut-off voltage is that the battery tester is not able to charge beyond 5.0 V and to circumvent measurement accuracies the maximum voltage was set to 4.9 V (both potentials vs.  $\text{Li}/\text{Li}^+$ ). However, it should be considered that the capacity at voltages beyond 4.9 V vs.  $\text{Li}/\text{Li}^+$  constitutes a mixture of the capacity of the cathode reaction and electrolyte decomposition. Another reason for the different capacities is the varying cycling conditions. Compared to the CCC the delithiation of the cathode during cyclic voltammetry is carried through slowly. Thus, on the one hand the cathode is able to deliver more lithium and on the other hand more electrolytes can be decomposed reflecting in a higher capacity.

The CCC shows a flat discharge voltage profile at 4.7 V vs.  $\text{Li}/\text{Li}^+$  indeed, but the capacities decrease strongly after only few cycles - an effect that is called capacity fading (depicted as yellow area in Figure 52, page 54). The ideal performance of the CCC is constituted as horizontal blue dashed arrow, which would imply no lithium loss and therefore, no capacity fade. However, the real cycling exhibits an actual loss of discharge capacity and specific energy of about 66.17 % after 100 cycles. Furthermore, a high voltage drop (IR-drop) can be detected (red ellipse in Figure 52, page 54) reflecting a high ohmic polarization and resistance overpotential, which originates from inner resistances of the electrolyte system or film formation caused by massive electrolyte decomposition at the cathode surface. The formed film inhibits further lithium exchange and leads to the strong loss of the obtained specific capacity and energy (the graphical performance of the specific energy is depicted in Figure 53, page 55).

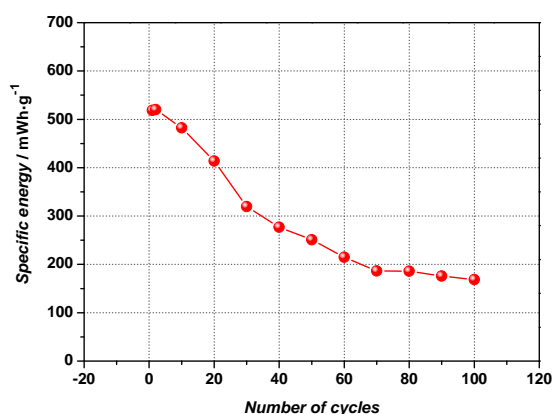


**Figure 53:** graphic presentation of specific energy performance of every 10<sup>th</sup> cycle of the before shown CCC (cf. Figure 52).

Despite the apparently too high voltage of 4.9 V vs.  $\text{Li}/\text{Li}^+$  scanning electron microscope (SEM) images shed light on the film formation, because they show a high porosity of the cathode. As a result the layer of active material is exposed to lots of direct contact to the liquid electrolyte system, which favors massive electrolyte decomposition (cf. Figure 54).

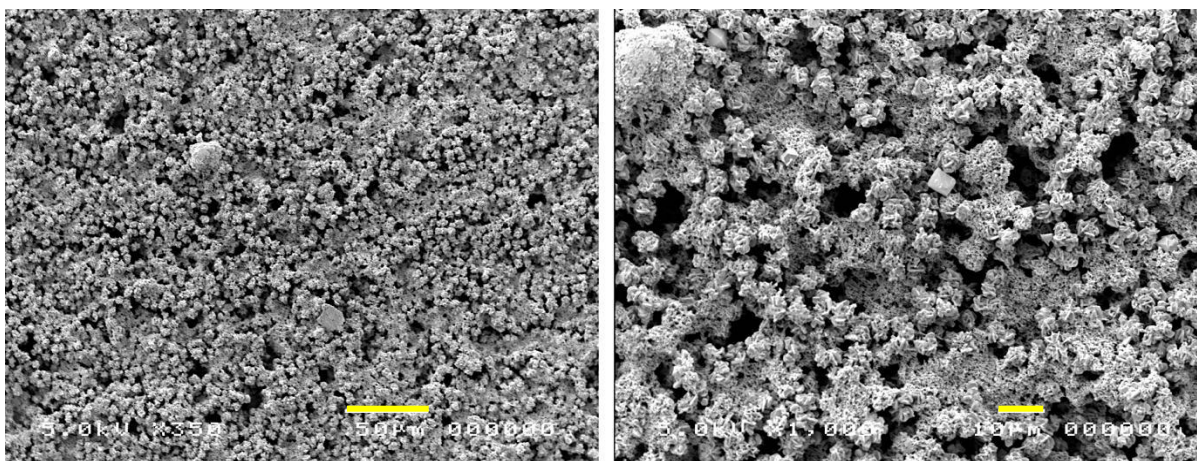


**Figure 54:** scanning electron microscope (SEM) images of a not calendered BASF NMO cathode; magnification: left) x350 (the yellow line symbolizes 50 μm) and right) x1000 (the yellow line symbolizes 10 μm).

Additionally,  $\text{LiNi}_{0.5}\text{Mn}_{1.5}\text{O}_4$  (NMO) was cycled against an industrial manufactured  $\text{Li}_4\text{Ti}_5\text{O}_{12}$  (LTO) anode to proof a possible dissolution of the active material particles and/or electrolyte decomposition products. The reason for the implementation of LTO is that electrolyte decomposition solely occurs on side of the cathode, because the working potential range of LTO is outside of the potential range in which SEI formation occurs. After the cycling both electrodes were cleaned in diethyl-carbonate (DEC) to get rid of the conductive salt and dried under vacuum. Thus, X-ray fluorescence analysis of LTO (proof of active material dissolution) and scanning electron microscope (SEM) analysis were carried through for the proof of possible electrolyte or even separator decomposition products (cf. Figure 55).

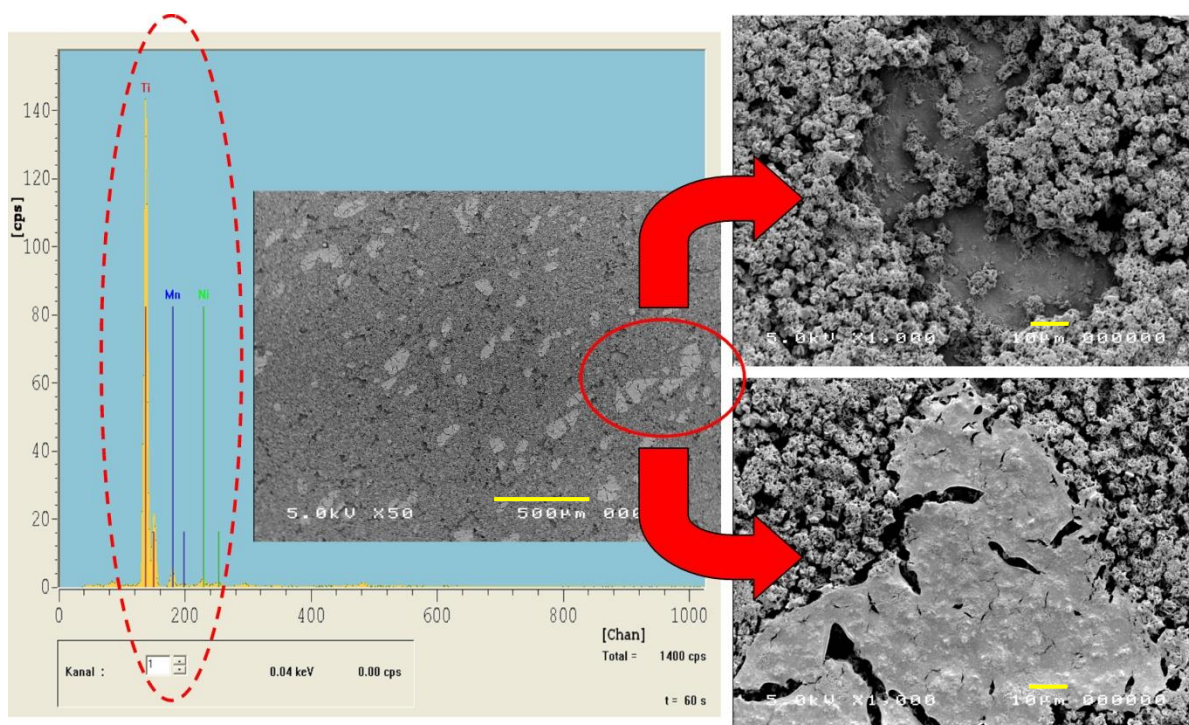


**Figure 55:** X-ray fluorescence analysis of a cycled  $\text{Li}_4\text{Ti}_5\text{O}_{12}$  electrode and scanning electron microscope (SEM) images investigate the constitution of a cycled BASF NMO cathode; magnifications of the SEM images: left) x50 (yellow line corresponds to 500 μm), top and bottom) x1000 (yellow line signifies 10 μm); besides the dissolution of the active material layer electrolyte or separator decomposition products are detectable (white spots on the electrode surface).

During the decomposition reactions of  $\text{LiPF}_6$  hydrofluoric acid (HF) is formed, which attacks the active material of the electrode. Besides, the bivalent manganese-ion arises from disproportionation reaction and can be extracted from the active material layer and gets deposited at the surface of the negative electrode. The counter electrode of the electrochemical experiment (CCC) was Lithium-titanate (LTO), which is actually free of manganese and nickel. After cycling the deposition of manganese and nickel on the LTO surface could be proved by the X-ray fluorescence analysis (XRF) (cf. Figure 55). Furthermore, the scanning electron microscope (SEM) images demonstrate deep holes in the active material layer of the cathode. In addition, white spots were detected upon the electrode surface that may arise from electrolyte or even separator decomposition.

Despite the bad cycling behavior a very bad adhesion of the active material on the aluminum current collector can be observed. The active material chipped off not only during punching out the electrodes, but also by gently touching them with tweezers during the Swagelok®-cell assembling. As a consequence the electrode sheets were calendered before the electrode discs were punched out. A compression of the active material by calendering should achieve improvements concerning the electrochemical behavior by minimizing the surface for a direct contact between the liquid electrolyte and the electrode. On the other hand the adhesion of the active material particles on the current collector should be improved as well. The calender consists of two high-grade polished coils made of stainless steel, which are depicted in Figure 56.

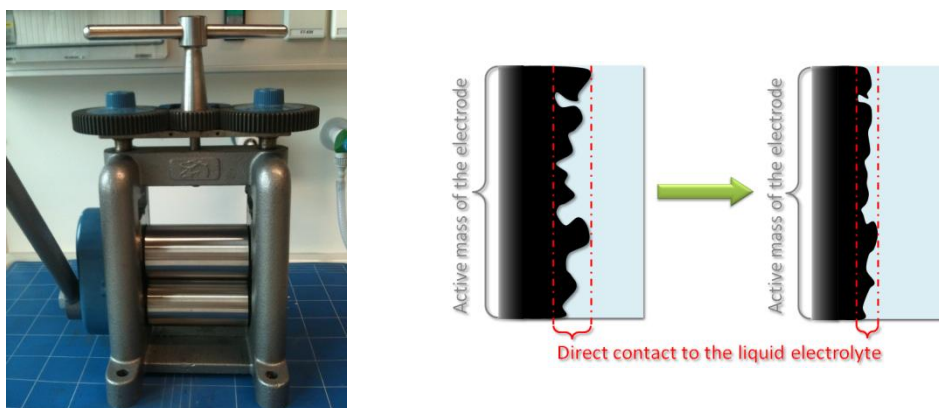


**Figure 56:** left) image of the used calendar machine; right) calendering should minimize the active electrode surface to improve the cycling behavior of the NMO electrodes (source of both: author).

The entire thickness of a strongly calendered (maximal strength) electrode is  $37 \mu\text{m}$ , whereby the thickness of aluminum foil amounts to  $29 \mu\text{m}$ . After deducting the thickness of the aluminum foil the total layer thickness of the active material plane is  $8.0 \mu\text{m}$ . This constitutes a compression of about 69 % compared to a not calendered electrode. The following electrochemical measurement illustrates the performance of a calendered electrode, while other parameters were not changed to achieve matchable results.

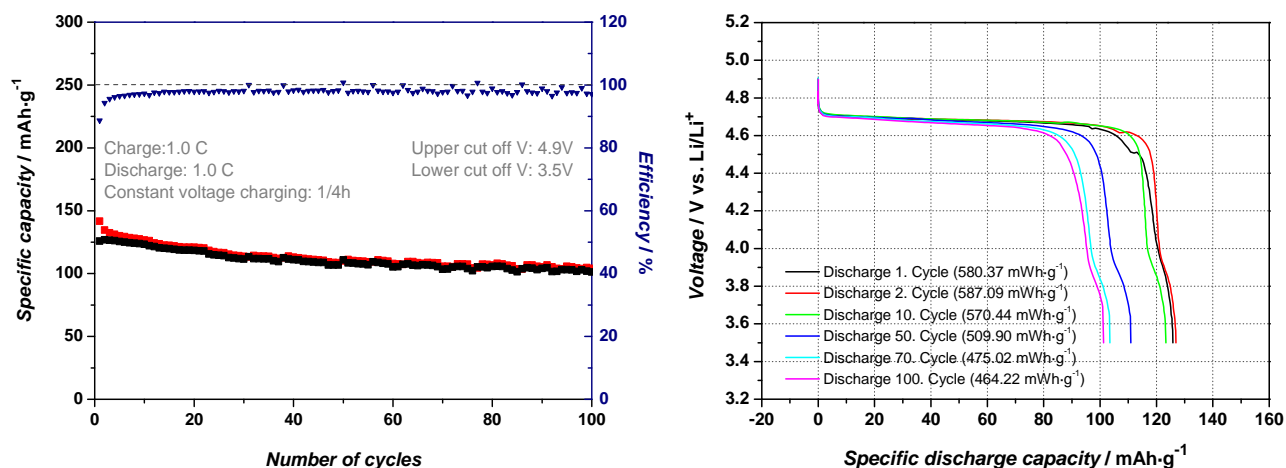


**Figure 57:** left) constant current cycling (CCC) of a strongly calendered BASF NMO spinel in combination with the electrolyte system EC/PC (1:1, v:v), 1 M LiPF<sub>6</sub> and metallic lithium as counter electrode; right) selected discharge profiles of the CCC measurement and their specific energies (integration of the area beneath the discharge curve).

From mechanical point of view the adhesion problem can be eliminated with the calendering process. Attempts to scratch off the active material layer from the current collector resulted in a total destruction of the electrode. From electrochemical aspects the calendered NMO electrode shows an improvement as well. Compared to not calendered NMO electrodes substantial differences in terms of the obtained capacities and cycle capabilities are detectable. For instance, initially charge capacities at around 140 mAh·g<sup>-1</sup> and discharge capacities at around 125 mAh·g<sup>-1</sup> can be achieved. The capacity loss is reduced after 100 cycles to 19.6 %. Even the IR-drop is crucial decreased and the performance of the specific energies is crowded together and lies above 460 mWh·g<sup>-1</sup> after 100 cycles from before approx. 580 mWh·g<sup>-1</sup>.

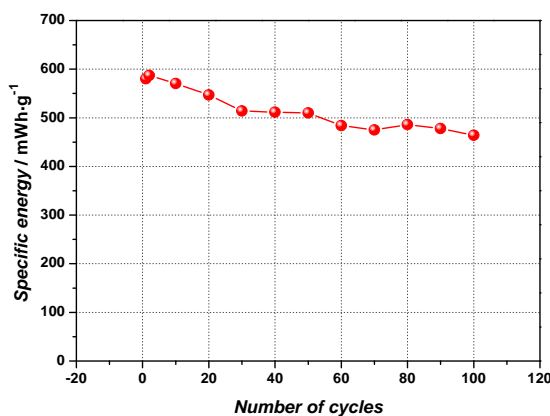


**Figure 58:** graphic presentation of specific energy performance of every 10<sup>th</sup> cycle of the before shown CCC (cf. Figure 57, page 58).

The calendering process leads to an envisaged compression of the active material, which should decrease the possible exposures to the liquid electrolyte that lead to electrolyte decomposition. The layer of the active material gets highly compressed and provides a lower porosity as a consequence. SEM images show the reduction of the porosity, whereby grooves of the calender steel coils actually can be seen (red ellipses within the SEM pictures in Figure 59).

However, the electrochemical performance has still to be improved for fulfilling the aim that this cathode material gets implemented within Lithium-Ion-Batteries, because the still remaining capacity fading (lithium

and manganese loss and especially film formation caused by electrolyte decomposition) cannot be eliminated by a simple calendaring step.

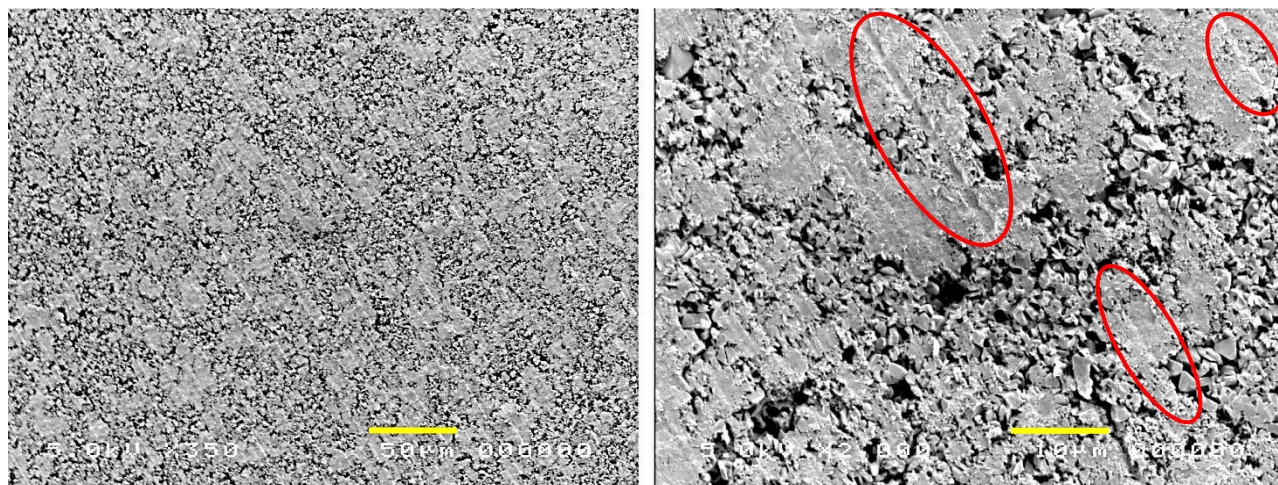


**Figure 59:** scanning electron microscope (SEM) images from a strongly calendared BASF NMO electrode show even the grooves of the calender coils (red ellipses); magnification: left x350 (yellow line symbolizes 50  $\mu\text{m}$ ), right x2000 (yellow line symbolizes 10  $\mu\text{m}$ ).

### 3.3.2 Concepts for Improving the Electrochemical Behavior of $\text{Li}_{0.5}\text{Mn}_{1.5}\text{O}_4$

The insufficient cycling behavior of the  $\text{LiNi}_{0.5}\text{Mn}_{1.5}\text{O}_4$  material is a well-known problem. Therefore, many battery research groups made many efforts to improve structure, stability while lithium insertion and extraction and especially capacity retention upon cycling. Many approaches deal with a doping of the NMO spinel similar to the previous explained doping process of the  $\text{LiMn}_2\text{O}_4$  spinel (cf. chapter 3.1.1, page 45). Various dopants have been proposed like titanium (Ti), chromium (Cr), ruthenium (Ru), aluminum (Al), magnesium (Mg), cobalt (Co), iron (Fe) or fluorine (F). Their doping effects are summarized in Table 8.

**Table 8:** constitution of mainly used dopants and their improvements and drawbacks in terms of the electrochemical behavior of  $\text{LiNi}_{0.5}\text{Mn}_{1.5}\text{O}_4$  spinels <sup>(196), (199), (211), (212), (213), (214), (215), (216), (217)</sup>.

Dopant	Valence	Possible improvements/drawbacks compared to the undoped NMO according to literature
Titanium (Ti)	$\text{Ti}^{3+}$	Better electrochemical performance, higher operating voltage area, faster lithium diffusion and a better rate capability and similar capacities due to lowering of the primitive simple cubic structure ( $P4_332$ ) to the face centered spinel (Fd-3m)
Chromium (Cr)	$\text{Cr}^{3+}$	Due to stronger Cr-O bonding than Mn-O and Ni-O and less Jahn-Teller distortion better chemical and structural stability during cycling, high electrical conductivity, higher discharge capacity and capacity retention and similar capacities
Ruthenium (Ru)	$\text{Ru}^{4+}$	Better rate capability and cycling performance even at high C-rates due to minimized polarization and improved electronic conductivity and better structural stability
Aluminum (Al)	$\text{Al}^{3+}$	Slightly better electrochemical performance, but ordered (simple cubic structure, $P4_332$ ) and lower capacities
Magnesium (Mg)	$\text{Mg}^{2+}$	Stabilization of the structure, higher voltage profile (4.70 V – 4.75 V vs. $\text{Li}/\text{Li}^+$ ), good Li-conductivity at room temperature, good stability upon cycling even at high C-rates, but lower capacities
Cobalt (Co)	$\text{Co}^{3+}$	$\text{Co}^{3+}$ in oxide matrix improves electronic conductivity and strengthens the bonding of transition metal and oxygen, better electrochemical properties and higher Li-diffusion, but lower capacities
Iron (Fe)	$\text{Fe}^{3+}$	Improves electrochemical performance due to better structure stability (stabilization caused by $\text{Fe}^{3+}$ in tetrahedral sites), but lower capacities
Fluorine (F)	$\text{F}^-$	Improved performance with higher rate capabilities especially at high C-rates and structural properties due to the suppression of the formation of Ni-O impurity during synthesis and better resistance against HF attack reducing dissolution of particles into the electrolyte

Summarizing up, doping can improve the performance of NMO by prevention of phase transitions and stabilization of the structure. Doping constitutes a trend of development of 5 V cathode materials within Lithium-Ion-Batteries. Other research groups tried to achieve electrochemical improvements with a surface modification to prevent electrolyte decomposition and dissolution of active material particles caused by HF attacks. As a consequence particles of the active material were coated with a stabilizing surface layer composed of carbons, oxides ( $\text{ZnO}$ ,  $\text{ZrO}_2$ ,  $\text{SnO}_2$ ,  $\text{SiO}_2$ ,  $\text{BiOF}$ ), phosphates ( $\text{Li}_3\text{PO}_4$ ) or different metals (Zn, Au, Ag) entailing an improved cycling behavior actually <sup>(196), (218), (219), (220), (221)</sup>.



**Figure 60:** schematic illustration of the state of the art single particle coating of active materials like  $\text{Li}_{0.5}\text{Mn}_{1.5}\text{O}_4$ , which are prepared as electrodes after the coating process <sup>(source: author)</sup>.

However, particle coating is an elaborate process. By contrast, a new idea to advance towards a solution for the stability problems of NMO is the usage of hybrid electrolytes, which is understood as the combination of an artificial solid electrolyte interphase (SEI) and a conventional liquid electrolyte. In broader sense this approach constitutes a surface modification of an already prepared electrode. Thus, an artificial protection layer is deposited on the positive electrode surface and should behave in terms of an in-situ formed SEI on the negative electrode surface.

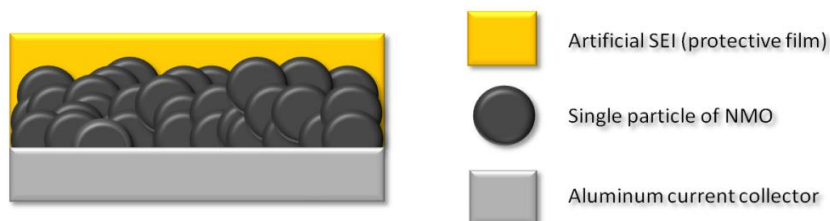


**Figure 61:** draft of the artificial protective film on the surface of an already prepared electrode like the NMO spinel (source: author).

Materials for the barrier layer or artificial SEI are basically solid components, but in contrast to the before mentioned (semi-conducting-) coating materials the usage of conducting materials as SEI component constitutes the envisaged aim. Hence, all solid, conducting components and solid electrolytes, respectively, with following properties come into consideration for hybrid electrolytes:

- Oxidative stability above 5 V vs. Li/Li<sup>+</sup> (LiSICON, LiPON, etc.)
- Insolubility of the solid electrolytes towards organic solvents of the used electrolyte
- Lithium conductivity ( $10^{-12}$  S·cm<sup>-1</sup> up to  $10^{-1}$  S·cm<sup>-1</sup> at room temperature)
- Chemical resistance against all cell components

A solid electrolyte shall assume the protection of the cathode surface and a better Li<sup>+</sup>-ion conductivity than conventional oxides from particle coating simultaneously. A further advantage of the higher lithium conductivity is the possibility to coat a thick and dense SEI on the cathode to circumvent electrolyte decomposition completely. As a consequence the liquid electrolyte has to be tailored merely to the negative electrode. In addition, the solid electrolyte layer enables despite the NMO spinel even other 5 V cathode materials for a possible implementation within Lithium-Ion-Batteries, because the oxidative stability of organic solvents is not an issue and can be disregarded in this respect.

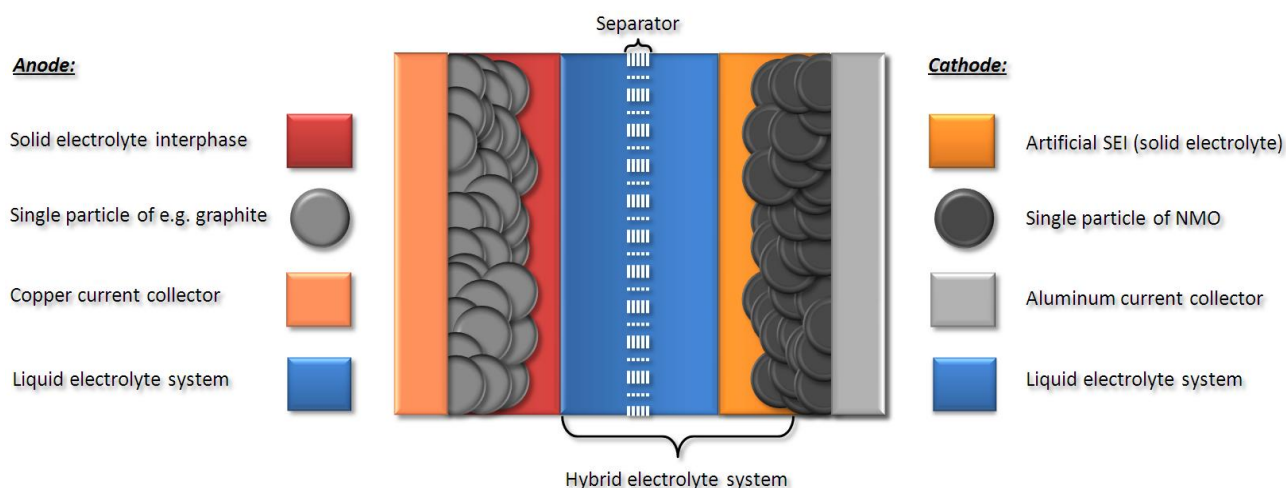


**Figure 62:** schematic setup of a battery cell containing the hybrid electrolyte, which consists of the combination of an artificial solid electrolyte interphase and common liquid electrolyte system (source: author).

Before electrochemical measurements can be carried through with modified electrodes, already prepared NMO electrodes have to be coated by electrospray-deposition (ESD). The basic principle of ESD is based on the fact that a solution which contains the material to be processed is pumped through a capillary in which a high electrostatic potential is applied. As a result an electrostatic spraying takes place combined with the formation of ions of the processing material analog to the mechanism of electrospray ionization. In further consequence, the formed pseudo molecule ions are deposited specifically on the substrate and electrode surface, respectively, by use of electrostatic lens systems and a controllable x-y table.

A crucial difference to all related methods like inkjet printing lies in the fact that formed ions impinge dry (without any solvent) upon the target which enables the formation of multilayer. If solvents are existent, first deposited layers would be resolved partially and destroyed (e.g. spin coating).

It has to be mentioned that all deposition procedures (ESD) were carried through within the course of the doctoral thesis by Dipl.-Ing. Olivia Moser at the Institute for Chemistry and Technology of Materials (ICTM) of the University of Technology Graz. Therefore, all parameters that are necessary for a successful coating of the BASF NMO electrodes reside with the company secret and are not regarded within this doctoral thesis.

### 3.3.3 Electrochemical Comparison of Modified and Unmodified NMO Electrodes

#### 3.3.3.1 Cyclic Voltammetry and Constant Current Cycling Behavior

After preparatory works, including the calendaring process, BASF NMO electrodes were modified with a SiO<sub>2</sub> layer by use of ESD (layer thickness of SiO<sub>2</sub> < 1µm). The reason for the choice of SiO<sub>2</sub> instead of the scheduled solid electrolytes is that they are not commercial available at the moment meaning that they needed to be synthesized “in-house” initially. To get a benchmark system cyclic voltammograms of unmodified BASF NMO electrodes were recorded at first. The CV measurements consist of 15 cycles in total to identify possible improvements in terms of the capacity and efficiency.

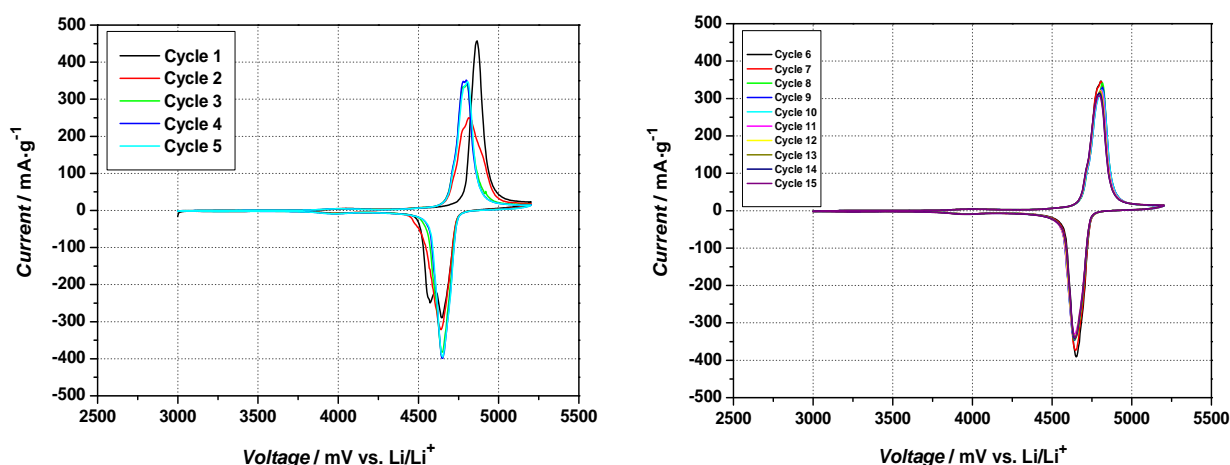


**Figure 63:** cyclic voltammograms (CVs) of an unmodified BASF NMO electrode (both CVs constitute the same measurement; merely for a better visual difference between the first five cycles and their subsequent cycles the CVs are split); the used electrolyte system is EC/PC (1:1, v:v), 1M LiPF<sub>6</sub>, the voltage range is between 3.0 V and 5.2 V vs. Li/Li<sup>+</sup> and the scan rate is 0.1 mV·s<sup>-1</sup>.

**Table 9:** obtained data from cyclic voltammetry analysis of an unmodified BASF NMO cathode (cf. Figure 63).

Electrolyte	Cycle	Charge capacity [mAh·g <sup>-1</sup> ]	Discharge capacity [mAh·g <sup>-1</sup> ]	Efficiency [%]
EC/PC 1:1 (v:v), 1M LiPF <sub>6</sub>	1.	163.5	140.2	85.76
	2.	154.5	138.1	89.36
	3.	149.8	136.3	90.97
	4.	146.1	134.4	91.98
	5.	144.3	133.6	92.62
	6.	142.4	132.3	92.86
	7.	141.5	131.9	93.25
Mass of electrode [mg] 2.571	8.	140.5	131.1	93.33
	9.	139.3	130.3	93.56
	10.	138.1	129.3	93.63
	11.	137.1	128.7	93.91
	12.	135.7	127.7	94.10
	13.	134.9	126.9	94.07
	14.	133.9	126.1	94.19
	15.	133.1	125.1	93.99

Figure 64 comprises a cyclic voltammogram in which a modified (SiO<sub>2</sub> coated) BASF NMO cathode is investigated. Equal to the before shown measurement 15 cycles were recorded to draw an analogy between SiO<sub>2</sub> coated and pristine NMO electrodes in terms of capacity and efficiency.

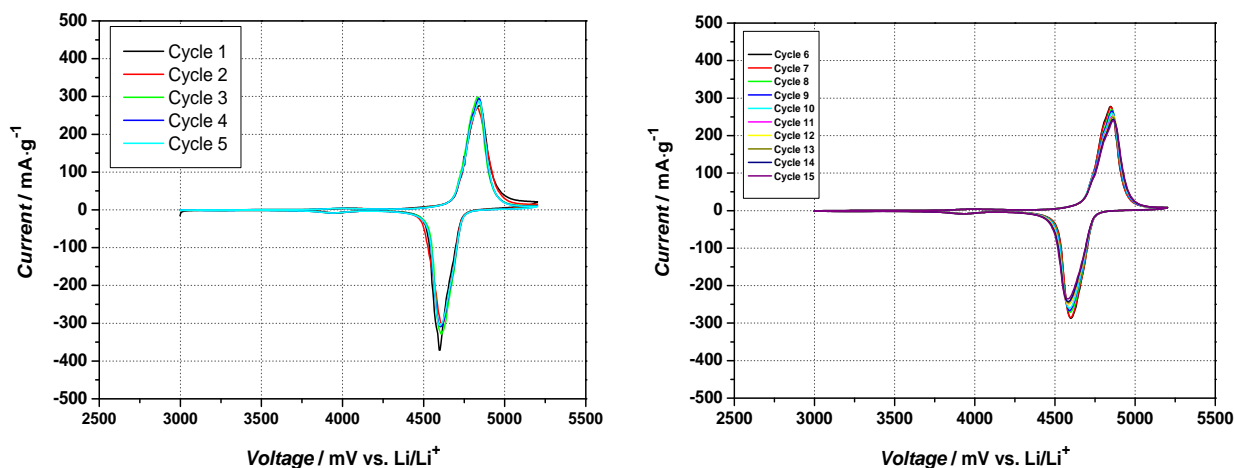


**Figure 64:** cyclic voltammograms of a **modified** BASF NMO electrode (both CVs constitute the same measurement; merely for a better visual difference between the first five cycles and their subsequent cycles the CVs are split); the used electrolyte system is EC/PC (1:1, v:v), 1M LiPF<sub>6</sub>, the voltage area is between 3.0 V and 5.2 V vs. Li/Li<sup>+</sup> and the scan rate is 0.1 mV·s<sup>-1</sup>.

**Table 10:** obtained data from cyclic voltammetry analysis of a **modified** BASF NMO cathode (cf. Figure 64).

Electrolyte	Cycle	Charge capacity [mAh·g <sup>-1</sup> ]	Discharge capacity [mAh·g <sup>-1</sup> ]	Efficiency [%]
EC/PC 1:1 (v:v), 1M LiPF <sub>6</sub>	1.	158.7	133.9	84.35
	2.	147.9	131.9	89.19
	3.	142.5	130.6	91.70
	4.	140.0	130.2	92.97
	5.	138.3	129.6	93.75
	6.	136.7	128.9	94.29
	7.	135.7	128.3	94.55
Mass of electrode [mg] 2.183	8.	134.5	127.7	94.97
	9.	133.7	127.3	95.21
	10.	132.7	126.7	95.49
	11.	132.3	126.3	95.47
	12.	131.5	126.0	95.76
	13.	131.1	125.5	95.75
	14.	130.5	124.9	95.73
	15.	129.9	124.5	95.83

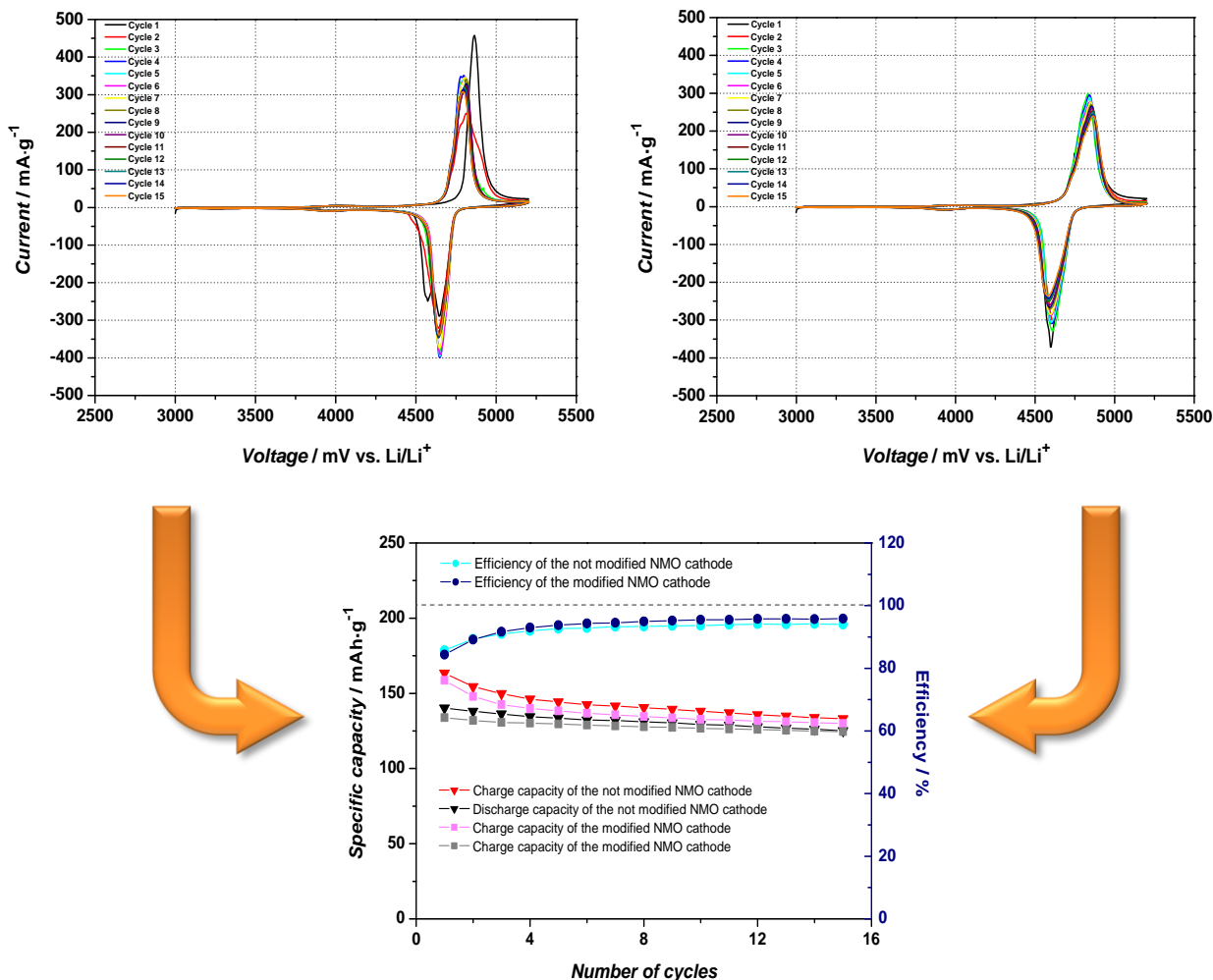


**Figure 65:** direct comparison of the obtained capacities and efficiencies of the before shown CVs (top on the left) unmodified NMO electrode; top on the right) modified NMO electrode; following the orange arrows these CV capacities are plotted within the bottom.

As a result both cyclic voltammograms show typical redox peaks of the  $\text{LiNi}_{0.5}\text{Mn}_{1.5}\text{O}_4$  spinel containing the 4 V and 5 V redox plateaus, whereas the peaks of the  $\text{SiO}_2$  coated electrode are broader. Hence, it can be concluded that  $\text{SiO}_2$  is coated successfully upon the cathode surface due to the fact that broad peaks indicate a higher resistance and impedance, respectively, indicating on slower kinetics.

The direct comparison of the cyclic voltammograms shows a slight difference concerning capacity and efficiency. On the one hand, the capacity of the unmodified electrode is little higher indeed, which is up to the higher impedance of the modified electrode. On the other hand the capacity fading is less, because the loss of capacity amounts to 10.8 % for the unmodified electrode and 7.02 % for the modified electrode. Furthermore, the efficiencies of the modified electrode demonstrate better values than the unmodified electrode. However, the efficiencies exhibit too low and the charge capacities too high values, which can be attributed to electrolyte decomposition.

Constant current cycling was carried through parallel to the cyclic voltammetry. The Swagelok®-cell arrangement included a  $\text{SiO}_2$  coated NMO electrode, while all other parameters such as the electrolyte system or charging program remained unchanged. The results of the calendered electrode from the basic characterization of the NMO spinel (cf. Figure 57, page 58) shall be matched with the following measurements.

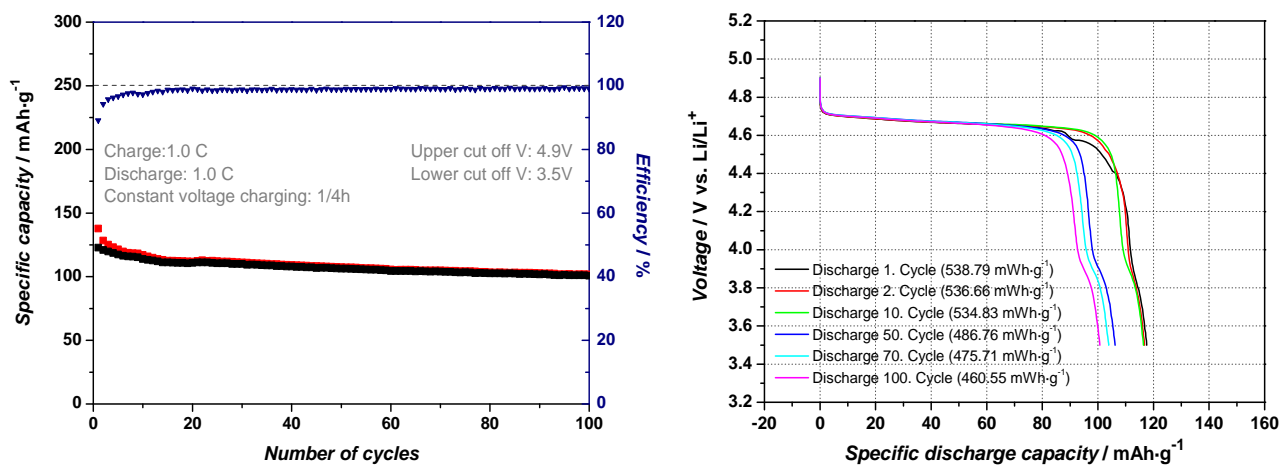


**Figure 66:** left) constant current cycling (CCC) of a calendered and SiO<sub>2</sub> coated BASF NMO spinel in combination with the electrolyte system EC/PC (1:1, v:v), 1 M LiPF<sub>6</sub> and metallic lithium as counter electrode; right) selected discharge profiles of the CCC measurement and their specific energies (integration of the area beneath the discharge curve).

The constant current cycling shows initially a charge capacity of 137.8 mAh·g<sup>-1</sup> and a discharge capacity of 122.8 mAh·g<sup>-1</sup> with an efficiency of 89.2 % and a capacity retention of 82.0 % (capacity loss 18.0 %) after 100 cycles. Furthermore, the IR-drop does not increase, which indicates no massive electrolyte decomposition. But in fact the CCC results resemble those of the cyclic voltammetry and connote only a slight improvement towards a calendered, but not coated NMO electrode.

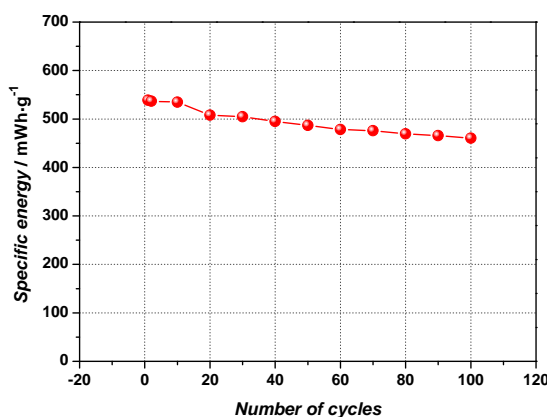


**Figure 67:** graphic presentation of specific energy performance of every 10<sup>th</sup> cycle of the before shown CCC (cf. Figure 66, page 66).

Compared to the calendered electrode performance a slightly improvement concerning lower capacity fading, minor loss of specific energy and lower IR-drop is obviously. The active layer even closer packed up by strongly calendaring is protected additionally against electrolyte decomposition by the SiO<sub>2</sub> layer.

Expectedly, due the very thin protective SiO<sub>2</sub> layer the SEM images show a similar morphology like the calendered NMO electrode (cf. SEM pictures from before in Figure 59, page 59).

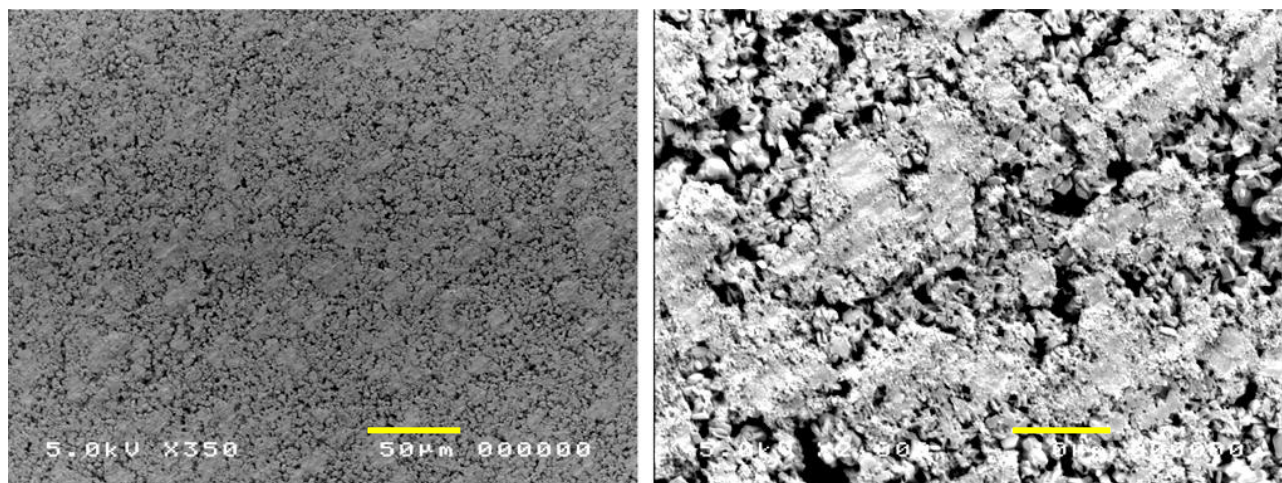


**Figure 68:** scanning electron microscope (SEM) images from a calendered and coated BASF NMO electrode; magnification: left) x350 (yellow line symbolizes 50 μm), right) x2000 (yellow line symbolizes 10 μm).

A possible reason for the relatively small improvement of the electrochemical behavior of the electrode could be found in the minor thickness of the coated SiO<sub>2</sub> layer, which does not cover the particles within the holes of the porous active material layer. In addition, a HF attack could dissolve the protective film and as a consequence the native electrode surface is in direct contact to the electrolyte system again. Another reason is the mitigated, but still remaining porosity behind the electrode surface, which is accessible for the electrolyte. However, all in all this SiO<sub>2</sub> single layer coating could not prevent the electrolyte from decomposition and as further consequence an optimization of the protective layer is necessary to obtain better electrochemical results. Therefore, the next idea was a coating of a not calendered electrode with the same protecting layer as before trusting that this SiO<sub>2</sub> layer seals the hollow spaces of the electrode by a subsequent calendaring step. For the protection of the external particles of the active layer a second protective film consisting of SiO<sub>2</sub> was applied once again. This kind of modification is called “sandwich-type” in the following.

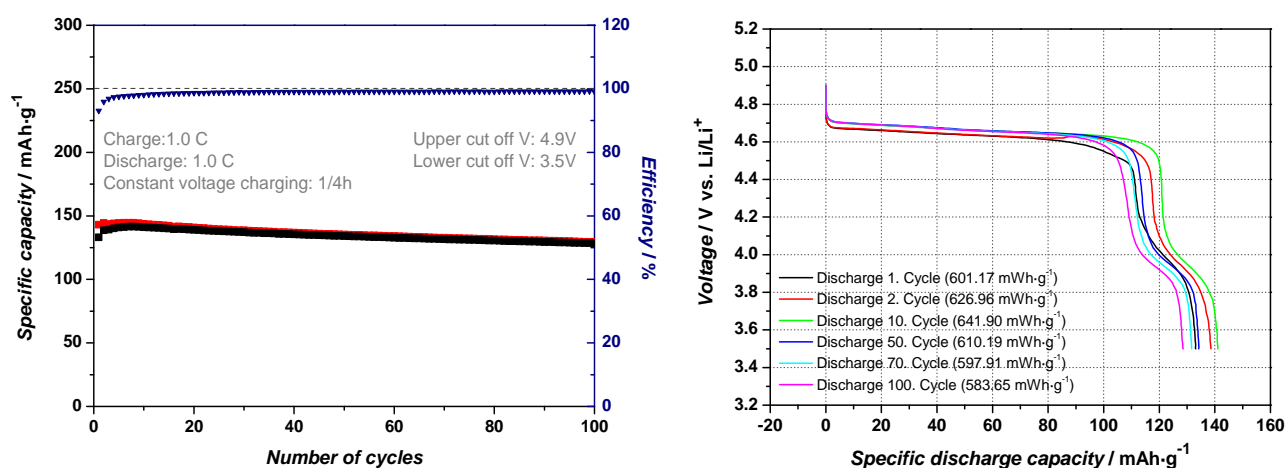


**Figure 69:** left) constant current cycling (CCC) of a calendered and SiO<sub>2</sub> coated BASF NMO electrode (sandwich-type) in combination with the electrolyte system EC/PC (1:1, v:v), 1 M LiPF<sub>6</sub> and metallic lithium as counter electrode; right) selected discharge profiles of the CCC measurement and their specific energies (integration of the area beneath the discharge curve).

The CCC shows higher capacities than any electrochemical measurement so far. At the beginning of the cycling charge capacities around 143 mAh·g<sup>-1</sup> and discharge capacities exceeding values higher than

130 mAh·g<sup>-1</sup> are obtained combined with efficiencies above 93 %. Furthermore, the capacity fading is crucial lower exhibiting capacity retention of little bit more than 96 % after 100 cycles.

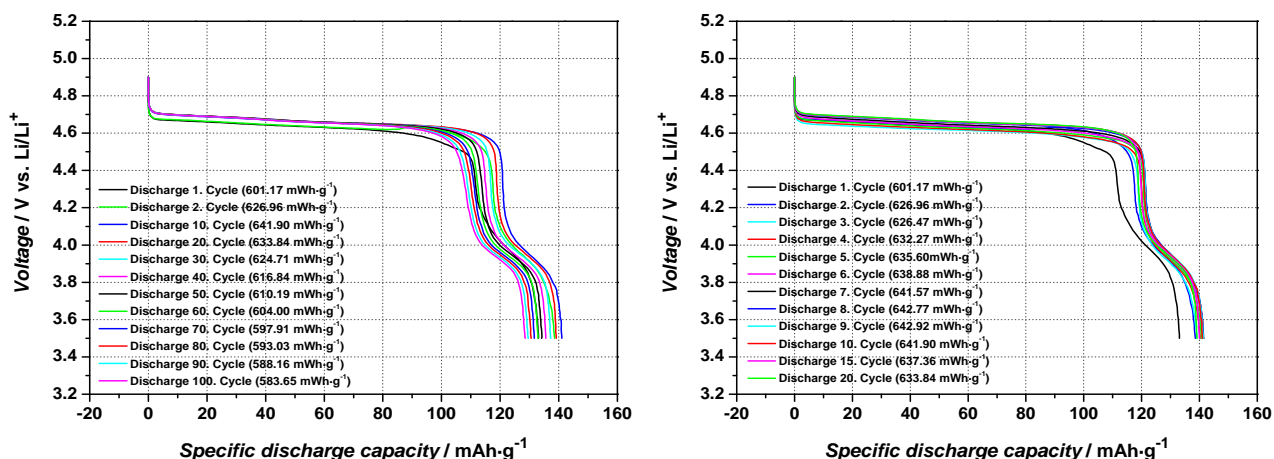


Figure 70: comparison of the specific discharge capacities obtained during the before shown constant current cycling; left) every 10<sup>th</sup> cycle is depicted up to the 100<sup>th</sup> and right) every cycle up to the 20<sup>th</sup>.

The electrochemical results proof of a better protection of the cathode by the artificial SEI. Surprisingly, capacities and specific energies drop down between the 20<sup>th</sup> and 30<sup>th</sup> cycle (cf. Figure 70), which can be attributed to the dissolution of the SiO<sub>2</sub>-layer caused by HF attack. Anyway, the sandwich-type modification improves the electrochemical behavior obviously (cf. Figure 71).

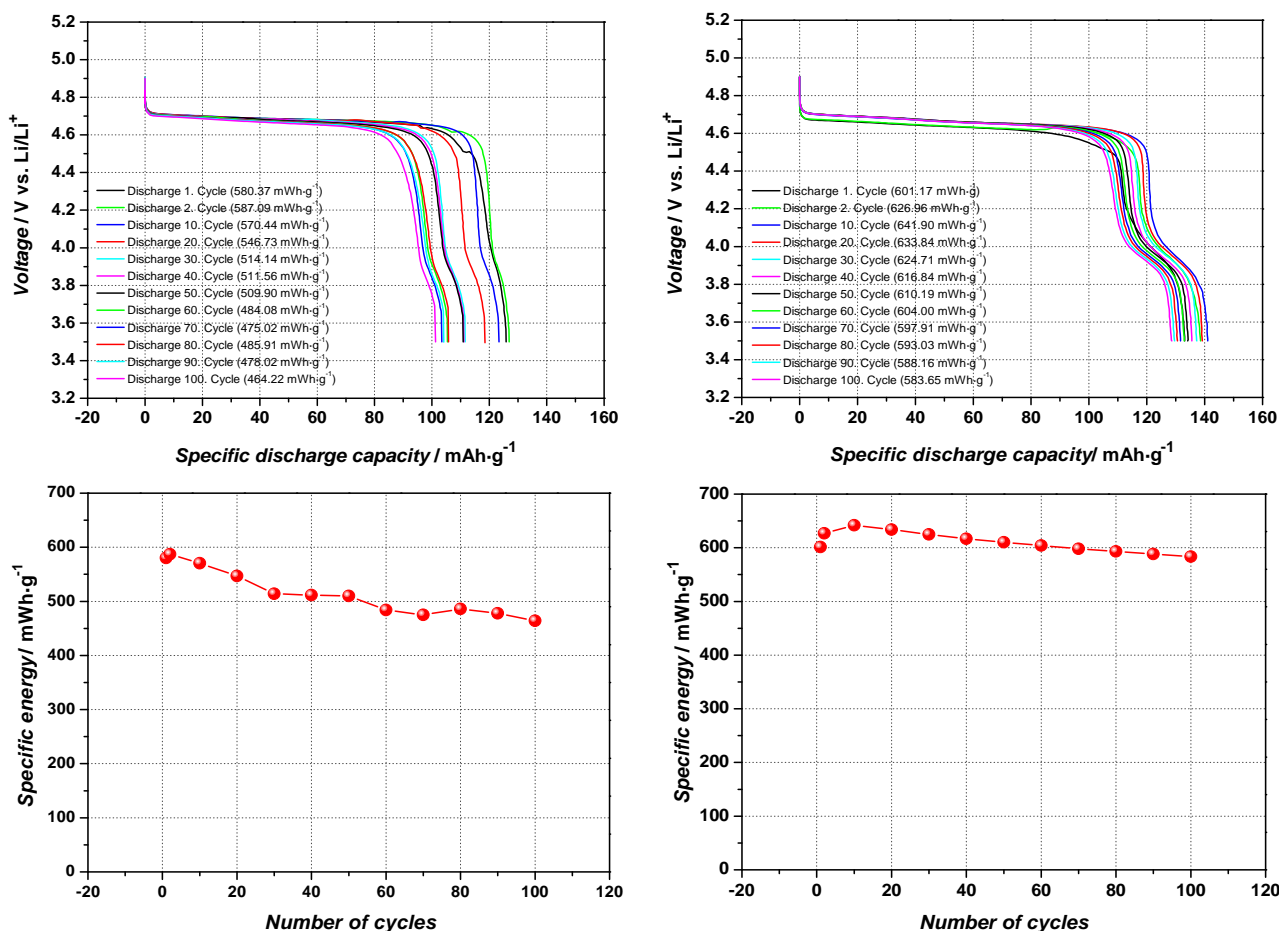
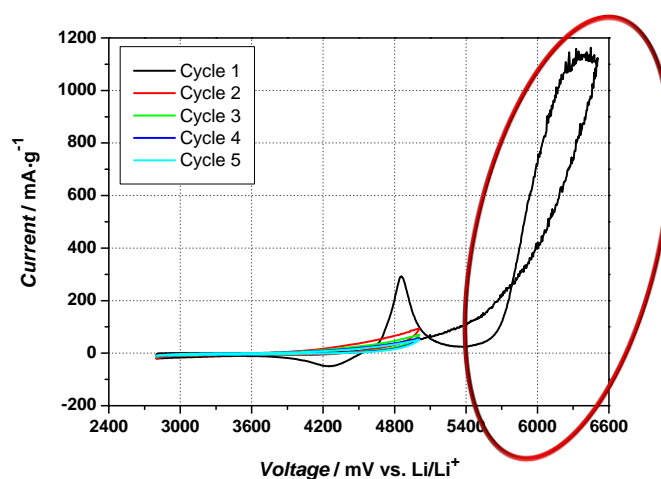


Figure 71: comparison of the calendared (the two plots on the left side) and the SiO<sub>2</sub> coated (sandwich-type) BASF NMO electrode (both plots on the right side).

### 3.3.3.2 Investigation of Electrolyte Decomposition via In-Situ Mass Spectroscopy

#### 3.3.3.2.1 Introduction

As already mentioned in chapter 2.3.6 (page 36 ff.), electrolytes establish a connection between anode and cathode and assure concomitant ion flow and electronic isolation. High working potentials of positive electrodes beyond 4.2 V vs.  $\text{Li}/\text{Li}^+$  put the oxidative stability of electrolyte systems, organic solvents or conductive salts to the proof. Figure 72 emphasizes the importance of stable electrolytes for the proper functioning of Lithium-Ion-Batteries. On the other side electrolyte decomposition is connected to gas evolution, which actually induces an internal pressure increase leading to a cell blowing up, delamination of anode and cathode and furthermore to possible short circuits, which constitutes a big safety issue<sup>(222), (223)</sup>.



**Figure 72:** cyclic voltammogram of the BASF NMO electrode vs. metallic lithium with the electrolyte system PC 1 M  $\text{LiPF}_6$ ; the voltage range is appointed to 2.8 V and 6.5 V vs.  $\text{Li}/\text{Li}^+$ , the scan rate is  $0.2 \text{ mV}\cdot\text{s}^{-1}$ ; the red ellipse signifies the irreversible electrolyte degradation.

At the beginning of the cyclic voltammogram the typical oxidation peak of  $\text{Ni}^{2+}/\text{Ni}^{4+}$  is flawlessly detectable. The vertex (upper cut-off voltage) was appointed to 6.5 V to induce consciously an oxidative decomposition of the electrolyte, which can be easily seen as huge anodic current (red ellipse in Figure 72). The proof for electrolyte destruction is given by the facts that after the electrolyte oxidation no reduction peak and furthermore no redox peaks in the subsequent cycles could be noticed. Thus, solely reactions originating from electrolyte decomposition could have taken place.

However, electrolyte decomposition concerns both components of the electrolyte and takes place at anode and cathode. Merely the type of degradation product depends on oxidation or reduction. For instance, it is claimed that reductive film formation (SEI) on anode surface is accompanied by different gaseous products compared to electrochemical oxidation of the electrolyte solution on cathode materials, which result in a surface layer as well. Arakawa et al. investigated electrolyte oxidation and identified decomposition products of propylene-carbonate (PC) via GC-MS. As a result they found propylene-oxide, propanal, 2-ethyl-4-methyl-1,3-dioxalane and especially as the main gaseous component carbon-dioxide. Additionally, Kumai et al. and Ohsaki et al. claim that  $\text{CO}_2$  arises as a result of degradation of the overcharged cathode material combined with an oxygen release that in turn reacts with organic solvents by forming  $\text{CO}_2$  and  $\text{H}_2\text{O}$ . The oxygen release leads to destruction of the cathode material and again to a reduced life time of the Lithium-Ion-Battery. It should be mentioned for completion that other ascertained gaseous products such as  $\text{CH}_4$ ,  $\text{C}_2\text{H}_4$ ,  $\text{C}_2\text{H}_6$ ,  $\text{C}_3\text{H}_6$ ,  $\text{C}_3\text{H}_8$  and  $\text{CO}$  are produced by the reduction of the solvents

DEC, DMC, EC or PC on the negative electrode surface. Even small amounts of CO<sub>2</sub> are built on the anode side due to trace contaminants within the electrolyte such as HF and H<sub>2</sub>O<sup>(224), (225), (226), (227), (228)</sup>.

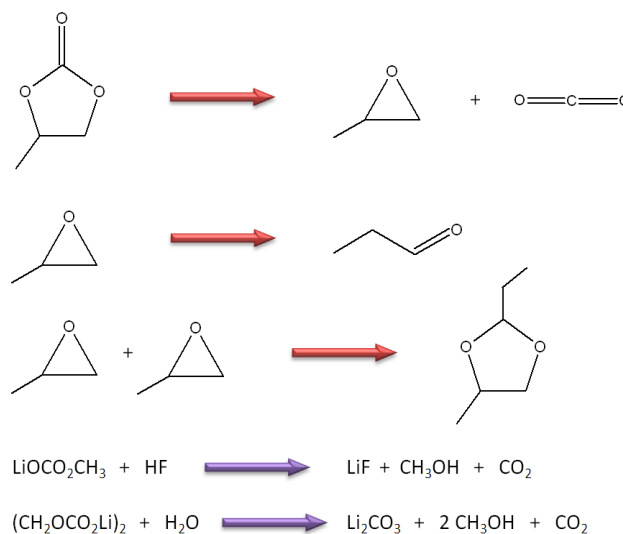


**Figure 73:** anodic degradation reactions of propylene-carbonate into propylene-oxide, propanal, 2-ethyl-4-methyl-1,3-dioxolane (reactions with red arrows), while electrolyte impurities like HF and H<sub>2</sub>O lead the formation of carbon-dioxide and lithium-carbonate on lithium surface (reactions with purple arrows)<sup>(49), (225)</sup>.

To detect the onset of electrolyte degradation gaseous products of the anodic destruction can be qualified by an “online” (in-situ) mass spectrometer in combination with a potentiostatic device (Autolab from Metrohm Autolab B.V.). Hence, the measurement is based on headspace analysis, whereby the gaseous reaction products are pumped off continuously from the top of the Swagelok®-cell (reference electrode) into the mass spectrometer Balzers QMS 200 from Pfeiffer Vacuum Austria for in-situ detection.

Due to the continuously pumping off, merely electrolyte components with a small vapor pressure and high boiling point, respectively, come into consideration for this investigation. Otherwise the electrochemical cell will run dry and as a consequence its functionality is not given any longer. On that account the electrolyte system EC/PC (1:1, v:v), 1 M LiPF<sub>6</sub> was chosen again.

Furthermore it has to be said that the online MS measurements were carried out without any gas carrier flow. Thus, the recipient still includes atmospheric components such as hydrogen, oxygen, carbon-dioxide, argon, etc. and causes a background of these substances at any time. This background in turn results in ion currents at interesting m/z ratios of CO<sub>2</sub> and O<sub>2</sub>, which are not originating from electrolyte decomposition actually. As a consequence solely a strong increase or decrease of these oxidic degradation products has priority for detection. But basically this investigation is aiming for the comparison of the oxidation behavior of the electrolyte system in combination with an unmodified and modified BASF LiNi<sub>0.5</sub>Mn<sub>1.5</sub>O<sub>4</sub> cathode.

### 3.3.3.2.2 Electrochemical and Mass Spectrometric Results

Within the cyclic voltammetry three cycles were measured in all, which differ in terms of the cut-off voltages. Thus, the upper vertex was set to 4.9 V vs. Li/Li<sup>+</sup> for the first two cycles to achieve matchable results to the constant current cyclings of chapter 3.3.1, page 52 and chapter 3.3.3.1, page 63. The cut-off voltage of the third cycle was appointed to 6.0 V vs. Li/Li<sup>+</sup> to cause on the one hand electrolyte decomposition consciously and on the other side to obtain information about the redox behavior during the subsequent reduction (lithium intercalation). Parallel to the cyclic voltammetry gaseous products of possible electrolyte decomposition were detected in-situ by the mass spectrometer. Additionally, following parameters for Swagelok®-cell assembling and mass spectrometer were selected:

Parameter for cell assembling containing an unmodified BASF NMO cathode:

- **Working electrode (WE):** calendered, but unmodified BASF NMO cathode
- **Counter electrode (CE):** lithium metal
- **Reference electrode (RE):** lithium metal
- **Electrolyte system:** EC/PC (1:1, v:v), 1M LiPF<sub>6</sub> (due to the small vapor pressure of both components)

Parameter for cell assembling containing a SiO<sub>2</sub> coated BASF NMO cathode:

- **Working electrode (WE):** calendered and modified BASF NMO cathode (sandwich type)
- **Counter electrode (CE):** lithium metal
- **Reference electrode (RE):** lithium metal
- **Electrolyte system:** EC/PC (1:1, v:v), 1M LiPF<sub>6</sub> (due to the small vapor pressure of both components)

Parameter for one mass spectrometric cycle (for both MS measurements always the same!):

- **MS scan range:** from 0 to 50 atomic mass units (amu)
- **MS scan rate:** 5 amu·s<sup>-1</sup>
- **MS vacuum:** around 1·10<sup>-6</sup> mbar (recipient)

Calculation of the required MS-cycles per one cyclic voltammetry cycle:

$$\text{Cycle}_{\text{MS}} = \frac{\left( \frac{|V_{\text{IP}} [\text{mV}] - V_{\text{EP}} [\text{mV}]| \cdot 2}{\text{SR}_{\text{CV}} [\text{mV} \cdot \text{s}^{-1}]} \right)}{\left( \frac{\text{MS}_{\text{Scan range}} [\text{amu}]}{\text{MS}_{\text{Scan rate}} [\text{amu} \cdot \text{s}^{-1}]} + 1[\text{s}] \right)}$$

V<sub>IP</sub> ... Potential at the initial point (starting point)

V<sub>EP</sub> ... Potential at the end point (vertex- or reversal point)

SR<sub>CV</sub> ... Scan rate of the cyclic voltammogramm

(1s ... Delay of one second of the MS after 50 amu to start a new MS cycle)

**Eq. 50**

For a better visual distinguishing all three cycles are depicted individually with their corresponding mass spectra of oxygen and especially carbon-dioxide (1<sup>st</sup> CV and its corresponding MS cycles are depicted in black, 2<sup>nd</sup> CV and the proper MS cycles are constituted red and the 3<sup>rd</sup> CV cycle and its associated MS cycles are plotted in blue color).

First of all the 1<sup>st</sup> cycle of the cyclic voltammetry of an **unmodified** NMO electrode and its corresponding mass spectrometric data for possible electrolyte cleavage products are presented.

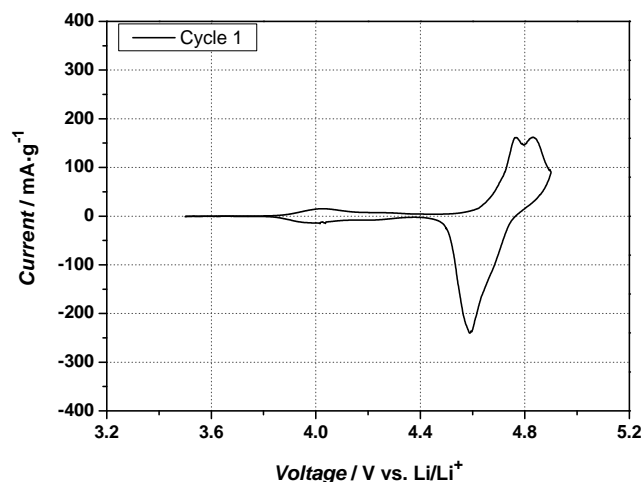


**Figure 74:** 1<sup>st</sup> cycle of the cyclic voltammetry in which an **unmodified** BASF NMO electrode in combination with the electrolyte system EC/PC (1:1, v:v), 1M LiPF<sub>6</sub> was measured within a voltage area between 3.5 V and 4.9 V vs. Li/Li<sup>+</sup>; the scan rate was appointed to 0.1 mV·s<sup>-1</sup>.

The cyclic voltammogram (CV) shows the typical NMO redox peaks at 4 and 5 V domains and proves the functionality of this electrochemical measurement. Hence, if propylene-carbonate (PC) or ethylene-carbonate (EC) decomposes already at this potential (as less as 4.9 V vs. Li/Li<sup>+</sup>), characteristic decomposition products should be detectable, for instance oxygen, propane/ethane or carbon-dioxide peaks according to the NIST database (cf. Figure 75). Due to the fact that O<sub>2</sub> and CO<sub>2</sub> are the main generated gaseous components of electrolyte degradation on the surface of the positive electrode, mass spectrometric results are solely depicted within the amu-range of oxygen and carbon-dioxide (includes propane bonds). Additionally, the mass spectrometric data of a possible oxygen release from cathode material is depicted.

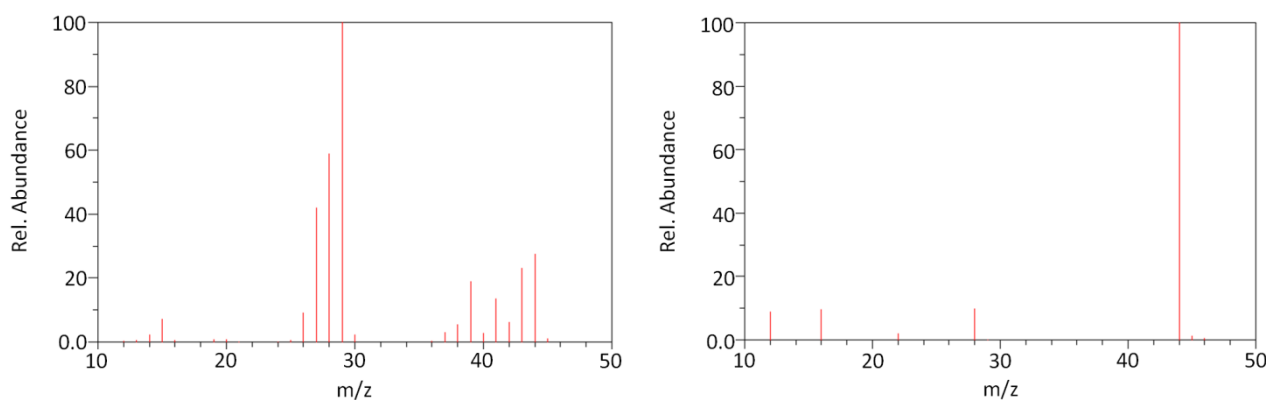


**Figure 75:** mass spectrometric data for cleavage products like propane (C<sub>3</sub>H<sub>8</sub>; left) and carbon-dioxide (CO<sub>2</sub>; right) from the NIST database <sup>(229), (230)</sup>.

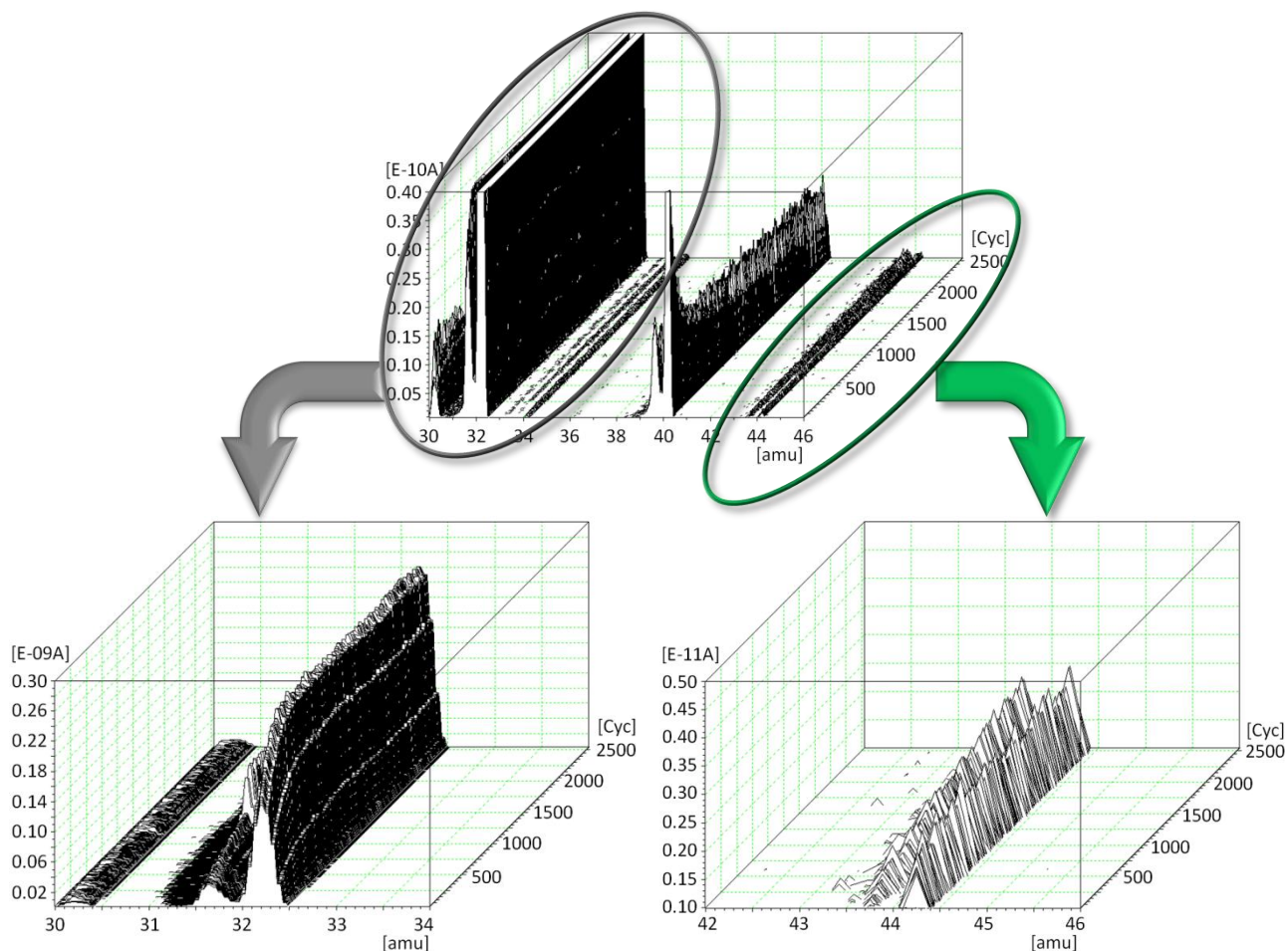


**Figure 76:** three-dimensional constitution of the mass spectrometric data ranges of possible electrolyte degradation, which correspond to the before shown CV of the unmodified BASF NMO electrode during the 1<sup>st</sup> cycle; top) MS range including the range from oxygen to carbon-dioxide, bottom left) enlarged MS range for the O<sub>2</sub> release, bottom right) enlarged MS range for the evolution of CO<sub>2</sub>.

Due to the fact that propylene-carbonate is one of the electrolyte components Figure 76 should show characteristic propane edges between 37 to 45 amu if electrolyte decomposition and reduction on the anode surface takes place respectively. If electrolyte oxidation occurs, characteristic CO<sub>2</sub> edges should be obtained at m/z = 44. According to literature CO<sub>2</sub> generation takes place with an oxygen release of the cathode material, which should be attended by an oxygen decrease (detectable at m/z = 32). Anyhow, no considerable increase of the ion current for either oxidation or reduction products is detectable, especially at the presumed high oxidative potential 4.9 V vs. Li/Li<sup>+</sup>.

It should be mentioned that two ion current peaks appear at m/z ratios instead of a well-defined one. The reason for that is the tuning of the mass spectrometer. As a result the obtained ion current peaks are shifted, whereby the measurements deliver reliable results in terms of the detection of O<sub>2</sub>, CO<sub>2</sub> and C<sub>3</sub>H<sub>6</sub>.

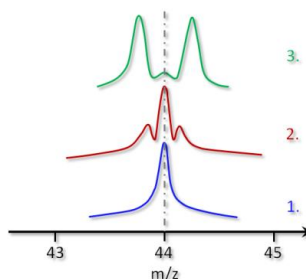


**Figure 77:** schematic of different tunings of the MS-device: the blue peak (no. 1.) appears in the case of an optimal calibrated MS, the red one (no. 2.) for a moderate “tune-up” and the green line (no. 3.) arises from a not perfect calibrated MS <sup>(source: author)</sup>.

In the following diagrams the subsequent (2<sup>nd</sup>) cycle with the corresponding MS-results is depicted.

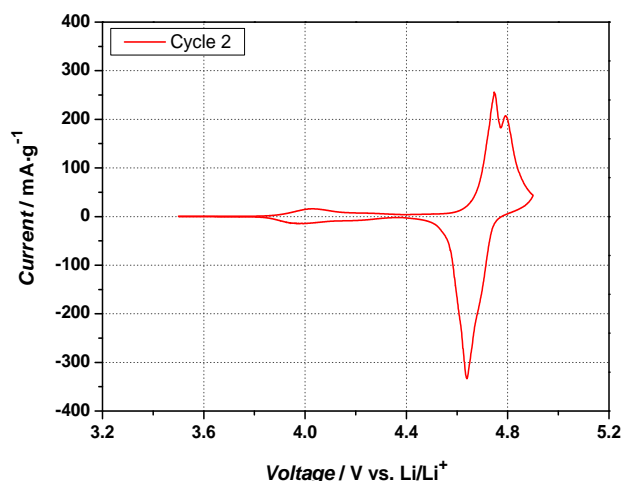


**Figure 78:** second cycle of the cyclic voltammetry in which an unmodified BASF NMO electrode in combination with the electrolyte system EC/PC (1:1, v:v), 1M LiPF<sub>6</sub> was measured within a voltage area between 3.5 V and 4.9 V vs. Li/Li<sup>+</sup>; the scan rate was appointed to 0.1 mV·s<sup>-1</sup>.

The 2<sup>nd</sup> cycle of the CV shows sharp and well-defined redox peaks of LiNi<sub>0.5</sub>Mn<sub>1.5</sub>O<sub>4</sub> as well. The MS-results demonstrate a constant ion current for O<sub>2</sub> and a nearly constant ion current for the CO<sub>2</sub> peaks. A slight increase of the CO<sub>2</sub> amount is detectable within the black marked area. By comparing the ion current of the 1<sup>st</sup> cycle with that of the 2<sup>nd</sup> one, a higher value can be noticed: instead of around 0.25·10<sup>-11</sup> the ion current increased to 0.30·10<sup>-11</sup> assuming a slight but constant formation of CO<sub>2</sub> (see dashed ellipse in Figure 79).

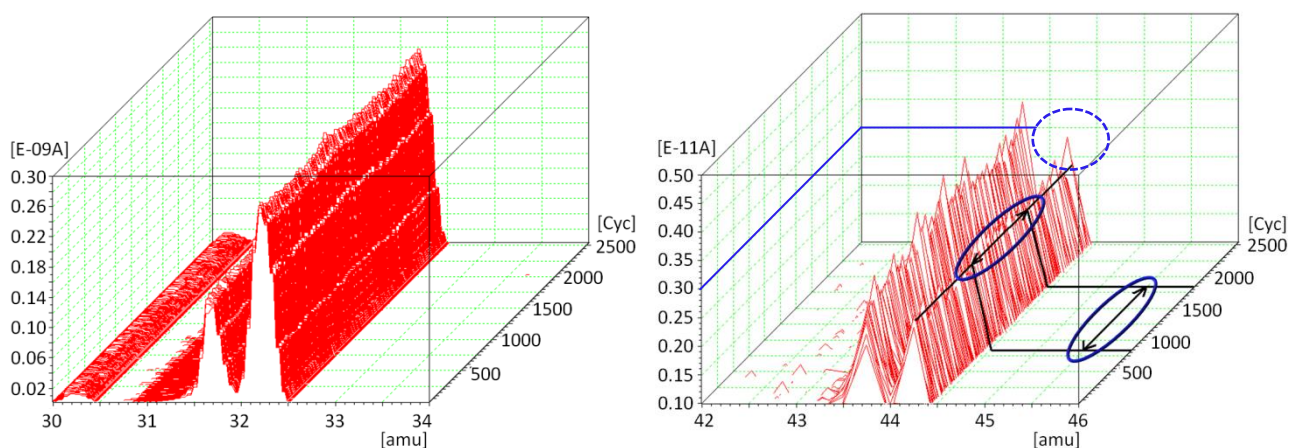


**Figure 79:** three-dimensional constitution of the mass spectrometric data range of a possible oxygen release (MS range within left image) and carbon-dioxide evolution (MS range within the right image) of the unmodified BASF NMO electrode during the 2<sup>nd</sup> cycle of the cyclic voltammogram.

Further results demonstrate the analysis of the 3<sup>rd</sup> cycle with a changed upper cut-off voltage (6.0 V instead of 4.9 V vs. Li/Li<sup>+</sup>) and its proper MS-results.

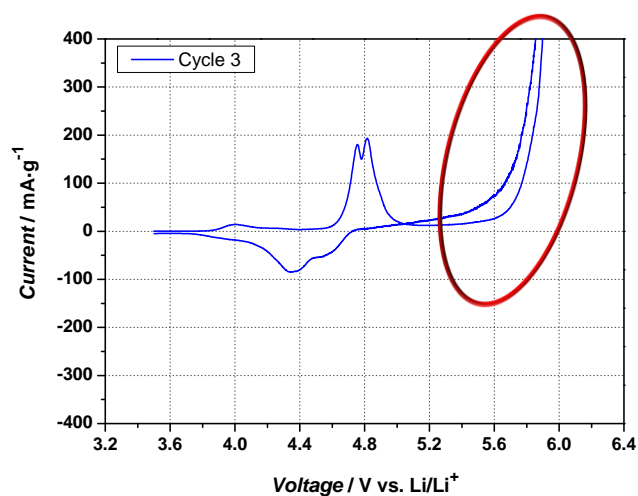


**Figure 80:** third cycle of the cyclic voltammetry in which an unmodified BASF NMO electrode in combination with the electrolyte system EC/PC (1:1, v:v), 1M LiPF<sub>6</sub> was measured within a voltage area between 3.5 V and 6.0 V vs. Li/Li<sup>+</sup>; the scan rate was appointed to 0.1 mV·s<sup>-1</sup>.

The cyclic voltammogram shows the typical oxidation peaks which can be estimated for a Ni doped manganese spinel. On the other hand the changed vertex at 6.0 V induces oxidation of the electrolyte, which can be seen after 5.2 V vs. Li/Li<sup>+</sup> due to an ongoing anodic current flow. If no delithiation, oxidation of the electrolyte or decomposition of the cathode material in terms of oxygen release takes place, no current and anodic current, respectively, should be observed at least. After 5.2 V an anodic current is detectable which indicates severe electrolyte degradation (red ellipse in the above shown CV). Therefore, characteristic CO<sub>2</sub> edges must be obtained from the MS results.

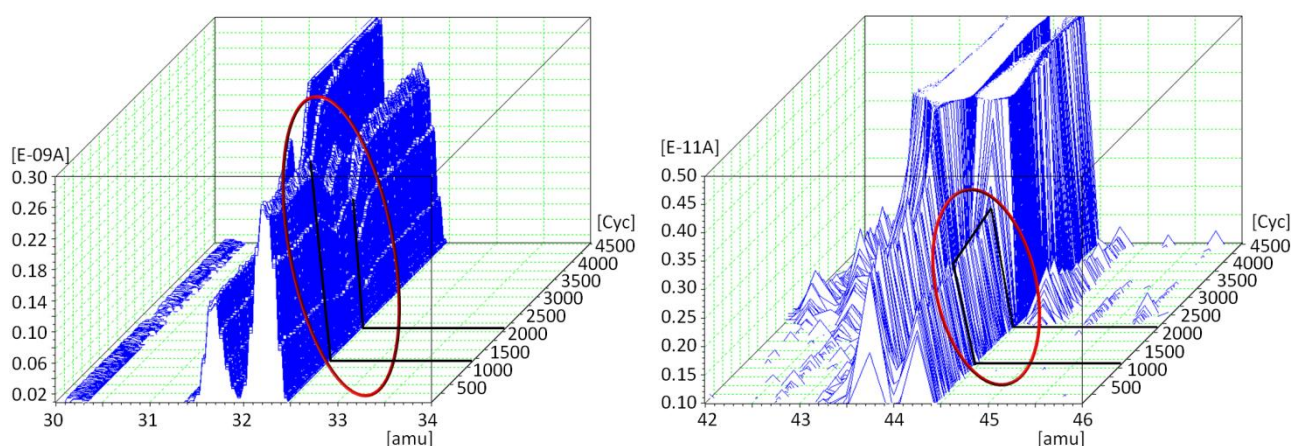


**Figure 81:** three-dimensional constitution of the mass spectrometric data range of a possible oxygen release (MS range within left image) and carbon-dioxide evolution (MS range within the right image) of the unmodified BASF NMO electrode during the 3<sup>rd</sup> cycle of the cyclic voltammogram.

Actually, Figure 81 shows significant O<sub>2</sub> peaks at m/z = 32 amu and CO<sub>2</sub> peaks at m/z = 44 amu indicating the assumed cathode and electrolyte decomposition. In particular the beginning of the increase of these

edges is detectable from the 1200<sup>th</sup> to the 2100<sup>th</sup> mass spectrometric cycle. Furthermore it is of peculiar interest at which potential of the CV the formation of the gaseous products starts. Therefore, following calculation was used:

$$V_{\text{decomp.}} = n_{\text{MS cycles}} \cdot t_{\text{MS cycle}} \cdot \text{SR}_{\text{CV}} + V_{\text{IP}}$$

$V_{\text{decomp.}}$	... Potential at which the electrolyte decomposition begins
$n_{\text{MS cycles}}$	... Number of required mass spectrometric cycles
$t_{\text{MS cycle}}$	... Time which is necessary for one mass spectrometric cycle
$\text{SR}_{\text{CV}}$	... Scan rate of the CV
$V_{\text{IP}}$	... Potential at the initial point (starting point) of the CV

**Eq. 51**

Based on that calculation it is possible to convert MS-cycles into the potential of the CV. Due to the fact that the increase of electrolyte decomposition and increase of CO<sub>2</sub>, respectively, occurs by visual determination solely an approach can be determined in which degradation takes place. Therefore, it can be said that the decomposition begins slightly at 4.8 V vs. Li/Li<sup>+</sup> at least followed by a huge CO<sub>2</sub> formation beyond 5.1 V vs. Li/Li<sup>+</sup>.

$$V_{\text{decomp.}} = 1200 \cdot 11 \text{ s} \cdot 0.1 \text{ mV} \cdot \text{s}^{-1} + 3500 \text{ mV} = 4820 \text{ mV}$$

The circumscribed starting point of the ion current increase for the mass signal  $m/z = 44$  (CO<sub>2</sub>) correlates with the MS-cycles at which an oxygen loss is detectable ( $m/z = 32$ ) and furthermore, both converted MS cycles into CV potentials correlate with the increase of the anodic current within the before shown CV (anodic current gain at about 5.2 V vs. Li/Li<sup>+</sup>). Thus, it can be claimed that electrolyte oxidation and CO<sub>2</sub> evolution, respectively, occurs within cyclic voltammetry potentials of 4.8 V and not later than 5.1 V vs. Li/Li<sup>+</sup> if an unmodified BASF NMO electrode is used.

Initially the 1<sup>st</sup> cycle of the cyclic voltammetry of a **modified** NMO electrode and its corresponding mass spectrometric data for possible CO<sub>2</sub> and O<sub>2</sub> generation during the cyclic voltammetry is presented.

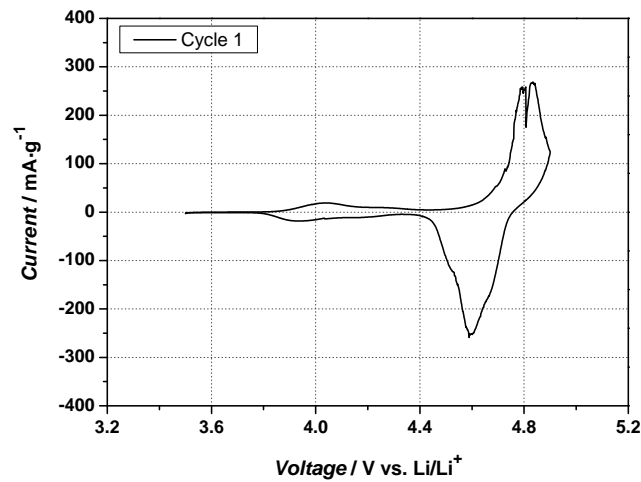


**Figure 82:** 1<sup>st</sup> cycle of the cyclic voltammetry in which a **modified** BASF NMO electrode in combination with the electrolyte system EC/PC (1:1, v:v), 1M LiPF<sub>6</sub> was measured within a voltage area between 3.5 V and 4.9 V vs. Li/Li<sup>+</sup>; the scan rate was appointed to 0.1 mV·s<sup>-1</sup>.

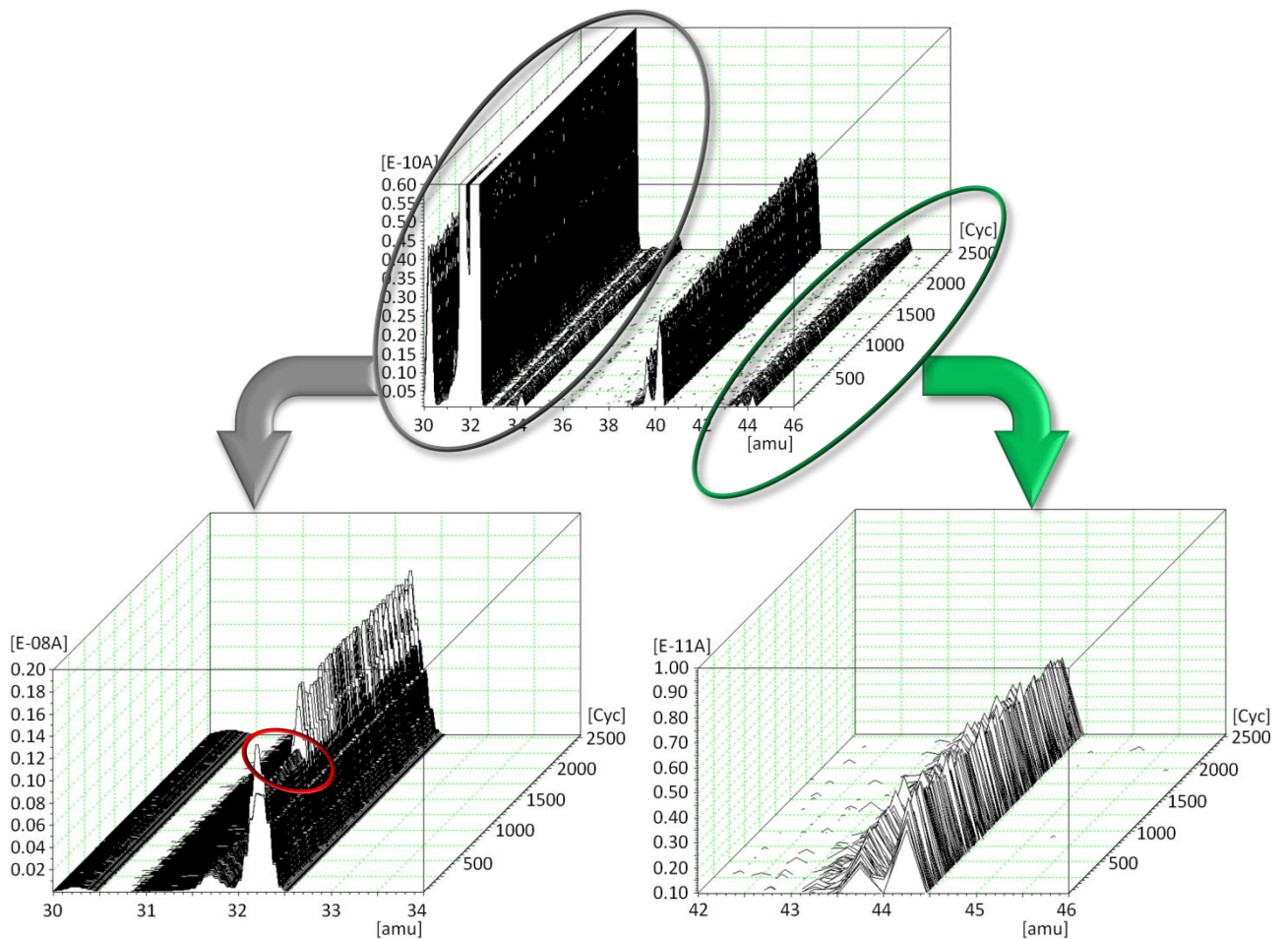


**Figure 83:** three-dimensional constitution of the mass spectrometric data ranges of possible electrolyte degradation, which correspond to the before shown CV of the **modified** BASF NMO electrode during the 1<sup>st</sup> cycle; top) MS range including the range from oxygen to carbon-dioxide, bottom left) enlarged MS range for the O<sub>2</sub> release, bottom right) enlarged MS range for the evolution of CO<sub>2</sub>.

Similar to the cyclic voltammogram performance of the unmodified electrode the modified one shows the typical NMO redox peaks at 4 and 5 V domains and no significant changes in terms of ion currents for CO<sub>2</sub> or O<sub>2</sub>. The missing high peaks after the very few cycles at the m/z ratio of O<sub>2</sub> are attributed to the not well tuned mass spectrometer (see red ellipse in Figure 83, page 77).

In the following diagrams the subsequent (2<sup>nd</sup>) cycle with the corresponding MS-results is depicted.

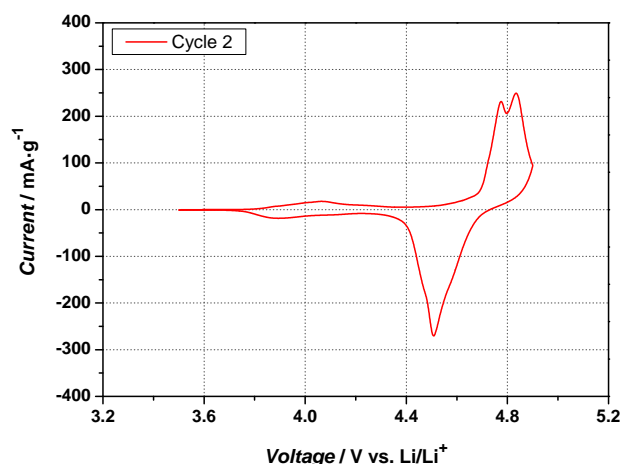


**Figure 84:** 2<sup>nd</sup> cycle of the cyclic voltammetry in which a **modified** BASF NMO electrode in combination with the electrolyte system EC/PC (1:1, v:v), 1M LiPF<sub>6</sub> was measured within a voltage area between 3.5 V and 4.9 V vs. Li/Li<sup>+</sup>; the scan rate was appointed to 0.1 mV·s<sup>-1</sup>.

The second CV cycle and its proper MS-results show the same behavior as before in the first cycle. Neither any considerable increase of O<sub>2</sub> peaks nor CO<sub>2</sub> peaks can be detected, while the ion currents increased slightly within the 2<sup>nd</sup> cycle using an unmodified electrode.

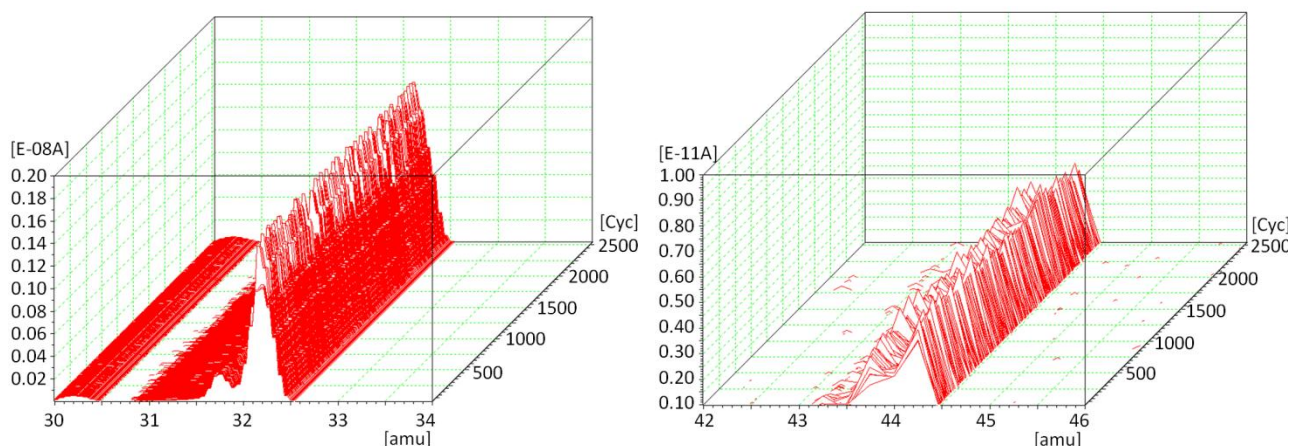


**Figure 85:** three-dimensional constitution of the mass spectrometric data range of a possible oxygen (MS range within left image) and carbon-dioxide evolution (enlarged MS range within the right image) of the modified BASF NMO electrode during the 2<sup>nd</sup> cycle of the cyclic voltammogram.

The following result demonstrates the electrochemical behavior during the 3<sup>rd</sup> cycle in which the upper cut-off voltage was appointed to 6.0 V instead of 4.9 V vs. Li/Li<sup>+</sup>.

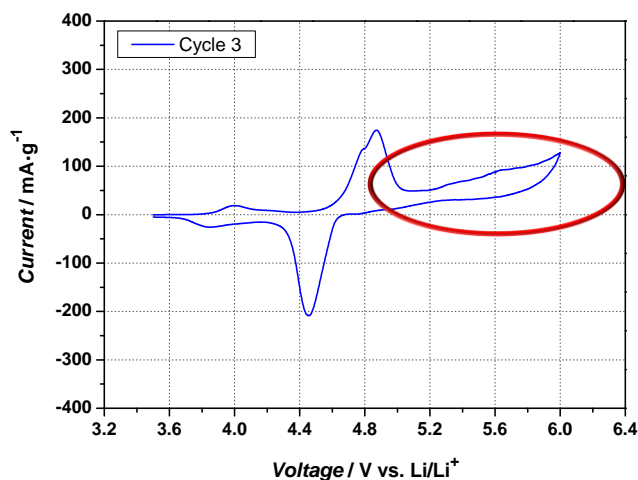


**Figure 86:** 3<sup>rd</sup> cycle of the cyclic voltammetry in which a modified BASF NMO electrode in combination with the electrolyte system EC/PC (1:1, v:v), 1M LiPF<sub>6</sub> was measured within a voltage area between 3.5 V and 6.0 V vs. Li/Li<sup>+</sup>; the scan rate was appointed to 0.1 mV·s<sup>-1</sup>.

The cyclic voltammogram shows the typical oxidation peaks of LiNi<sub>0.5</sub>Mn<sub>1.5</sub>O<sub>4</sub> again. The high vertex induces oxidation of the electrolyte after 5.2 V vs. Li/Li<sup>+</sup> as well (subsequent anodic current flow). Compared to the 3<sup>rd</sup> cycle of an unmodified NMO electrode the same height of the anodic current is not detectable. On the contrary the current value is not approximately as high as with the unmodified electrode, even at 6.0 V (red ellipse in the above shown CV).

Furthermore, it was very interesting that the mass spectrometric analysis does not show either any ion current flow for oxygen or carbon-dioxide. Solely a very slight decrease of O<sub>2</sub> and CO<sub>2</sub> could be detected after around 2150 MS-cycles, which correlates - applied to Eq. 51 - with a potential of 5.87 V vs. Li/Li<sup>+</sup>.

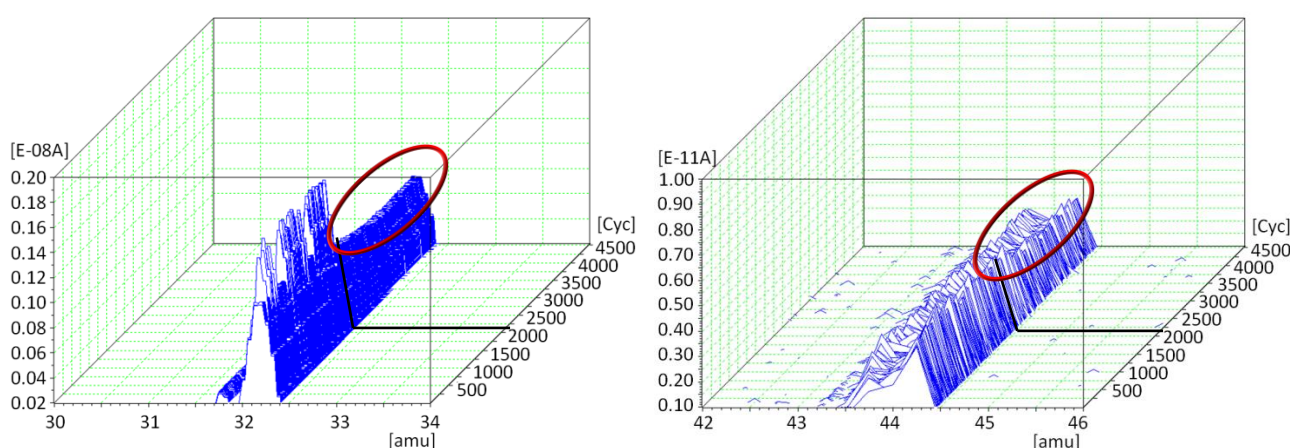


**Figure 87:** three-dimensional constitution of the mass spectrometric data range of a possible oxygen (MS range within left image) and carbon-dioxide evolution (enlarged MS range within the right image) of the modified BASF NMO electrode during the 3<sup>rd</sup> cycle of the cyclic voltammogram.

Summarizing it can be said that the modification affects the electrochemical behavior of the nickel-manganese spinel in a positive way. The proof for that shows a direct comparison of all three CV cycles. First of all the oxidation peak after 5.2 V is much smaller and furthermore another big difference to a “pristine” NMO cathode is detectable, the subsequent lithiation or reduction nearly constitutes a common performance.

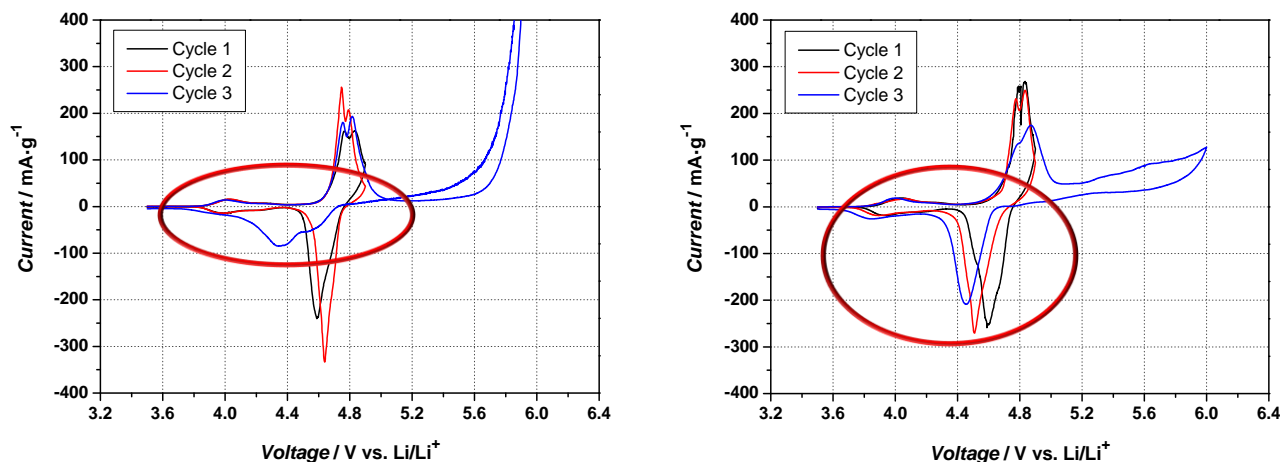


**Figure 88:** comparison of the entire cyclic voltammetry measurements in which an **unmodified** (left CV) and a **modified** (right CV) BASF NMO electrode in combination with the electrolyte system EC/PC (1:1, v:v), 1M LiPF<sub>6</sub> were measured within a voltage area between 3.5 V and 4.9 V (or 6.0 V for the 3<sup>rd</sup> cycle) vs. Li/Li<sup>+</sup>; the scan rate was appointed to 0.1 mV·s<sup>-1</sup> for both.

The comparison of the mass spectrometric results obtained during the 3<sup>rd</sup> CV cycle shows different results. If an unmodified electrode was used an increase of CO<sub>2</sub> could be detected after 4.82 V, while MS-results reveal no CO<sub>2</sub> generation. It has to be said that carbon-dioxide exhibits certain solubility into the electrolyte which complicates its evidence. Maybe this is the reason why a slight decrease of O<sub>2</sub> and CO<sub>2</sub> could be detected in the MS bar-graphs after 5.87 V vs. Li/Li<sup>+</sup> <sup>(231)</sup>.

The consideration of CV and MS results of this chapter implies a crucial lower oxidation potential of the electrolyte system or higher stability of the LiNi<sub>0.5</sub>Mn<sub>1.5</sub>O<sub>4</sub> lattice, respectively, which can be attributed to the artificial SEI on the cathode surface probably.

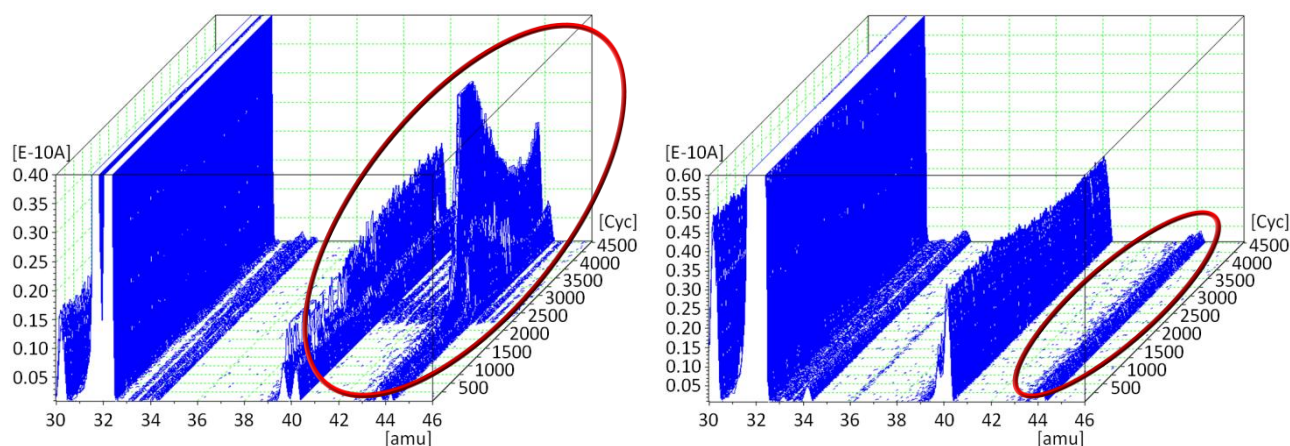


**Figure 89:** obtained mass spectrometric data including both gaseous electrolyte degradation products (CO<sub>2</sub> and O<sub>2</sub>) during cyclic voltammetry up to 6.0 V vs. Li/Li<sup>+</sup> in which a BASF NMO electrode was used: left) **unmodified** cathode, right) **modified** cathode.

### 3.3.3.3 *In-Situ Pressure Detection during Constant Current Cycling*

This chapter deals with electrochemical investigations concerning the pressure gain, which arises from electrolyte oxidation during constant current cycling if 5 V cathodes are used (in this case  $\text{LiNi}_{0.5}\text{Mn}_{1.5}\text{O}_4$ ). Hence, the gas evolution of electrolyte decomposition products should be quantified in-situ. Basically, the knowledge of developed pressure and possible pressure differences between the unmodified and the modified ( $\text{SiO}_2$  coated, sandwich-type) NMO electrode are investigated.

For this measurements a special Swagelok®-cell is needed, which is modified by a pressure sensor, otherwise the cell assembling does not require any further changes. However, to ensure an isotherm process these electrochemical experiments are carried through within an isolated box at constant temperature at 25°C and 40°C controlled by a cryostat.



**Figure 90:** modified Swagelok®-cell; the yellow ellipse marks the pressure sensor <sup>(source: author)</sup>.

Additionally, the cell chemistry has to be changed to circumvent electrolyte reduction on the negative electrode surface. Hence,  $\text{Li}_4\text{Ti}_5\text{O}_{12}$  (LTO) was chosen, because its high average working potential of 1.5 V vs.  $\text{Li}/\text{Li}^+$  excludes any electrolyte decomposition for the SEI formation (cf. chapter 2.3.4.5, page 26). As a consequence exclusively the evolved pressure from electrolyte oxidation will be detected.

All following steps were carried out in an argon filled glove box. First of all LTO anodes were removed from an industrial manufactured battery pouch-bag from Kokam, punched out with the same diameter as before (12 mm) and afterwards cleaned with DEC to get rid of electrolyte and especially conductive salt traces. After the drying process representative samples of LTO electrodes were weight for the subsequent calculation of the specific capacities. Initially an electrochemical characterization was carried through to proof the redox potentials of theses LTO anodes.

#### Parameters of Swagelok®-cell assembling for basic electrochemical characterization:

- **Working electrode:** obviously calendered and industrial manufactured LTO anode
- **Counter electrode:** lithium metal
- **Reference electrode:** lithium metal
- **Electrolyte system:** EC/PC (1:1, v:v), 1M  $\text{LiPF}_6$

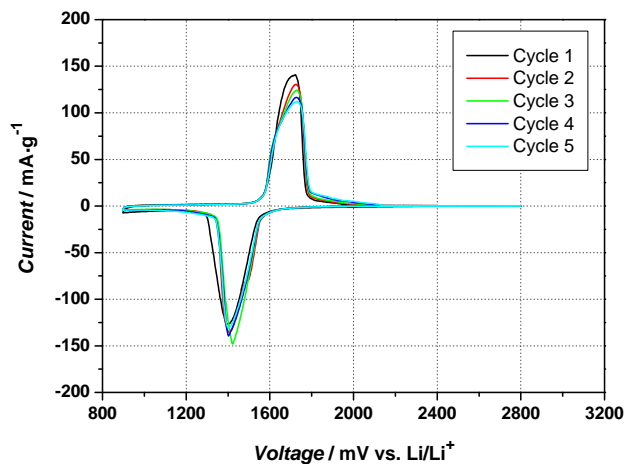


**Figure 91:** cyclic voltammogram (CV) of an industrial manufactured  $\text{Li}_4\text{Ti}_5\text{O}_{12}$  (LTO) electrode (Kokam) with the electrolyte system EC/PC (1:1, v:v), 1M  $\text{LiPF}_6$ , the voltage area is between 0.9 V and 2.8 V vs.  $\text{Li}/\text{Li}^+$  and the scan rate is  $0.05 \text{ mV}\cdot\text{s}^{-1}$ .

The CV (cf. Figure 91) shows reversible reduction and oxidation peaks and especially sharp peaks demonstrating good kinetic behavior. On the one hand this can be attributed to the spinel and to the three-dimensionally  $\text{Li}^+$ -ion diffusion and on the other hand to the increase of electronic conductivity by surface particle coatings. The obtained capacities proof the functionality of these anodes as well.

**Table 11:** obtained data from cyclic voltammetry analysis of the Kokam LTO anode between 0.9 V and 2.8 V vs.  $\text{Li}/\text{Li}^+$  (cf. Figure 91).

Electrolyte	Cycle	Charge capacity [ $\text{mAh}\cdot\text{g}^{-1}$ ]	Discharge capacity [ $\text{mAh}\cdot\text{g}^{-1}$ ]	Efficiency [%]
EC/PC 1:1 (v:v), 1M $\text{LiPF}_6$	1.	127.39	115.57	90.72
	2.	118.79	115.57	97.29
Mass of electrode [mg] 13.145	3.	117.34	115.40	98.35
	4.	116.23	114.68	98.66
	5.	115.31	113.94	98.81

After this basic characterization full cells were assembled by use of the modified Swagelok®-cell containing industrial manufactured LTO as counter electrode, lithium metal as reference electrode and an unmodified BASF NMO cathode as working electrode in combination with the same electrolyte system EC/PC (1:1, v:v), 1 M  $\text{LiPF}_6$  as before.

From the constant current cycling a relatively strong capacity fading gets apparent associated with insufficient efficiencies (cf. Figure 92, page 83). On the one hand this can be attributed to the counter electrode LTO due to the fact that LTO is oversized towards the NMO cathode. Additionally LTO seems to exhibit lower kinetics than NMO. As a result, kinetic inhibitions cause a shifting of its working potentials to a higher voltage leading to the capacity fading at least. On the other hand, the possible disproportionation reaction of manganese and thus, partial dissolution of the active layer is an issue and causes manganese deposition on the LTO surface. As a consequence less active material is available for reversible lithium intercalation and deintercalation lowering the capacity. In the middle part of the cycling (after 37 cycles) slightly higher capacities combined with lower efficiencies are obtained which can be attributed to the temperature shift from  $25^\circ\text{C}$  up to  $40^\circ\text{C}$ .

Although the bad balance of the full cell system LTO/NMO causes a not that good cell performance during the constant current cycling, the actual aim to gain knowledge of the developed pressure by possible electrolyte decomposition could be observed anyhow (see text below Figure 92).

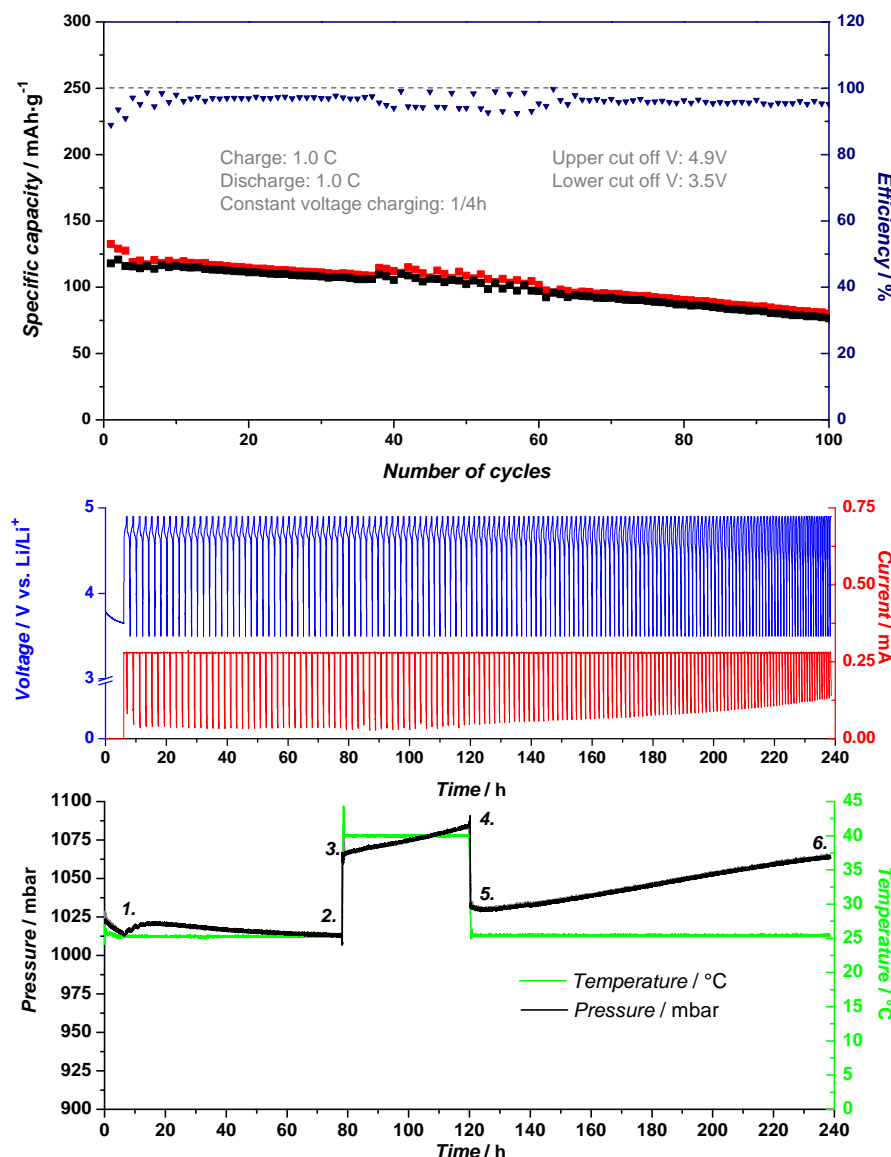


**Figure 92:** constitution of the entire constant current cycling: top) constant current cycling of the full cell LTO/NMO in combination with the electrolyte system EC/PC (1:1, v:v), 1 M LiPF<sub>6</sub> between 3.5 V and 4.9 V vs. Li/Li<sup>+</sup>; middle) time based constant current cycling of the same measurement and bottom) in-situ detection of pressure evoked during the same constant current cycling.

The black line within the lowest measurement in Figure 92 characterizes the pressure performance during the above described constant current cycling. At the starting point a decrease of the pressure is detectable. In further consequence an increase of pressure arises, which merely can be ascribed to electrolyte degradation. Thus, CO<sub>2</sub> must be formed, which in turn exhibits a high solubility in the electrolyte constituting a possible explanation of the subsequent decrease of pressure. The reason of this aspect within this investigation is not verified, because an alternative possibility for this surprising phenomenon is the assumption of a cell leakage. For leakproofness the temperature was appointed to 40°C to force thermal rise in pressure (see pressure performance from point 2 to 3 in Figure 92). If the Swagelok®-cell is not tight, the same pressure drop must be observed between point 3 and 4, but obviously quite the contrary is the case. Due to the possibility of a better tightness behavior of the PFA (perfluoroalkoxyl-

alkane) sealing rings of the Swagelok®-cell the temperature was reset to the initial temperature of 25°C. If the cell is gas-tight a pressure decrease must not appear actually. The proof for tightness is the pressure performance between point 5 and 6 demonstrating a continuously growing pressure.

From single data points of the pressure measurement a rise of pressure 52.9 mbar are obtained at the variation in temperature from point 2 to 3. At a temperature of 40°C the pressure increases about 19.1 mbar between point 3 and 4. After reducing temperature to 25°C 31.77 mbar were gained until the end up of cycling. Altogether a total pressure was generated with the amount of around 50 mbar.

The middle of Figure 92 shows the potential performance of the constant current cycling against the time and reflects the context between cycling and variation in pressure. Analog to the pressure increase caused by electrolyte degradation especially after 40°C, the distances of time between every charge and discharge steps get smaller meaning the cut-off limits are reached at frequent intervals. Hence, it can be inferred that electrolyte decomposition, loss of mobile lithium and active material induce the strong capacity fading.

**Table 12:** separate data points of the pressure gain during the constant current cycling (cf. Figure 93).

Number within pressure performance (cf. Figure 93)	Pressure [mbar]
1.	1013.8
2.	1013.0
3.	1065.9
4.	1085.0
5.	1032.1
6.	1063.9

In the following the same type of measurement will be constituted in which all parameters were the same as in the before described measurement. The only difference exists at the side of the cathode, because instead of an unmodified NMO electrode a modified (SiO<sub>2</sub> coated, sandwich-type) NMO electrode was used.

In comparison with the constant current cycling in which the “pristine” NMO electrode was used the coated cathode demonstrates a similar cell performance. Basically, the capacity fading linked with bad efficiencies is nearly the same, but the capacities are slightly higher than before. However, the cell performance can be attributed to the bad anode/cathode balancing.

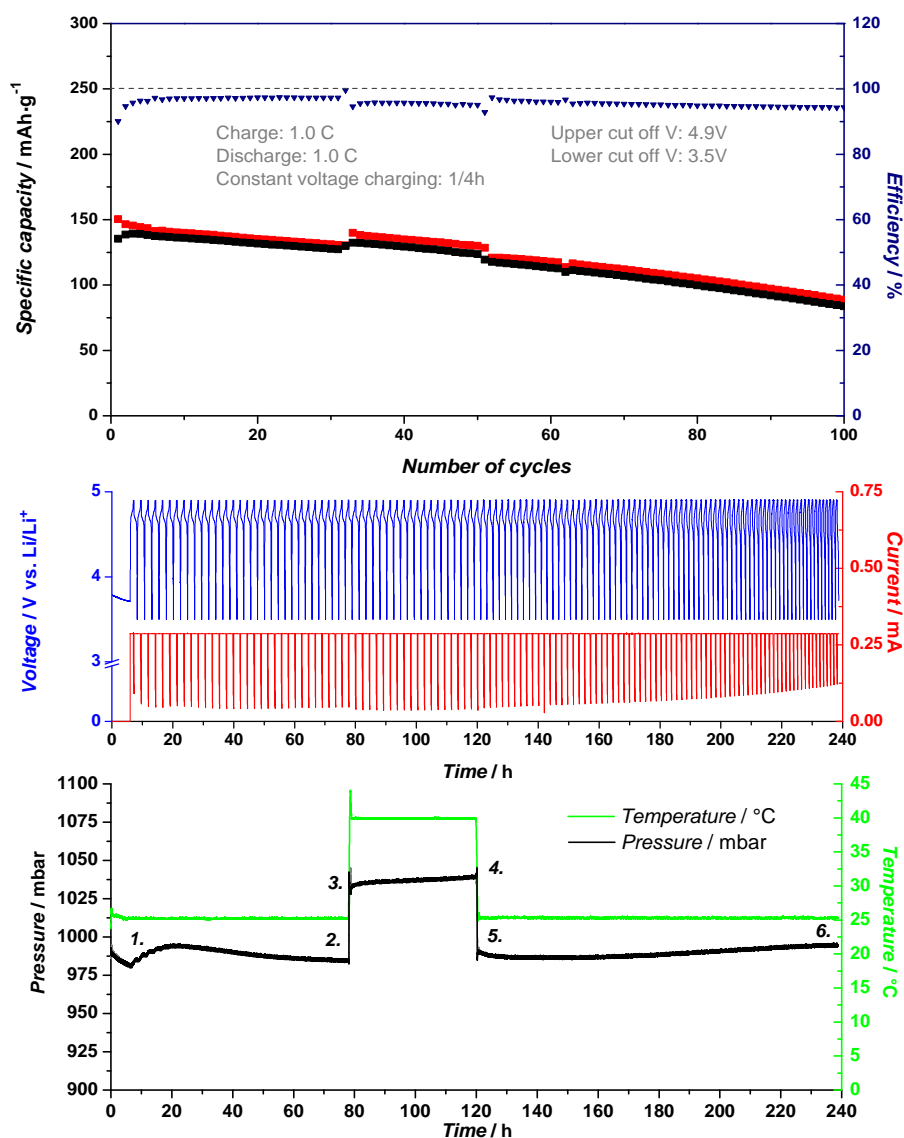


**Figure 93:** constitution of the entire constant current cycling: top) constant current cycling of the full cell LTO/NMO<sub>modified</sub> in combination with the electrolyte system EC/PC (1:1, v:v), 1 M LiPF<sub>6</sub> between 3.5 V and 4.9 V vs. Li/Li<sup>+</sup>; middle) time based constant current cycling of the same measurement and bottom) in-situ detection of pressure evoked during the same constant current cycling.

As already mentioned before, the rest step is the initial point of each electrochemical measurement and ensures complete wetting of the active materials with the electrolyte and provides temperature equilibration of the test cell at 25°C as well. During this rest step the pressure decreases in the same way as

before, whereby this effect is caused thermally. Due to the difference in temperature between cell assembling in the argon filled glove box (hand-warmth) and the adjusted 25°C from the isothermal box. On that account the temperature of the Swagelok®-cell drops and induces a low vacuum and in further consequence a pressure decrease, which is different from cell to cell. Therefore, each in-situ pressure measurement exhibits different initial pressure values.

The pressure performance at the very beginning resembles that one of the pristine NMO electrode. The assumption of resolution of the gaseous electrolyte degradation products applies here too. A big difference is not detectable until the temperature is changed to 40°C. From point 3 to 4 in Figure 93 merely 6.4 mbar are evolved, while the pressure before was 19.1 mbar. Even between point 5 and 6 a crucial differences in terms of evolved pressure gain is prevalent – instead of measured 31.8 mbar the pressure is now 4.2 mbar. Altogether an entire gas evolution occurs with an about 80 % minimization if a modified  $\text{LiNi}_{0.5}\text{Mn}_{1.5}\text{O}_4$  electrode and hybrid-electrolyte is used respectively.

**Table 13:** separate data points of the pressure gain during the constant current cycling (cf. Figure 93).

Number in pressure performance (cf. Figure 93)	Pressure [mbar]
1.	981.3
2.	984.8
3.	1033.3
4.	1039.7
5.	990.4
6.	994.6

### 3.3.4 Further Progress

#### 3.3.4.1 New NMO Batch – Introduction

The BASF provided new batches of  $\text{LiNi}_{0.5}\text{Mn}_{1.5}\text{O}_4$  from time to time. Nevertheless the very first batches did not distinguish themselves significantly in terms of electrode preparation or electrochemical behavior and are named batch A. By contrast, the last received batch (named batch B) showed different properties.

During slurry preparation minor volume of active material is necessary than with NMO batch A, which can be attributed to possible bigger particles and higher compression of the active material itself respectively. Although both slurries were coated with the same thickness of coating (80  $\mu\text{m}$ ) and were calendered with the same gap between the steel coils after the drying procedure, different electrode thicknesses and degrees of compaction were obtained.

**Table 14:** calendering of a BASF NMO batch B electrode leads to a compression of 64 %.

Effective thickness of the electrode with NMO batch A [ $\mu\text{m}$ ]					
Before:	Electrode	Aluminum	Afterwards:	Electrode	Aluminum
	52	30		39	29
	52	30		37	29
	51	30		36	29
<b>Average thickness:</b>	<b>52</b>	<b>30</b>	<b>Average thickness:</b>	<b>37</b>	<b>29</b>

**Table 15:** calendering of a BASF NMO batch B electrode leads to a compression of 58 %.

Effective thickness of the electrode with NMO batch B [ $\mu\text{m}$ ]					
Before:	Electrode	Aluminum	Afterwards:	Electrode	Aluminum
	62	29		43	29
	63	30		43	29
	64	30		44	29
<b>Average thickness:</b>	<b>63</b>	<b>30</b>	<b>Average thickness:</b>	<b>43</b>	<b>29</b>

Furthermore it should be mentioned that merely electrodes with NMO active material from batch B were used for all electrochemical measurements within the upcoming chapters.

### 3.3.4.2 Comparison of Morphology by the Use of SEM

To explain the difference between the various compressions after the calendaring process of the BASF NMO batches A and B, scanning electron microscopy (SEM) images were taken from active material powders, already prepared electrodes (calendered and not calendered). All microscopic investigations within this chapter were carried through on the TESCAN VEGA3 SBU scanning electron microscope with a secondary electron detector.

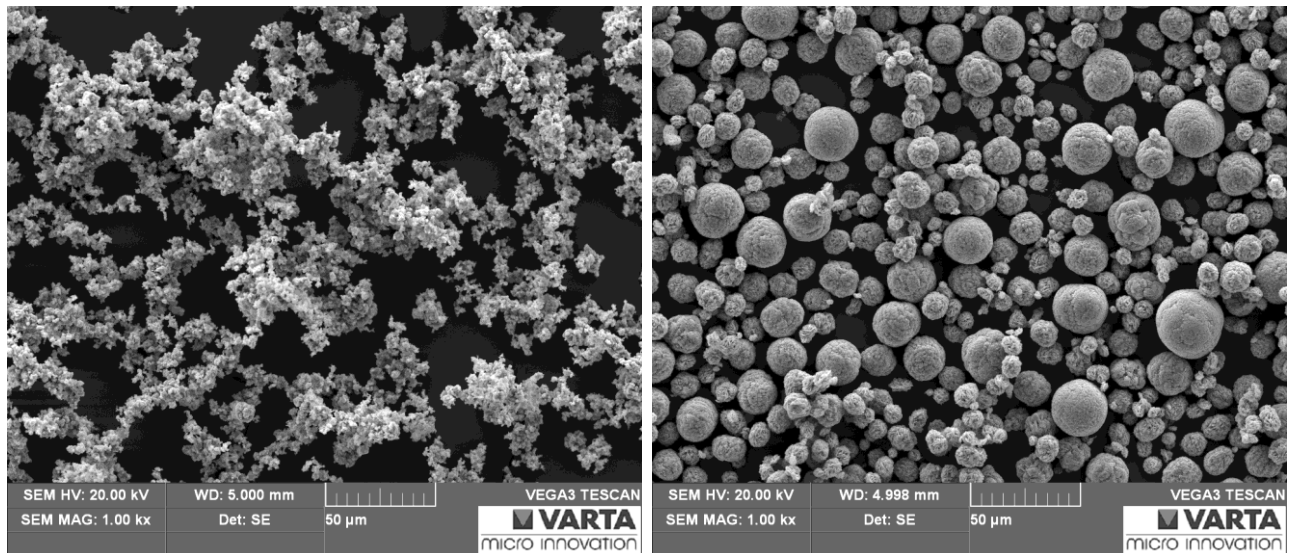


**Figure 94:** scanning electron microscope (SEM) images from BASF NMO batch A (left) and batch B (right); magnification of both is x1,000.

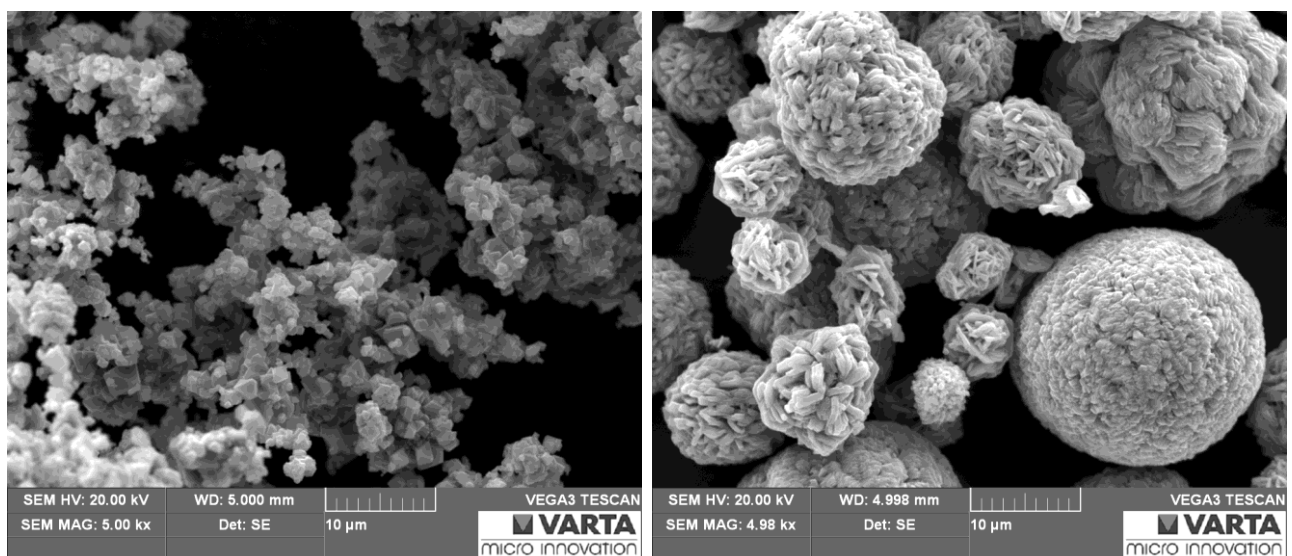
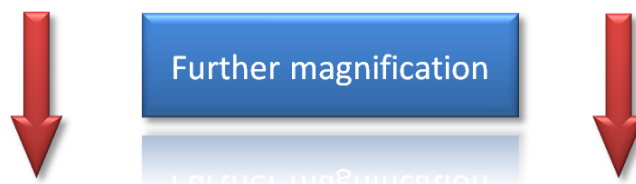


**Figure 95:** scanning electron microscope (SEM) images from BASF NMO batch A (left) and batch B (right); magnification of both is x5,000.

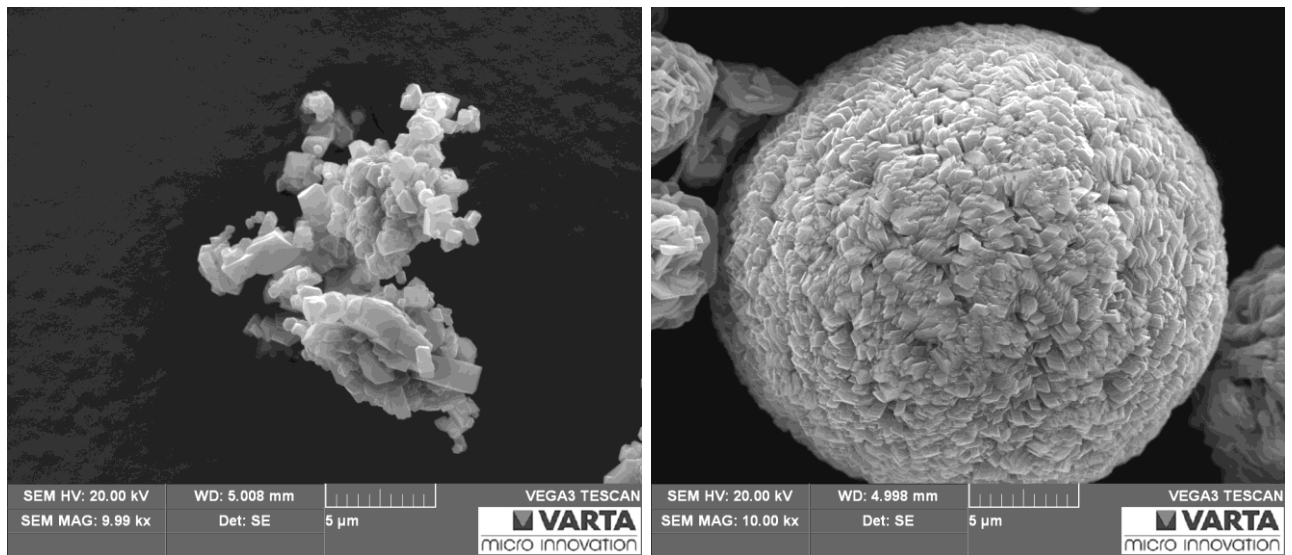


**Figure 96:** scanning electron microscope (SEM) images of single particles from BASF NMO batch A (left) and batch B (right); magnification of both is x10,000.

The comparison of the SEM images of both batches of the BASF NMO spinels shows a big difference concerning the particle size. While batch A exists of smaller particles, the active material of the batch B is composed spherically. The diameter of the bigger balls amounts to approximately 22 µm (cf. Figure 98, page 90, the particle size is determined with a 3D software program of the company Alicona). The following enlargement displays spatial appreciation (3D) of the single particle of the NMO batch B from Figure 96:

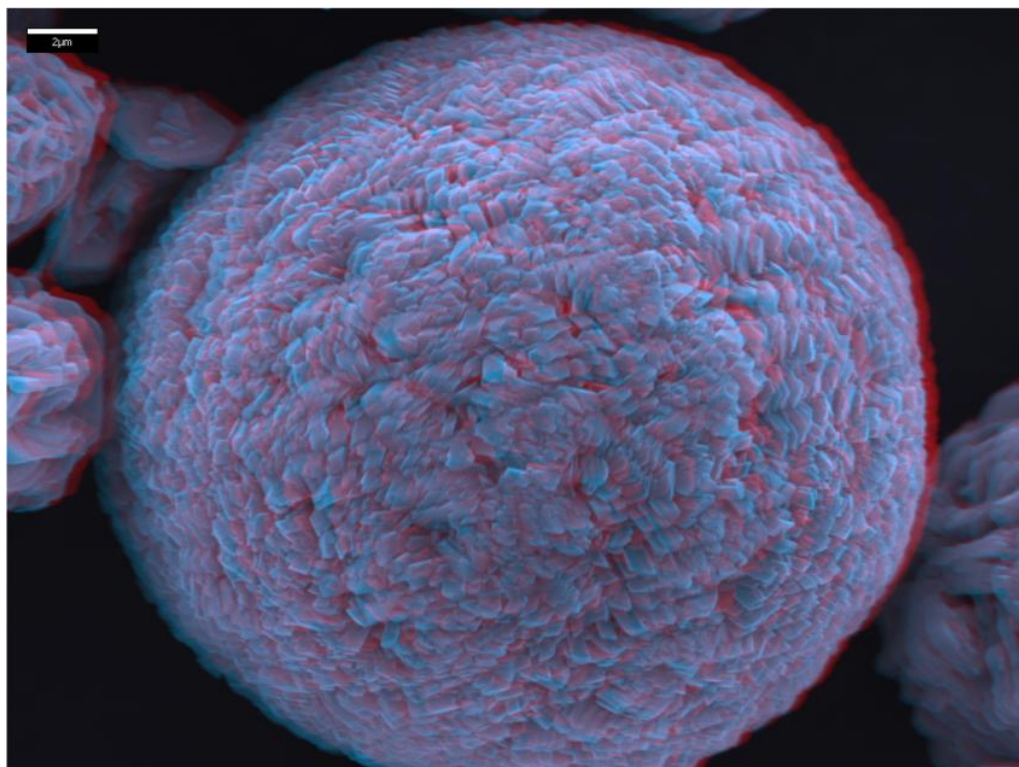


**Figure 97:** 3D image of the before shown BASF NMO particle of the batch B (for the 3D effect please use the glasses attached, which is attached in the last page of this doctoral thesis!).

By the fact that the powders of both batches strongly differ in the particle size an essential difference is also detectable within the comparison of the electrodes. Initially SEM images of not calendered electrodes are shown:

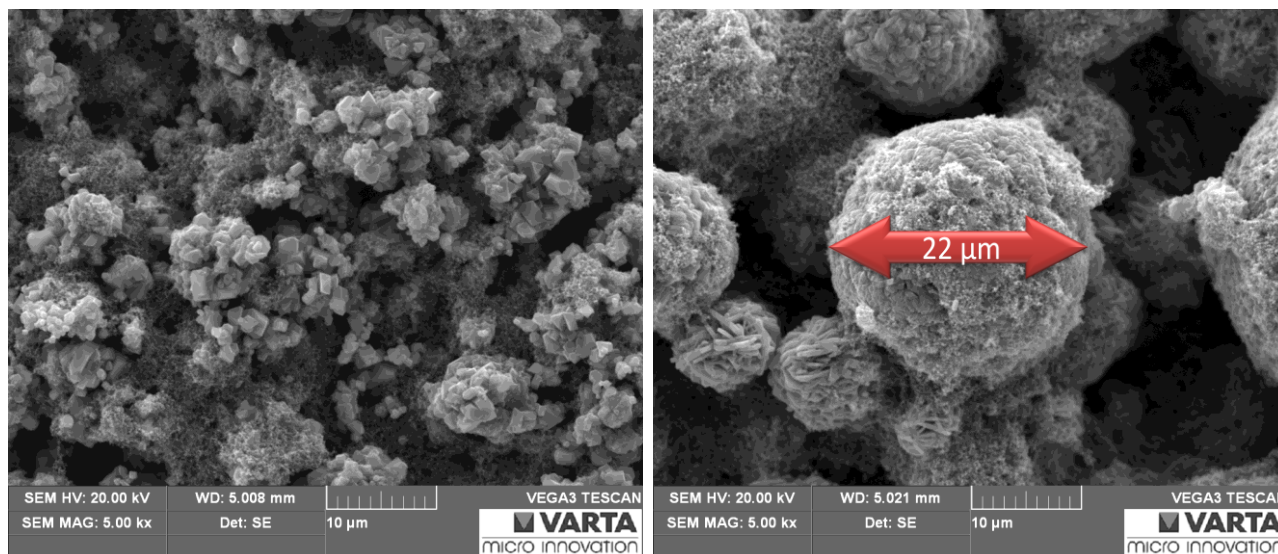


**Figure 98:** scanning electron microscope (SEM) images from not calendered BASF NMO electrodes containing batch A (left) and batch B (right) as active material; magnification of both is x5,000.

After calendering the surfaces of the prepared electrodes exhibit following morphology:

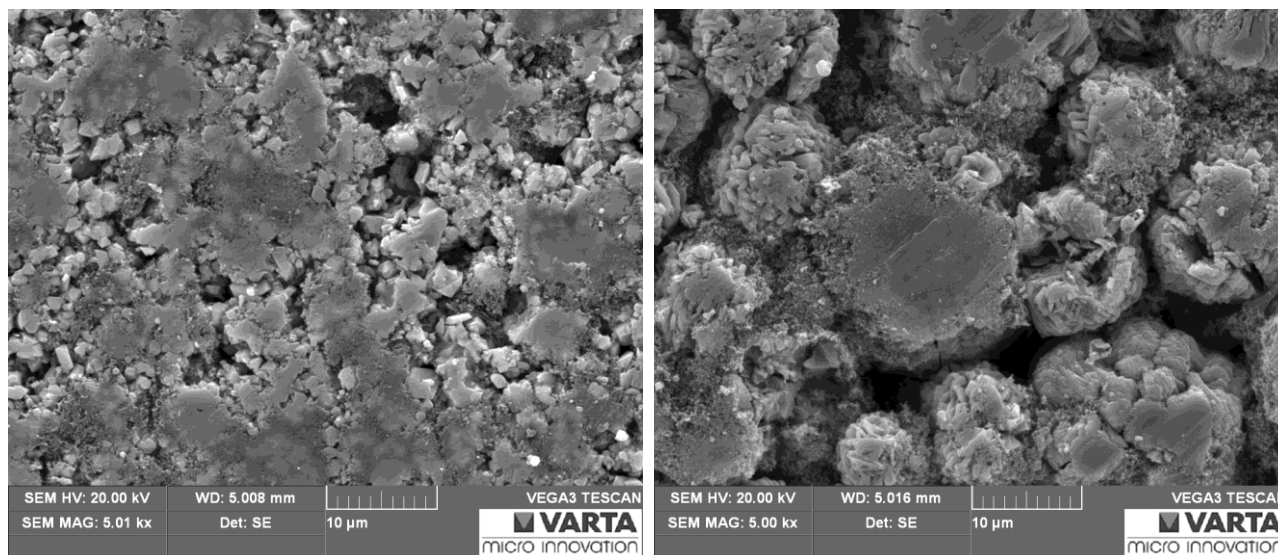


**Figure 99:** scanning electron microscope (SEM) images from calendered BASF NMO electrodes containing batch A (left) and batch B (right) as active material; magnification of both is x5,000.

Due to the fact that the active material of batch A consists of small and unconsolidated particles it seems that the electrode itself can be compressed in a more uniform way than electrodes of batch B. Within the right SEM image of Figure 99 a higher porosity and grooves of the calender steel coils are detectable meaning that the strong compression induces a cracking of the spherical particles of batch B. Furthermore a

crucial difference in terms of porosity is obviously. Therefore, batch B provides deeper holes between single particles than those of batch A. As a consequence it is conceivable that the resulting higher surface with direct contact between particle and electrolyte provides space for more parasitic reactions. The depth of the holes of electrodes originating from batch B can be determined with the 3D software.

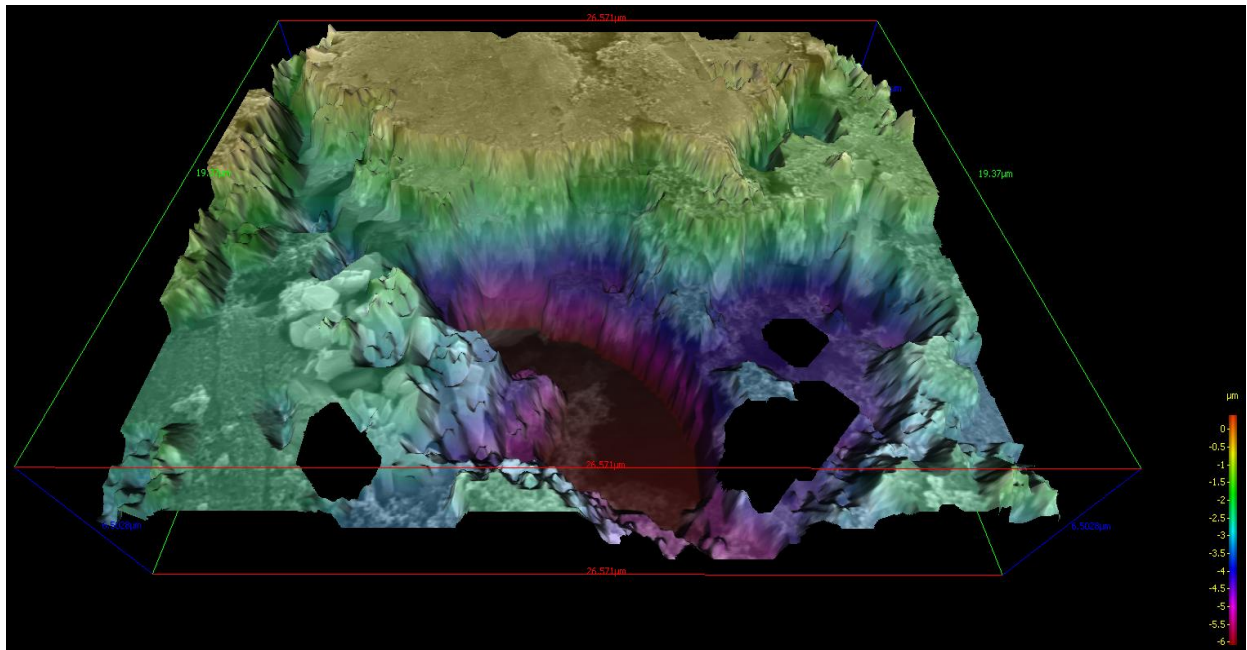


**Figure 100:** three dimensional image of a calendared BASF NMO electrode of batch B; the color bar on the bottom right determines the depth of the holes between particles of the electrode.

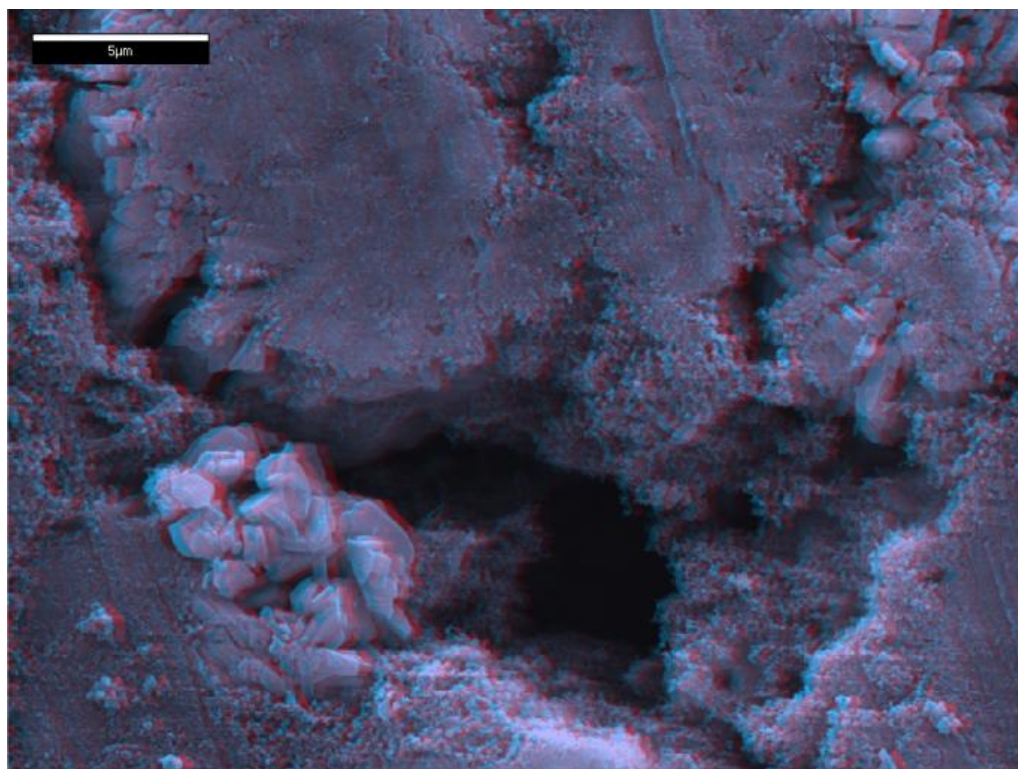


**Figure 101:** 3D image of the before shown calendared BASF NMO electrode from batch B (for the 3D effect please use the glasses, which is attached in the last page of this doctoral thesis!).

### 3.3.4.3 Electrochemical Differences of Both Batches

For the constant current cyclings the same electrolyte EC/DEC (3:7, v:v), 1 M LiPF<sub>6</sub> is used. As a consequence the same electrode performance can be estimated, but quite the contrary is observed: NMO batch A exhibits higher capacities at the beginning than batch B indeed, but a higher capacity fading as well. Furthermore the efficiencies show minor values than those compared with batch B (see green ellipses in Figure 102).

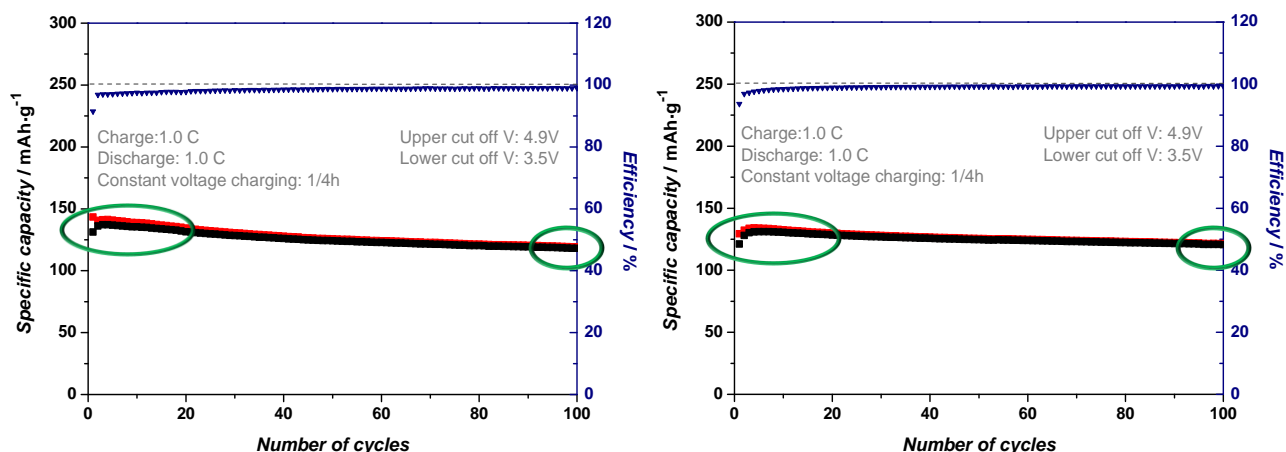


**Figure 102:** constant current cycling (CCC) of BASF NMO spinel batch A (left) and batch B (right) in combination with the electrolyte system EC/DEC (3:7, v:v), 1 M LiPF<sub>6</sub> and metallic lithium as counter electrode.

A more precisely point of view concerning electrochemical differences can be observed through the following measurements. A constant current cycling test including different charging current rates displays the distinction in terms of rate capability of the two batches.

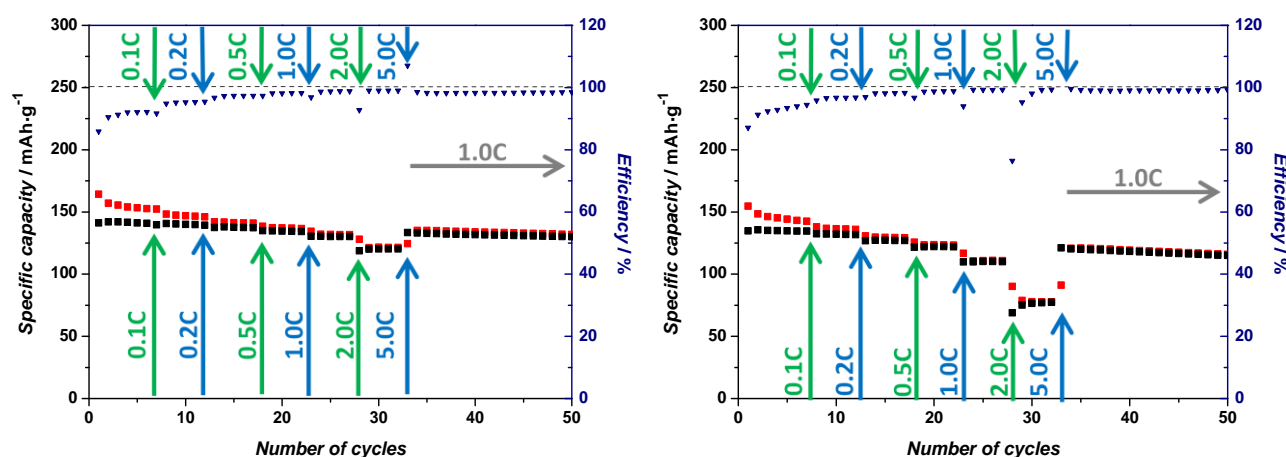


**Figure 103:** constant current cycling (CCC) of BASF NMO spinel batch A (left) and batch B (right) with different current charging (C-rates); as electrolyte system EC/DEC (3:7, v:v), 1 M LiPF<sub>6</sub> and as counter electrode metallic lithium are used.

As a result, they show nearly the same capacities within the cycles of the 0.1 C steps, merely batch A exhibits slight higher capacities, but minor efficiencies than batch B. The same applies to the subsequent C-rates during the entire cycling. By contrast, the efficiencies getting better due to less electrolyte decomposition, because the cell is located at high voltages only for short times while charging. Especially

after 1.0 C a major difference exists at high C-rates concerning charge and discharge capacities. Batch A solely loses about  $15 \text{ mAh}\cdot\text{g}^{-1}$  from increasing the current strains from 1.0 C to 5.0C, while the electrode from batch B loses about  $50 \text{ mAh}\cdot\text{g}^{-1}$  inside of the same current range.

**Table 16:** comparison of the obtained capacities and efficiencies of both batches from the before shown C-rate tests; the denoted capacities correspond to the average capacities of five cycles for each C-rate.

C-rate	BASF LiNi <sub>0.5</sub> Mn <sub>1.5</sub> O <sub>4</sub> batch A			BASF LiNi <sub>0.5</sub> Mn <sub>1.5</sub> O <sub>4</sub> batch B		
	Charge capacity [mAh·g <sup>-1</sup> ]	Discharge capacity [mAh·g <sup>-1</sup> ]	Efficiency [%]	Charge capacity [mAh·g <sup>-1</sup> ]	Discharge capacity [mAh·g <sup>-1</sup> ]	Efficiency [%]
0.1 C	154.09	141.20	91.64	144.95	134.89	93.07
0.2 C	146.71	139.86	95.33	136.38	131.92	96.73
0.5 C	141.31	137.57	97.35	129.43	127.12	98.22
1.0 C	136.99	134.54	98.21	123.49	122.00	98.79
2.0 C	131.84	130.23	98.78	110.78	109.99	99.29
5.0 C	121.44	120.26	99.02	77.98	76.42	98.00

After 50 cycles of the C-rate testing an OCV step for 72 hours was carried out to gain knowledge on the self-discharge behavior. As a result, both batches lose merely 0.01 V within 3 days at fully charge of the electrochemical cell. Furthermore it is obvious that the measurement with batch B was completed inside of a shorter time. This arises from the diminished cycling behavior at high C-rates by reaching cut-off criterions more quickly.

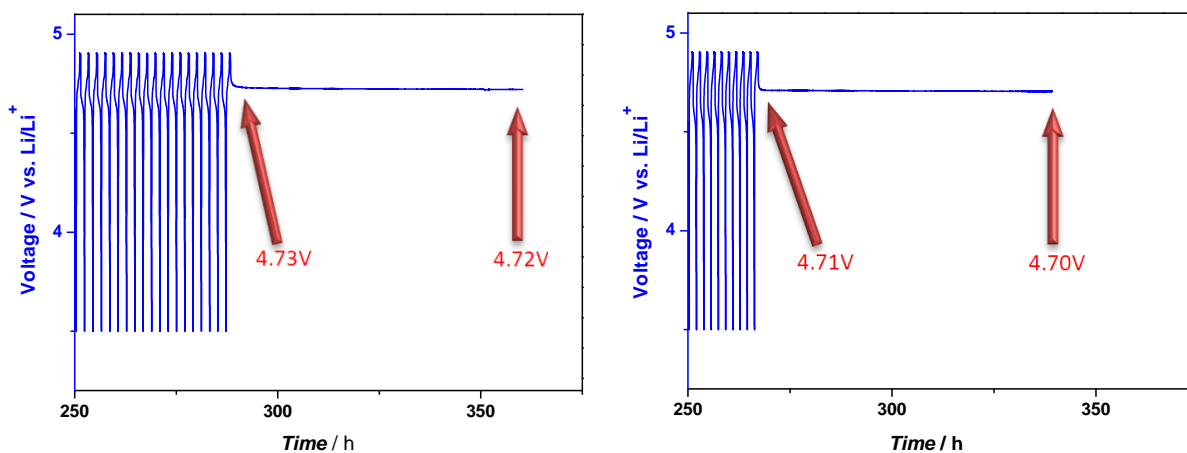


**Figure 104:** direct comparison potential profiles during the C-rate tests including the self-discharge behavior of NMO batch A (left) and NMO batch B (right).

Taking all aspects into account, the differences seem to depend strongly on particle size of the active material. Due to the smaller particle sizes the electrode can be compressed more homogenous leading on the one hand to a minor porosity of the electrode itself, which reduces maybe electrolyte decomposition. On the other hand the strong calendaring causes (too) thin electrodes with low electrode weights. As a consequence more parasitic reactions can take place due to a worse ratio of capacity to particle surface leading to a higher capacity fading (cf. Figure 102, page 92). Another possibility for the divergent electrochemistry could be a difference in terms of the space group, which according to literature causes a different electrochemical behavior. On this account radiological measurements were the logical consequence.

### 3.3.4.4 Determination of the Space Group with XRD and TEM

Structural identification concerning space group (non-stoichiometric Fd-3m or stoichiometric  $P4_332$ ) of both NMO batches could be observed by the use of X-ray diffraction (XRD). All XRD analysis was carried through by Ao.Univ.-Prof. Dipl.-Ing. Dr.techn. Franz Mautner at the “Institut für physikalische und theoretische Chemie“ at the University of Technology Graz. According to Kim et al. both space groups NMO spinels provide exhibit slight differences in terms of their XRD peaks. If the stoichiometric compound is present peaks at  $15.3^\circ$ ,  $39.7^\circ$ ,  $57.5^\circ$  and  $65.6^\circ$  arise, which cannot be observed for non-stoichiometric spinel<sup>(195)</sup>. The Rietveld refinements of the XRD data of the two NMO batches showed the same results. In fact they exhibit the face-centered crystal structure (Fd-3m), because no additional peaks at the before denoted degrees could be obtained. To give proof further measurements were carried through within the range in which the additional peak at  $39.7^\circ$  (zone [320]) should arise if the spinel exhibits the primitive cubic structure. However, for both batches no peak could be observed.

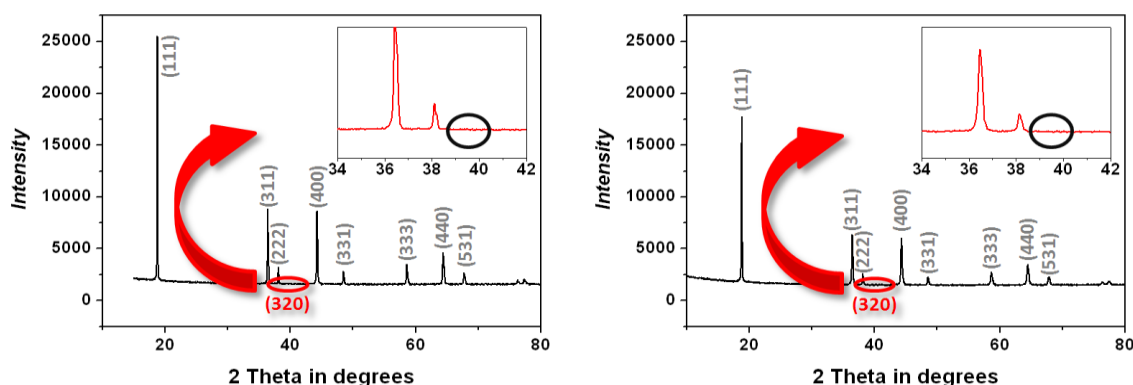


Figure 105: XRD profiles of both BASF NMO batches; left) batch A, right) batch B.

For confirmation of the XRD results the space groups were determined by use of the transmission electron microscope (TEM) at the same time. The TEM measurements were carried out by Dr. Christian Gspan from the Institute for Electron Microscopy and Fine Structure Research (FELMI) at the Graz University of Technology. The electron diffraction patterns obtained from the TEM measurements demonstrate numerous superlattice peaks in the [100] zone (corresponds to the cubic structure). The real crystal structure of both NMO powders exhibits the primitive cubic structure  $P4_332$  actually, which is in direct contradiction to the clear statement of the XRD analysis. The divergent results are attributed to the low intensities the additional peaks provide and thus, they disappear inside of the background, while the resolution of TEM allows identifying even small peaks. However, the slight difference concerning electrochemistry between both batches seems to originate from particle size and electrode masses and maybe from different vacancies inside of the NMO lattice actually.

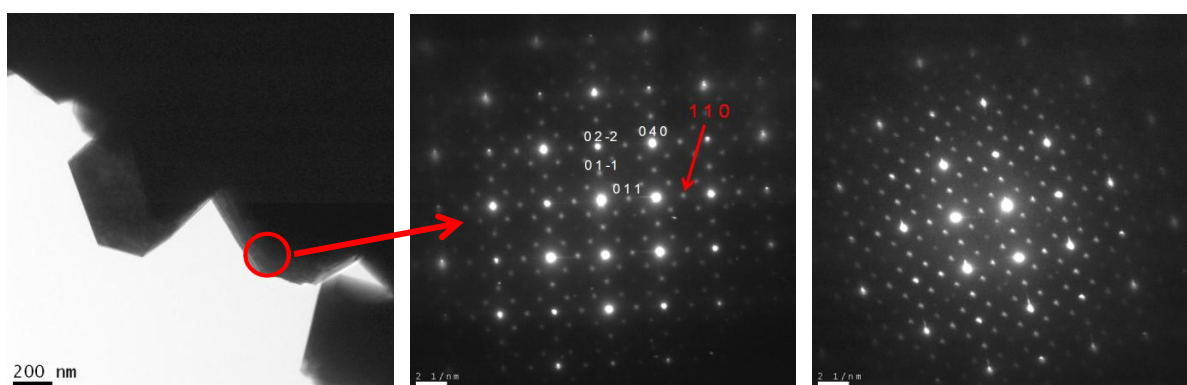


Figure 106: TEM bright field image of NMO batch A (left) and electron diffraction patterns of batch A (middle) and batch B (right).

### 3.3.4.5 *Modification of Non-Aqueous Electrolyte Systems for Electrochemical Improvements*

#### 3.3.4.5.1 **Electrochemical Impact of Additives**

Many efforts were made to improve the performance of Lithium-Ion-Batteries with a very economic and effective method, namely by the use of electrolyte additives. They are defined as chemical compounds that are added with an amount of not more than 5 % (volume or weight) to an already existing electrolyte system. Due to a huge number of possible electrolyte additives the choice depends merely on the desired effect, which is usually a compromise between physical and electrochemical properties. Usually additives get assigned with tasks like <sup>(232), (233)</sup>:

- Improvement or facilitation of the SEI on anode surfaces
- Reduction of the irreversible capacity, gas evolution during SEI formation
- Improvement of the ionic conductivity, viscosity, volatility or wetting ability of the electrolyte
- Mitigation of safety issues such as reduction of flammability of organic solvents or termination of battery operation in terms of abuse conditions (overcharge protection)
- Thermal stabilization of the conductive salt  $\text{LiPF}_6$
- Protection of cathode materials from structure dissolution (scavenger of water and HF)

In respect of high voltage cathodes (working potential  $> 4.3 \text{ V}$  vs.  $\text{Li/Li}^+$ ) the physical properties of propylene-carbonate (PC) are remarkable. Unfortunately, PC cannot be used in combination with the commercially used graphite as anode material without any SEI forming additive, because apart from that solvated co-intercalation would take place leading to an irreversible damage of the carbonaceous anode materials and therefore, the battery (cf. chapter 2.3.7, page 40). The application of film forming electrolyte additives shows an actual method to suppress this undesirable effect. This chapter deals with the question if such film forming additives exhibit a sufficient oxidative stability on account of a full cell containing graphite and  $\text{LiNi}_{0.5}\text{Mn}_{1.5}\text{O}_4$ .

During the last two decades an optimization of electrolyte systems, especially by use of additives, was attempted in view of the functionality of negative electrodes. Intensive studies delivered knowledge about the behavior and reaction mechanisms of additives mainly for anodes. But besides, it would be important to gain information if it is possible in principal that additives are able to form a protective layer on the high voltage cathode surfaces (especially NMO) in a similar way to the SEI formation on the negative electrode. The merit might be that this film enables the envisaged electrochemical improvement of NMO, which could be already demonstrated with hybrid electrolytes (cf. chapter 3.3.3, page 60). Compared to the before shown artificial SEI (hybrid electrolyte) the main advantage would be an absolutely homogenous and in particular in-situ formed SEI. Furthermore, battery manufacturing would be simplified, because solely the electrolyte system needs to be adapted.

Ideally, an electrolyte or more exactly an additive would have to be found that supports SEI formation not only on cathode surfaces, but also on anode surfaces too. According to literature and investigations of the battery working group at the TU Graz merely additives were used for the electrochemical measurements within this doctoral thesis, which already were proven to have a positive impact on battery performance by film formation on graphite surface. Furthermore, electrochemical tests of related chemical compounds and derivatives of the approved additives constituted the logical consequence.

Basically it is proposed in literature that vinylene containing compounds can electro-polymerize. Its reduction or oxidation strongly depends on the functional group of the vinylene monomer. Hence,

reductive electro-polymerization takes place if functional groups such as CN are the organic residual of the monomer. These electron withdrawing groups induce a more electrophilic character and facilitate reduction and SEI formation respectively, which occurs around 0.8 V vs. Li/Li<sup>+</sup>. Due to a more nucleophilic character of the double bond, vinylene monomers polymerize oxidative if electron-pushing groups constitute the organic residual<sup>(232), (234)</sup>. Ideally the oxidative polymeric film behaves like a protective layer and thus, extinguishes problems concerning electrolyte corrosion of the NMO spinel.

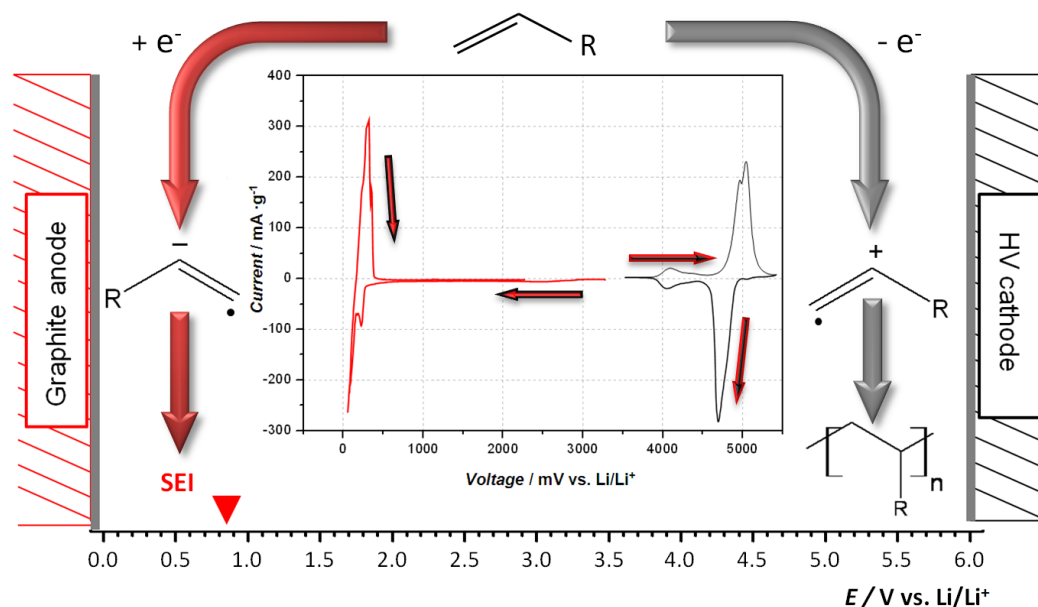


**Figure 107:** in the middle of this illustration typical CVs of graphite and NMO are depicted, while beside them reduction and oxidation of vinylene monomers on anode and cathode surface are shown<sup>(drawn from (232), (234))</sup>.

Within preparatory works all additives were adjusted to the electrolyte EC/DEC (3:7, v:v), 1 M LiPF<sub>6</sub> as received without any purification steps. The water content of the resulting electrolyte systems was determined with a Karl-Fischer titration device CA-100/VA-100 from Mitsubishi Chemical Corporation. As far as substance classes do not react with the Karl-Fischer reagents, H<sub>2</sub>O values below 20 ppm could be obtained. The additive amounts belong to experience- or literature values if 2 v/w% and below were adjusted to the base electrolyte. Otherwise all additive concentrations were set to 5 v/w% to investigate a possible influence on the electrode performance. If no sufficient electrochemical reactions could be obtained the amount of additive was reduced to 1 v/w% whether the polymer film on cathode surface is Li<sup>+</sup>-ion permeable or not.

Following substance groups were chosen for electrochemical testing:

- carbonates (-CO<sub>3</sub>)
- nitriles (-CN)
- thiolane, oxazoline, isocyanates (compounds containing hetero atoms like S, O, N)

Due to a huge number of investigated additives merely the best additive is depicted. For a better overview all used additives are summarized within Table 20 on page 107. Within the family containing carbonates (-CO<sub>3</sub>) group two representatives were used which effectively form a sufficient SEI on graphite surface, vinylene-carbonate (VC) and fluoroethylene-carbonate (FEC)<sup>(232), (233)</sup>. In addition, a double fluorinated EC, namely difluoroethylene-carbonate (F<sub>2</sub>EC) was tested. All three additives were

electrochemical investigated with base electrochemical tools like cyclic voltammetry and constant current cycling.

VC and FEC can be counted to the family of the reduction-type additives. Especially, VC exhibits a C-C double bond, which has a high electron affinity. Therefore, polymerization is induced electrochemically forming a radical anion which in turn is usually terminated by the solvent molecules and composes an insoluble and stabile polymer film on graphite <sup>(232), (233)</sup>.

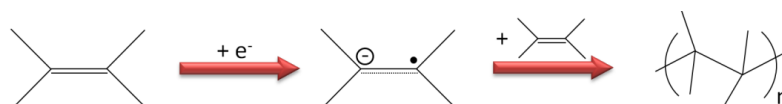


**Figure 108:** mechanism of polymerization of reduction-type additives <sup>(drawn from (233))</sup>.

In addition, oxidative polymerization occurs as well and increases impedance and irreversibility of the cathode. Among these three CO<sub>3</sub> compounds VC exhibits no sufficient oxidative stability and the formed polymeric film does not exhibit Li<sup>+</sup>-ion permeability due to the fact that electrochemical measurements could not achieve satisfying results meaning already after only few cycles the capacity of the cell dropped down to nearly zero. Nevertheless, sufficient electrochemical measurements could be observed with FEC and F<sub>2</sub>EC as additives (only measurements of FEC are depicted, because they exhibit very similar electrochemical behavior).

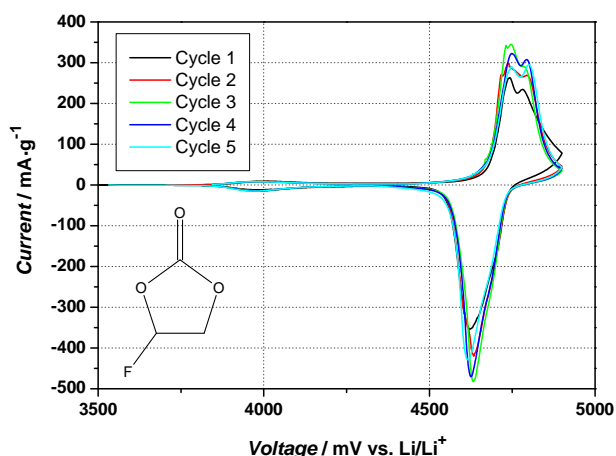


**Figure 109:** cyclic voltammogramm (CV) of the BASF NMO cathode (batch B) with the electrolyte system EC/DEC (3:7, v:v) + 2 v% FEC, 1M LiPF<sub>6</sub>, cycled between 3.5 V and 4.9 V vs. Li/Li<sup>+</sup> against metallic lithium, the scan rate was appointed to 0.1 mV·s<sup>-1</sup>.

**Table 17:** obtained data from cyclic voltammetry analysis of the BASF NMO electrode (batch B) between 3.5 V and 4.9 V vs. Li/Li<sup>+</sup>.

Electrolyte	Cycle	Charge capacity [mAh·g <sup>-1</sup> ]	Discharge capacity [mAh·g <sup>-1</sup> ]	Efficiency [%]
EC/DEC 3:7 (v:v) + 2 v% FEC, 1M LiPF <sub>6</sub>	1.	135.43	129.83	95.87
	2.	138.90	134.63	96.93
Mass of electrode [mg] 4.2625	3.	141.30	135.16	95.66
	4.	140.50	134.63	95.83
	5.	138.36	133.56	96.53

The CV demonstrates typical redox peaks of the nickel-manganese spinel with sufficient capacities, but exhibits no improvement compared to the measurement without any additive actually.

Interestingly, the difference between VC and FEC merely is the double bond and the fluorinated carbon atom respectively. Therefore, FEC does not contain a Vinylene group, but can lose a hydrofluoric acid molecule and forms VC, which in turn polymerizes again during cycling. Following reaction takes place <sup>(233)</sup>:



**Figure 110:** constitution of the formation of HF from a FEC molecule leading to VC at least <sup>(drawn from (233))</sup>.

Hence, one can estimate a bad cycling behavior in the same way than VC after few cycles at least if FEC is adjusted to the electrolyte system. However, even the constant current cycling shows a sufficient cycling behavior. After 100 cycles capacity retention of 90.24 % could be obtained which is nearly the same as without additive (92.40 %).

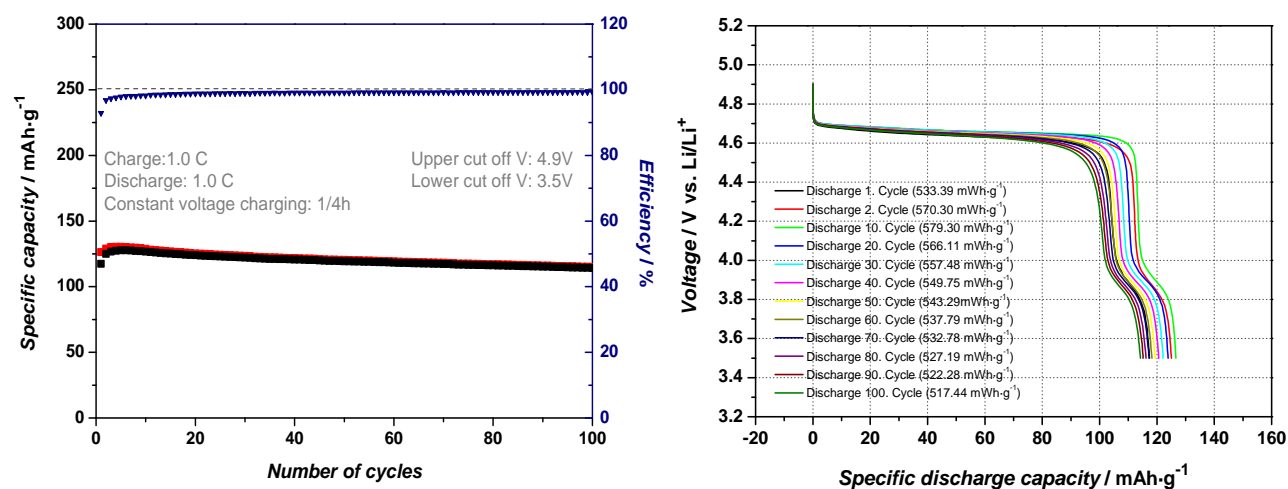


**Figure 111:** left) CCC of the BASF NMO spinel (batch B) in combination with the electrolyte system EC/DEC (3:7, v:v) + 2 v% FEC, 1 M LiPF<sub>6</sub> and metallic lithium as counter electrode; right) selected discharge profiles of the CCC measurement and their specific energies.

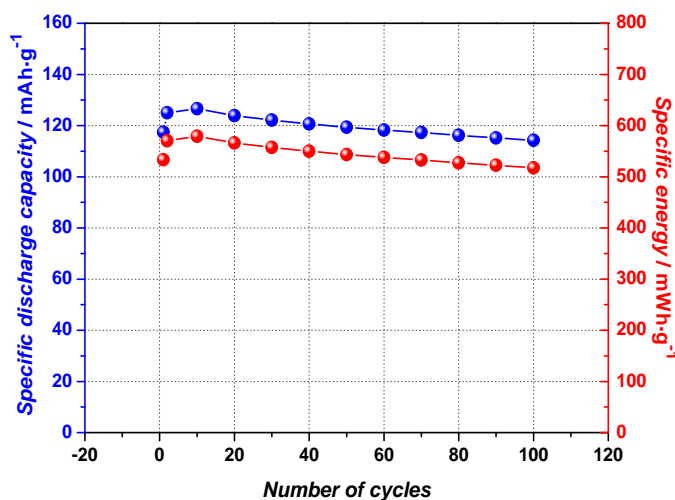


**Figure 112:** comparison of specific discharge capacity and specific energy performance for every 10<sup>th</sup> cycle during the entire CCC; the loss of capacity amounts to 9.76 % and the loss of specific energy amounts to 10.68 %.

The spectroscopic detection by SEM shows only few electrolyte decomposition products compared to the NMO electrode, which was cycled with VC as additive.

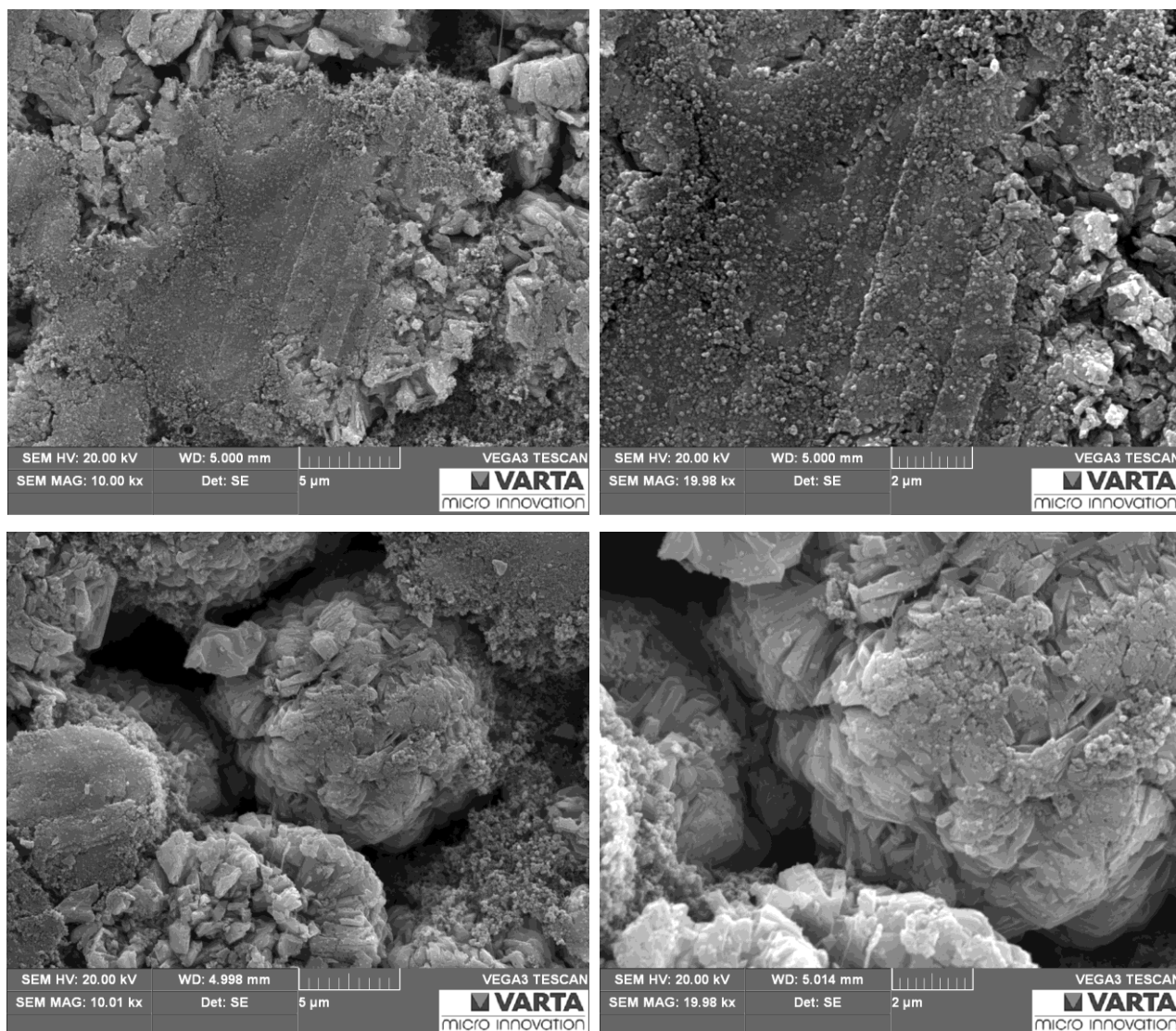


**Figure 113:** SEM images of the BASF NMO cathode (batch B) after the CCC in which VC (top left and top right) or FEC (bottom left and bottom right) was added to EC/DEC (3:7, v:v), 1 M LiPF<sub>6</sub>.

Other types of additives are compounds with the functional group  $-CN$ , which have a positive impact on the SEI formation on graphite anodes. Especially acrylo-nitrile (AN,  $n_{\text{carbon}} = 2$ , one  $-CN$  group) exhibits excellent film forming properties and enables the usage of PC as organic solvent. Santner et al. investigated even the oxidative behavior of AN at  $\text{LiMn}_2\text{O}_4$  with cyclic voltammetry and could verify a sufficient electrochemical window for the use of “4V” cathodes. Additionally, they claimed that maybe the formation of a protective layer on cathode/electrolyte interface is responsible for the good cycling conditions of the manganese spinel. On that account AN and nitrile compounds in general, respectively, suggest themselves as additive candidates for electrochemical experiments<sup>(232)</sup>. Moreover, nitrile compounds like butyronitrile (BN,  $n_{\text{carbon}} = 3$ , one  $-CN$  group) and valero-nitrile (VN,  $n_{\text{carbon}} = 4$ , one  $-CN$ ) were tested. The idea was to gain information about the oxidation behavior of nitrile compounds with a longer carbon chain without a C-C double bond. The same applies to nitrile compounds with two cyano-groups, so called dinitriles, which were tested, fumaro-nitrile (FN,  $n_{\text{carbon}} = 2$ , C-C double bond, two  $-CN$  groups), succino-nitrile (SN,  $n_{\text{carbon}} = 2$ , two  $-CN$  groups) and adiponitrile (ADN,  $n_{\text{carbon}} = 4$ , two  $-CN$  groups).

In the following the best measurement of all nitriles will be shown, namely those with 1 v% AN.

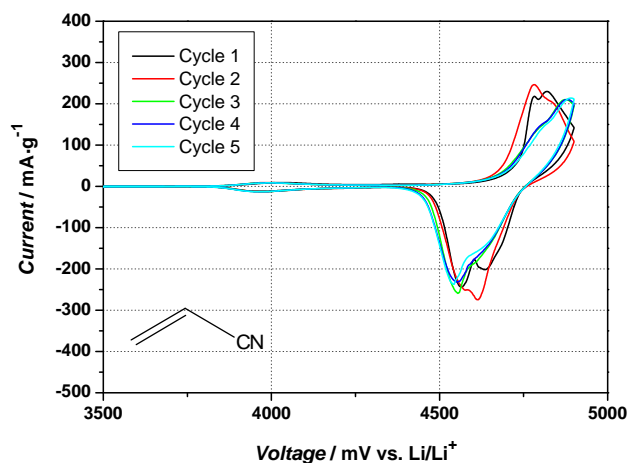


**Figure 114:** cyclic voltammogram (CV) of the BASF NMO cathode with the electrolyte system EC/DEC (3:7, v:v) + 1 v% AN, 1M  $\text{LiPF}_6$ , cycled between 3.5 V and 4.9 V vs.  $\text{Li/Li}^+$  against metallic lithium, the scan rate was appointed to  $0.1 \text{ mV}\cdot\text{s}^{-1}$ .

**Table 18:** obtained data from cyclic voltammetry analysis of the BASF NMO electrode between 3.5 V and 4.9 V vs.  $\text{Li/Li}^+$ .

Electrolyte	Cycle	Charge capacity [ $\text{mAh}\cdot\text{g}^{-1}$ ]	Discharge capacity [ $\text{mAh}\cdot\text{g}^{-1}$ ]	Efficiency [%]
EC/DEC 3:7 (v:v) + 1 v% AN, 1M $\text{LiPF}_6$	1.	125.60	120.31	95.78
	2.	132.17	128.99	97.60
Mass of electrode [mg] 5.365	3.	122.21	120.10	98.27
	4.	121.58	119.46	98.26
	5.	118.83	116.92	98.40

Acrylo-nitrile belongs to the reductive type additives as well. Therefore, it was very interesting to observe an oxidative polymerization which in turn forms a lithium-ion permeable film on the cathode surface. But in fact, it was very surprising that sufficient electrochemical results could not be obtained until an additive concentration reduction from 5 v% down to 1 v% was done.

The CV shows the estimated redox peaks indeed, but their shape is significant broader than “normal” NMO peaks are. In addition, the capacities fade rapidly within those five cycles. In comparison, the CCC confirms

the trend that the use of AN does not improve the cathode performance actually. Within 100 cycles capacity retention of 87.30 % could be obtained. In general, AN can be applied to electrolyte systems to improve at least the SEI formation on the anode surface and in further consequence, PC could be used in combination with graphite and NMO.

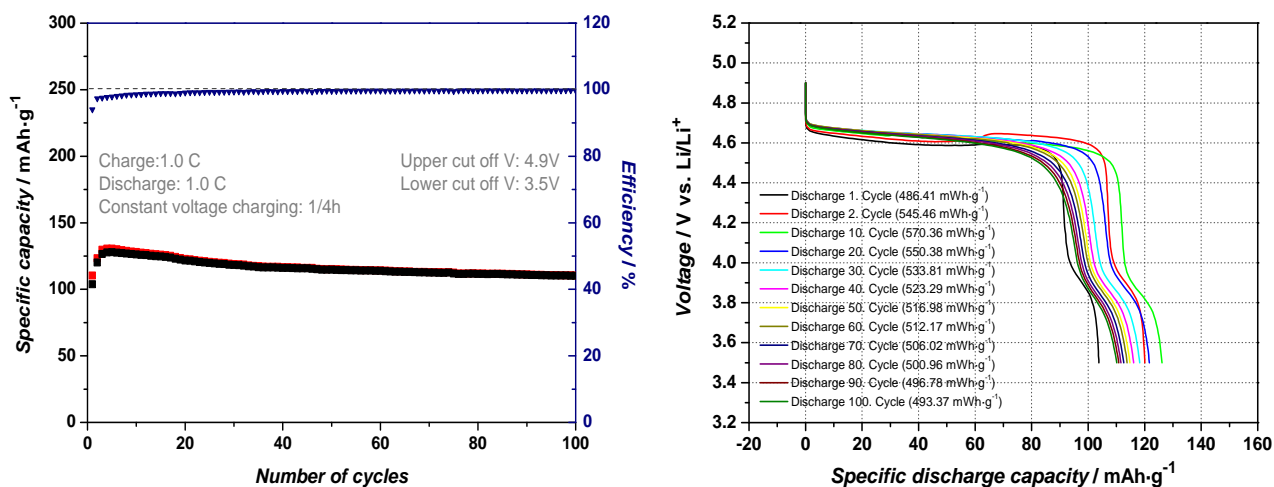


Figure 115: left) CCC of the BASF NMO spinel in combination with the electrolyte system EC/DEC (3:7, v:v) + 1 v% AN, 1 M LiPF<sub>6</sub> and metallic lithium as counter electrode; right) selected discharge profiles of the CCC measurement and their specific energies.

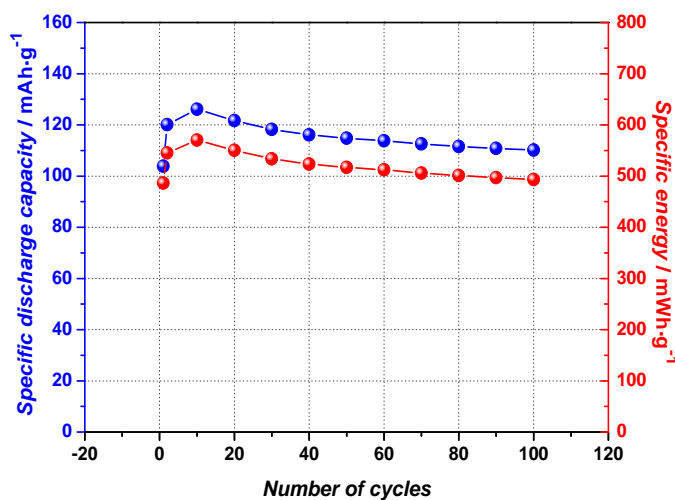
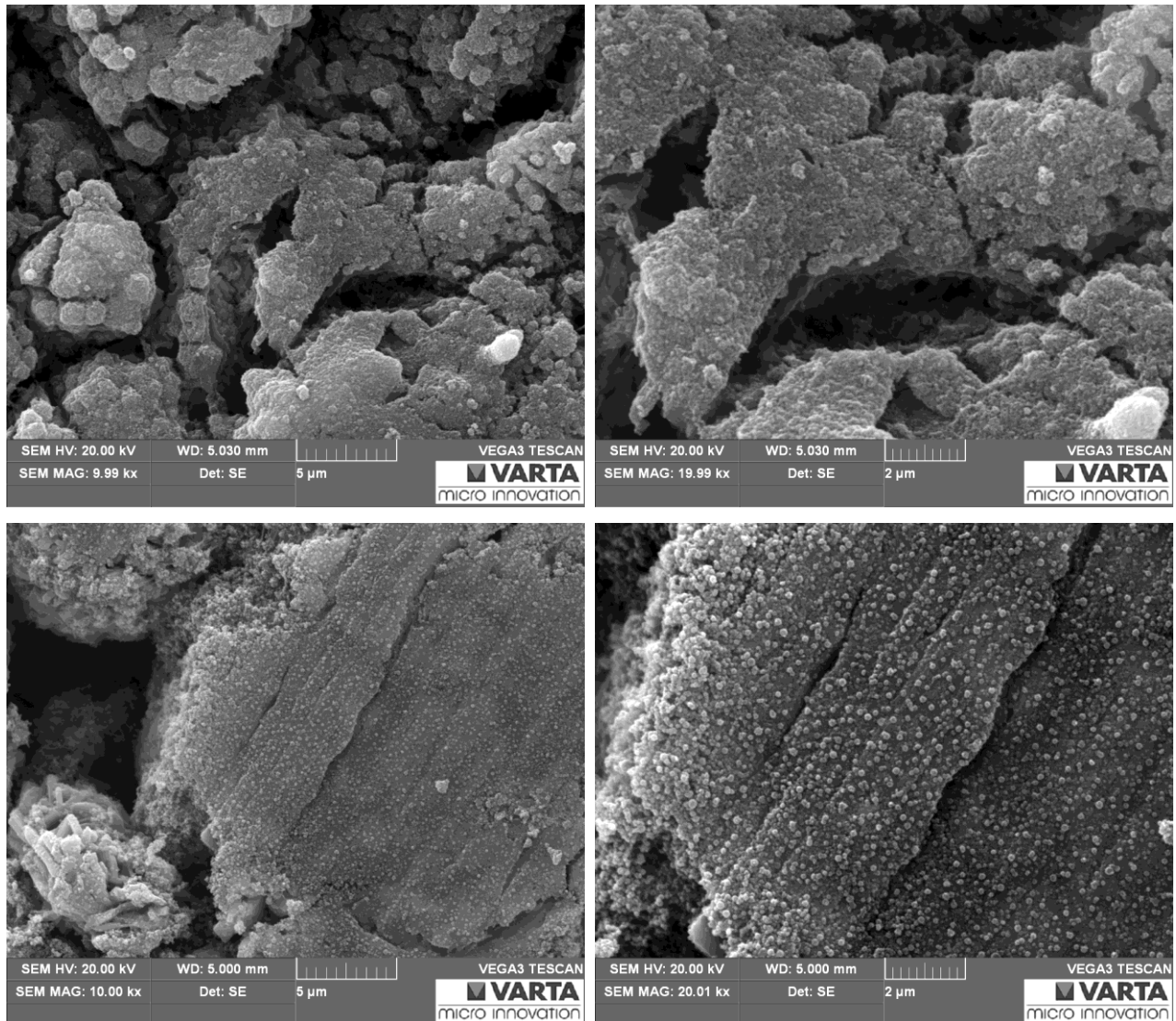


Figure 116: comparison of specific discharge capacity and specific energy performance for every 10<sup>th</sup> cycle during the entire CCC; the loss of capacity amounts to 12.70 % and the loss of specific energy amounts to 13.50 %.

Within the following SEM images cathode surfaces after electrochemical investigations are compared in which acrylo-nitrile with both concentrations were tested (5 v% and 1 v%). The difference between both concentrations concerning the oxidation of the electrolyte and acrylo-nitrile, respectively, delivers different cathode surfaces. In general, the spectroscopic detection shows less electrolyte decomposition products on the cathode surface for the lower concentration.



**Figure 117:** SEM images of the BASF NMO cathode after the CCC in which fumaro-nitrile (top left and top right) or acrylo-nitrile (bottom left and bottom right) was added to EC/DEC (3:7, v:v), 1 M LiPF<sub>6</sub>.

The next group of additives which was tested belongs to chemical compounds containing at least one hetero atom within their structures. Additives containing nitrogen, sulfur and/or oxygen like 2-chloro-4-phenylthiocyanate (CPT) were used for investigations within this doctoral thesis, because Bayer et al. demonstrated an improvement of the SEI formation upon graphite surfaces with these types of additives. Moreover, it was possible to use PC as organic solvent for the electrolyte system in combination with carbonaceous anode materials<sup>(235)</sup>. The same promising electrochemical results were observed with benzene-sulfonicacid-2-propinylester ( $S_1$ ) and dimethyl-trifluoroacetamide (DMA)<sup>(236)</sup>. Another compound 2-methyl-2-oxazoline (MO) was investigated due to the fact of its cationic polymerization ability<sup>(237)</sup>. Hence, the question comes up, if such polymeric film can be lithium-ion permeable and additionally, if it is able to prevent dissolution of the bivalent manganese ion at the same time.

In addition, sulfur based compounds such as ethylene-sulfite (ES) and 1,3,2-dioxathiolane-2,2-dioxide (DOD) belong to reductive type additives and facilitate SEI formation on anodes through the affinity of molecular moieties of their reduced products to the catalytic active graphite sites (adsorption). Furthermore, these compounds and ES respectively allow the usage of cathode materials above 4 V vs.  $\text{Li/Li}^+$  due a high oxidative potential and/or formation of a protective cathode/electrolyte interface<sup>(233), (238), (239)</sup>.

Thinking of anode materials with high capacity, like silicon, already patented additives which affect the film formation on the silicon surface positively. The functional group of such compounds is isocyanate, e.g. phenyl-isocyanate (PI) and 4-fluorophenyl-isocyanate (FPI)<sup>(240)</sup>.

On that account all these additives were investigated with the same electrochemical tools as before. Compared with all additives of this group DMA, DOD, but especially ES exhibited the best electrochemical performance. By contrast, CPT,  $S_1$ , MO, PI and FPI did not show any reversible redox reactions.

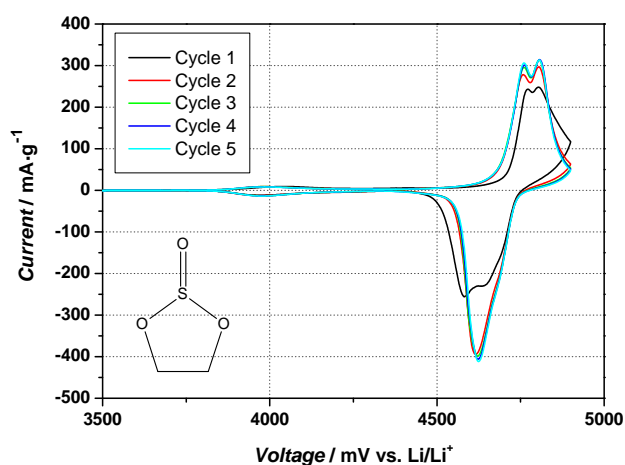


**Figure 118:** cyclic voltammogram (CV) of the BASF NMO cathode with the electrolyte system EC/DEC (3:7, v:v) + 1 v% ES, 1M  $\text{LiPF}_6$ , cycled between 3.5 V and 4.9 V vs.  $\text{Li/Li}^+$  against metallic lithium; the scan rate was appointed to  $0.1 \text{ mV}\cdot\text{s}^{-1}$ .

**Table 19:** obtained data from cyclic voltammetry analysis of the BASF NMO electrode between 3.5 V and 4.9 V vs.  $\text{Li/Li}^+$ .

Electrolyte	Cycle	Charge capacity [ $\text{mAh}\cdot\text{g}^{-1}$ ]	Discharge capacity [ $\text{mAh}\cdot\text{g}^{-1}$ ]	Efficiency [%]
EC/DEC 3:7 (v:v) + 5 v% ES, 1M $\text{LiPF}_6$	1.	128.55	121.16	94.25
	2.	135.41	130.66	96.49
Mass of electrode [mg] 4.305	3.	135.94	131.98	97.09
	4.	135.15	131.45	97.27
	5.	134.09	130.66	97.44

The addition of 5 v% ES affects whether positively or negatively on the cyclic voltammogram behavior of NMO electrodes actually. While Wrodnigg et al. claim a high oxidative stability of ES Zhang supposes instability at high potentials. In fact, the CV shows lower efficiencies originating from bad charge/discharge capacity ratio. These high charge capacities can be attributed to electrolyte decomposition and maybe degradation of ES actually.

After 100 cycles capacity retention of 91.77 % within the CCC could be obtained, whereby the capacities are slightly lower compared to measurements without an additive (125.3 mAh·g<sup>-1</sup> instead of 130.5 mAh·g<sup>-1</sup>).

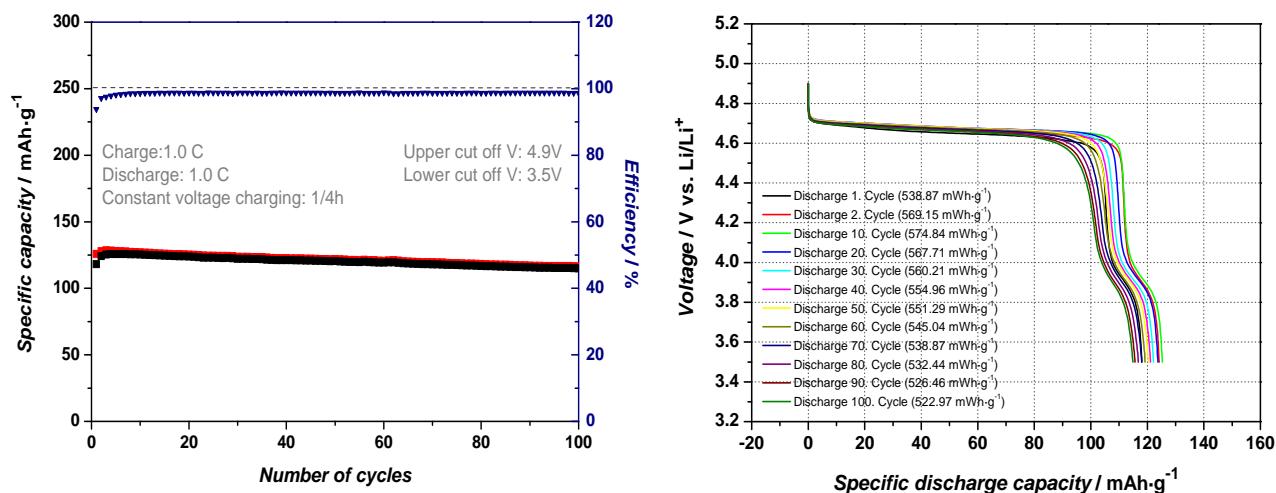


**Figure 119:** left) CCC of the BASF NMO spinel in combination with the electrolyte system EC/DEC (3:7, v:v) + 5 v% ES, 1 M LiPF<sub>6</sub> and metallic lithium as counter electrode; right) selected discharge profiles of the CCC measurement and their specific energies.

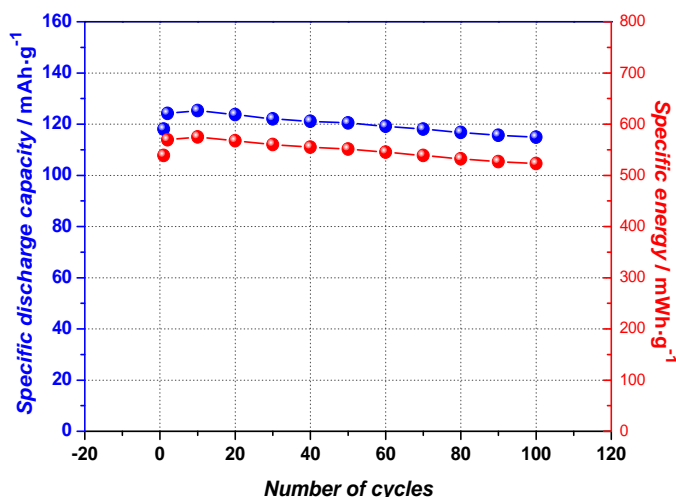


**Figure 120:** comparison of specific discharge capacity and specific energy performance for every 10<sup>th</sup> cycle during the entire CCC; the loss of capacity amounts to 8.23 % and the loss of specific energy amounts to 9.02 %.

SEM images show the difference between NMO cathode surfaces after the constant current cycling in which two additive compounds were used. On the one hand the usage of 2-chloro-4-phenylthiocyanate (CPT) induces a strong decomposition of the electrolyte system, while ethylene-sulfite (ES) merely decomposes to a smaller extent.

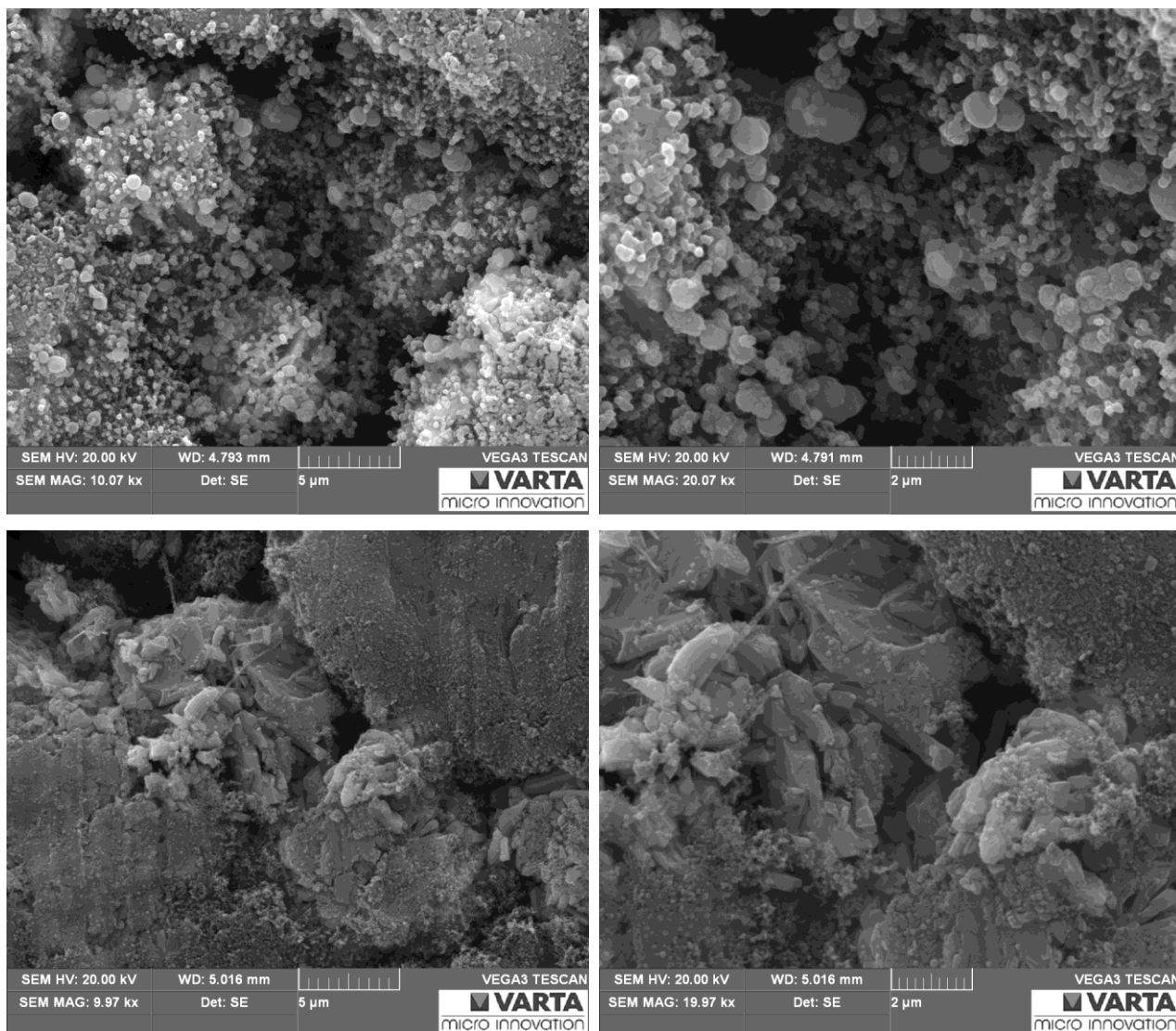


**Figure 121:** SEM images of the BASF NMO cathode after the CCC in which 2-chloro-4-phenylthiocyanate (top left and top right) or ethylene-sulfite (bottom left and bottom right) was added to EC/DEC (3:7, v:v), 1 M LiPF<sub>6</sub>.

By comparing all electrochemical results of the measurements in which additives were adjusted to a base electrolyte a general trend can be observed. It is already proven that additive compounds consisting of carbonates ( $-\text{CO}_3$ ) like VC, FEC,  $\text{F}_2\text{EC}$  improve the SEI formation on the graphite surface. On the other hand the compound VC cannot be used in combination with high voltage cathodes ( $> 4.4 \text{ V vs. Li/Li}^+$ ) due to a very strong polymerization of this additive. In fact the polymer film exhibits no  $\text{Li}^+$ -ion permeability and causes the damage of the battery at least. According to literature this polymerization can be attributed to the C-C double bond. Therefore, additives containing such unsaturated carbons induce at least polymerization below  $4.9 \text{ V vs. Li/Li}^+$  (the decomposition products could be observed within SEM images very well!). Although the fluorine atom can be eliminated from FEC resulting in the formation of HF and VC, the formation of them might take place only in a low extent, because in direct contradiction to pure VC sufficient electrochemical results could be obtained. Furthermore measurements in which FEC was adjusted to the electrolyte system demonstrated no or minor electrolyte degradation.

Additionally, nitriles (functional group  $-\text{CN}$ ) were used, which differ in terms of the carbon chain length, number of cyano-groups and presence/absence of a C-C double bond. However, the same trend is valid that compounds having a C-C double bond (AN, FN) form a lithium ion impermeable polymer film on the cathode surface beneath  $4.9 \text{ V vs. Li/Li}^+$ . Interestingly, a reduction of the additive concentration from  $5 \text{ v/w\%}$  to  $1 \text{ v/w\%}$  led to a sufficient electrode performance, which is merely valid for AN. FN in turn seals the cathode surface even at low concentrations, which might be attributed to the second cyano group. Basically, by comparison of all remaining nitriles (BN, VN, SN and ADN) no remarkable difference is evident concerning electrode performance and received capacities respectively.

In general, battery cycling can be carried through if sulfur compounds like ES or DOD are used as additives. The obtained results resemble those of fluorinated carbonates (FEC,  $\text{F}_2\text{EC}$ ). Apparently there is no difference between the inserted atom group (sulfur or carbon) within these cyclic compounds, because electrochemistry as well as SEM images could not observe any remarkable difference compared to investigations with base electrolyte systems. However, if sulfur compounds like CPT or  $\text{S}_1$  are used electrolyte degradation takes place leading to an insufficient electrochemical behavior. Degradation products can be observed easily upon cathode surface by the use of SEM.

According to literature reductive polymerization of oxazolines is a well known procedure. The claimed oxidative polymerization could be confirmed within electrochemical and microscopic investigations. Anyway, the formed film on cathode surface is not permeable for  $\text{Li}^+$ -ions. Isocyanates and especially fluorinated cyanate compounds cause positive film forming properties at the side of anodes (graphite and in particular silicon), but causes whether cycle capability or protection of the cathode surface from electrolyte dissolution. Both tested cyanate additives formed oxidative a  $\text{Li}^+$ -ion impervious layer.

On account of the huge number of examined additives the main results of each measurement are summarized again in tabular form (see next page!).

**Table 20:** summary of all investigated additive compounds: the shown capacities refer to the particular 10<sup>th</sup> cycle; the loss refers to capacity loss from the 10<sup>th</sup> cycle until the 100<sup>th</sup> cycle of the constant current cycling (CCC); within improvements compare capacities with those of the CCC with EC/DEC (3:7, v:v), 1 M LiPF<sub>6</sub> (NMO batch B, 130.5 mAh·g<sup>-1</sup>, loss 7.60 %, cf. Figure 102, page 92).

EC/DEC (3:7, v:v), 1 M LiPF <sub>6</sub> +	Abbr.	Structure	Purity	Amount	Discharge capacity		Improvement
					mAh·g <sup>-1</sup>	loss	yes / no / similar
Vinylene-carbonate	VC		97 %	2 v%	-	-	no
Fluoroethylene-carbonate	FEC		-	2 v%	126.56	9.76 %	similar
Difluoroethylene-carbonate	F <sub>2</sub> EC		-	0.5 v%	129.66	10.3 %	similar
2-Chloro-4-phenyl thiocyanate	CPT		97 %	5 w%	-	-	no
				2 w%	-	-	
Benzene-sulfonic-acid-2-propinylester	S <sub>1</sub>		96 %	2 w%	-	-	no
Dimethyl-trifluoro-acetamide	DMA		> 99 %	5 v%	111.13	7.35 %	similar
Acrylo-nitrile	AN		≥ 99.5 %	5 v%	-	-	no
				1 v%	126.14	12.7 %	similar
Butyro-nitrile	BN		≥ 99.0 %	5 v%	124.85	10.8 %	similar
Valero-nitrile	VN		99.5 %	5 v%	130.27	13.3 %	similar
Fumaro-nitrile	FN		≥ 98.0 %	5 w%	-	-	no
				1 w%	-	-	
Succino-nitrile	SN		99 %	5 w%	124.95	13.9 %	similar
Adipo-nitrile	ADN		99 %	5 v%	122.24	17.4 %	similar
Ethylene-sulfite	ES		98 %	5 v%	125.25	8.23 %	similar
1,3,2-Dioxathiolan-2,2-dioxide	DOD		98 %	5 w%	128.14	12.7 %	similar
2-Methyl-2-oxazoline	MO		98 %	5 w%	-	-	no
Phenyl-isocyanate	PI		≥ 98 %	1 v%	-	-	no
4-Fluorophenyl-isocyanate	FPI		99 %	1 v%	-	-	no

### 3.3.4.5.2 Few Aspects on High Oxidative Stable Electrolyte Systems

As already shown in the chapters before, carbonate based cannot sustain high voltages of 5 V cathode materials working and trigger safety issues as a consequence. The permanent search of high oxidative electrolyte systems for the usage above 5 V vs. Li/Li<sup>+</sup> led to countless variations of electrolytes and solvents respectively. For instance, sulfone based electrolytes provide a wide electrochemical stability window up to 5 – 5.9 V vs. Li/Li<sup>+</sup> indeed, but cause instability problems in combination with graphite due to an insufficient SEI formation. Besides, synthetic sulfones exhibit high melting points hampering their breakthrough for Lithium-Ion-Batteries. On that account mixtures of different solvents were investigated consisting of sulfone and ester solvents for instance. Investigations with full cells containing LTO/NMO in combination with sulfone based electrolytes demonstrated a good cycle behavior over 1000 cycles. However, poor cycleabilities of half or full cells containing lithium metal or graphite as anode and high voltage cathodes were the result so far as well <sup>(241), (242), (243)</sup>.

According to Abu-Lebdeh et al. another oxidative stable electrolyte system consists of nitrile solvents. They used dinitriles like glutaro-nitrile (GN,  $n_{\text{carbon}} = 3$ , two -CN) and adipo-nitrile (ADN,  $n_{\text{carbon}} = 4$ , two -CN) due to their high anodic stability up to 8.3 V vs. Li/Li<sup>+</sup>. The high stability of these compounds is attributed to the unique molecular structure of the cyano-group including a very strong triple bonding between carbon and nitrogen. In addition, three and four electron donating methylene groups, respectively, stabilize the entire structure of these nitrile compounds. Furthermore both exhibit a high boiling- and flash point combined with high dielectric constants and low viscosities. However, the high melting point of ADN (5°C) limits the utilizable temperature range and induces the necessity of a co-solvent. Basically, ADN and all other aliphatic nitriles are not able to form a sufficient SEI on graphite surface in a similar way as sulfone based solvents. On that account Abu-Lebdeh et al. chose EC due to the high dielectric constant and good SEI forming properties leading to an excellent cycle capability. Due to the bad solubility of LiPF<sub>6</sub> in ADN they used as conductive salt 1 M lithium-bis-(trifluoro-methanesulfonyl)-imide (LiTFSI) and could achieve an anodic stability of 6.2 V vs. Li/Li<sup>+</sup>, which is merely assigned to the oxidation of the imide anion, while the nitrile compound remains stable <sup>(243), (244)</sup>.

Anyway, these stability tests were carried through against an inert electrode (platinum) and on the other hand they did not show any cycling behavior of this electrolyte system in their publication. In fact Aluminum is thermodynamically unstable and gets oxidized at a potential of 1.39 V vs. Li/Li<sup>+</sup>. The high cathode working potentials induce Al oxidation/corrosion would not be a formation of a native passivation layer consisting of less soluble products such as AlF<sub>3</sub>, Al<sub>2</sub>(CO<sub>3</sub>)<sub>3</sub> or Al<sub>2</sub>O<sub>3</sub>, which derives from electrolyte and conductive salts, respectively, like LiClO<sub>4</sub> and fluorinated salts such as LiPF<sub>6</sub>, LiAsF<sub>6</sub>, and LiBF<sub>4</sub>. In contrast, imide salts cause no passivation and thus, a severe corrosion on the Al current collector surface reflected in shorted calendar life and strong capacity fading of the battery <sup>(38), (245)</sup>.

For that reason a film forming and especially Al corrosion inhibiting salt was added to a base electrolyte system. For instance lithium-bis (oxalate) borate (LiBOB) forms a stable functioning SEI by reduction below 1.5 V vs. Li/Li<sup>+</sup> <sup>(38), (246)</sup>. Based on investigations of Abu-Lebdeh an electrolyte system was established consisting of EC/ADN (1:1, v:v), 1 M LiTFSI + 0.1 M LiBOB. They claimed that the high anodic stability of ADN would improve the cycleability of high voltage cathodes significantly. On those accounts electrochemical investigations of this electrolyte system at LiNi<sub>0.5</sub>Mn<sub>1.5</sub>O<sub>4</sub> constituted the logical consequence.

For the preparation of the electrolyte system containing those conductive salts, LiBOB (from Chemetall) and LiTFSI (from Solvionic) were dried under vacuum at 100°C for 72 hours at first. EC and ADN were dried with a molecular sieve from Roth (4 Å) up to water content below 20 ppm (proof by use of Karl-Fischer).

Cyclic voltammetry of the BASF NMO spinel and EC/ADN (1:1, v:v), 1 M LiTFSI was carried out to proof the claimed Al-corrosion (cf. Figure 122, page 109). The result is a very soon oxidation after 3.7 V vs. Li/Li<sup>+</sup> with

a charge capacity of  $277.08 \text{ mAh}\cdot\text{g}^{-1}$  and discharge of  $1.83 \text{ mAh}\cdot\text{g}^{-1}$ . After the first two cycles all subsequent cycles showed either oxidation or reduction peaks. Hence, Al-corrosion must have taken place.

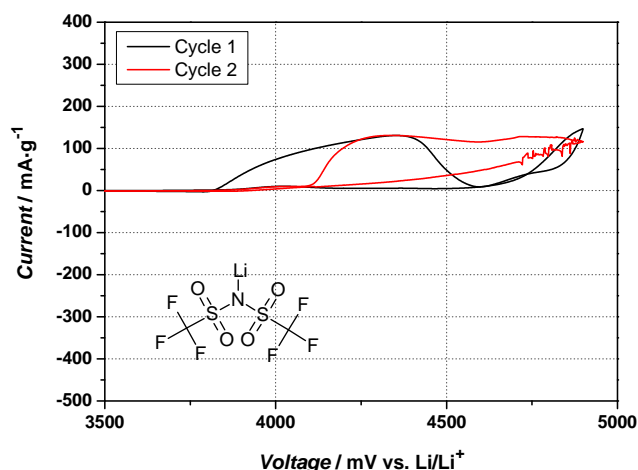


**Figure 122:** Al current collector corrosion during a cyclic voltammogram of a BASF NMO electrode in combination with EC/ADN (1:1, v:v), 1 M LiTFSI cycled between 3.5 V and 4.9 V vs.  $\text{Li}/\text{Li}^+$  against metallic lithium as counter electrode, the scan rate is appointed to  $0.1 \text{ mV}\cdot\text{s}^{-1}$ .

In the following measurements with the supposed oxidative stable electrolyte system EC/ADN (1:1, v:v), 1 M LiTFSI + 0.1 M LiBOB are constituted.

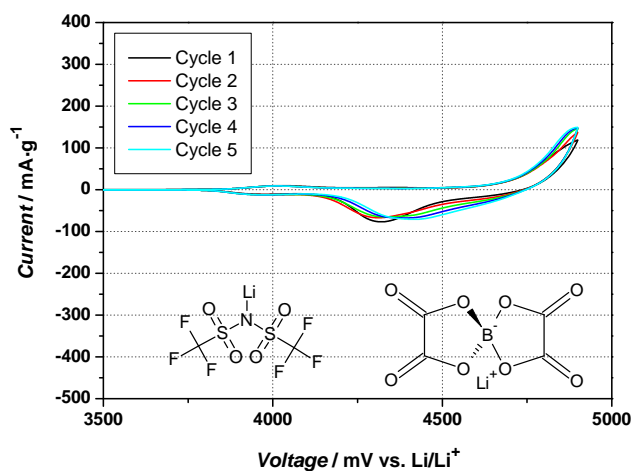


**Figure 123:** cyclic voltammogram (CV) of the BASF NMO cathode with the electrolyte system EC/ADN (1:1, v:v), 1 M LiTFSI + 0.1 M LiBOB cycled between 3.5 V and 4.9 V vs.  $\text{Li}/\text{Li}^+$  against lithium metal as counter electrode, the scan rate is appointed to  $0.1 \text{ mV}\cdot\text{s}^{-1}$ .

**Table 21:** data from cyclic voltammetry analysis of the BASF NMO electrode between 3.5 V and 4.9 V vs.  $\text{Li}/\text{Li}^+$ .

Electrolyte	Cycle	Charge capacity [ $\text{mAh}\cdot\text{g}^{-1}$ ]	Discharge capacity [ $\text{mAh}\cdot\text{g}^{-1}$ ]	Efficiency [%]
EC/ADN 1:1 (v:v), 1M LiTFSI + 0.1M LiBOB	1.	72.67	68.16	93.79
	2.	74.17	72.42	97.64
Mass of electrode [mg] 4.535	3.	77.18	75.67	98.05
	4.	79.43	77.93	98.11
	5.	81.44	80.18	98.46

By contrast to the Al-corrosion measurement very low capacities are obtained during cyclic voltammetry as well as constant current cycling. Furthermore the CCC shows a very strong capacity fading. Nearly at the same time, Lebdeh et al. published the same electrochemical experiments with a better cycling performance indeed, but without any electrochemical improvement by no means<sup>(247)</sup>. Although these electrochemical measurements were repeated and the electrolyte system was prepared once more, merely the same results as before were achieved. Thus, the “good” literature values could not be verified. In contrast, the behavior of the potential shows growing impedance from cycle to cycle. This is detectable through the discharge potential shifting to lower voltages indicated by the dark blue arrow in Figure 124.

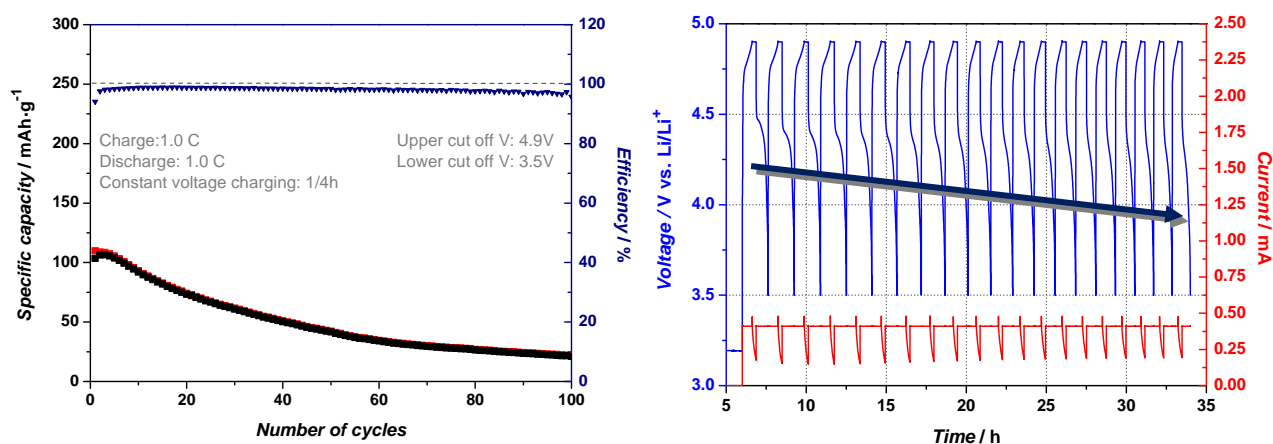


**Figure 124:** left) CCC of the BASF NMO spinel in combination with the electrolyte system EC/ADN (1:1, v:v), 1 M LiTFSI + 0.1 M LiBOB and metallic lithium as counter electrode; right) performance of the voltage profiles within the first 20 cycles of the CCC, the dark blue arrow symbolizes ongoing electrolyte decomposition increasing impedance.

The SEM investigations confirm the assumption of massive electrolyte degradation; furthermore NMO particles are covered with a polymeric film entirely. Unfortunately, no conclusion can be made if the electrolyte dissolution originates from film forming LiBOB or from ADN.

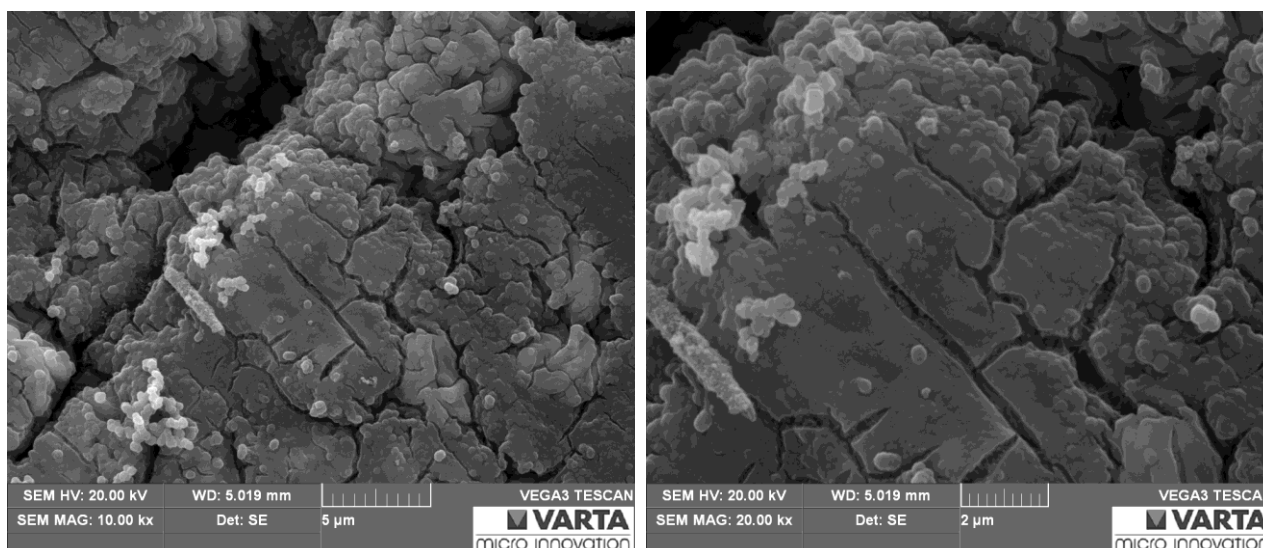


**Figure 125:** SEM images of the BASF NMO cathode after the before shown CCC in which EC/ADN (1:1, v:v), 0.9 M LiTFSI + 0.1 M LiBOB was used, magnifications: left) x10,000, right) x20,000.

On that account LiBOB was substituted by LiPF<sub>6</sub>, which is known as AI passivating agent as well. The resulting electrolyte system is EC/ADN (1:1, v:v), 1 M LiTFSI + 0.1 M LiPF<sub>6</sub>. As a result a strong capacity fading from the beginning is observed and the electrolyte decomposition on cathode surface resembles the before shown one of Figure 125.

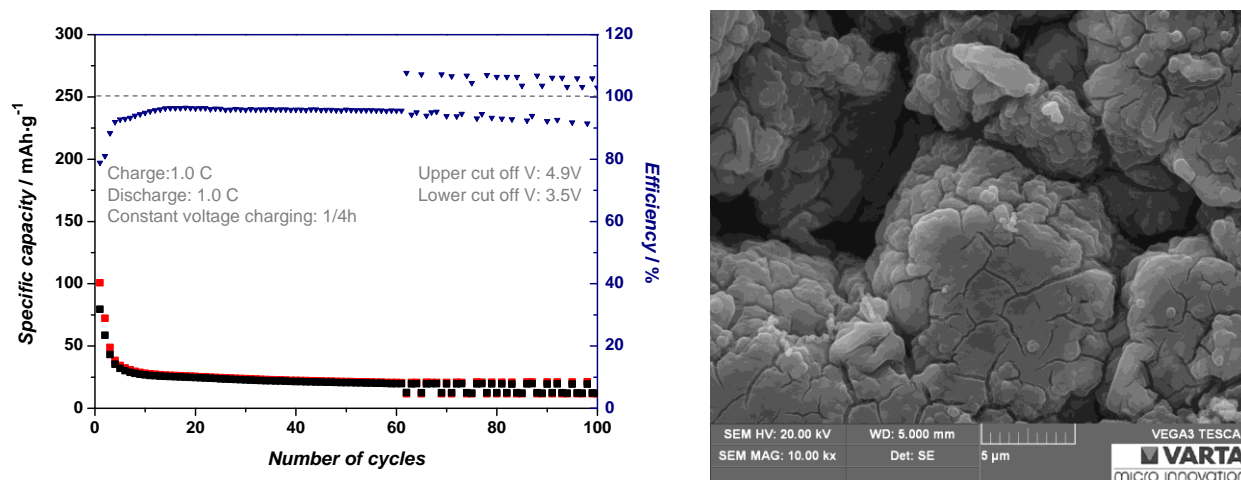


**Figure 126:** left) CCC of the NMO electrode with the LiBOB substituted electrolyte system EC/ADN (1:1, v:v), 1 M LiTFSI + 0.1 M LiPF<sub>6</sub>, right) SEM image of the cycled electrode with a magnification of x10,000.

Based on these results it can be claimed that these electrolyte systems cannot exhibit a sufficient oxidative stability. Nevertheless this raises the question whether LiTFSI or nitrile compounds cause the extreme anodic electrolyte decomposition. Investigations with another nitrile (valero-nitrile, VN,  $n_{\text{carbon}} = 4$ , one -CN) as solvent for an electrolyte but without LiTFSI showed the same poor cycle ability indeed, but a different electrolyte degradation upon the cathode surface.

Other systems exhibiting a high anodic stability are ionic-liquids (ILs), which were tested as well. ILs are oxidative stable up to 6 V vs. Li/Li<sup>+</sup>, but exhibit a too high viscosity as well<sup>(164)</sup>. Hence, due to the very high viscosity and bad wetting properties no single electrochemical characterization could be carried through at standard conditions (room temperature, 1 C or 0.1 mV·s<sup>-1</sup>) and thus, Aurbach's assumptions meaning that ILs are proper for LiNi<sub>0.5</sub>Mn<sub>1.5</sub>O<sub>4</sub> could not be confirmed in this way<sup>(248)</sup>.

**Table 22:** constitution of all electrochemical investigated ionic-liquids.

Electrolyte	Abbr.	Ionic liquid	Structure	CV/CCC possible?
Ionic liquid + 0.5M LiPF <sub>6</sub>	BMIM-PF <sub>6</sub>	1-butyl-3-methylimidazolium-hexafluorophosphate		no
	EMIM-TFSI	1-ethyl-3-methylimidazolium-bis-(trifluoromethylsulfonyl)imide		no
	Pyr <sub>13</sub> TFSI	1-propyl-1-methylpyrrolidinium-bis-(fluorosulfonyl)imide		no
	Pyr <sub>13</sub> TFSI	1-propyl-1-methylpyrrolidinium-bis-(trifluoromethylsulfonyl)imide		no
	Pyr <sub>14</sub> TFSI	1-butyl-1-methylpyrrolidinium-bis-(trifluoromethylsulfonyl)imide		no

### 3.3.4.6 Cell Assembling – Balancing Graphite and the BASF NMO Spinel

Most of before shown electrochemical measurements belong to so called half-cell tests, meaning reference- and counter electrode consist merely of metallic lithium. Within real or industrial battery cells mainly graphite or LTO are applied as anodes. Therefore, capacities of the lithium donating cathode and lithium accepting anode have to be balanced. If the negative electrode is undersized or equal balanced to the positive electrode, too much lithium can be provided, which causes lithium plating at the anode surface and engenders in further consequence safety issues. By contrast, too much oversized anodes consume the entire lithium reflecting in high irreversible capacities and finally to bad cycling behavior. For instance, the very first attempts to combine graphite and NMO failed because of an insufficient balancing of these electrodes. In this case the anode was too oversized inducing a shift of its potential beyond 3 V vs. Li/Li<sup>+</sup> during discharge and led to corrosion of the copper current collector in the end. This chapter deals with endeavors to form a full cell consisting of a common graphite anode and the BASF LiNi<sub>0.5</sub>Mn<sub>1.5</sub>O<sub>4</sub> spinel.

For all following electrochemical tests an approximately 10 % oversized graphite anode and a NMO cathode were used resulting in a full cell with a nominal capacity around 1 mAh. Applied to a standard Swagelok<sup>®</sup>-cell both electrodes were separated by six layers of the Freudenberg 2126 separator saturated with 80  $\mu$ l of a common used electrolyte system EC/DEC (3:7, v:v), 1 M LiPF<sub>6</sub>. The applied charging program remained unchanged compared with all before shown measurements.

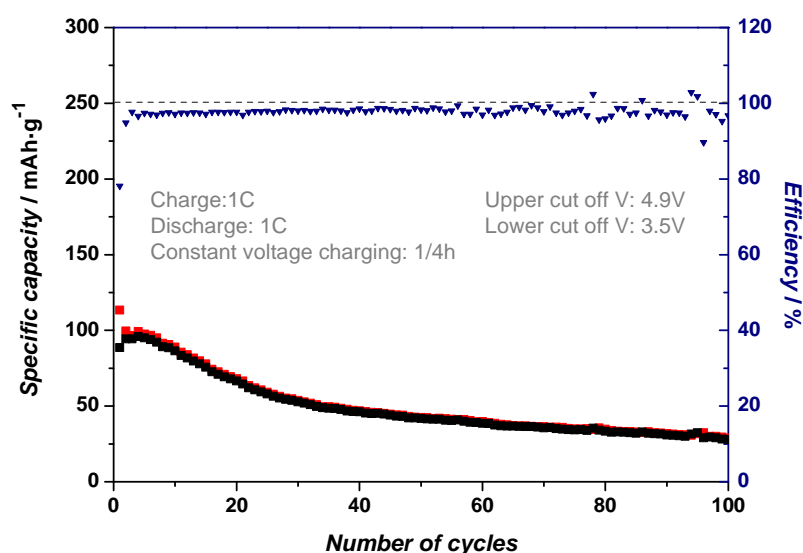


**Figure 127:** performance of a full cell containing graphite and the BASF NMO spinel in combination with the electrolyte system EC/DEC (3:7, v:v), 1 M LiPF<sub>6</sub>; the demonstrated specific capacities are referred to the amount of the active mass of the NMO cathode.

The constant current cycling shows clearly a continuous capacity fading within 100 cycles. Furthermore, the obtained capacities are referred to the active mass of the cathode and thus, should reach the theoretical capacity of NMO (around 140 mAh·g<sup>-1</sup>) within the first cycles of the CCC at least, which could not be observed. The reason for this insufficient cycling behavior gets apparent by examining the anode and cathode potential performances. On that account the anode potential obviously shifts to more negative potentials and finally below 0 V vs. Li/Li<sup>+</sup> during the charging step, which can induce lithium plating. On the one hand this problem can be attributed to a not adequate capacity of the anode. On the other hand kinetic inhibition could be the reason for that. However, in this case the graphite anode exhibits a too slow Li<sup>+</sup>-ion intercalation kinetic out of two points: on the one hand lithium plating requires a nucleation at first taking place at about -0.08 V vs. Li/Li<sup>+</sup>, which could not be observed within the first 30 cycles. On the other

hand the anode potential relaxes to slight higher potentials during constant voltage charging indicating a “too” slow lithium ion uptake.

Furthermore another difference, which takes effect in comparison to half-cell experiments, is the fact that industrial manufactured batteries do not have the possibility of implemented reference electrodes. Therefore, charging and discharging steps of the full cell are not monitored via the potential of the cathode or anode, but rather the charging and discharging cut-off criterions are determined by the cell potential. For simulation of this monitoring procedure all full cell tests were proceeded via the cell potential, whereby the single anode and cathode potential were monitored by auxiliary channels. In addition, the charging step was finished as soon as the cell potential reached 4.9 V and skipped to the constant voltage charging for 15 minutes followed by the subsequent discharge process to a final cell voltage of 3.8 V vs. Li/Li<sup>+</sup>. In any case the cell potential is the difference between cathode potential and anode potential. As a result, the cut-off criterions shifted, meaning the positive electrode gets lithiated merely until 4.45 V instead of 3.5 V (half cell criterion) during the discharge step actually. By contrast, the negative electrode achieves 0.65 V in the first discharge step, which indicates a kinetically inhibited negative electrode and loss of mobile lithium at the same time (marked in Figure 128). Within the ongoing CCC the anode is forced to compensate this lithium loss by shifting to even higher potentials. As a consequence a bad cycling behavior is detectable.

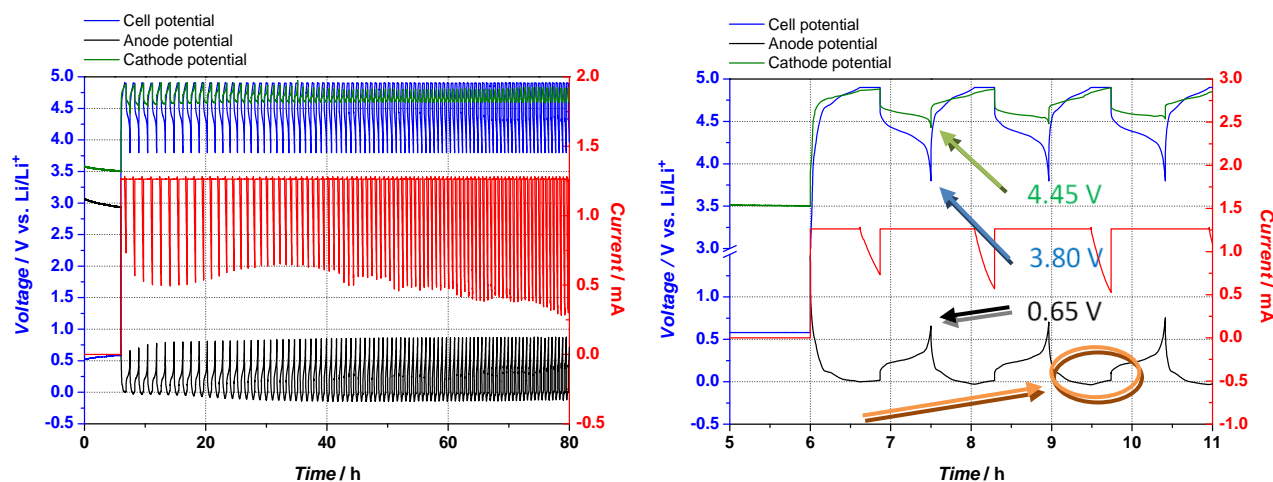


**Figure 128:** left) performance of the anode potential (black line), cathode potential (green line) and of the entire cell potential (blue line) during 100 cycles of the constant current cycling (cf. Figure 127, page 112); additionally, the progress of the current is constituted as red line; right) enlargement of all potentials for the first three cycles (the ellipse denotes the relaxation of the anode potential).

Another problem states the use of a high current rate (1 C) to charge and discharge this full cell. Especially during the first cycles this high current rate causes that the anode is only a short period of time within the potential window of the SEI formation (around 0.9 – 1.0 V) resulting in an insufficient solid electrolyte interphase formation. On that account the charging program of the following measurements was modified –the charge current rate was adjusted to 0.5 C instead of 1 C, whereby the discharge current rate remained unchanged (the measurement is depicted on next page!).

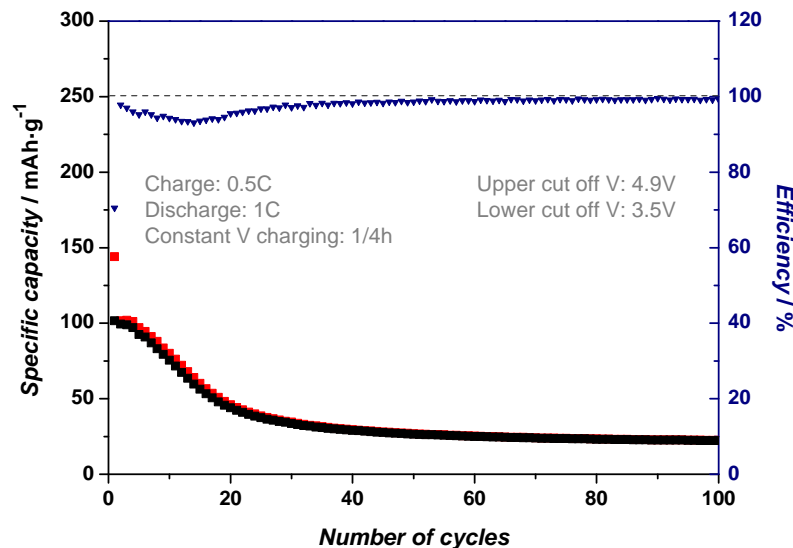


**Figure 129:** performance of a slowly charged full cell containing graphite and the BASF NMO spinel in combination with the electrolyte system EC/DEC (3:7, v:v), 1 M LiPF<sub>6</sub>; the demonstrated specific capacities are referred to the amount of the active mass of the NMO cathode.

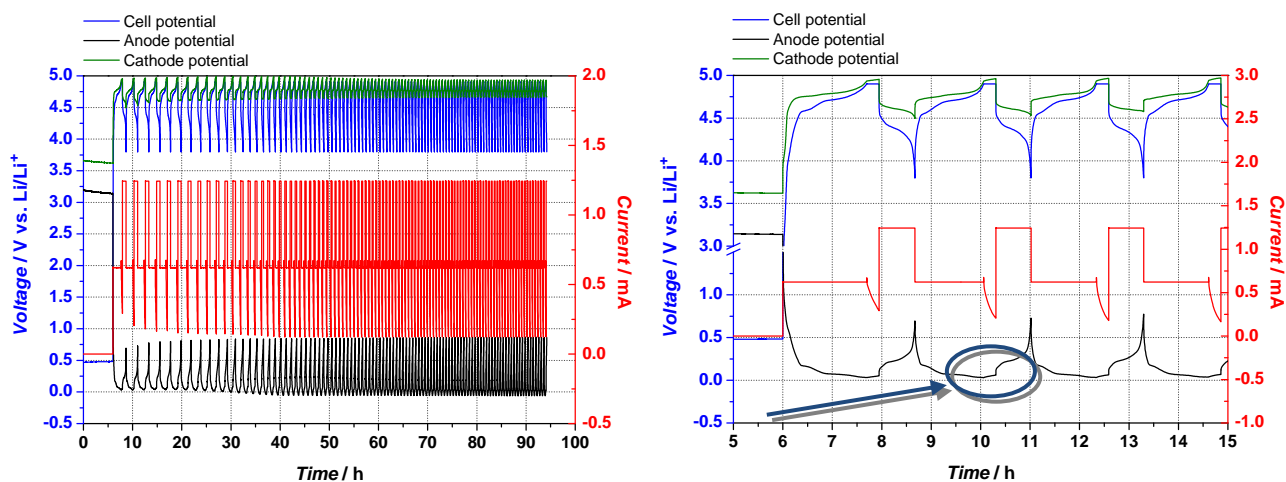


**Figure 130:** left) performance of the anode potential (black line), cathode potential (green line) and of the entire cell potential (blue line) during 100 cycles of the constant current cycling (cf. Figure 129, page 114); additionally, the progress of the current is constituted as red line; right) enlargement of all potentials for the first three cycles (the ellipse denotes the relaxation of the anode potential).

The constant current cycling measurement (Figure 129 and Figure 130) actually does not show an improvement concerning electrode performance. During the constant voltage charging step the relaxation of the anode potential is observable again. However, about over ten cycles the anode potential does not shift into the negative potential range. Because of that a special formation program was used for the additional CCC investigations. Beyond that six layers of the Freudenberg 2126 separator were substituted by merely one layer of Separion<sup>®</sup> from Evonik (formerly known as Degussa) to minimize the cell resistance.

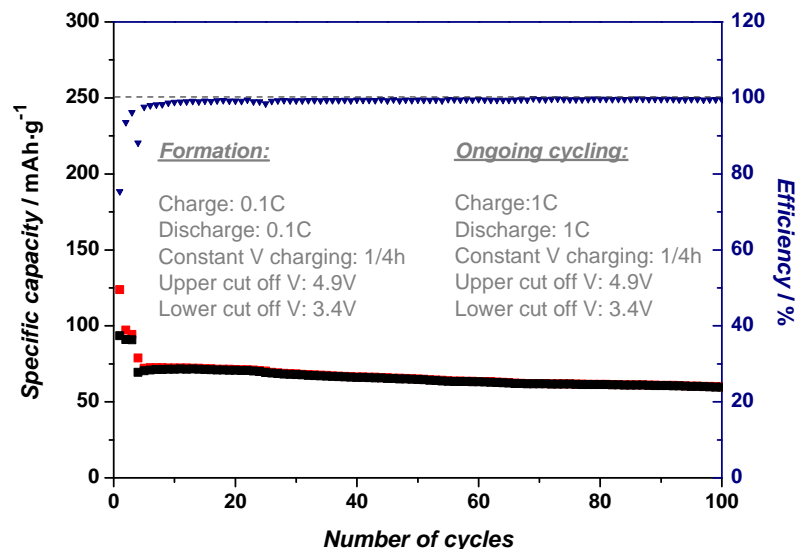


**Figure 131:** performance of the full cell graphite/NMO with a formation process within the first three cycles; as electrolyte system EC/DEC (3:7, v:v), 1 M LiPF<sub>6</sub> in combination with a Separion® separator instead of the before used Freudenberg 2126 separator is used; the demonstrated specific capacities are referred to the amount of the active mass of the NMO cathode.

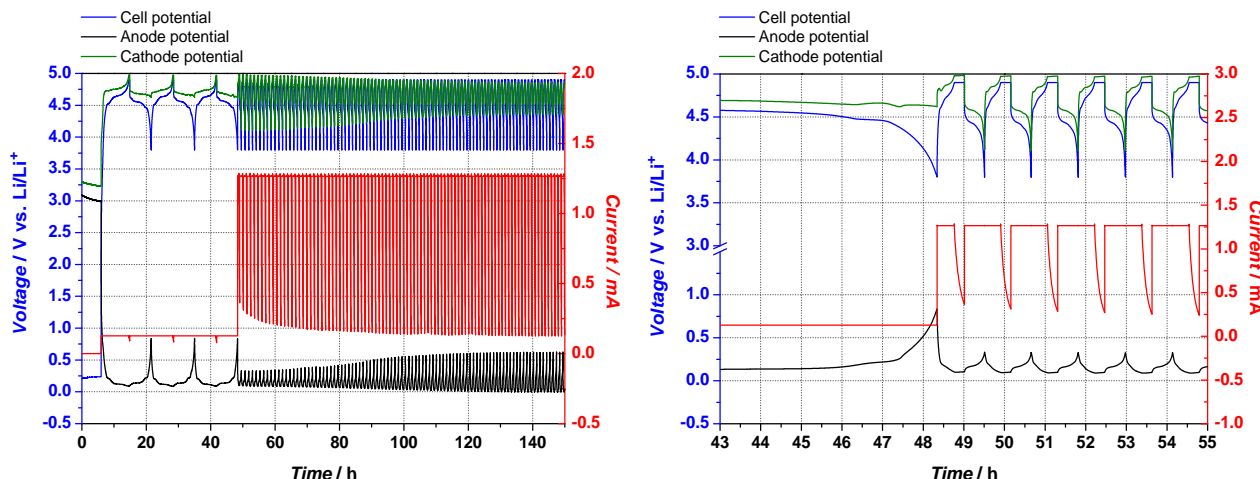


**Figure 132:** left) performance of the anode potential (black line), cathode potential (green line) and of the entire cell potential (blue line) during 100 cycles of the constant current cycling (cf. Figure 131, page 115); additionally, the progress of the current is constituted as red line; right) enlargement of all potentials after the three formation cycles.

Figure 131 and Figure 132 illustrate a constant current cycling measurement of a graphite/NMO full cell, cycled with the above mentioned formation process and only one layer of Separion® separator. This combination delivers the best full cell constant current cycling measurement up to now. Merely after about 50<sup>th</sup> cycle the anode shifts into the negative potential range, but the potential of lithium plating was not reached and the before observed potential relaxation was not detected. Anyway, an improvement in terms of capacity is still favorable, whereby an increase of the cathode capacity from 70 mAh·g<sup>-1</sup> up to 100 mAh·g<sup>-1</sup> is aimed. For that reason the cut off voltage of the full cell is lowered to 3.4 V from initially 3.8 V vs. Li/Li<sup>+</sup> to reach the desired discharge capacities.

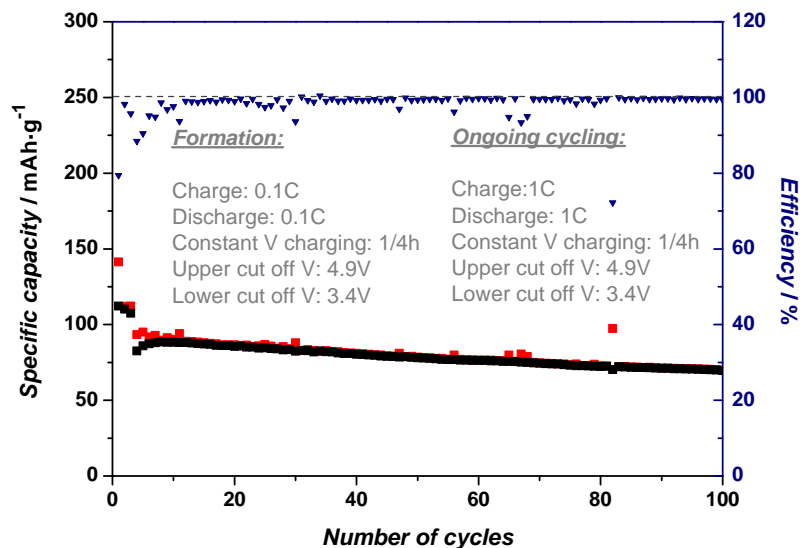


**Figure 133:** performance of the full cell graphite/NMO with a formation process within the first three cycles; as electrolyte system EC/DEC (3:7, v:v), 1 M LiPF<sub>6</sub> in combination with a Separion® separator is used; the demonstrated specific capacities are referred to the amount of the active mass of the NMO cathode.

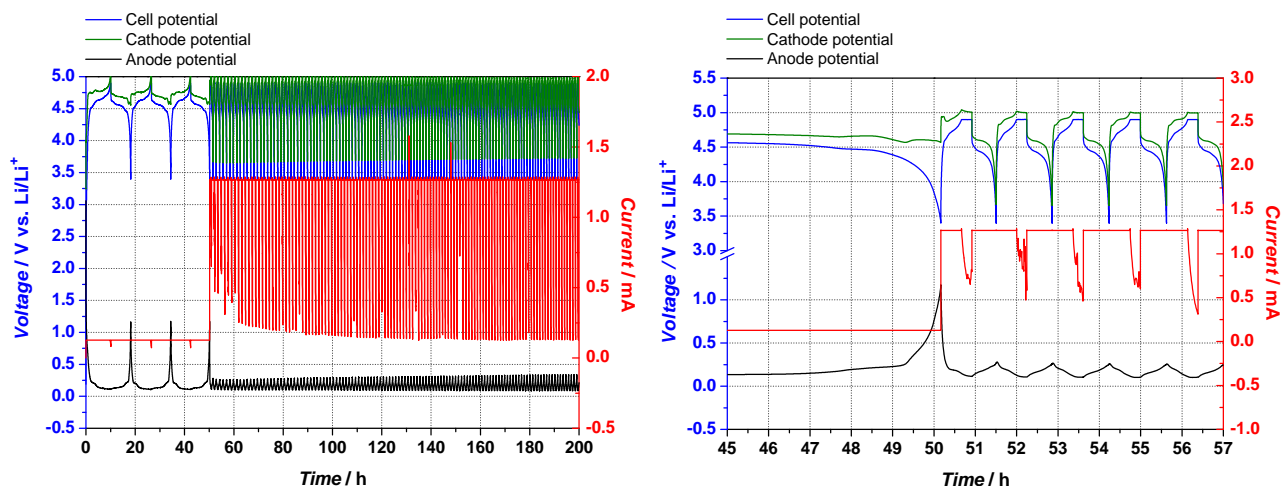


**Figure 134:** left) performance of the anode potential (black line), cathode potential (green line) and of the entire cell potential (blue line) during the 100 cycles of the constant current cycling (cf. Figure 133, page 116); additionally, the progress of the current is constituted as red line; right) enlargement of all potentials after the three formation cycles.

The measurement shown in Figure 133 and Figure 134 is comparable with the previous constant current cycling measurement (cf. Figure 131). The lower cut off voltage leads to an increase of the capacities indeed, but the desired values cannot be reached.

Furthermore, the calculated theoretical specific energy for the full cell system graphite/NMO is 460 mWh·g<sup>-1</sup> with no incorporated lithium loss at all (cf. chapter 3.1.2, page 48). If an initial irreversible lithium loss of 10 – 15 % is assumed, a theoretical specific capacity of about 120 mAh·g<sup>-1</sup> could be reached only. Table 23 shows the specific energies generated from the constant current cycling measurement (Figure 133 and Figure 134). The three formation cycles deliver specific capacities of about 113 mAh·g<sup>-1</sup> and the subsequently cycles about 90 mAh·g<sup>-1</sup>. To get further improvements in the specific capacity of these full cells the electrode balancing as well as the electrode kinetics needs to be improved.

**Table 23:** calculated average discharge voltages and the corresponding specific energies of the full cell graphite/NMO (cf. Figure 133, page 116)

Cycle	Average discharge voltage [V]	Specific energy [mWh·g <sup>-1</sup> ]
1	4.486	341.73
2	4.486	335.33
3	4.480	326.71
4	4.326	242.39
5	4.327	252.51
6	4.331	256.68
7	4.334	258.91
8	4.335	260.04
9	4.336	259.97
10	4.335	259.59
20	4.324	251.27
30	4.313	241.37
40	4.299	234.65
50	4.289	227.12
60	4.277	221.60
70	4.268	215.50
80	4.261	209.20
90	4.252	205.18
100	4.245	200.48

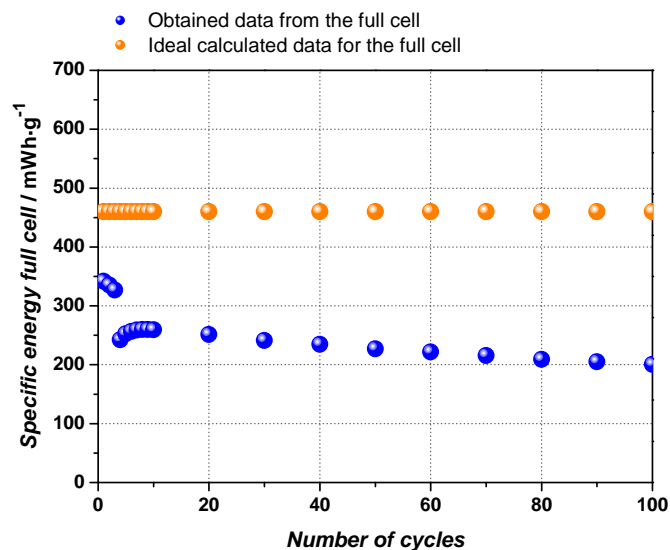


**Figure 135:** comparison of obtained specific energies (cf. Figure 133, page 116) and idealized data from a graphite/NMO full cell; the average discharge voltages of the first ten cycles and the subsequent 10<sup>th</sup> cycle are depicted (blue line); the orange colored line corresponds to ideal calculated specific energies (without any lithium loss) which such a full cell could provide.

In the following additional cyclovoltammetric half-cell measurements of the both electrodes (NMO and graphite) were performed (see next page!).

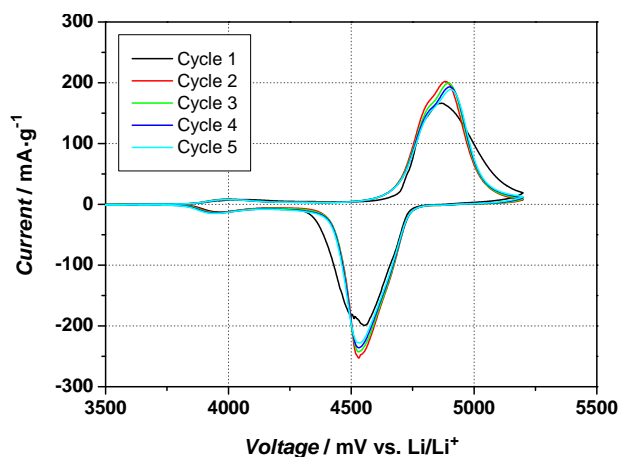


**Figure 136:** cyclic voltammetry of the BASF NMO electrode in combination with the electrolyte system EC/DEC (3:7, v:v), 1M LiPF<sub>6</sub> within the voltage area 3.5 V and 5.2 V vs. Li/Li<sup>+</sup>; the scan rate is 0.1 mV·s<sup>-1</sup>.

**Table 24:** obtained data from cyclic voltammetry of the BASF NMO cathode (cf. Figure 136).

Electrolyte	Cycle	Charge capacity [mAh·g <sup>-1</sup> ]	Discharge capacity [mAh·g <sup>-1</sup> ]	Efficiency [%]
EC/DEC 3:7 (v:v), 1M LiPF <sub>6</sub>	1.	148.53	141.46	95.25
	2.	146.73	141.69	96.56
Mass of electrode [mg] 10.1375	3.	145.84	141.35	96.93
	4.	145.05	141.02	97.22
	5.	144.60	140.57	97.21

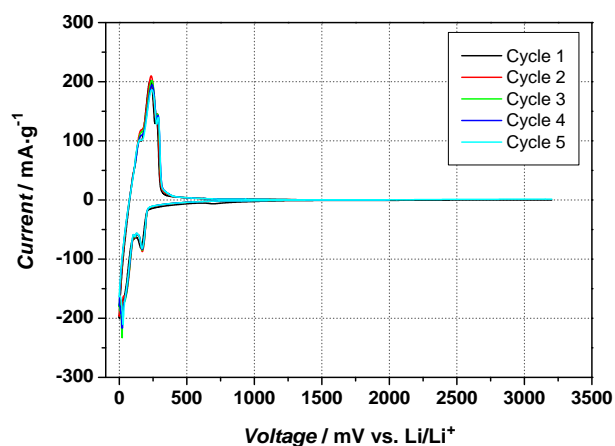


**Figure 137:** cyclic voltammetry of the graphite electrode in combination with the electrolyte system EC/DEC (3:7, v:v), 1M LiPF<sub>6</sub> within the voltage area 3.5 V and 0.0 V vs. Li/Li<sup>+</sup>; the scan rate is 0.03 mV·s<sup>-1</sup>.

**Table 25:** obtained data from cyclic voltammetry (cf. Figure 137).

Electrolyte	Cycle	Charge capacity [mAh·g <sup>-1</sup> ]	Discharge capacity [mAh·g <sup>-1</sup> ]	Efficiency [%]
EC/DEC 3:7 (v:v), 1M LiPF <sub>6</sub>	1.	144.84	122.73	84.73
	2.	135.56	131.91	97.31
Mass of electrode [mg] 5.178	3.	134.12	131.80	98.27
	4.	131.35	129.70	98.74
	5.	127.26	131.35	103.21

The positive NMO electrode nearly delivers the theoretical specific capacity of  $140 \text{ mAh}\cdot\text{g}^{-1}$  indeed, but the negative graphite electrode does not reach the theoretical specific capacity of  $372 \text{ mAh}\cdot\text{g}^{-1}$ . Additionally, in the case of the NMO spinel broader oxidation- and reduction-peaks arise, which originate from the high thickness of the electrode. The reason for this is the high mass load and the thickness of the active layer respectively, which leads to different electrode kinetics (especially compared to thinner electrodes). Due to the spinel structure lithiation and delithiation of the NMO-spinel proceeds faster than the lithiation/delithiation of the layered graphite. By using a thick graphite electrode the lithiation and delithiation of deeper graphite particles is inhibited. That could be possibly the reason why the entire capacity of the graphite cannot be used.

Another reason for the bad performance could be found into the calendaring of the graphite electrode, which was possibly too strong leading to a destruction of the graphene structure.

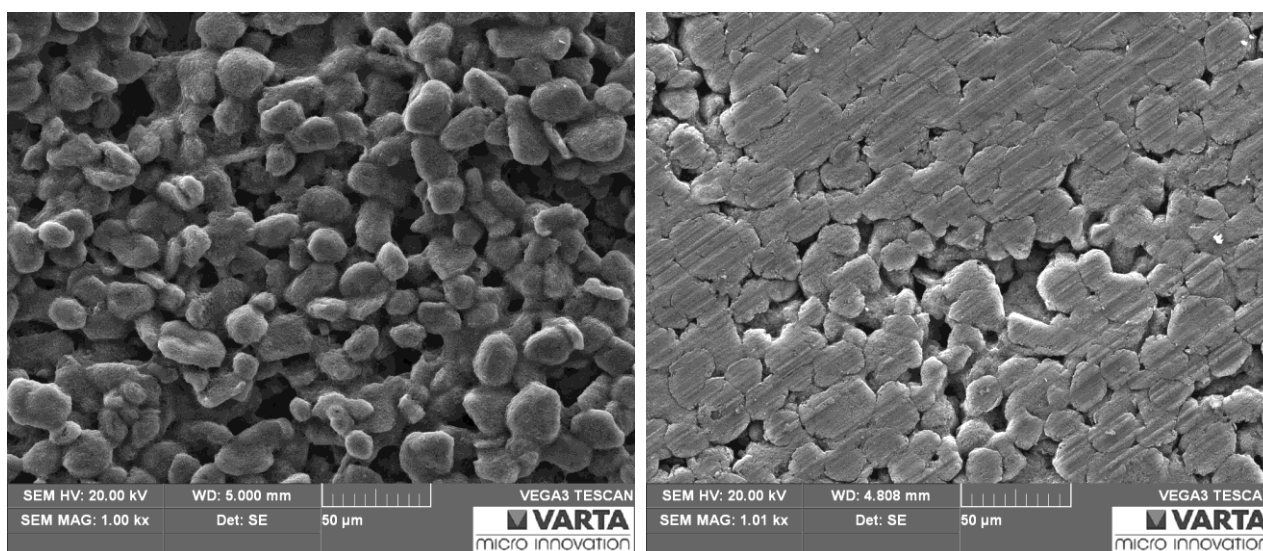


**Figure 138:** SEM images of a pristine (left) and calendared (right) graphite electrode; both magnifications:  $\times 1,000$ .

As already mentioned in chapter 3.1.1 (page 45) a main problem of manganese-containing positive electrodes is the dissolution of bivalent manganese ions into the electrolyte and their subsequent cathodic plating on the negative electrode surface. This in turn leads to a poisoning of the solid electrolyte interphase and in further consequence to failure of the entire battery. Figure 139 illustrates the SEM image of a graphite electrode after constant current cycling signifying obviously manganese stripping, which could be confirmed by energy-dispersive-X-ray spectroscopy (EDX) measurements (cf. Figure 140). The manganese amount could not be investigated clearly by the mapping method, because the lateral expansion of the “stripping spots” isn’t large enough. At present there’s no investigation method, which can clearly answer this question. At least it would also be interesting which effect a surface modification of the NMO electrode could achieve in terms of the before explained hybrid electrolyte.

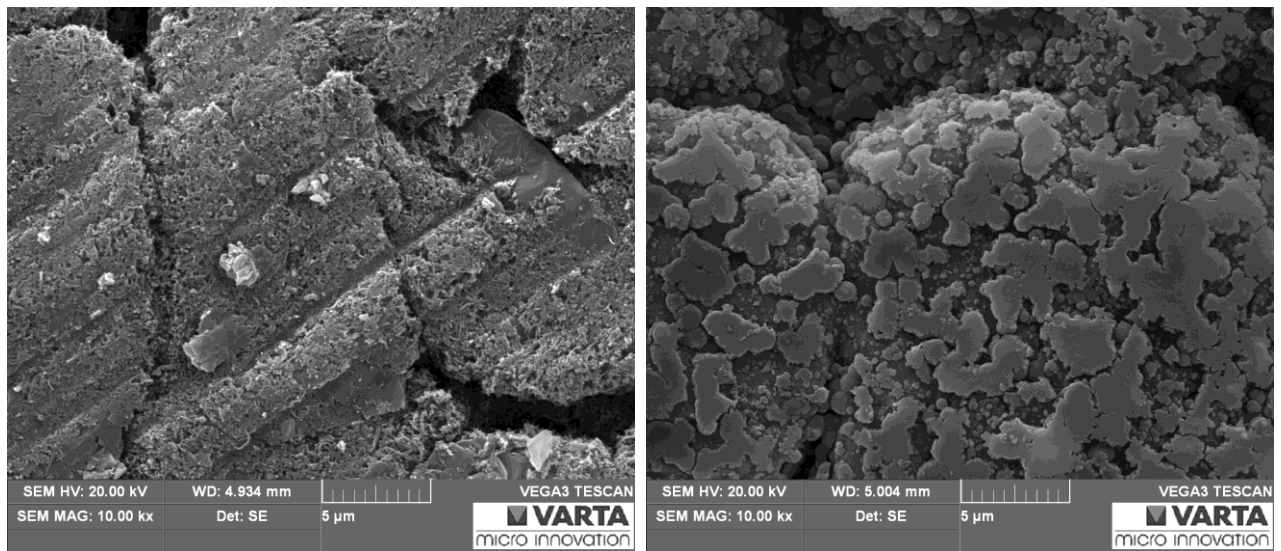


**Figure 139:** SEM illustrations of a pristine, calendared (left) and a cycled (right) graphite electrode after CCC; both magnifications: x10,000.

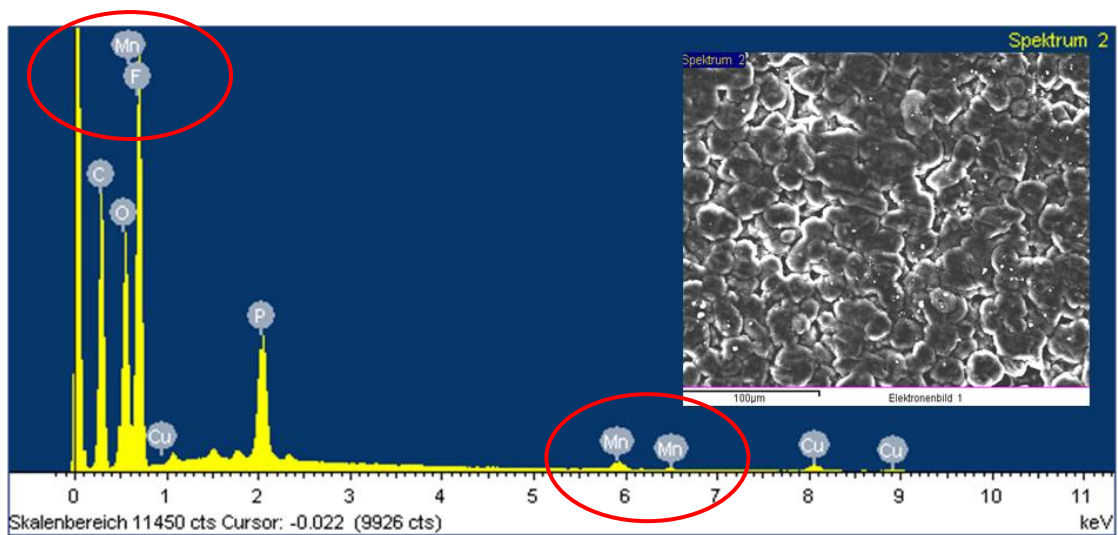


**Figure 140:** EDX including mapping results of a cycled graphite electrode from the full cell (measurement not shown within this doctoral thesis).

## 4 Conclusion

Nowadays, the topic of electrochemical energy storage moves into spotlight even more and more due to the protection of our environment by partial replacement of fossil fuels. In particular, the automotive industry focuses on hybrid vehicles at least with the prime target to substitute common combustion engines over the course of the next decades. Among all available energy storage systems Lithium-Ion-Batteries seem to be the key technology to fulfill this envisaged purpose. In this connection, research groups are compelled to improve the battery performance concerning the enhancement of specific energy ( $\text{Wh}\cdot\text{kg}^{-1}$ ) and energy density ( $\text{Wh}\cdot\text{l}^{-1}$ ) to be competitive with common cars in terms of the cruising range. On that account many efforts were made to implement on the one hand high capacity anodes (e.g. pure silicon with about  $4200 \text{ mAh}\cdot\text{g}^{-1}$ ) and on the other hand cathode materials with a high working potential ( $> 4.3 \text{ V vs. Li/Li}^+$ ). Unfortunately, due to the high working potentials, the use of these 5 V cathode materials implies an essential drawback, namely an insufficient oxidative stability of common used organic electrolyte systems. Within the scope of this doctoral thesis such a high voltage cathode material in terms of a nickel-manganese spinel with the composition  $\text{LiNi}_{0.5}\text{Mn}_{1.5}\text{O}_4$  (NMO) should be investigated to gain information about its electrochemical properties. Additionally, an electrolyte system that exhibits a sufficient anodic stability up to 5 V vs.  $\text{Li/Li}^+$  and above should be developed. Finally full cells containing the common anode material graphite and the cathode material NMO spinel (from BASF-SE) should be manufactured.

An insufficient electrode performance of this special cathode material during electrochemical experiments could be attributed to the partial dissolution of the active material layer. Unavoidable water impurities of organic electrolytes react with fluorinated conducting salts and form hydrofluoric acid, which is responsible for the dissolution of the soluble bivalent manganese-ion into the electrolyte (disproportionation reaction in which two trivalent manganese-ions split into one tetravalent- and one bivalent manganese-ion). However, this dissolution leads on the one hand to the poisoning of the SEI-layer and on the other hand to a loss of active material and finally to a worse cycling performance of the electrode (capacity fading, etc.). The dissolution of the active material layer as well as the manganese plating on the anode surface could be proven by use of SEM and X-ray fluorescence analysis. The second reason for the bad cycling behavior was the massive electrolyte decomposition, which could be observed by SEM investigations showing white spots upon the cathode surface. The electrode performance and the electrolyte decomposition could be improved by decreasing the porosity of the electrode through calendaring, whereby the intensity of calendaring process takes a main effect. The lower the electrode porosity the better the electrolyte performance gets. The reason for this is the reduced contact area between the electrolyte and the catalytic active sites of the cathode active material, which induce electrolyte decomposition. Unfortunately, the calendaring process solely constitutes lowers electrolyte degradation and bad electrode performance indeed, but was not able to provide a final solution (cf. chapter 3.3.1, page 52 ff.).

An alternative solution for both problems was found by application of an artificial SEI upon the cathode surface (an artificial SEI is a hybrid electrolyte system, which is defined as the combination of a common liquid electrolyte and a solid electrolyte already coated on the cathode surface). As a result, manganese dissolution as well as the mitigation of the direct contact of the liquid electrolyte with cathode was prevented. In this context this artificial SEI serves as barrier layer. Due to the inhibition of the contact electrolyte/NMO all oxidative stability problems concerning the positive electrode would become negligible and liquid electrolyte systems merely had to be tailored for the negative electrode. Furthermore, not only this nickel-manganese spinel would be accessible for industrial applications, but rather all high voltage cathode materials. Electrochemical measurements of BASF NMO electrodes, which were modified with a

SiO<sub>2</sub> layer, confirmed all these assumptions. Within the first 15 cycles nearly no decrease of capacities and specific energies are detectable. Additionally, the electrochemical improvement of the electrode/electrolyte system can be confirmed by in-situ measurements of the pressure gain caused by electrolyte degradation during constant current cycling (CCC) and the cyclic voltammetry (CV) combined with a mass spectrometry. Both investigation methods ensured a clear improvement by use of modified BASF NMO electrodes. Nevertheless, it should be considered that further optimization for an absolutely homogenous artificial SEI is still necessary to eradicate the problems completely. In this connection, investigations with real solid electrolyte such as LiSICON or LiPON are necessary. Furthermore, in a broader sense, an improvement of the anodic stability cannot only be achieved by alternative electrolyte components, but rather through a suitable combination of electrode/electrolyte, whereby the functionality of the hybrid electrolyte system is without any doubt (cf. chapter 3.3.3, page 63 ff.).

The prevention of electrolyte decomposition can be also achieved by adjusting additives to an already existing electrolyte system. This electrolyte modification should improve the electrochemical performance of NMO (or other 5 V cathode materials) by forming a SEI in-situ by anodic decomposition on the cathode surface during the first cycles. Summarizing all investigated additives within the scope of this doctoral thesis no remarkable improvements compared to “pristine” electrolytes could be observed. Additives containing at least one carbon-carbon double bond (e.g. VC) polymerized and generated a film on cathode surface indeed, but these films deliver poor lithium-ion permeability. This leads to a negative impact on the battery performance and its cycle and calendar life. Nevertheless, SEI forming additives such as FEC, F<sub>2</sub>EC, or ES had neither a negative nor positive impact on the cycling behavior. As a consequence, these compounds can be used for graphite/NMO full cells forming a sufficient SEI on the negative electrode side (cf. chapter 3.3.4.5.1, page 95 ff.). According to literature, high oxidative stable electrolyte systems up to 5 V vs. Li/Li<sup>+</sup> and above consist of nitrile compounds as solvents and LiBOB and/or LiTFSI as conductive salts. However, neither aluminum current collector corrosion nor conductive salt or nitrile decomposition could be prevented, which resulted in cell damage within merely a few cycles. Thus, the envisaged prevention of electrolyte degradation or improvement of the anodic stability of electrolyte systems could not be observed (cf. chapter 3.3.4.5.2, page 108 ff.).

The successful cell balancing of graphite anodes and the BASF NMO spinel cathodes and an additional reduction of the inner cell resistance by the use of a thin separator (Separion®) delivered a sufficient cycling behavior for more than 100 cycles. The obtained capacities and specific energies are beneath theoretical achievable values indeed, but these theoretical energies are calculated without any loss of manganese, lithium or even electrolyte decomposition and other side reactions. Furthermore, similar good results could not be observed within literature so far (cf. chapter 3.3.4.6, page 112 ff.).

All obtained results gained information about the possible electrochemical behavior of the BASF NMO spinel. In particular, the hybrid electrolyte, which is applied for a patent by the BASF-SE, seems to be a very promising possibility for the electrochemical improvement of this 5 V cathode material. Solely it is arguable to what extent the implementation of a hybrid electrolyte can improve even the electrochemical performance and prevention of electrolyte and active material degradation within graphite/NMO full cells.

## 5 Appendix

### 5.1 References

1. [http://en.wikipedia.org/wiki/Main\\_Page](http://en.wikipedia.org/wiki/Main_Page). [Online] [http://en.wikipedia.org/wiki/Charles\\_H.\\_Duell](http://en.wikipedia.org/wiki/Charles_H._Duell).
2. <http://de.wikipedia.org>. [Online] [Cited: 06 06, 2011.] <http://de.wikipedia.org/wiki/IBM>.
3. <http://de.wikipedia.org>. [Online] [Cited: 06 06, 2011.] [http://de.wikipedia.org/wiki/Thomas\\_J.\\_Watson](http://de.wikipedia.org/wiki/Thomas_J._Watson).
4. <http://diepresse.com>. [Online] [Cited: 06 06, 2011.] <http://diepresse.com/home/science/631424/Eine-Wissenschaft-ohne-Raetsel>.
5. <http://diepresse.com>. [Online] [Cited: 06 06, 2011.] [http://diepresse.com/home/bildung/universitaet/477967/FWFBudget\\_Mittel-fuer-derzeit-2600-Forscher](http://diepresse.com/home/bildung/universitaet/477967/FWFBudget_Mittel-fuer-derzeit-2600-Forscher).
6. [Online] [Cited: 10 04, 2011.] <http://www.lastfm.de/music/Metallica/+images/30737731>.
7. <http://www.forschungsinformationssystem.de>. [Online] [Cited: 06 16, 2011.] <http://www.forschungsinformationssystem.de/servlet/is/332825/?clsId0=276664&clsId1=276668&clsId2=0&clsId3=0>.
8. **J.-M. Tarascon, M. Armand.** *Nature*. 414, 2001, 359-367.
9. [Online] [Cited: 06 17, 2011.] <http://knol.google.com/k/les-voitures-%C3%A9lectriques-et-leurs-sources-d-%C3%A9nergie#>.
10. <http://www.motorlexikon.de>. [Online] [Cited: 06 20, 2011.] <http://www.motorlexikon.de/?I=9478>.
11. **U. Kasavajjula, C. Wang, A.J. Appleby.** *Journal of Power Sources*. 163, 2007, 1003-1039.
12. **S. Koller, M. Schmuck.** Lecture. *Batteries and Supercapacitors*. s.l. : TU Graz, 2010.
13. **M. Winter, R.J. Brodd.** *Chemical Reviews*. 104, 2004, 4245-4269.
14. **J.O. Besenhard.** *Handbook of Battery Materials*. Weinheim : Wiley-VCH GmbH, 1999.
15. **G. Kickelbick.** *Chemie für Ingenieure*. München : Pearson Education Verlag Deutschland GmbH, 2008.
16. **P.W. Atkins.** *Physical Chemistry 5th edition*. s.l. : W.H. Freeman & Company, 1994.
17. **H.A. Kiehne.** *Battery Technology Handbook*. Renningen-Malsheim : Expert-Verlag GmbH, 2000.
18. **C.H. Hamann, A. Hamnett, W. Vielstich.** *Electrochemistry*. Weinheim : Wiley-VCH Verlag GmbH, 1998.
19. **H. Ebert.** *Elektrochemie*. Würzburg : Vogel-Verlag, 1979.
20. **D. Linden.** *Handbook of Batteries*. New York : McGraw-Hill Inc., 1995.
21. **K.V. Vetter.** *Electrochemical Kinetics*. New York : Academic Press Inc., 1967.
22. **A. Semmler.** *Adsorption ionischer Tenside*. München : Herbert Utz Verlag GmbH, 1998.
23. **J.O'M. Bockris, S.U.M. Khan.** *Surface Electrochemistry*. New York : Plenum Press, 1993.

24. [Online] [Cited: 04 26, 2011.] <http://www.uni-mainz.de/FB/Chemie/fbhome/physc/Dateien/QCM-Skript.pdf>.
25. [Online] [Cited: 05 02, 2011.] [http://www.chemie.uni-erlangen.de/pctc/praktikum/f\\_praktikum/zyklovoltametrie/CVSW\\_14.html](http://www.chemie.uni-erlangen.de/pctc/praktikum/f_praktikum/zyklovoltametrie/CVSW_14.html).
26. **N. Kanani.** *Electroplating*. Oxford : ElsevierAdvanced Technology, 2004.
27. **M. Aliofkhazraei.** *Nanocoatings*. s.l. : Springer-Verlag Berlin Heidelberg, 2011.
28. **R. Holze.** *Leitfaden der Elektrochemie*. Stuttgart-Leipzig : Teubner , 1998.
29. **C. Stangl.** Doctoral Thesis. 2011.
30. [Online] [Cited: 07 07, 2011.] <http://bibliothek.fzk.de/zb/berichte/FZKA5594.pdf>.
31. **N. Kanani.** *Galvanotechnik*. s.l. : Carl Hanser Verlag München Wien, 2009.
32. **S. Koller, M. Schmuck.** Lecture. *Primäre und wiederaufladbare Lithium-Batterien*. TU Graz : s.n., 2009.
33. **M. Winter, J.O. Besenhard, M.E. Spahr, P. Novak.** *Advanced Materials*. 10, 1998, 725-763.
34. **H. Kren.** About the Continuous Growth of the Solid Electrolyte Interphase in Lithium Ion Batteries. *Doctoral Thesis*. TU Graz : s.n., 2011.
35. [Online] [Cited: 05 11, 2011.] <http://www.a123systems.com/products-cells-26650-cylindrical-cell.htm>.
36. **J.O. Besenhard, G. Eichinger.** *Journal of Electroanalytical and Interfacial Electrochemistry*. 68, 1976, 1-18.
37. **G. Eichinger, J.O. Besenhard.** *Journal of Electroanalytical and Interfacial Electrochemistry*. 72, 1976, 1-31.
38. **K. Xu.** *Chemical Reviews*. 104, 2004, 4303-4417.
39. **K. Ozawa.** *Solid state ionics*. 69, 1994, 212-221.
40. **M. Winter, J.O. Besenhard.** *Electrochemical intercalation of lithium into carbonaceous materials*. Tokyo-Weinheim : Kodansha/Wiley VCH, 1998.
41. **K. Ozawa.** *Lithium Ion Rechargeable Batteries*. Weinheim : Wiley-VCH Verlag GmbH & Co, 2009.
42. **J.B. Goodenough, K. Mizushima.** *Patent. GB 11953/79* April 1979.
43. [Online] [Cited: 07 21, 2011.] [http://www.varta-microbattery.com/en/mb\\_data/documents/sales\\_literature\\_varta/HANDBOOK\\_Primary\\_Lithium\\_Cells\\_en.pdf](http://www.varta-microbattery.com/en/mb_data/documents/sales_literature_varta/HANDBOOK_Primary_Lithium_Cells_en.pdf).
44. [www.sony.net](http://www.sony.net). [Online] [Cited: 05 31, 2011.] [http://www.sony.net/SonyInfo/News/Press\\_Archive/200412/04-060E/](http://www.sony.net/SonyInfo/News/Press_Archive/200412/04-060E/).
45. **P. Arora, R.E. White, M. Doyle.** *Journal of The Electrochemical Society*. 145, 1998, 3647-3667.
46. **T. Ohzuku, R.J. Brodd.** *Journal of Power Sources*. 174, 2007, 449-456.

47. **G.-A. Nazri, G. Pistoia.** *Lithium-Batteries, Science and Technology.* Dordrecht/Netherlands : Kluwer Academic Publishers Group, 2004.
48. **M. Sternad.** Entwicklung von Hochtemperaturelektrolyten für Lithium-Ionen-Batterien. *Diploma Thesis.* TU Graz : s.n., 2005.
49. **W.A. van Schalkwijk, B. Scrosati.** *Advances in Lithium-Ion Batteries.* New York : Kluwer Academic/Plenum Publishers, 2002.
50. **K. Ozawa.** *Solid State Ionics.* 69, 1994, 212-221.
51. <http://www.a123systems.com>. [Online] [Cited: 06 01, 2011.] <http://www.a123systems.com/Collateral/Images/English-US/Photo%20Gallery/A123-Cell-Family.jpg>.
52. [Online] [Cited: 06 01, 2011.] <http://tech.groups.yahoo.com/group/ETList/message/7427>.
53. <http://www.batteriesinaflash.com>. [Online] [Cited: 06 01, 2011.] <http://www.batteriesinaflash.com/assembly-cells/li-ion/tenergy-li-ion-18650-3-7v-rechargeable-battery-with-tabs-2600mah>.
54. **M. Wakihara.** *Materials Science and Engineering.* R33, 2001, 109-134.
55. **J.R. Dahn, A.K. Sleight, H. Shi, J.N. Reimers, Q. Zhong, B.M. Way.** *Electrochimica Acta.* 9, 1993, Vol. 38, 1179-1191.
56. **I. Mochida, S.-H. Yoon, W. Qiao.** *Journal of the Brazilian Chemical Society.* 17, 2006, 1059-1073.
57. **L.H. Lie.** Diploma Thesis. *Characterisation of new fluorinated aprotic solvents as electrolyte component for lithium ion cells.* Trondheim : s.n., 1998.
58. **H. Azuma, H. Imoto, S. Yamada, K. Sekai.** *Journal of Power Sources.* 81-82, 1999, 1-7.
59. **H. Li, Z. Wang, L. Chen, X. Huang.** *Advanced Materials.* 21, 2009, 4593-4607.
60. **A. Hérold.** *Bulletin de la Société Chimique de France.* 187, 1955, 999.
61. **J.T. Titantah, D. Lamoen, M. Schowalter, A. Rosenauer.** *Carbon.* 47, 2009, 2501-2510.
62. **J.R. Dahn.** *Physical Review B.* 44, 1991, 9170-9177.
63. **S.J. Harris, A. Timmons, D.R. Baker, C. Monroe.** *Chemical Physics Letters.* 485, 2010, 265-274.
64. **M. Inaba, H. Yoshida, Z. Ogumi, T. Abe, Y. Mizutani, M. Asano.** *Journal of the Electrochemical Society.* 142, 1995, 20-26.
65. **J. Yang, M. Winter, J.O. Besenhard.** *Solid State Ionics.* 90, 1996, 281-287.
66. **A.N. Dey.** *Journal of The Electrochemical Society.* 118, 1971, 1547-1549.
67. **R.A. Sharma, R.N. Seefurth.** *Journal of The Electrochemical Society.* 123, 1976, 1763-1768.
68. **J.O. Besenhard, J. Yang, M. Winter.** *Journal of Power Sources.* 68, 1997, 87-90.
69. **C.M. Park, J.H. Kim, H. Kim, H.J. Sohn.** *Chemical Society Reviews.* 39, 2010, 3115-3141.
70. **K. Zaghib, M. Simoneau, M. Armand, M. Gauthier.** *Journal of Power Sources.* 81-82, 1999, 300-305.

71. **H. Yu.** *Electrochimica Acta*. 53, 2008, 4200.
72. **L. Kavan, M. Grätzel.** *Electrochemical Solid-State Letters*. 5, 2002, A39.
73. **P. Poizot, S. Laruelle, S. Grugeon, L. Dupont, J.M. Tarascon.** *Nature*. 407, 2000, 496-499.
74. **P.G. Bruce, B. Scrosati, J.M. Tarascon.** *Angewandte Chemie International Edition*. 47, 2008, 2930-2946.
75. **M. Armand, J.M. Tarascon.** *Nature*. 451, 2008, 652-657.
76. **J.B. Goodenough.** *Journal of Power Sources*. 174, 2007, 996-1000.
77. **J.W. Fergus.** *Journal of Power Sources*. 195, 2010, 939-954.
78. **W.F. Howard, R.M. Spotnitz.** *Journal of Power Sources*. 165, 2007, 887-891.
79. **M.M. Doeff, Y. Hu, F. McLarnon, R. Kostecki.** *Electrochemical and Solid-State Letters*. 6, 2003, Vol. 10, A207-A209.
80. **A.K. Padhi, K.S. Nanjundaswamy, J.B. Goodenough.** *Journal of The Electrochemical Society*. 144, 1997, 1188-1194.
81. **M.S. Whittingham.** *Chemical Reviews*. 104, 2004, 4271-4301.
82. <http://homepage3.nifty.com>. [Online] [Cited: 06 27, 2011.]  
<http://homepage3.nifty.com/mnakayama/research/tips5/qm.htm>.
83. **M. Tang, W.C. Carter, Y.M. Chiang.** *Annual Review of Materials Research*. 40, 2010, 501-529.
84. **M.S. Islam, D.J. Discoll, C.A.J. Fisher, P.R. Slater.** *Chemistry of Materials*. 17, 2005, 5085-5092.
85. **L. Wang, Y. Huang, R. Jiang, D. Jia.** *Electrochimica Acta*. 52, 2007, 6778-6783.
86. **Y. Li, S. Zhao, C. Nan, B. Li.** *Journal of Alloys and Compounds*. 509, 2011, 957-960.
87. **P.P. Prosini, M. Carewska, S. Scaccia, P. Wisniewski, M. Pasquali.** *Electrochimica Acta*. 48, 2003, 4205-4211.
88. **F. Croce, A.D'Epifanio, J. Hassoun, A. Deptula, T. Olczac, B. Scrosati.** *Electrochemical and Solid-State Letters*. 5, 2002, A47-A50.
89. **M. Takahashi, S. Tobishima, K. Takei, Y. Sakurai.** *Journal of Power Sources*. 97-98, 2001, 508-511.
90. **C. Lai, Q. Xu, H. Ge, G. Zhou, J. Xie.** *Solid State Ionics*. 179, 2008, 1736-1739.
91. **H. Gabrisch, R. Yazami, B. Fultz.** *Electrochemical and Solid-State Letters*. 5, 2002, A111-A114.
92. <http://homepage3.nifty.com>. [Online] [Cited: 06 27, 2011.]  
[http://homepage3.nifty.com/mnakayama/research/tips7/sample\\_qm.htm](http://homepage3.nifty.com/mnakayama/research/tips7/sample_qm.htm).
93. **G.G. Amatucci, J.M. Tarascon, L.C. Klein.** *Solid State Ionics*. 83, 1996, 167-173.
94. **H. Gabrisch, R. Yazami, B. Fultz.** *Journal of The Electrochemical Society*. 151, 2004, A891-A897.
95. **E.I. Santiago, A.V.C. Andrade, C.O. Paiva-Santos, L.O.S. Bulhões.** *Solid State Ionics*. 158, 2003, 91-102.
96. **E. Antolini.** *Solid State Ionics*. 170, 2004, 159-171.

97. **S. Laubach**. Doctoral Thesis. 2008.
98. <http://www.soton.ac.uk>. [Online] [Cited: 06 14, 2011.] [http://www.soton.ac.uk/chemistry/research/projects/magnetic\\_and\\_electronic\\_materials.page](http://www.soton.ac.uk/chemistry/research/projects/magnetic_and_electronic_materials.page).
99. **H. Xia, Y.S. Meng, L. Lu, G. Ceder**. *Advanced Materials for Micro- and Nano-Systems*. 2007.
100. **G.T.K. Fey, C.Z. Lu, T.P. Kumar, Y.C. Chang**. *Surface & Coatings Technology*. 199, 2005, 22-31.
101. **H. Wang, Y.I. Jang, B. Huang, D.R. Sadoway, Y.M. Chiang**. *Journal of The Electrochemical Society*. 146, 1999, 473-480.
102. **J. Cho, Y.J. Kim, B. Park**. *Chemistry of Materials*. 12, 2000, 3788-3791.
103. **L.P.L.M. Rabou, A. Roskam**. *Journal of Power Sources*. 54, 1995, 316-318.
104. **B.L. Ellis, K.T. Lee, L.F. Nazar**. *Chemistry of Materials*. 22, 2010, Vol. 3, 691-714.
105. **D.D. MacNeil, J.R. Dahn**. *Journal of The Electrochemical Society*. 149, 2002, A912-A919.
106. [Online] [Cited: 06 30, 2011.] <http://www.theo3.physik.uni-stuttgart.de/beck/bravais.html>.
107. **A. Patil, V. Patil, D.W. Shin, J.W. Choi, D.S. Paik, S.J. Yoon**. *Materials Research Bulletin*. 43, 2008, 1913-1942.
108. **C. Li, H.P. Zhang, L.J. Fu, H. Liu, Y.P. Wu, E. Rahm, R. Holze, H.Q. Wu**. *Electrochimica Acta*. 51, 2006, 3872-3883.
109. **D. Aurbach, B. Markovsky, A. Rodkin, E. Levi, Y.S. Cohen, H.J. Kim, M. Schmidt**. *Electrochimica Acta*. 47, 2002, 4291-4306.
110. **Y.J. Kim, T.J. Kim, J.W. Shin, B. Park, J. Cho**. *Journal of The Electrochemical Society*. 149, 2002, A1337-A1341.
111. **Z. Chen, J.R. Dahn**. *Electrochemical and Solid-State Letters*. 6, 2003, A221-A224.
112. **G. Li, Z. Yang, W. Yang**. *Journal of Power Sources*. 183, 2008, 741-748.
113. **J. Jiang, K.W. Eberman, L.J. Krause, J.R. Dahn**. *Journal of The Electrochemical Society*. 152, 2005, A566-A569.
114. **T.H. Cho, S.M. Park, M. Yoshio, T. Hirai, Y. Hideshima**. *Journal of Power Sources*. 142, 2005, 306-312.
115. **M.M. Thackeray, W.I.F. David, P.G. Bruce, J.B. Goodenough**. *Materials Research Bulletin*. 18, 1983, 961.
116. **V. Kusigerski, D. Marković, V. Spasojević, N. Cvjetičanin, M. Mitrić, D. Jugović, D. Uskoković**. *Journal of Magnetism and Magnetic Materials*. 320, 2008, 943-949.
117. **Y. Takahashi, J. Akimoto, Y. Gotoh, K. Dokko, M. Nishizawa, I. Uchida**. *Journal of the Physical Society of Japan*. 72, 2003, 1483-1490.
118. **C.Y. Ouyang, S.Q. Shi, Z.X. Wang, H. Li, X.J. Huang, L.Q. Chen**. *Europhysics Letters*. 67, 2004, 28-34.
119. **H. Berg, K. Göransson, B. Noläng, J.O. Thomas**. *Journal of Materials Chemistry*. 9, 1999, 2813-2820.

120. <http://people.seas.harvard.edu/~sparks/index.html>. [Online] [Cited: 06 21, 2011.] <http://people.seas.harvard.edu/~sparks/publications/apfest2011%20thermopower%20limn2o4.pdf>.
121. [Online] [Cited: 06 28, 2011.] [http://chemistry.berkeley.edu/publications/journal/volume10/no1/reimer\\_tan.php](http://chemistry.berkeley.edu/publications/journal/volume10/no1/reimer_tan.php).
122. **M.M. Thackeray, A. de Kock, M.H. Rossouw, D. Liles, R. Bittihn, D. Hoge.** *Journal of The Electrochemical Society*. 139, 1992, 363-366.
123. **R.J. Gummow, M.M. Thackeray.** *Journal of The Electrochemical Society*. 141, 1994, 1178-1182.
124. **G. Amatucci, J.M. Tarascon.** *Journal of The Electrochemical Society*. 149, 2002, K31-K46.
125. [Online] [Cited: 07 05, 2011.] <http://chemlab.truman.edu/CHEM131Labs/MolecularModeling1.asp>.
126. [Online] [Cited: 07 05, 2011.] [http://www.geocities.jp/ohba\\_lab\\_ob\\_page/structure4.html](http://www.geocities.jp/ohba_lab_ob_page/structure4.html).
127. **M. Yonemura, A. Yamada, H. Kobayashi, M. Tabuchi, T. Kamiyama, Y. Kawamoto, R. Kanno.** *Journal of Materials Chemistry*. 14, 2004, 1948-1958.
128. **B. Ying, W. Chuan, W. Feng, W. Guo-qing.** *Transactions of Nonferrous Metals Society of China*. 16, 2006, 402-408.
129. **K. Oikawa, T. Kamiyama, F. Izumi, B.C. Chakoumakos, H. Ikuta, M. Wakahira, J. Li, Y. Matsui.** *Solid State Ionics*. 109, 1998, 35-41.
130. **C.Y. Ouyang, S.Q. Shi, M.S. Lei.** *Journal of Alloys and Compounds*. 474, 2009, 370-374.
131. **M.M. Thackeray, P.J. Johnson, L.A. de Piciotto, P.G. Bruce, J.B. Goodenough.** *Materials Research Bulletin*. 19, 1984, 179-187.
132. **Y.P. Wu, E. Rahm, R. Holze.** *Electrochimica Acta*. 47, 2002, 3491-3507.
133. **A.M. Kannan, A. Manthiram.** *Electrochemical and Solid-State Letters*. 5, 2002, A167-A169.
134. **Y. Kobayashi, Y. Mita, S. Seki, Y. Ohno, H. Miyashiro, M. Nakayama, M. Wakihara.** *Journal of The Electrochemical Society*. 155, 2008, A14-A19.
135. **J.S. Gnanaraj, V.G. Pol, A. Gedanken, D. Aurbach.** *Electrochemistry Communications*. 5, 2003, 940-945.
136. **M. Galiński, A. Lewandowski, I. Stępniaik.** *Electrochimica Acta*. 51, 2006, 5567-5580.
137. **M. Sternad.** Doctoral Thesis. *Silicon Insertion Electrodes for Lithium-Ion Batteries*. TU Graz : s.n., 2008.
138. **J.M. Tarascon, D. Guyomard.** *Solid State Ionics*. 69, 1994, 293-305.
139. **M. Winter, J.O. Besenhard.** *Chemie in unserer Zeit*. 33, 1999, Vol. 5, 252-266.
140. **D. Aurbach, B. Markovsky, G. Salitra, E. Markevich, Y. Talyossef, M. Koltypin, L. Nazar, B. Ellis, D. Kovacheva.** *Journal of Power Sources*. 165, 2007, 491-499.
141. **J.B. Goodenough, Y. Kim.** *Chemistry of Materials*. 22, 2010, 587-603.
142. **M. Winter, J.O. Besenhard.** *Chemie in unserer Zeit*. 33, 1999, Vol. 6, 320-332.

143. **T. Sasaki, T. Abe, Y. Iriyama, M. Inaba, Z. Ogumi.** *Journal of Power Sources.* 150, 2005, 208-215.
144. **D. Yaakov, Y. Gofer, D. Aurbach, I.C. Halalay.** *Journal of The Electrochemical Society.* 157, 2010, A1383-A1391.
145. **J. Yan, J. Zhang, Y.C. Su, X.G. Zhang, B.J. Xia.** *Electrochimica Acta.* 55, 2010, 1785-1794.
146. **J.O. Besenhard, W. Sitte, F. Stelzer, H. Gamsjäger.** *Electroactive Materials.* Wien : Springer, 2001.
147. **R. Jasinski, S. Carroll.** *Journal of The Electrochemical Society.* 117, 1970, 218-219.
148. **R. Marom, O. Haik, D. Aurbach, I.C. Halalay.** *Journal of The Electrochemical Society.* 157, 2010, A972-A983.
149. **M. Park, X. Zhang, M. Chung, G.B. Less, A.M. Sastry.** *Journal of Power Sources.* 195, 2010, 7904-7929.
150. **Y. Matsuda, H. Satake.** *Journal of The Electrochemical Society.* 127, 1980, 877-879.
151. **Y. Matsuda, H. Nakashima, M. Morita, Y. Takasu.** *Journal of The Electrochemical Society.* 128, 1981, 2552-2556.
152. **Y. Matsuda, M. Morita, K. Kosaka.** *Journal of The Electrochemical Society.* 130, 1983, 101-104.
153. **Y. Matsuda, M. Morita, T. Yamashita.** *Journal of The Electrochemical Society.* 131, 1984, 2821-2827.
154. **H.J. Santner.** Doctoral Thesis. *Development and characterization of new film formin electrolyte additives for Lithium-Ion batteries.* TU Graz : s.n., 2003.
155. **A.K. Shukla, T.P. Kumar.** *Current Science.* 94, 2008, 314-331.
156. **T. Yamamoto, T. Hara, K. Segawa, K. Honda, H. Akashi.** *Journal of Power Sources.* 174, 2007, 1036-1040.
157. **F. Croce, S. Sacchetti, B. Scrosati.** *Journal of Power Sources.* 161, 2006, 560-564.
158. **A.M. Stephan, K.S. Nahm.** *Polymer.* 47, 2006, 5952-5964.
159. **P. Knauth.** *Solid State Ionics.* 180, 2009, 911-916.
160. **B.B. Owens.** *Journal of Power Sources.* 90, 2000, 2-8.
161. **T. Inada, T. Kobayashi, N. Sonoyama, A. Yamada, S. Kondo, M. Nagao, R. Kanno.** *Journal of Power Sources.* 194, 2009, 1085-1088.
162. **M.R. Palacín.** *Chemical Society Reviews.* 38, 2009, 2565-2575.
163. **W.C. West, J.F. Whitacre, J.R. Lim.** *Journal of Power Sources.* 126, 2004, 134-138.
164. **A. Lewandowski, A. Świdorska-Mocek.** *Journal of Power Sources.* 194, 2009, 601-609.
165. **P. Verma, P. Maire, P. Novák.** *Electrochimica Acta.* 55, 2010, 6332-6341.
166. **E. Peled.** *Journal of The Electrochemical Society.* 126, 1979, 2047-2051.
167. **D. Aurbach, B. Markovsky, A. Shechter, Y. Ein-Eli, H. Cohen.** *Journal of The Electrochemical Society.* 143, 1996, 3809-3820.

168. **K. Edström, M. Herstedt, D.P. Abraham.** *Journal of Power Sources.* 153, 2006, 380-384.
169. **T. Yoshida, M. Takahashi, S. Morikawa, C. Ihara, H. Katsukawa, T. Shiratsuchi, J.I. Yamaki.** *Journal of The Electrochemical Society.* 153, 2006, A576-A582.
170. **S.P. Kim, A.C.T. van Duin, V.B. Shenoy.** *Journal of Power Sources.* 196, 2011, 8590-8597.
171. **D. Aurbach, Y. Ein-Eli, B. Markovsky, A. Zaban, S. Luski, Y. Carmeli, H. Yamin.** *Journal of The Electrochemical Society.* 142, 1995, 2882-2890.
172. **M. Herstedt, A.M. Andersson, H. Rensmo, H. Siegbahn, K. Edström.** *Electrochimica Acta.* 49, 2004, 4939-4947.
173. **D. Aurbach, B. Markovsky, I. Weissman, E. Levi, Y. Ein-Eli.** *Electrochimica Acta.* 45, 1999, 67-86.
174. **D. Aurbach, M.D. Levi, E. Levi, A. Schechter.** *The Journal of Physical Chemistry B.* 101, 1997, 2195-2206.
175. **A.N. Dey, B.P. Sullivan.** *Journal of The Electrochemical Society.* 117, 1970, 222-224.
176. **D. Aurbach, M.L. Daroux, P.W. Faguy, E. Yeager.** *Journal of The Electrochemical Society.* 134, 1987, 1611-1620.
177. **Y. Matsuda, S. Wang, J. Mondori.** *Journal of The Electrochemical Society.* 142, 1995, 2914-2918.
178. **K. Xu.** *Journal of The Electrochemical Society.* 156, 2009, A751-A755.
179. **G.V. Zhuang, H. Yang, B. Blizanac, P.N. Ross.** *Electrochemical and Solid-State Letters.* 8, 2005, A441-A445.
180. **G.V. Zhuang, P.N. Ross.** *Electrochemical and Solid-State Letters.* 6, 2003, A136-A139.
181. **A.M. Andersson, M. Herstedt, A.G. Bishop, K. Edström.** *Electrochimica Acta.* 47, 2002, 1885-1898.
182. **J. Jones, M. Anouti, M. Caillon-Caravanier, P. Willmann, P.Y. Sizaret, D. Lemordant.** *Fluid Phase Equilibria.* 305, 2011, 121-126.
183. **S. Koller.** About the Nature of the Electrochemical Formation of Binary Lithium-Silicon Intermetallic Phases from Nonaqueous Electrolytes. *Doctoral Thesis.* TU Graz : s.n., 2009.
184. **D. Zhang, B.N. Popov, R.E. White.** *Journal of Power Sources.* 76, 1998, 81-90.
185. **P. Arora, B.N. Popov, R.E. White.** *Journal of The Electrochemical Society.* 145, 1998, 807-815.
186. **T. Ohzuku, S. Takeda, M. Iwanaga.** *Journal of Power Sources.* 81-82, 1999, 90-94.
187. **A. Eftekhari.** *Journal of Power Sources.* 124, 2003, 182-190.
188. **B.J. Hwang, Y.W. Wu, M. Venkateswarlu, M.Y. Cheng, R. Santhanam.** *Journal of Power Sources.* 193, 2009, 828-833.
189. **X. Wu, S.B. Kim.** *Journal of Power Sources.* 109, 2002, 53-57.
190. **S. Patoux, L. Sannier, H. Lignier, Y. Reynier, C. Bourbon, S. Jouanneau, F. Le Cras, S. Martinet.** *Electrochimica Acta.* 53, 2008, 4137-4145.

191. **S. Patoux, L. Daniel, C. Bourbon, H. Lignier, C. Pagano, F. Le Cras, S. Jouanneau, S. Martinet.** *Journal of Power Sources*. 189, 2009, 344-352.
192. **N. Biškup, J.L. Martínez, M.E. Arroyo y de Dompablo, P. Díaz-Carrasco, J. Morales.** *Journal of Applied Physics*. 100, 2006, 093908.
193. **H. Xia, Y.S. Meng, L. Lu, G. Ceder.** *Journal of The Electrochemical Society*. 154, 2007, A737-A743.
194. **M.L.P. Le, P. Strobel, F. Alloin, T. Pagnier.** *Electrochimica Acta*. 56, 2010, 592-599.
195. **J.H. Kim, S.T. Myung, C.S. Yoon, S.G. Kang, Y.K. Sun.** *Chemistry of Materials*. 16, 2004, 906-914.
196. **R. Santhanam, B. Rambabu.** *Journal of Power Sources*. 195, 2010, 5442-5451.
197. **Q. Zhong, A. Bonakdarpour, M. Zhang, Y. Gao, J.R. Dahn.** *Journal of The Electrochemical Society*. 144, 1997, 205-213.
198. **J. Shu, T.F. Yi, M. Shui, Y. Wang, R.S. Zhu, X.F. Chu, F. Huang, D. Xu, L. Hou.** *Computational Materials Science*. 50, 2010, 776-779.
199. **T.F. Yi, Y. Xie, M.F. Ye, L.J. Jiang, R.S. Zhu, Y.R. Zhu.** *Ionics*. 17, 2011, 383-389.
200. **H. Xia, L. Lu.** *Physica Scripta*. T129, 2007, 43-48.
201. **X. Ma, B. Kang, G. Ceder.** *Journal of The Electrochemical Society*. 157, 2010, A925-A931.
202. **L. Wang, H. Li, X. Huang, E. Baudrin.** *Solid State Ionics*. 193, 2011, 32-38.
203. **M. Kunduraci, G.G. Amatucci.** *Journal of The Electrochemical Society*. 153, 2006, A1345-A1352.
204. **M. Yoshio, R.J. Brodd, A. Kozawa.** *Lithium-Ion Batteries*. New York : Springer Science + Business Media, 2009.
205. **K. Zaghib, K. Striebel, A. Guerfi, J. Shim, M. Armand, M. Gauthier.** *Electrochimica Acta*. 50, 2004, 263-270.
206. **T.T. Fang, H.Y. Chung.** *Journal of the American Ceramic Society*. 91, 2008, 342-345.
207. [Online] [Cited: 05 09, 2011.] <http://www.buchi.com/Glass-Oven-B-585-Drying.82.0.html>.
208. **R. Imhof, P. Novák.** *Journal of The Electrochemical Society*. 146, 1999, 1702-1706.
209. **M. Ue, M. Takeda, M. Takehara, S. Mori.** *Journal of The Electrochemical Society*. 144, 1997, 2684-2688.
210. [Online] [Cited: 09 05, 2011.] <http://de.wikipedia.org/wiki/Cyclovoltammetrie>.
211. **G.T.K. Fey, C.Z. Lu, T.P. Kumar.** *Journal of Power Sources*. 115, 2003, 332-345.
212. **S.B. Park, W.S. Eom, W.I. Cho, H. Jang.** *Journal of Power Sources*. 159, 2006, 679-684.
213. **G. Liu, H. Xie, L. Liu, X. Kang, Y. Tian, Y. Zhai.** *Materials Research Bulletin*. 42, 2007, 1955-1961.
214. **C. Locati, U. Lafont, L. Simonin, F. Ooms, E.M. Kelder.** *Journal of Power Sources*. 174, 2007, 847-851.
215. **A. Ito, D. Li, Y. Lee, K. Kobayakawa, Y. Sato.** *Journal of Power Sources*. 185, 2008, 1429-1433.

216. **S.W. Oh, S.H. Park, J.H. Kim, Y.C. Bae, Y.K. Sun.** *Journal of Power Sources.* 157, 2006, 464-470.
217. **G. Du, Y. NuLi, J. Yang, J. Wang.** *Materials Research Bulletin.* 43, 2008, 3607-3613.
218. **Y.K. Sun, K.J. Hong, J. Prakash, K. Amine.** *Electrochemistry Communications.* 4, 2002, 344-348.
219. **H.M. Wu, I. Belharouak, A. Abouimrane, Y.K. Sun, K. Amine.** *Journal of Power Sources.* 195, 2010, 2909-2913.
220. **Y. Fan, J. Wang, Z. Tang, W. He, J. Zhang.** *Electrochimica Acta.* 52, 2007, 3870-3875.
221. **H.B. Kang, S.T. Myung, K. Amine, S.M. Lee, Y.K. Sun.** *Journal of Power Sources.* 195, 2010, 2023-2028.
222. **N. Takami, T. Ohsaki, H. Hasebe, M. Yamamoto.** *Journal of The Electrochemical Society.* 149, 2002, A9-A12.
223. **K.H. Lee, E.H. Song, J.Y. Lee, B.H. Jung, H.S. Lim.** *Journal of Power Sources.* 132, 2004, 201-205.
224. **M. Matsui, K. Dokko, K. Kanamura.** *Journal of The Electrochemical Society.* 157, 2010, A121-A129.
225. **J.S. Shin, C.H. Han, U.H. Jung, S.I. Lee, H.J. Kim, K. Kim.** *Journal of Power Sources.* 109, 2002, 47-52.
226. **A. Wuersig, W. Scheifele, P. Novák.** *Journal of The Electrochemical Society.* 154, 2007, A449-A454.
227. **T. Ohsaki, T. Kishi, T. Kuboki, N. Takami, N. Shimura, Y. Sato, M. Sekino, A. Satoh.** *Journal of Power Sources.* 146, 2005, 97-100.
228. **F. La Mantia, F. Rosciano, N. Tran, P. Novák.** *Journal of Applied Electrochemistry.* 38, 2008, 893-896.
229. [Online] [Cited: 09 09, 2011.]  
<http://webbook.nist.gov/cgi/cbook.cgi?ID=C74986&Units=SI&Mask=200#Mass-Spec>.
230. [Online] [Cited: 09 09, 2011.]  
<http://webbook.nist.gov/cgi/cbook.cgi?ID=C124389&Units=SI&Mask=200#Mass-Spec>.
231. **M. Holzapfel, A. Würsig, W. Scheifele, J. Vetter, P. Novák.** *Journal of Power Sources.* 174, 2007, 1156-1160.
232. **H.J. Santner, K.C. Möller, J. Ivančo, M.G. Ramsey, F.P. Netzer, S. Yamaguchi, J.O. Besenhard, M. Winter.** *Journal of Power Sources.* 119-121, 2003, 368-372.
233. **S.S. Zhang.** *Journal of Power Sources.* 162, 2006, 1379-1394.
234. **K.C. Möller, H.J. Santner, W. Kern, S. Yamaguchi, J.O. Besenhard, M. Winter.** *Journal of Power Sources.* 119-121, 2003, 561-566.
235. **C. Bayer, C. God, M. Schmuck, C. Stangl, S. Koller.** *2-Chloro-4-phenylthiocyanate - A new film-forming additive for electrolytes in lithium-ion batteries.* 15th Meeting of IMLB, Montréal : s.n., June27 to July 2 2010.
236. **C. Bayer.** *Elektrolytkomponenten für Hochleistungs-Lithium-Ionen Batterien. Diploma Thesis.* TU Graz : s.n., 2008.
237. **F. Wiesbrock, R. Hoogenboom, M.A.M. Leenen, M.A.R. Meier, U.S. Schubert.** *Macromolecules.* 38, 2005, 5025-5034.

238. **G.H. Wrodnigg, J.O. Besenhard, M. Winter.** *Journal of The Electrochemical Society.* 146, 1999, 470-472.
239. **G.H. Wrodnigg, T.M. Wrodnigg, J.O. Besenhard, M. Winter.** *Electrochemistry Communications.* 1, 1999, 148-150.
240. **Y. Ohashi, T. Fujii, S. Kinoshita, M. Winter, M. Sternad.** *Nonaqueous electrolyte solution for secondary battery and nonaqueous electrolyte secondary battery.* WO 2009035054 (A1) 03 19, 2009.
241. **A. Abouimrane, I. Belharouak, K. Amine.** *Electrochemistry Communications.* 11, 2009, 1073-1076.
242. **Y. Watanabe, S. Kinoshita, S. Wada, K. Hoshino, H. Morimoto, S. Tobishima.** *Journal of Power Sources.* 179, 2008, 770-779.
243. **Y. Abu-Lebdeh, I. Davidson.** *Journal of The Electrochemical Society.* 156, 2009, A60-A65.
244. **Q. Wang, P. Pechy, S.M. Zakeeruddin, I. Exnar, M. Grätzel.** *Journal of Power Sources.* 146, 2005, 813-816.
245. **P. Isken, C. Dippel, R. Schmitz, R.W. Schmitz, M. Kunze, S. Passerini, M. Winter, A. Lex-Balducci.** *Electrochimica Acta.* 56, 2011, 7530-7535.
246. **B.T. Yu, W.H. Qiu, F.S. Li, G.X. Xu.** *Electrochemical and Solid-State Letters.* 9, 2006, A1-A4.
247. [Online] [Cited: 09 22, 2011.]  
[http://www.umanitoba.ca/outreach/conferences/phev2007/PHEV2007/proceedings/PluginHwy\\_PHEV2007\\_Session1\\_Yaser.pdf](http://www.umanitoba.ca/outreach/conferences/phev2007/PHEV2007/proceedings/PluginHwy_PHEV2007_Session1_Yaser.pdf).
248. **E. Markevich, V. Baranchugov, D. Aurbach.** *Electrochemistry Communications.* 8, 2006, 1331-1334.
249. <http://www.vartamicroinnovation.at/>. [Online] [Cited: 06 06, 2011.]  
[http://www.vartamicroinnovation.at/main/DE/VARTA/Unternehmen\\_VMI/Management/index,method=main.html](http://www.vartamicroinnovation.at/main/DE/VARTA/Unternehmen_VMI/Management/index,method=main.html).
250. [Online] [Cited: 09 09, 2011.]  
<http://webbook.nist.gov/cgi/cbook.cgi?ID=C96491&Units=SI&Mask=200#Mass-Spec>.
251. [Online] [Cited: 09 09, 2011.]  
<http://webbook.nist.gov/cgi/cbook.cgi?ID=C108327&Units=SI&Mask=200#Mass-Spec>.

## 5.2 List of Figures

Figure 1: left) distribution of different battery technologies contributed by volumetric vs. gravimetric energy densities<sup>(8)</sup>; right) well to wheel constitution of produced greenhouse house gases, in this case produced CO<sub>2</sub> in gram per km, for fossil and renewable sources. Biodiesel has a negative balance within the well to tank (WtT) process due to optimal utilization of exploitable side products during manufacturing process<sup>(drawn from (7))</sup> .....1

Figure 2: left) illustration of merits and drawbacks between electrical and gasoline vehicles<sup>(9)</sup>; middle) cruising ranges of HEV and EV (pie chart shows only cruising ranges of HEVs powered by a battery, in combination with a combustion machine, Chevy Volt reaches 640 km, Toyota Prius 600 km)<sup>(9)</sup>; right) time for fully recharge of the batteries<sup>(drawn from (9))</sup> .....2

Figure 3: potential vs. capacity – possibilities to enhance energy of Lithium-Ion-Batteries<sup>(12)</sup> .....3

Figure 4: schematic draft of a galvanic cell or Daniell element<sup>(source: author)</sup>; the negative electrode (zinc) dissolves and the remaining electrons flow to the positive electrode (copper) and reduce the bivalent copper ions (deposition on the electrode surface).....4

Figure 5: determination of the electromotive force (EMF) and the chemical reactions and their potentials of each half cell with the total reaction<sup>(drawn from (14))</sup> .....5

Figure 6: electrochemical series of metals with their specific standard electrode potentials measured against SHE; the difference of the potentials (EMF) red marked corresponds to the above described Daniell element (cf. figure 4, page 4)<sup>(drawn from (14))</sup> .....5

Figure 7: electrode/electrolyte interface in the equilibrium state<sup>(drawn from (14))</sup> .....6

Figure 8: possibilities for the procedures of an electrochemical process<sup>(drawn from (14))</sup> .....8

Figure 9: Stern model of the potential distribution within the double layer for a positively a) and negatively b) charged electrode<sup>(drawn from (16), (18), (21), (22), (23), (24))</sup> .....10

Figure 10: sketch draft of the Butler-Volmer equation with different values for the symmetry factor  $\alpha$ <sup>(drawn from (18), (25))</sup> .....14

Figure 11: constitution of a discharge profile of a battery and their overpotentials<sup>(29)</sup> .....15

Figure 12: simplified model of the Nernst diffusion layer<sup>(drawn from (16))</sup> .....15

Figure 13: a) diffusion of ions to energetic favorable place for crystal nucleation (e.g. edges); b) ions pass through the electric double layer to these energetic favorable positions<sup>(drawn from (31))</sup> .....16

Figure 14: discharge characteristics of a commercial available battery (A123, 26650 with nominal capacity 2.3 Ah and nominal voltage 3.3 V)<sup>(34), (35)</sup> .....17

Figure 15: a) mechanism of the formation of dendrites; b) schematic constitution of the formation of isolated lithium dendrites; c) the growth of dendrites from anode surface through the electrolyte to the cathode leading to an internal short circuit<sup>(32), (38)</sup> .....19

Figure 16: left) variety of primary button cells from Varta (the notation 2450 means 24 mm in diameter and 5.0 mm height)<sup>(43)</sup>; right) new generation or advanced Lithium-Ion-Batteries established by Sony in 2004<sup>(44)</sup> .....20

Figure 17: schematic draft of the electrode processes within a common Lithium-Ion-Battery<sup>(revision from (48))</sup> .....21

Figure 18: left) different shapes of commercial available Lithium-Ion-Batteries<sup>(51)</sup>; right) setup of cylindrical manufactured 18650 (18 mm diameter, 65 mm height)<sup>(52), (53)</sup> .....21

Figure 19: left) crystal structure (AB) of the hexagonal shape of  $\alpha$ -graphite, right) arm-chair or zig-zag face - vertical view through the separate basal and edge plane<sup>(33)</sup> .....22

Figure 20: different artificial types of non-graphitic carbons and their arrangement of crystalline and amorphous phases<sup>(33), (56)</sup> .....23

Figure 21: schematic constitution of the three types of the carbonaceous materials<sup>(54)</sup> .....23

Figure 22: left) scheme of the AA stacking order of lithiated graphite, middle) distribution of lithium within LiC<sub>6</sub><sup>(33)</sup>; right) AA stacking order of the Li intercalated LiC<sub>6</sub> with ab-initio DFT relaxation<sup>(61)</sup> .....24

Figure 23: left) electrochemical stage formation during lithium intercalation within organic electrolytes containing lithium salts; right) electrochemical proof of the stepwise lithium insertion process into graphite, cyclic voltammetry with a scan rate of  $10 \mu\text{V}\cdot\text{s}^{-1}$ , electrolyte system EC/DEC, 3:7, v:v, 1M  $\text{LiPF}_6$ ; bottom) pictures of graphite, taken after different lithiation degrees: a) pristine graphite, b) graphite shows blue color (stage III,  $\text{LiC}_{18}$ ), c) three lithiation stages blue (stage III,  $\text{LiC}_{18}$ ), red and gold (stage I,  $\text{LiC}_6$ ) and d) two stages are visible - the red (stage II,  $\text{LiC}_{12}$ ) and golden one (stage I,  $\text{LiC}_6$ ) <sup>(33), (34), (63)</sup> .....24

Figure 24: constitution of the charge and discharge capacities during constant current cycling (CCC); left) CCC for the first cycle showing the irreversible capacity  $C_{\text{irr}}$ ; right) CCC for the following second cycle <sup>(33)</sup> ..25

Figure 25: left) packing densities of several lithium alloys in comparison to metallic lithium <sup>(drawn from (65), (68))</sup>, right) schematic comparison of volume expansions between graphite and lithium alloy compounds  $\text{Li}_x\text{M}$  after lithiation <sup>(12)</sup> .....26

Figure 26: schematic draft of an insertion (top) and a conversion (bottom) reaction, whereby a maximum of one electron can be removed within an insertion reaction and 2 – 6 electrons inside of a conversion one <sup>(75)</sup> . .....27

Figure 27: crystal structures of cathode host materials constituting different lithium diffusions; a) one dimensional (1D) insertion within olivine structure (e.g.  $\text{LiFePO}_4$ ); b) two dimensional (2D) insertion upon layered materials (e.g.  $\text{LiCoO}_2$ ) and c) three dimensional (3D) insertion of spinel structures (e.g.  $\text{LiMn}_2\text{O}_4$ ) <sup>(revision from (46))</sup> .....28

Figure 28: left) SEM image of  $\text{LiFePO}_4$  <sup>(source: author)</sup> with the crystal structure of  $\text{LiFePO}_4$ ; the green spots correspond to Li, purple to the  $\text{PO}_4$  tetrahedron and yellow to the  $\text{FeO}_6$  octahedron <sup>(83), (84)</sup>; right) distribution of the electron density of  $\text{LiFePO}_4$ , calculated by Wien2k (FLAPW method) and drawn with Venus developed by R.A. Dilanian & F. Izumi <sup>(82)</sup> .....29

Figure 29: left) typical flat charge and discharge profile of  $\text{LiFePO}_4$  at 3.5 V and 3.4 V vs.  $\text{Li/Li}^+$  <sup>(90)</sup> and right) its corresponding cyclic voltammetry (CV) with a scan rate of  $30 \mu\text{V}\cdot\text{s}^{-1}$  (CV provided by M. Scharfegger/Varta Micro Innovation GmbH) .....30

Figure 30: left) SEM image of  $\text{LiCoO}_2$  <sup>(source: author)</sup> with the crystal structure of  $\text{LiCoO}_2$ , the red spots correspond to Li, the  $\text{CoO}_6$  octahedras are constituted in blue <sup>(98)</sup>; middle) explanation of the arrangement of the  $\alpha\text{-NaFeO}_2$  crystal structure for  $\text{LiCoO}_2$  <sup>(99)</sup>; right) Vienna ab initio simulation package (VASP) used for computation of the electron density of  $\text{LiCoO}_2$  for determination of the bond character <sup>(92)</sup> .....31

Figure 31: left) CCC of  $\text{LiCoO}_2$  – the red line corresponds to charge and the blue line to the discharge profile; the green arrow indicates the area of reversible and the red arrow the area of irreversible lithium extraction/insertion <sup>(data provided by A. Droisner/Varta Micro Innovation GmbH, edited by author)</sup>; right) the corresponding cyclic voltammogram (CV) showing the oxidation peaks during delithiation with hexagonal (blue) and monoclinic (purple) phases <sup>(data provided by M. Scharfegger/Varta Micro Innovation GmbH, edited by author), (106)</sup> .....32

Figure 32: left) SEM image of  $\text{LiMn}_2\text{O}_4$  <sup>(source: author)</sup> with the crystal structure of the spinel  $\text{LiMn}_2\text{O}_4$ ; the cyan tetrahedras correspond to Li ( $\text{LiO}_4$ ), purple octahedras ( $\text{MnO}_6$ ) represent Mn and in red oxygen atoms are constituted <sup>(120)</sup>; right) spatial constitution of  $\text{LiMn}_2\text{O}_4$  and the distribution of the electron density calculated by FLAPW method <sup>(117), (121)</sup> .....33

Figure 33: excerpt of the ternary Li-Mn-O phase diagram showing the defect spinel phases (orange area) and defect rock salt phases (green area) <sup>(drawn from (122))</sup> with the tetrahedral structure (left) and the cubic close packed structure (right) <sup>(125), (126)</sup>; Li-extraction from  $\text{LiMn}_2\text{O}_4$  leads to cubic  $\lambda\text{-MnO}_2$  ( $\text{Mn}^{4+}$ , blue line) and Li-insertion to tetragonal  $\text{Li}_2\text{Mn}_2\text{O}_4$  ( $\text{Mn}^{3+}$ , red line) <sup>(122), (124), (127)</sup> .....33

Figure 34: left) charge (red line) and discharge (blue line) profile of  $\text{LiMn}_2\text{O}_4$ ; <sup>(data provided by A. Droisner/Varta Micro Innovation GmbH, edited by author)</sup>; right) the corresponding cyclic voltammetry (CV) shows oxidation and reduction peaks within the cubic (4 V region, blue area;  $\text{LiMn}_2\text{O}_4$ ) and tetragonal (3 V region, red area;  $\text{Li}_2\text{Mn}_2\text{O}_4$ ) phases, respectively, and the range for the utilizable working potential for LIBs (green box) <sup>(data provided by A. Droisner/Varta Micro Innovation GmbH, edited by author)</sup> .....34

Figure 35: left) variation of the conductivity of  $\text{LiClO}_4$  in a mixed electrolyte PC/DME with different electrolyte compositions for two salt concentrations,  $c = 0.1 \text{ mol}\cdot\text{l}^{-1}$  (black curve) and  $c = 1.0 \text{ mol}\cdot\text{l}^{-1}$  (red curve) <sup>(drawn from (152))</sup>; right) dependency of the conductivity of salt concentrations without varying the solvent composition <sup>(revision from (32))</sup> .....39

Figure 36: sketch draft of the SEI formation during cycling for a) on carbonaceous and b) metallic host materials; the different formations of the SEI arising due to different volume changes of metal compounds and graphite during lithiation/delithiation are depicted as shaded areas <sup>(revision from (146))</sup> .....41

Figure 37: schematic composition of the solid electrolyte interphase (SEI) on a graphite surface in non-aqueous organic electrolytes; on other anodes (lithium metal, lithium alloys) the SEI formation can be found as well <sup>(drawn from (142))</sup> .....41

Figure 38: reductive decomposition of organic solvents like cyclic carbonates (EC, PC; green and red arrows) and linear carbonates (DEC, DMC; blue arrows) on anode surfaces <sup>(revision from (38), (176) (178))</sup> .....42

Figure 39: nucleophilic attack by  $\text{LiOH}$  on a cyclic carbonate solvent leading to lithium-carbonate <sup>(revision from (38), (176))</sup> .....43

Figure 40: left) schematic of lithium intercalation into graphite <sup>(drawn from (33))</sup>; right) solvated  $\text{Li}^+$ -ions are intercalated and form a ternary graphite intercalation compound (GIC)  $\text{Li}_x(\text{solv})_y\text{C}_n$ , which leads to an extreme volume expansion of about 150 % <sup>(183)</sup> .....44

Figure 41: potential regions in which SEI formation should occur, namely before  $\text{Li}^+$ -intercalation into graphite  $\text{LiC}_n$  and/or solvated lithium intercalation  $\text{Li}_x(\text{solv})_y\text{C}_n$  into graphite takes place <sup>(revision from (146))</sup> .....44

Figure 42: cyclic voltammetry behaviors of different spinels of the compound a)  $\text{LiMn}_2\text{O}_4$ , b)  $\text{LiFe}_{0.5}\text{Mn}_{1.5}\text{O}_4$ , c)  $\text{LiCo}_{0.5}\text{Mn}_{1.5}\text{O}_4$ , and d)  $\text{LiNi}_{0.5}\text{Mn}_{1.5}\text{O}_4$  with the electrolyte system EC/DEC (1:1, v:v), 1 M  $\text{LiPF}_6$  at a scan rate of  $0.2 \text{ mV}\cdot\text{s}^{-1}$  <sup>(drawn from (186))</sup> .....45

Figure 43: left) measured cyclic voltammogram (CV) of the BASF  $\text{LiNi}_{0.5}\text{Mn}_{1.5}\text{O}_4$  (NMO) spinel with the electrolyte system EC/DEC (3:7, v:v), 1 M  $\text{LiPF}_6$  and a scan rate of  $0.1 \text{ mV}\cdot\text{s}^{-1}$ ; right) typical discharge profile of this NMO spinel (blue dashed line symbolizes the border between oxidized or reduced redox-couple Mn and Ni <sup>(source of both diagrams: author)</sup> .....46

Figure 44: left) draft diffusion pathway of lithium into the disordered  $\text{LiNi}_{0.5}\text{Mn}_{1.5}\text{O}_4$  (Fd-3m) spinel <sup>(drawn from (193))</sup>; right) two possible lithium diffusion pathways into the ordered  $\text{LiNi}_{0.5}\text{Mn}_{1.5}\text{O}_4$  (P4<sub>3</sub>2) spinel <sup>(drawn from (201))</sup> .....47

Figure 45: in-situ XRD patterns of disordered NMO spinel (left) and ordered NMO spinel (right) showing their phase transitions during cycling <sup>(revision from (203))</sup> .....47

Figure 46: left) charge and discharge voltage profiles of disordered  $\text{LiNi}_{0.5}\text{Mn}_{1.5}\text{O}_4$  (Fd-3m) spinel and ordered  $\text{LiNi}_{0.5}\text{Mn}_{1.5}\text{O}_4$  (P4<sub>3</sub>2) spinel; right) cycle performance of the different spinel phases between 3.5 V and 4.9 V vs.  $\text{Li}/\text{Li}^+$  at 0.2 C <sup>(both illustrations from (202))</sup> .....48

Figure 47: left) comparison of main cathode materials showing their typical charge and discharge profiles at characteristic voltages <sup>(drawn from (191))</sup>; right) table of theoretical capacities of left depicted cathode materials (colored) and two anodes (grey) <sup>(values obtained from (78), (104), (122), (190))</sup> .....48

Figure 48: left) coating process of the electrode paste (slurry) onto the current collector <sup>(32)</sup>; right) glastube furnish (Büchi) of the drying process of several electrode types <sup>(207)</sup> .....51

Figure 49: schematic drawing of the Swagelok®-test cell for all electrochemical measurements showing the three electrode arrangement <sup>(revision from (137))</sup> .....51

Figure 50: example of the applied voltage leading to the triangle voltage method <sup>(drawn from (210))</sup> .....53

Figure 51: typical cyclic voltammogram (CV) of the BASF  $\text{LiNi}_{0.5}\text{Mn}_{1.5}\text{O}_4$  (NMO) electrode in combination with the electrolyte system EC/PC (1:1, v:v), 1M  $\text{LiPF}_6$  within the voltage area 3.0 V and 5.2 V vs.  $\text{Li}/\text{Li}^+$  and metallic lithium as counter electrode; the scan rate is  $0.1 \text{ mV}\cdot\text{s}^{-1}$  .....53

Figure 52: left) constant current cycling (CCC) of a not calendared BASF NMO spinel electrode in combination with the electrolyte system EC/PC (1:1, v:v), 1 M  $\text{LiPF}_6$  and metallic lithium as counter electrode (cycling conditions are given within the diagram; red boxes correspond to charge and black boxes

to discharge capacity, the yellow area indicates the capacity fade); right) selected discharge profiles of the CCC measurement and their specific energies (integration of the area beneath the discharge curve); the ellipse symbolizes the IR-drop.....54

Figure 53: graphic presentation of specific energy performance of every 10<sup>th</sup> cycle of the before shown CCC (cf. figure 52). .....55

Figure 54: scanning electron microscope (SEM) images of a not calendered BASF NMO cathode; magnification: left) x350 (the yellow line symbolizes 50 μm) and right) x1000 (the yellow line symbolizes 10 μm). .....56

Figure 55: X-ray fluorescence analysis of a cycled Li<sub>4</sub>Ti<sub>5</sub>O<sub>12</sub> electrode and scanning electron microscope (SEM) images investigate the constitution of a cycled BASF NMO cathode; magnifications of the SEM images: left) x50 (yellow line corresponds to 500 μm), top and bottom) x1000 (yellow line signifies 10μm); besides the dissolution of the active material layer electrolyte or separator decomposition products are detectable (white spots on the electrode surface). .....56

Figure 56: left) image of the used calendar machine; right) calendaring should minimize the active electrode surface to improve the cycling behavior of the NMO electrodes <sup>(source of both: author)</sup> .....57

Figure 57: left) constant current cycling (CCC) of a strongly calendered BASF NMO spinel in combination with the electrolyte system EC/PC (1:1, v:v), 1 M LiPF<sub>6</sub> and metallic lithium as counter electrode; right) selected discharge profiles of the CCC measurement and their specific energies (integration of the area beneath the discharge curve).....58

Figure 58: graphic presentation of specific energy performance of every 10<sup>th</sup> cycle of the before shown CCC (cf. figure 57, page 58).....58

Figure 59: scanning electron microscope (SEM) images from a strongly calendered BASF NMO electrode show even the grooves of the calender coils (red ellipses); magnification: left) x350 (yellow line symbolizes 50 μm), right) x2000 (yellow line symbolizes 10 μm). .....59

Figure 60: schematic illustration of the state of the art single particle coating of active materials like Li<sub>0.5</sub>Mn<sub>1.5</sub>O<sub>4</sub>, which are prepared as electrodes after the coating process <sup>(source: author)</sup> .....60

Figure 61: draft of the artificial protective film on the surface of an already prepared electrode like the NMO spinel <sup>(source: author)</sup> .....61

Figure 62: schematic setup of a battery cell containing the hybrid electrolyte, which consists of the combination of an artificial solid electrolyte interphase and common liquid electrolyte system <sup>(source: author)</sup> .....61

Figure 63: cyclic voltammograms (CVs) of an unmodified BASF NMO electrode (both CVs constitute the same measurement; merely for a better visual difference between the first five cycles and their subsequent cycles the CVs are split); the used electrolyte system is EC/PC (1:1, v:v), 1M LiPF<sub>6</sub>, the voltage range is between 3.0 V and 5.2 V vs. Li/Li<sup>+</sup> and the scan rate is 0.1 mV·s<sup>-1</sup>. .....63

Figure 64: cyclic voltammograms of a modified BASF NMO electrode (both CVs constitute the same measurement; merely for a better visual difference between the first five cycles and their subsequent cycles the CVs are split); the used electrolyte system is EC/PC (1:1, v:v), 1M LiPF<sub>6</sub>, the voltage area is between 3.0 V and 5.2 V vs. Li/Li<sup>+</sup> and the scan rate is 0.1 mV·s<sup>-1</sup>. .....64

Figure 65: direct comparison of the obtained capacities and efficiencies of the before shown CVs (top on the left) unmodified NMO electrode; top on the right) modified NMO electrode; following the orange arrows these CV capacities are plotted within the bottom. ....65

Figure 66: left) constant current cycling (CCC) of a calendered and SiO<sub>2</sub> coated BASF NMO spinel in combination with the electrolyte system EC/PC (1:1, v:v), 1 M LiPF<sub>6</sub> and metallic lithium as counter electrode; right) selected discharge profiles of the CCC measurement and their specific energies (integration of the area beneath the discharge curve). .....66

Figure 67: graphic presentation of specific energy performance of every 10<sup>th</sup> cycle of the before shown CCC (cf. figure 66, page 66).....66

Figure 68: scanning electron microscope (SEM) images from a calendered and coated BASF NMO electrode; magnification: left) x350 (yellow line symbolizes 50  $\mu\text{m}$ ), right) x2000 (yellow line symbolizes 10  $\mu\text{m}$ ). .....67

Figure 69: left) constant current cycling (CCC) of a calendered and  $\text{SiO}_2$  coated BASF NMO electrode (sandwich-type) in combination with the electrolyte system EC/PC (1:1, v:v), 1 M  $\text{LiPF}_6$  and metallic lithium as counter electrode; right) selected discharge profiles of the CCC measurement and their specific energies (integration of the area beneath the discharge curve). .....67

Figure 70: comparison of the specific discharge capacities obtained during the before shown constant current cycling; left) every 10<sup>th</sup> cycle is depicted up to the 100<sup>th</sup> and right) every cycle up to the 20<sup>th</sup>. .....68

Figure 71: comparison of the calendered (the two plots on the left side) and the  $\text{SiO}_2$  coated (sandwich-type) BASF NMO electrode (both plots on the right side). .....68

Figure 72: cyclic voltammogram of the BASF NMO electrode vs. metallic lithium with the electrolyte system PC 1 M  $\text{LiPF}_6$ ; the voltage range is appointed to 2.8 V and 6.5 V vs.  $\text{Li/Li}^+$ , the scan rate is 0.2  $\text{mV}\cdot\text{s}^{-1}$ ; the red ellipse signifies the irreversible electrolyte degradation. ....69

Figure 73: anodic degradation reactions of propylene-carbonate into propylene-oxide, propanal, 2-ethyl-4-methyl-1,3-dioxalane (reactions with red arrows), while electrolyte impurities like HF and  $\text{H}_2\text{O}$  lead the formation of carbon-dioxide and lithium-carbonate on lithium surface (reactions with purple arrows) <sup>(49), (225)</sup> .....70

Figure 74: 1<sup>st</sup> cycle of the cyclic voltammetry in which an unmodified BASF NMO electrode in combination with the electrolyte system EC/PC (1:1, v:v), 1M  $\text{LiPF}_6$  was measured within a voltage area between 3.5 V and 4.9 V vs.  $\text{Li/Li}^+$ ; the scan rate was appointed to 0.1  $\text{mV}\cdot\text{s}^{-1}$ . .....72

Figure 75: mass spectrometric data for cleavage products like propane ( $\text{C}_3\text{H}_8$ ; left) and carbon-dioxide ( $\text{CO}_2$ ; right) from the NIST database <sup>(229), (230)</sup> .....72

Figure 76: three-dimensional constitution of the mass spectrometric data ranges of possible electrolyte degradation, which correspond to the before shown CV of the unmodified BASF NMO electrode during the 1<sup>st</sup> cycle; top) MS range including the range from oxygen to carbon-dioxide, bottom left) enlarged MS range for the  $\text{O}_2$  release, bottom right) enlarged MS range for the evolution of  $\text{CO}_2$ . .....73

Figure 77: schematic of different tunings of the MS-device: the blue peak (no. 1.) appears in the case of an optimal calibrated MS, the red one (no. 2.) for a moderate “tune-up” and the green line (no. 3.) arises from a not perfect calibrated MS <sup>(source: author)</sup> .....73

Figure 78: second cycle of the cyclic voltammetry in which an unmodified BASF NMO electrode in combination with the electrolyte system EC/PC (1:1, v:v), 1M  $\text{LiPF}_6$  was measured within a voltage area between 3.5 V and 4.9 V vs.  $\text{Li/Li}^+$ ; the scan rate was appointed to 0.1  $\text{mV}\cdot\text{s}^{-1}$ . .....74

Figure 79: three-dimensional constitution of the mass spectrometric data range of a possible oxygen release (MS range within left image) and carbon-dioxide evolution (MS range within the right image) of the unmodified BASF NMO electrode during the 2<sup>nd</sup> cycle of the cyclic voltammogram. ....74

Figure 80: third cycle of the cyclic voltammetry in which an unmodified BASF NMO electrode in combination with the electrolyte system EC/PC (1:1, v:v), 1M  $\text{LiPF}_6$  was measured within a voltage area between 3.5 V and 6.0 V vs.  $\text{Li/Li}^+$ ; the scan rate was appointed to 0.1  $\text{mV}\cdot\text{s}^{-1}$ . .....75

Figure 81: three-dimensional constitution of the mass spectrometric data range of a possible oxygen release (MS range within left image) and carbon-dioxide evolution (MS range within the right image) of the unmodified BASF NMO electrode during the 3<sup>rd</sup> cycle of the cyclic voltammogram. ....75

Figure 82: 1<sup>st</sup> cycle of the cyclic voltammetry in which a modified BASF NMO electrode in combination with the electrolyte system EC/PC (1:1, v:v), 1M  $\text{LiPF}_6$  was measured within a voltage area between 3.5 V and 4.9 V vs.  $\text{Li/Li}^+$ ; the scan rate was appointed to 0.1  $\text{mV}\cdot\text{s}^{-1}$ . .....77

Figure 83: three-dimensional constitution of the mass spectrometric data ranges of possible electrolyte degradation, which correspond to the before shown CV of the modified BASF NMO electrode during the 1<sup>st</sup> cycle; top) MS range including the range from oxygen to carbon-dioxide, bottom left) enlarged MS range for the  $\text{O}_2$  release, bottom right) enlarged MS range for the evolution of  $\text{CO}_2$ . .....77

Figure 84: 2<sup>nd</sup> cycle of the cyclic voltammetry in which a modified BASF NMO electrode in combination with the electrolyte system EC/PC (1:1, v:v), 1M LiPF<sub>6</sub> was measured within a voltage area between 3.5 V and 4.9 V vs. Li/Li<sup>+</sup>; the scan rate was appointed to 0.1 mV·s<sup>-1</sup>. .....78

Figure 85: three-dimensional constitution of the mass spectrometric data range of a possible oxygen (MS range within left image) and carbon-dioxide evolution (enlarged MS range within the right image) of the modified BASF NMO electrode during the 2<sup>nd</sup> cycle of the cyclic voltammogramm. ....78

Figure 86: 3<sup>rd</sup> cycle of the cyclic voltammetry in which a modified BASF NMO electrode in combination with the electrolyte system EC/PC (1:1, v:v), 1M LiPF<sub>6</sub> was measured within a voltage area between 3.5 V and 6.0 V vs. Li/Li<sup>+</sup>; the scan rate was appointed to 0.1 mV·s<sup>-1</sup>. .....79

Figure 87: three-dimensional constitution of the mass spectrometric data range of a possible oxygen (MS range within left image) and carbon-dioxide evolution (enlarged MS range within the right image) of the modified BASF NMO electrode during the 3<sup>rd</sup> cycle of the cyclic voltammogramm.....79

Figure 88: comparison of the entire cyclic voltammetry measurements in which an unmodified (left CV) and a modified (right CV) BASF NMO electrode in combination with the electrolyte system EC/PC (1:1, v:v), 1M LiPF<sub>6</sub> were measured within a voltage area between 3.5 V and 4.9 V (or 6.0 V for the 3<sup>rd</sup> cycle) vs. Li/Li<sup>+</sup>; the scan rate was appointed to 0.1 mV·s<sup>-1</sup> for both.....80

Figure 89: obtained mass spectrometric data including both gaseous electrolyte degradation products (CO<sub>2</sub> and O<sub>2</sub>) during cyclic voltammetry up to 6.0 V vs. Li/Li<sup>+</sup> in which a BASF NMO electrode was used: left) unmodified cathode, right) modified cathode. ....80

Figure 90: modified Swagelok®-cell; the yellow ellipse marks the pressure sensor <sup>(source: author)</sup> .....81

Figure 91: cyclic voltammogramm (CV) of an industrial manufactured Li<sub>4</sub>Ti<sub>5</sub>O<sub>12</sub> (LTO) electrode (Kokam) with the electrolyte system EC/PC (1:1, v:v), 1M LiPF<sub>6</sub>, the voltage area is between 0.9 V and 2.8 V vs. Li/Li<sup>+</sup> and the scan rate is 0.05 mV·s<sup>-1</sup>. .....82

Figure 92: constitution of the entire constant current cycling: top) constant current cycling of the full cell LTO/NMO in combination with the electrolyte system EC/PC (1:1, v:v), 1 M LiPF<sub>6</sub> between 3.5 V and 4.9 V vs. Li/Li<sup>+</sup>; middle) time based constant current cycling of the same measurement and bottom) in-situ detection of pressure evoked during the same constant current cycling.....83

Figure 93: constitution of the entire constant current cycling: top) constant current cycling of the full cell LTO/NMO<sub>modified</sub> in combination with the electrolyte system EC/PC (1:1, v:v), 1 M LiPF<sub>6</sub> between 3.5 V and 4.9 V vs. Li/Li<sup>+</sup>; middle) time based constant current cycling of the same measurement and bottom) in-situ detection of pressure evoked during the same constant current cycling.....85

Figure 94: scanning electron microscope (SEM) images from BASF NMO batch A (left) and batch B (right); magnification of both is x1,000. ....88

Figure 95: scanning electron microscope (SEM) images from BASF NMO batch A (left) and batch B (right); magnification of both is x5,000. ....88

Figure 96: scanning electron microscope (SEM) images of single particles from BASF NMO batch A (left) and batch B (right); magnification of both is x10,000. ....89

Figure 97: 3D image of the before shown BASF NMO particle of the batch B (for the 3D effect please use the glasses attached, which is attached in the last page of this doctoral thesis!). .....89

Figure 98: scanning electron microscope (SEM) images from not calendered BASF NMO electrodes containing batch A (left) and batch B (right) as active material; magnification of both is x5,000.....90

Figure 99: scanning electron microscope (SEM) images from calendered BASF NMO electrodes containing batch A (left) and batch B (right) as active material; magnification of both is x5,000. ....90

Figure 100: three dimensional image of a calendered BASF NMO electrode of batch B; the color bar on the bottom right determines the depth of the holes between particles of the electrode. ....91

Figure 101: 3D image of the before shown calendered BASF NMO electrode from batch B (for the 3D effect please use the glasses, which is attached in the last page of this doctoral thesis!). .....91

Figure 102: constant current cycling (CCC) of BASF NMO spinel batch A (left) and batch B (right) in combination with the electrolyte system EC/DEC (3:7, v:v), 1 M LiPF<sub>6</sub> and metallic lithium as counter electrode. ....92

Figure 103: constant current cycling (CCC) of BASF NMO spinel batch A (left) and batch B (right) with different current charging (C-rates); as electrolyte system EC/DEC (3:7, v:v), 1 M LiPF<sub>6</sub> and as counter electrode metallic lithium are used. ....92

Figure 104: direct comparison potential profiles during the C-rate tests including the self-discharge behavior of NMO batch A (left) and NMO batch B (right). ....93

Figure 105: XRD profiles of both BASF NMO batches; left) batch A, right) batch B.....94

Figure 106: TEM bright field image of NMO batch A (left) and electron diffraction patterns of batch A (middle) and batch B (right). ....94

Figure 107: in the middle of this illustration typical CVs of graphite and NMO are depicted, while beside them reduction and oxidation of vinylene monomers on anode and cathode surface are shown <sup>(drawn from (232), (234))</sup> .....96

Figure 108: mechanism of polymerization of reduction-type additives <sup>(drawn from (233))</sup> .....97

Figure 109: cyclic voltammogram (CV) of the BASF NMO cathode (batch B) with the electrolyte system EC/DEC (3:7, v:v) + 2 v% FEC, 1M LiPF<sub>6</sub>, cycled between 3.5 V and 4.9 V vs. Li/Li<sup>+</sup> against metallic lithium, the scan rate was appointed to 0.1 mV·s<sup>-1</sup>. ....97

Figure 110: constitution of the formation of HF from a FEC molecule leading to VC at least <sup>(drawn from (233))</sup> ...98

Figure 111: left) CCC of the BASF NMO spinel (batch B) in combination with the electrolyte system EC/DEC (3:7, v:v) + 2 v% FEC, 1 M LiPF<sub>6</sub> and metallic lithium as counter electrode; right) selected discharge profiles of the CCC measurement and their specific energies. ....98

Figure 112: comparison of specific discharge capacity and specific energy performance for every 10<sup>th</sup> cycle during the entire CCC; the loss of capacity amounts to 9.76 % and the loss of specific energy amounts to 10.68 % .....98

Figure 113: SEM images of the BASF NMO cathode (batch B) after the CCC in which VC (top left and top right) or FEC (bottom left and bottom right) was added to EC/DEC (3:7, v:v), 1 M LiPF<sub>6</sub> .....99

Figure 114: cyclic voltammogram (CV) of the BASF NMO cathode with the electrolyte system EC/DEC (3:7, v:v) + 1 v% AN, 1M LiPF<sub>6</sub>, cycled between 3.5 V and 4.9 V vs. Li/Li<sup>+</sup> against metallic lithium, the scan rate was appointed to 0.1 mV·s<sup>-1</sup>. ....100

Figure 115: left) CCC of the BASF NMO spinel in combination with the electrolyte system EC/DEC (3:7, v:v) + 1 v% AN, 1 M LiPF<sub>6</sub> and metallic lithium as counter electrode; right) selected discharge profiles of the CCC measurement and their specific energies. ....101

Figure 116: comparison of specific discharge capacity and specific energy performance for every 10<sup>th</sup> cycle during the entire CCC; the loss of capacity amounts to 12.70 % and the loss of specific energy amounts to 13.50 % .....101

Figure 117: SEM images of the BASF NMO cathode after the CCC in which fumaro-nitrile (top left and top right) or acrylo-nitrile (bottom left and bottom right) was added to EC/DEC (3:7, v:v), 1 M LiPF<sub>6</sub>. ....102

Figure 118: cyclic voltammogram (CV) of the BASF NMO cathode with the electrolyte system EC/DEC (3:7, v:v) + 1 v% ES, 1M LiPF<sub>6</sub>, cycled between 3.5 V and 4.9 V vs. Li/Li<sup>+</sup> against metallic lithium; the scan rate was appointed to 0.1 mV·s<sup>-1</sup>. ....103

Figure 119: left) CCC of the BASF NMO spinel in combination with the electrolyte system EC/DEC (3:7, v:v) + 5 v% ES, 1 M LiPF<sub>6</sub> and metallic lithium as counter electrode; right) selected discharge profiles of the CCC measurement and their specific energies. ....104

Figure 120: comparison of specific discharge capacity and specific energy performance for every 10<sup>th</sup> cycle during the entire CCC; the loss of capacity amounts to 8.23 % and the loss of specific energy amounts to 9.02 % .....104

Figure 121: SEM images of the BASF NMO cathode after the CCC in which 2-chloro-4-phenylthiocyanate (top left and top right) or ethylene-sulfite (bottom left and bottom right) was added to EC/DEC (3:7, v:v), 1 M LiPF<sub>6</sub>.....105

Figure 122: Al current collector corrosion during a cyclic voltammogramm of a BASF NMO electrode in combination with EC/ADN (1:1, v:v), 1 M LiTFSI cycled between 3.5 V and 4.9 V vs. Li/Li<sup>+</sup> against metallic lithium as counter electrode, the scan rate is appointed to 0.1 mV·s<sup>-1</sup>.....109

Figure 123: cyclic voltammogramm (CV) of the BASF NMO cathode with the electrolyte system EC/ADN (1:1, v:v), 1 M LiTFSI + 0.1 M LiBOB cycled between 3.5 V and 4.9 V vs. Li/Li<sup>+</sup> against lithium metal as counter electrode, the scan rate is appointed to 0.1 mV·s<sup>-1</sup>. .....109

Figure 124: left) CCC of the BASF NMO spinel in combination with the electrolyte system EC/ADN (1:1, v:v), 1 M LiTFSI + 0.1 M LiBOB and metallic lithium as counter electrode; right) performance of the voltage profiles within the first 20 cycles of the CCC, the dark blue arrow symbolizes ongoing electrolyte decomposition increasing impedance.....110

Figure 125: SEM images of the BASF NMO cathode after the before shown CCC in which EC/ADN (1:1, v:v), 0.9 M LiTFSI + 0.1 M LiBOB was used, magnifications: left) x10,000, right) x20,000.....110

Figure 126: left) CCC of the NMO electrode with the LiBOB substituted electrolyte system EC/ADN (1:1, v:v), 1 M LiTFSI + 0.1 M LiPF<sub>6</sub>, right) SEM image of the cycled electrode with a magnification of x10,000. ....111

Figure 127: performance of a full cell containing graphite and the BASF NMO spinel in combination with the electrolyte system EC/DEC (3:7, v:v), 1 M LiPF<sub>6</sub>; the demonstrated specific capacities are referred to the amount of the active mass of the NMO cathode.....112

Figure 128: left) performance of the anode potential (black line), cathode potential (green line) and of the entire cell potential (blue line) during 100 cycles of the constant current cycling (cf. figure 127, page 112); additionally, the progress of the current is constituted as red line; right) enlargement of all potentials for the first three cycles (the ellipse denotes the relaxation of the anode potential). .....113

Figure 129: performance of a slowly charged full cell containing graphite and the BASF NMO spinel in combination with the electrolyte system EC/DEC (3:7, v:v), 1 M LiPF<sub>6</sub>; the demonstrated specific capacities are referred to the amount of the active mass of the NMO cathode.....114

Figure 130: left) performance of the anode potential (black line), cathode potential (green line) and of the entire cell potential (blue line) during 100 cycles of the constant current cycling (cf. figure 129, page 114); additionally, the progress of the current is constituted as red line; right) enlargement of all potentials for the first three cycles (the ellipse denotes the relaxation of the anode potential). .....114

Figure 131: performance of the full cell graphite/NMO with a formation process within the first three cycles; as electrolyte system EC/DEC (3:7, v:v), 1 M LiPF<sub>6</sub> in combination with a Separion<sup>®</sup> separator instead of the before used Freudenberg 2126 separator is used; the demonstrated specific capacities are referred to the amount of the active mass of the NMO cathode. ....115

Figure 132: left) performance of the anode potential (black line), cathode potential (green line) and of the entire cell potential (blue line) during 100 cycles of the constant current cycling (cf. figure 131, page 115); additionally, the progress of the current is constituted as red line; right) enlargement of all potentials after the three formation cycles. ....115

Figure 133: performance of the full cell graphite/NMO with a formation process within the first three cycles; as electrolyte system EC/DEC (3:7, v:v), 1 M LiPF<sub>6</sub> in combination with a Separion<sup>®</sup> separator is used; the demonstrated specific capacities are referred to the amount of the active mass of the NMO cathode. ....116

Figure 134: left) performance of the anode potential (black line), cathode potential (green line) and of the entire cell potential (blue line) during the 100 cycles of the constant current cycling (cf. figure 133, page 116); additionally, the progress of the current is constituted as red line; right) enlargement of all potentials after the three formation cycles. ....116

Figure 135: comparison of obtained specific energies (cf. figure 133, page 116) and idealized data from a graphite/NMO full cell; the average discharge voltages of the first ten cycles and the subsequent 10<sup>th</sup> cycle are depicted (blue line); the orange colored line corresponds to ideal calculated specific energies (without any lithium loss) which such a full cell could provide. ....117

Figure 136: cyclic voltammetry of the BASF NMO electrode in combination with the electrolyte system EC/DEC (3:7, v:v), 1M LiPF<sub>6</sub> within the voltage area 3.5 V and 5.2 V vs. Li/Li<sup>+</sup>; the scan rate is 0.1 mV·s<sup>-1</sup>....118

Figure 137: cyclic voltammetry of the graphite electrode in combination with the electrolyte system EC/DEC (3:7, v:v), 1M LiPF<sub>6</sub> within the voltage area 3.5 V and 0.0 V vs. Li/Li<sup>+</sup>; the scan rate is 0.03 mV·s<sup>-1</sup>..118

Figure 138: SEM images of a pristine (left) and calendered (right) graphite electrode; both magnifications: x1,000. ....119

Figure 139: SEM illustrations of a pristine, calendered (left) and a cycled (right) graphite electrode after CCC; both magnifications: x10,000.....120

Figure 140: EDX including mapping results of a cycled graphite electrode from the full cell (measurement not shown within this doctoral thesis).....120

## 5.3 Explanation of Abbreviations

### 5.3.1 Table of Chemicals

ADN	adiponitrile
$\text{Al}_2(\text{CO}_3)_3$	aluminum-carbonate
$\text{Al}_2\text{O}_3$	aluminum-oxide
$\text{AlF}_3$	aluminum-trifluoride
AN	acrylo-nitrile
$\text{AsF}_5$	arsenic-pentafluoride
$\text{BF}_3$	boron-trifluoride
BiOF	bismuth-oxyfluoride
BN	butyro-nitrile
$\text{C}_2\text{H}_4$	ethene
$\text{C}_2\text{H}_6$	ethane
$\text{C}_3\text{H}_6$	propene
$\text{C}_3\text{H}_8$	propane
$\text{CH}_4$	methane
CO	carbon-monoxide
$\text{CO}_2$	carbon-dioxide
CPT	2-chloro-4-phenylthiocyanate
DEC	diethyl-carbonate
DMA	dimethyl-trifluoroacetamide
DMC	dimethyl-carbonate
DME	dimethoxy-ethane
DOD	1,3,2-dioxathiolane-2,2-dioxide
EA	ethylacetate
EB	ethylbutyrate
EC	ethylene-carbonate
EMC	ethyl-methyl-carbonate
ES	ethylene-sulfite
$\text{F}_2\text{EC}$	difluoroethylene-carbonate
$\text{Fe}_3\text{O}_4$	iron-oxide
FEC	fluoroethylene-carbonate
FN	fumaro-nitrile
FPI	4-fluorophenyl-isocyanate
GBL	$\gamma$ -butyrolactone
GVL	$\gamma$ -valerolactone
HF	hydrofluoric-acid
HT-LiCoO <sub>2</sub>	high temperature lithium-cobalt-oxide
IL	ionic liquids
KOH	potassium-hydroxide

KS-6	special graphite
LCO	lithium-cobalt-oxide
LFP	lithium-iron-phosphate
$\text{Li}_2\text{C}_2\text{O}_4$	lithium-oxalate
$\text{Li}_2\text{CO}_3$	lithium-carbonate
$\text{Li}_2\text{Mn}_2\text{O}_4$	lithiated $\text{LiMn}_2\text{O}_4$
$\text{Li}_2\text{O}$	lithium-oxide
$\text{Li}_3\text{PO}_4$	lithium-phosphate
$\text{Li}_4\text{Ti}_5\text{O}_{12}$	lithium-titanate
$\text{LiAsF}_6$	lithium-hexafluoroarsenate
$\text{LiBF}_4$	lithium-tetraborate
LIBOB	lithium-bis (oxalate) borate
$\text{LiClO}_4$	lithium-perchlorate
$\text{LiCoO}_2$	lithium-cobalt-oxide
$\text{LiCoPO}_4$	lithium-cobalt-phosphate
$\text{LiF}$	lithium-fluoride
$\text{LiFe}_{0.5}\text{Mn}_{1.5}\text{O}_4$	iron-manganese spinel
$\text{LiFePO}_4$	lithium-iron-phosphate
$\text{LiMn}_2\text{O}_4$	lithium
$\text{LiMnPO}_4$	lithium-manganese-phosphate
$\text{LiNi}_{0.5}\text{Mn}_{1.5}\text{O}_4$	nickel-manganese spinel
$\text{LiNi}_{1/3}\text{Mn}_{1/3}\text{Co}_{1/3}\text{O}_2$	nickel-manganese-cobalt-oxide
$\text{LiNiO}_2$	lithium-nickeloxide
$\text{LiNiPO}_4$	lithium-nickel-phosphate
$\text{LiO}_2\text{C-CH}_2\text{CH}_2\text{CO}_2\text{Li}$	lithium-succinate
$\text{LiOCH}_3$	lithium-methoxide
$\text{LiOH}$	lithium-hydroxide
$\text{LiPF}_6$	lithium-hexafluorophosphate
LiPON	lithium-phosphor-oxynitride
LiSICON	lithium-superionic-conductor
LiTFSI	lithium-bis-(trifluoro-methanesulfonyl)-imide
LT-LiCoO <sub>2</sub>	low-temperature lithium-cobalt-oxide
LTO	lithium-titanate
MB	methylbutyrate
MgO	magnesium-oxide
MO	2-methyl-2-oxazoline
NaCl	sodium-chloride
NASICON	sodium-superionic-conductor
NiCd	nickel-cadmium
NMC	nickel-manganese-cobalt-oxide
NMO	nickel-manganese spinel
NMO	3-methyl-2-oxazolidinone
NMP	N-methyl-2-pyrrolidone

NO <sub>x</sub>	nitrogen-oxides
PC	propylene-carbonate
PEO	polyethylene-oxide
PF <sub>5</sub>	phosphor-pentafluoride
PFA	perfluoroalkoxyl-alkane
PI	phenyl-isocyanate
POF <sub>3</sub>	phospor-oxytrifluoride
PP	polypropylene
PVdF	polyvinylidene-difluoride
S <sub>1</sub>	benzene-sulfonicacid-2-propinylester
SiO <sub>2</sub>	silicon-oxide
SN	succino-nitrile
SnO <sub>2</sub>	tin-oxide
TiO <sub>2</sub>	titanium-dioxide
TiS <sub>2</sub>	titanium-sulfide
V <sub>2</sub> O <sub>5</sub>	vanadium-oxide
VC	vinylene-carbonate
VN	valero-nitrile
ZrO <sub>2</sub>	zirconium-oxide
α-NaFeO <sub>2</sub>	sodium-iron-oxide
λ-MnO <sub>2</sub>	manganese-oxide

### 5.3.2 Table of Miscellaneous Abbreviations

ΔG	free enthalpy
ΔH	enthalpy
Δ <sub>R</sub> G	free reaction enthalpy
Δ <sub>R</sub> G <sup>0</sup>	free reaction enthalpy at standard conditions
ΔS	entropy
μ	chemical potential of a substance <i>J</i>
μ <sup>0</sup>	chemical potential at standard conditions
aq	aqueous
c	concentration
CCC	constant current cycling
CE	counter electrode
C <sub>irr</sub>	irreversible capacity
CV	cyclic voltammogram/voltammetry
DOD	depth of discharge
E	equilibrium cell voltage or EMF
E <sup>0</sup>	standard electrode potential
EDX	energy-dispersive-X-ray spectroscopy

---

EMF	electromotoric force
ESD	electrospray-deposition
EV	electric vehicle
F	Faraday constant ( $96485 \text{ C}\cdot\text{mol}^{-1}$ )
FLAPW	full-potential linearized augmented-plane-wave method
G	reaction enthalpy
g	gaseous
GC	gas chromatography
GIC	graphite intercalation compound
HDS	high dielectric solvents
HEV	hybrid electric vehicle
I	current
IHP	inner Helmholtz plane
jA	anodic current density
jC	cathodic current density
LIB	Lithium-Ion-Battery
Li-GIC	lithium-graphite-intercalation-compounds
LiPB	Lithium-Ion-Polymer-Batteries
LVS	low viscosity solvents
MS	mass spectrometer
n	amount of a substance
OCV	open circuit voltage
OHP	outer Helmholtz plane
P	electric power
Q	charge
R	universal gas constant ( $8.314 \text{ J}\cdot\text{K}^{-1}\cdot\text{mol}^{-1}$ )
RE	reference electrode
SEI	solid electrolyte interphase
SEM	scanning electron microscope
SHE	standard hydrogen electrode
SOC	state of charge
T	temperature
TEM	transmission electron microscope
U	voltage
WE	working electrode
XRD	X-ray diffraction
XRF	X-ray fluorescence analysis
z	number of exchanged electrons
$\epsilon$	dielectric constant
$\eta$	viscosity
$\eta$	overpotential
v	stoichiometric factor
$\xi$	reaction duration